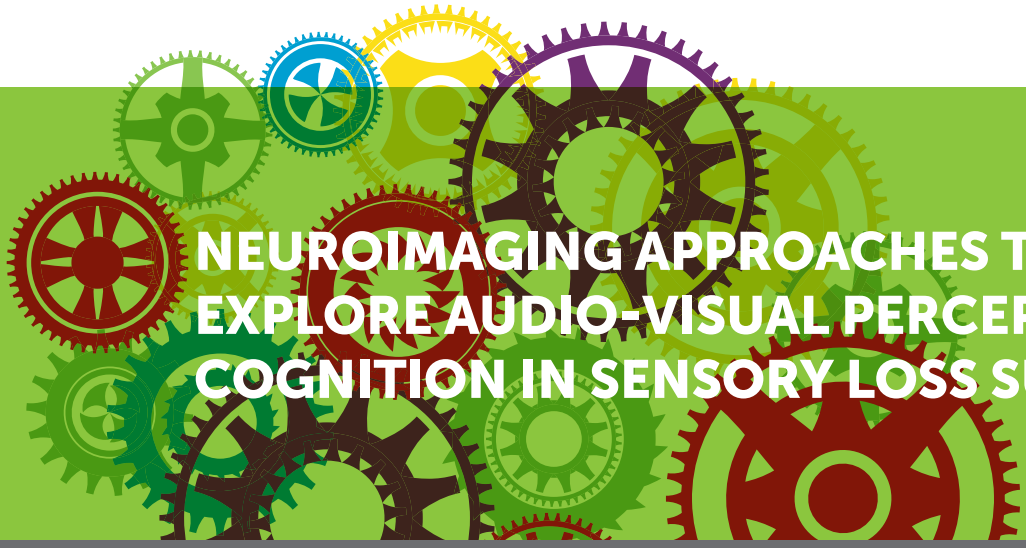

NEUROIMAGING APPROACHES TO EXPLORE AUDIO-VISUAL PERCEPTION AND COGNITION IN SENSORY LOSS SUBJECTS

EDITED BY: Yuexin Cai, Yu-Chen Chen, Han Lv, Jae-Jin Song and Vijaya Prakash Krishnan Muthaiah

PUBLISHED IN: Frontiers in Human Neuroscience and Frontiers in Neuroscience

frontiers Research Topics

frontiers

ISSN 1664-8714
ISBN 978-2-88976-959-9
DOI 10.3389/978-2-88976-959-9

About Frontiers

Frontiers is more than just an open-access publisher of scholarly articles: it is a pioneering approach to the world of academia, radically improving the way scholarly research is managed. The grand vision of Frontiers is a world where all people have an equal opportunity to seek, share and generate knowledge. Frontiers provides immediate and permanent online open access to all its publications, but this alone is not enough to realize our grand goals.

Frontiers Journal Series

The Frontiers Journal Series is a multi-tier and interdisciplinary set of open-access, online journals, promising a paradigm shift from the current review, selection and dissemination processes in academic publishing. All Frontiers journals are driven by researchers for researchers; therefore, they constitute a service to the scholarly community. At the same time, the Frontiers Journal Series operates on a revolutionary invention, the tiered publishing system, initially addressing specific communities of scholars, and gradually climbing up to broader public understanding, thus serving the interests of the lay society, too.

Dedication to Quality

Each Frontiers article is a landmark of the highest quality, thanks to genuinely collaborative interactions between authors and review editors, who include some of the world's best academicians. Research must be certified by peers before entering a stream of knowledge that may eventually reach the public - and shape society; therefore, Frontiers only applies the most rigorous and unbiased reviews.
Frontiers revolutionizes research publishing by freely delivering the most outstanding research, evaluated with no bias from both the academic and social point of view. By applying the most advanced information technologies, Frontiers is catapulting scholarly publishing into a new generation.

What are Frontiers Research Topics?

Frontiers Research Topics are very popular trademarks of the Frontiers Journals Series: they are collections of at least ten articles, all centered on a particular subject. With their unique mix of varied contributions from Original Research to Review Articles, Frontiers Research Topics unify the most influential researchers, the latest key findings and historical advances in a hot research area! Find out more on how to host your own Frontiers Research Topic or contribute to one as an author by contacting the Frontiers Editorial Office: frontiersin.org/about/contact

NEUROIMAGING APPROACHES TO EXPLORE AUDIO-VISUAL PERCEPTION AND COGNITION IN SENSORY LOSS SUBJECTS

Topic Editors:
Yuexin Cai, Sun Yat-sen University, China
Yu-Chen Chen, Nanjing Medical University, China
Han Lv, Capital Medical University, China
Jae-Jin Song, Seoul National University Bundang Hospital, South Korea
Vijaya Prakash Krishnan Muthaiah, University at Buffalo, United States

Citation: Cai, Y., Chen, Y.-C., Lv, H., Song, J.-J., Muthaiah, V. P. K., eds. (2022). Neuroimaging Approaches to Explore Audio-visual Perception and Cognition in Sensory Loss Subjects. Lausanne: Frontiers Media SA.
doi: 10.3389/978-2-88976-959-9

Table of Contents

frontiers in Human Neuroscience

ORIGINAL RESEARCH
published: 14 September 2021
doi: 10.3389/fnhum.2021.711713

Brain Activation Induced by Myopic and Hyperopic Defocus From Spectacles

Meng-Tian Kang[1,2†], *Bo Wang*[3†], *An-Ran Ran*[4], *Jiahe Gan*[1,2], *Jialing Du*[1,2], *Mayinuer Yusufu*[2], *Xintong Liang*[1,2], *Shi-Ming Li*[1,2*] and *Ningli Wang*[1,2*]

[1] Beijing Ophthalmology and Visual Science Key Lab, Beijing Tongren Eye Center, Beijing Tongren Hospital, Capital Medical University, Beijing, China, [2] Beijing Institute of Ophthalmology, Beijing Tongren Eye Center, Beijing Tongren Hospital, Capital Medical University, Beijing, China, [3] State Key Laboratory of Brain and Cognitive Science, Institute of Biophysics, Chinese Academy of Sciences, Beijing, China, [4] Department of Ophthalmology and Visual Sciences, The Chinese University of Hong Kong, Hong Kong, China

OPEN ACCESS

Edited by:
Han Lv,
Capital Medical University, China

Reviewed by:
Fang-Fang Yan,
University of Chinese Academy of Sciences, China
Ying Gao,
Institute of Automation (CAS), China

***Correspondence:**
Shi-Ming Li
lishiming81@163.com
Ningli Wang
wningli@vip.163.com

[†]These authors have contributed equally to this work and share first authorship

Specialty section:
This article was submitted to Sensory Neuroscience, a section of the journal Frontiers in Human Neuroscience

Received: 19 May 2021
Accepted: 28 July 2021
Published: 14 September 2021

Citation:
Kang M-T, Wang B, Ran A-R, Gan J, Du J, Yusufu M, Liang X, Li S-M and Wang N (2021) Brain Activation Induced by Myopic and Hyperopic Defocus From Spectacles. Front. Hum. Neurosci. 15:711713. doi: 10.3389/fnhum.2021.711713

Purpose: To assess neural changes in perceptual effects induced by myopic defocus and hyperopic defocus stimuli in ametropic and emmetropic subjects using functional magnetic resonance imaging (fMRI).

Methods: This study included 41 subjects with a mean age of 26.0 ± 2.9 years. The mean spherical equivalence refraction was −0.54 ± 0.51D in the emmetropic group and −3.57 ± 2.27D in the ametropic group. The subjects were instructed to view through full refractive correction, with values of +2.00D to induce myopic defocus state and −2.00D to induce hyperopic defocus state. This was carried over in three random sessions. Arterial spin labeling (ASL) perfusion was measured using fMRI to obtain quantified regional cerebral blood flow (rCBF). Behavioral tests including distant visual acuity (VA) and contrast sensitivity (CS), were measured every 5 min for 30 min.

Results: Myopic defocus induced significantly greater rCBF increase in four cerebral regions compared with full correction: right precentral gyrus, right superior temporal gyrus, left inferior parietal lobule, and left middle temporal gyrus ($P < 0.001$). The differences were less significant in low myopes than emmetropes. In the hyperopic defocus session, the increased responses of rCBF were only observed in the right and left precentral gyrus. Myopic defocused VA and CS improved significantly within 5 min and reached a plateau shortly after.

Conclusion: This study revealed that myopic defocus stimuli can significantly increase blood perfusion in visual attention-related cerebral regions, which suggests a potential direction for future investigation on the relationship between retinal defocus and its neural consequences.

Keywords: fMRI, myopia, defocus, neural change, arterial spin labeling

INTRODUCTION

Increasing evidence from a diverse range of animal studies indicates that ocular growth is strongly guided by visual error signals, specifically the optical defocus (Wildsoet, 1997; Wallman and Winawer, 2004). When myopic defocus induced by the lens (image-focused anterior to the retina) is imposed on the eyes of the animals, the eye rapidly compensates and becomes hyperopic by altering the depth of the vitreous chamber, increasing choroidal thickness, and slightly decreasing in ocular length (Wallman et al., 1995; Wildsoet and Wallman, 1995; Hung et al., 2000; Zhu et al., 2013). These responses function to reduce retinal blur and, thus, are generally accepted as a foundation for emmetropization, an optically guided process essential to the normal growth of the eye. In the study of Wildsoet and Wallman, they found that when interfering with neural communication between the retina and the brain of a chick by optic nerve section, hyperopic defocus induced myopia was impaired (Wildsoet and Wallman, 1995). However, little is known about what cues does the retina use to discern the defocus signal.

A perceptual mechanism has been shown to contribute to the regulation of image defocus. Blur adaption experiment suggested that myopic defocus could lead to visual function improvement as prolonged exposure to optical defocus would increase the ability to detect and recognize letters (Mon-Williams et al., 1998). In addition, blur adaptation improves the visual quality by adjusting the spatial frequency signal pathway through the neural adaptation process to maintain the spatial structure of the image (Webster et al., 2002). The study of Dillingham found that cutting the optic nerve nucleus of the isthmus (the connection between the central nervous system [CNS] and the retina) induced initial, transient hyperopia in the contralateral eye. This finding implicates ipsilaterally projecting centrifugal neurons in the regulation of emmetropization mechanisms, a process that may take over *via* nitric oxide/dopaminergic pathways. It further proves that light-dependent ocular development is closely related to the CNS (Dillingham et al., 2016).

The aim of the current study is to investigate two aspects of CNS and defocus stimuli: (1) the short-term effect of myopic and hyperopic defocus on cerebral blood flow (CBF), and (2) whether the response varies along with refractive status. Studying the effect of defocus signal on human brain function can facilitate our understanding of the changes in the human advanced nervous system caused by the optical correction.

METHODS

Subjects

A total of 41 subjects participated in this study. The inclusion criteria were as follows: (1) age ranged from 18 to 35 years, with either emmetropia or ametropia, (2) no more than 1.00D astigmatism and <1.50D anisometropia binocularly, and (3) had a normal or corrected-to-normal vision of logarithm of the minimum angle of resolution (logMAR) visual acuity (VA) 0.00 (Snellen 6/6 or 20/20) or better. The exclusion criteria were as follows: (1) any history of amblyopia, ocular pathologies, or other ocular anomalies (e.g., surgery, trauma) that might have influenced the measurement, and (2) any mental or nervous system disease, cardiovascular diseases, or other symptoms unsuitable for MRI scanning. Emmetrope was defined as having spherical equivalent refraction (SER) of +0.75D to −0.75D inclusive. Myope was defined as having a negative SER of at least −0.75D and was classified into three levels as low, moderate, and high myope (−3 to −0.75D, −6 to −3D, and ≤-6D, respectively). All procedures in this research adhered to the tenets of the Declaration of Helsinki and the experimental procedure was approved by the Institutional Review Board of Beijing MRI Center for Brain Research (BMCBR).

Ocular Examinations

The researchers performed ocular examinations for the subjects after explaining the nature and procedures of the study to them and obtaining their signed consent. Ocular examinations included logMAR VA, dominant eye test, manifest and cycloplegic refraction (Auto Ref/Keratometer WAM-5500, Grand Seiko, Japan). Tropicamide eye drops were administered two times for every 15 min during the examinations. In addition, the prescription of glasses, head circumference, height, and weight of the subjects were measured.

Behavior Test

The logMAR VA and contrast sensitivity (CS) were both measured monocularly at 5 min intervals over 30 min. During the course, all the emmetropes and full-corrected myopic subjects wore a non-magnetic trial frame with a convex plastic lens of +2D to induce the myopic defocus state. The subjects maintained a distance fixation of 4 m throughout the trial period. All the VA measurements were taken from the right eye, whereas the left eye was fully occluded.

Magnetic Resonance Imaging

Magnetic resonance imaging was performed on a Siemens 3T Prisma scanner (Erlangen, Germany) with a 20-channel receive head coil in BMCBR. During MRI scanning, subjects were asked to lie down still in the scanner, and the head movement was minimized by two pieces of foam surrounding the head of the subjects.

High-resolution ($1 \times 1 \times 1$ mm^3) structural image was acquired with a 3D magnetization-prepared rapid gradient-echo (MP-RAGE) sequence for T1 weighted (TR = 2530 ms, TE = 3.25 ms, flip angle = 9°, FOV = 256 × 256 mm, matrix = 256 × 256, 176 sagittal slices with 1 mm thickness).

Arterial spin labeling (ASL) perfusion MRI, which uses magnetically labeled arterial water as an endogenous tracer to obtain quantified CBF maps, was performed with 3D gradient and spin-echo (GRASE) pseudo-continuous arterial spin labeling (pCASL) sequence (TR = 4,000 ms, TE = 17.96 ms, FOV = 192 × 192 mm, voxel size = 3 × 3 mm, 24 slices acquired in ascending order, slice thickness = 5 mm with 1 mm gap between slices, labeling duration = 1,650 ms, post labeling delay = 1,200 ms, number of controls/labels = 30 pairs). The stimuli were generated by a computer and were back-projected on a screen located inside the MRI bore in front of the head of the patient. Subjects viewed

the screen at a total path length of 65 cm through a mirror situated above their eyes (**Figure 1**).

Apparatus and Stimuli

Custom algorithms written in MATLAB were used in all experiments to obtain stimulated images blurred with defocus. All the images were with a size of 613 × 613 pixels and presented as vertical black and white grating whose blur was manipulated (Sawides et al., 2010). The blur of the grating was intermediate between that of a square grating and a sine grating. This was achieved by replacing each of the sharp edges of a square grating with half cosine wave luminance profiles.

Procedure

Each subject attended three measurement sessions, each conducted in a randomized order. The CBF images were obtained before and at 15 min intervals, it was observed during 7 min whether the spectacle induced +2D spherical myopic defocus, −2D spherical hyperopic defocus, or clear vision. All the emmetropes and full-corrected myopic subjects wore a non-magnetic trial frame with a plastic lens of +2D to induce a myopic defocus state or a plastic lens of −2D to induce a hyperopic defocus state. The emmetropes wore plain glasses, and the myopic subjects wore glasses that provide the full correction to induce clear focus. During each experimental session, the

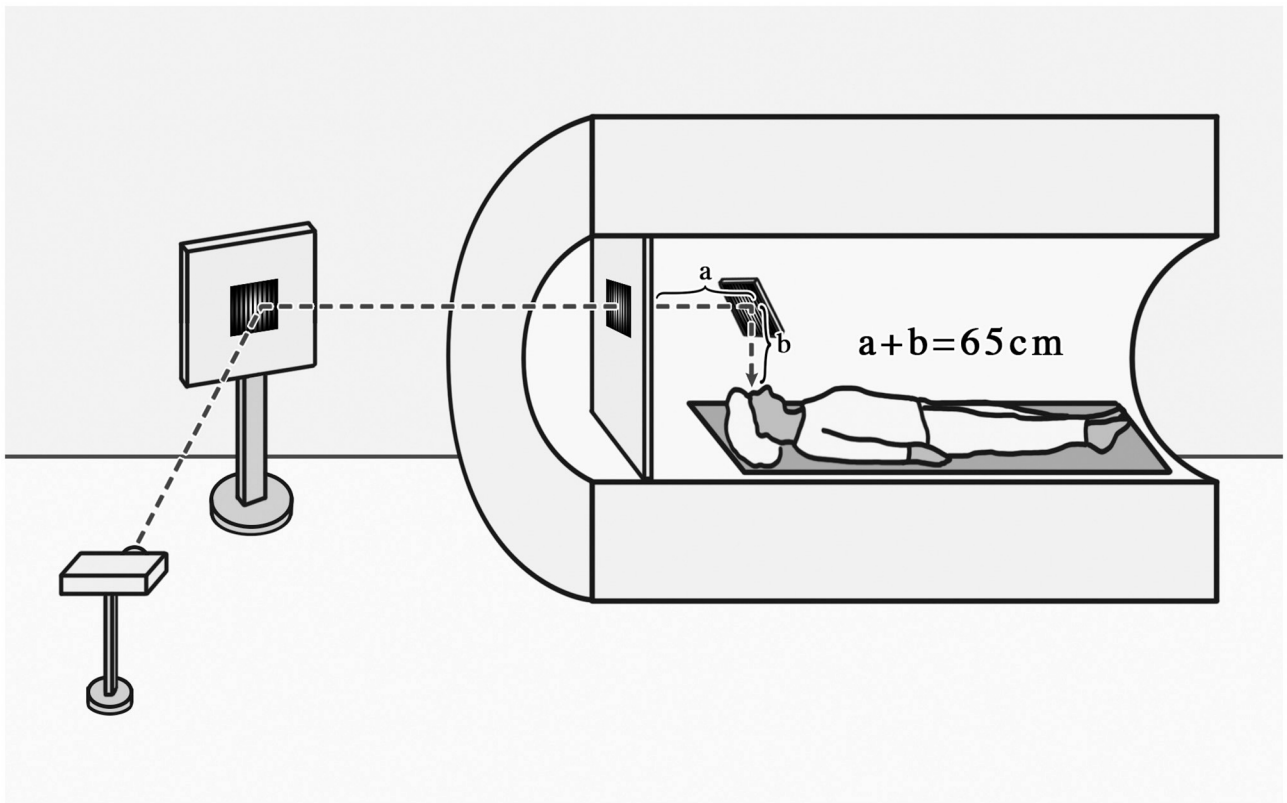

FIGURE 1 | Schematic diagram of the subjects receiving visual tasks.

TABLE 1 | Characteristics of the subjects.

	All	Emmetropes	Low myopes	Moderate myopes	High myopes
N	41	9	6	16	10
Age, mean (year)	26.0 ± 2.9	27.0 ± 4.4	25.5 ± 1.8	25.6 ± 2.3	25.9 ± 2.8
Gender (male/female)	15/26	6/3	2/4	3/13	4/6
Dominant eye (right/left)	22/19	4/5	3/3	9/7	6/4
Handedness (right/left)	40/1	8/1	6/0	16/0	10/0
Right eye SER, mean (D)	−3.64 ± 2.35	−0.53 ± 0.33	−2.22 ± 0.63	−4.02 ± 0.91	−6.67 ± 1.20
Left eye SER, mean (D)	−3.57 ± 2.27	−0.55 ± 0.51	−2.26 ± 0.40	−3.92 ± 0.99	−6.53 ± 0.84
Height, mean (cm)	168.2 ± 7.8	171.0 ± 7.6	168.3 ± 14.0	165.6 ± 5.2	169.9 ± 6.4
Weight, mean (kg)	61.7 ± 12.9	67.6 ± 13.8	61.8 ± 14.8	57.9 ± 11.1	62.4 ± 13.5

SER, spherical equivalent refraction; D, diopter.

subjects were asked to have a 7-min binocular distant viewing tasking of watching a grating image with 613 × 613 pixels projected on a translucent screen (subtending visual field of 60° at a viewing distance of 65 cm). The image was projected on the screen through a tilted mirror mounted on the head coil to achieve optimal viewing distance. The experiments were performed in a room with an illumination of 10 lux. Subjects were unknown to the effect of the stimulation condition.

Data Processing

The first two volumes of each functional run were discarded to allow for magnetization equilibration. Data were analyzed using statistical parametric mapping (SPM8) (Wellcome Trust Centre for Neuroimaging, University College London, UK) under MATLAB. Other images were realigned and resliced to correct for head motion with a mean volume created. The subject whose head motion exceeded 3 mm or rotation exceeded 3° during scanning were excluded. All realigned echo-planar images (EPI) were subsequently smoothed using an 8 mm full-width at half-maximum (FWHM) isotropic Gaussian kernel in SPM8. Images of CBF were then reconstructed from preprocessed EPI images, and the acquired CBF images were averaged to mean image for each condition (1 resting and 3 visual tasks). The mean CBF images were finally normalized to standard

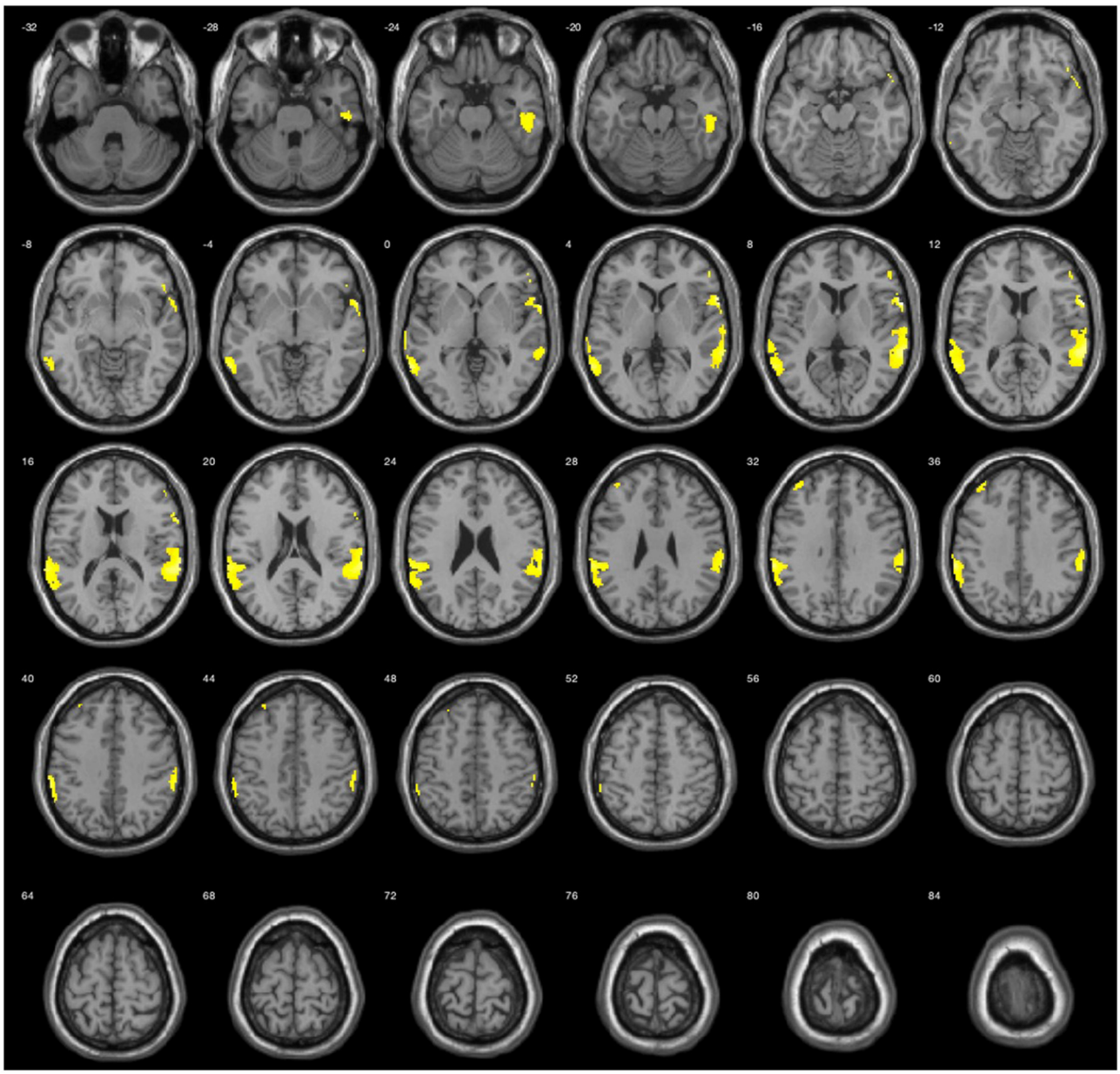

FIGURE 2 | Average activation maps resulting from group analysis, showing the increase of neural activation in myopic defocus relative to clear focus state. Color scale indicates score significance level.

Montreal Neurological Institute (MNI) space, and the voxels were resampled to isotropic $2 \times 2 \times 2$ mm^3.

The normalized mean CBF maps of defocus and clear focus were modeled in a paired *t*-test factorial design with SPM8. The brain areas showing a significant difference in the CBF between two visual tasks were filtered at threshold $P < 0.001$ (uncorrected, cluster size $\geq$30) as a region of interest (ROI).

The value of the regional CBF (rCBF) of each ROI over the threshold was extracted from the normalized mean CBF images and then normalized with the global mean of the whole volume. A paired *t*-test of the corrected rCBF values was conducted in SPSS 20 to reveal the significant difference between defocus signal and clear focus.

The individual who processed the data was masked to the stimulus condition.

RESULTS

After screening through the ophthalmic examination, 41 subjects met the inclusion criteria and completed the fMRI examination. According to their cycloplegic SER, the 41 subjects were grouped into emmetropes, low myopes, moderate myopes, and high myopes. Mean SER was -3.64 ± 2.35D in right eyes and -3.57 ± 2.27D in left eyes. There was no significant difference in mean age, gender, height, and weight among groups ($P > 0.05$, **Table 1**).

The results during the myopic defocus session showed increased CBF in several cerebral regions compared with clear focus stimulation (**Figure 2**, $P < 0.001$, cluster size $\geq$30, and **Table 2**). The rCBF of myopic defocus stimulation was significantly higher than clear focus in four ROIs: right precentral gyrus, right superior temporal gyrus, left inferior parietal lobule, and left middle temporal gyrus. The results during the hyperopic defocus session showed that the rCBF of hyperopic defocus stimulation was significantly higher than clear focus in the right precentral gyrus and left precentral gyrus (**Figure 3**, $P < 0.001$, cluster size $\geq$30, and **Table 2**).

When the brain received myopic defocus signal and the clear focus signal, the average elevation of rCBF was 78.12 ± 1.18 ml/100 g/min and 74.70 ± 1.26 ml/100 g/min respectively in the right precentral gyrus, 76.07 ± 0.78 ml/100 g/min and 73.67 ± 0.72 ml/100 g/min in the right superior temporal gyrus, 72.29 ± 0.90 ml/100 g/min and 70.42 ± 0.84 ml/100 g/min in the left inferior parietal lobule, and 79.48 ± 0.95 ml/100 g/min and 77.50 ± 0.89 ml/100 g/min in the left middle temporal gyrus. The differences between groups were statistically significant ($P < 0.05$) (**Figure 4**).

We further compared the magnitude of changes of rCBF in four ROIs among subjects with different myopia degrees (**Figure 5**). The rCBF changes in the right superior temporal gyrus area for subjects in four groups (emmetropia, low myopia, moderate myopia, and high myopia group) were 63.24, 60.23, 64.20, and 63.11 ml/100 g/min, the increase was the least significant in the low myopia group. In the left inferior parietal lobule, the increase was less significant in the low and high myopia groups, and the mean values for the four groups were 80.99, 77.51, 80.62, and 77.46 ml/100 g/min. One-way ANOVA among groups showed no significant statistical difference ($P > 0.05$).

The magnitude of the rCBF signal collected at each measurement time point was exported at 8 s intervals. During the 7-min visual tasks, the average rCBF signal intensities in four ROIs were collected (**Figure 6**) revealing that compared with clear focus visual tasks, average rCBF signal intensity was higher when receiving myopic defocus ($P < 0.05$). However, the changes in signal intensity reached a plateau within 1 min after exposure of defocus.

The logMAR VA and CS were assessed before and after myopic defocus. There were significant decreases of both VA and CS for all subjects at the point of perceiving +2D myopic defocus. Afterward, the defocus visual function was collected at 5 min intervals. The average VA and CS were improved over time ($P < 0.01$). Overall, 30 min of defocused viewing produced significant improvement of VA by 0.14 +0.09 logMAR and CS by 0.91 +0.51 logCS, respectively (**Figure 7**).

DISCUSSION

With the ASL technique of event-related-fMRI, we found that the myopic defocus visual stimulation induced the function and perfusion increase in the following cerebral regions relative to the clear focus stimulation: right precentral gyrus, right superior temporal gyrus, left inferior parietal lobule, and left middle temporal gyrus. The above regions were related to oculomotor response, enhancement of attention and awareness triggered by visual stimulation, contemplating distance, and recognition of the image. In addition, we found that hyperopic defocus had less improvement in the above regions. It suggested that the mechanism of the defocus signal involved the functional change of CNS. The functional changes will occur shortly after receiving the retinal defocus signal.

The event-related-fMRI method provides a new approach to assessing the neural underpinnings of visual perceptual effects induced by the defocus stimulus. The fMRI has millimeter spatial resolution and second-order temporal resolution. Through acquiring changes in MRI signals caused by changes in local blood oxygenation, blood flow, and volume caused by neuronal activity in the brain, the location, intensity, and dynamic changes of different functional activities can be measured without injury. This reveals the CNS mechanisms of audio and visual perception. In this study, the behavioral results and fMRI findings are consistent and correlated. Myopic defocus can improve visual function within 5 min; at the same time, the increase of blood flow in the visual attention area could be observed.

Animal research showed that visual error signals strongly guided ocular growth. Myopic defocus will slow myopia progression, and hyperopic defocus will accelerate myopia progression (Norton and Amedo, 2006; Benaventeperez et al., 2012; Benaventepérez et al., 2014; McFadden et al., 2014). Transecting the optic nerve can affect the occurrence of lens-induced myopia in lens-induced myopia in chicken, but it does

TABLE 2 | The active loci of myopic defocus and hyperopic defocus of increased regional cerebral blood flow (rCBF) response compared with clear defocus.

	Activation loci	Brodmann area	Z	MNI coordinates x, y, z (mm)		
Myopic defocus vs. clear focus	(1) Right precentral gyrus	44	4.59	66	10	8
	(2) Right superior temporal gyrus	22	4.06	66	−36	14
	(3) Left inferior parietal lobule	40	4.06	−64	−34	36
	(4) Left middle temporal gyrus	21	3.97	−62	−54	0
Hyperopic defocus vs. clear focus	(1) Right cerebrum, frontal lobe, precentral gyrus	4	4.98	26	−28	50
	(2) Right cerebrum, frontal lobe, precentral gyrus	4	4.51	44	−18	36
	(3) Left cerebrum, frontal lobe, precentral gyrus	40	4.93	−28	−36	44

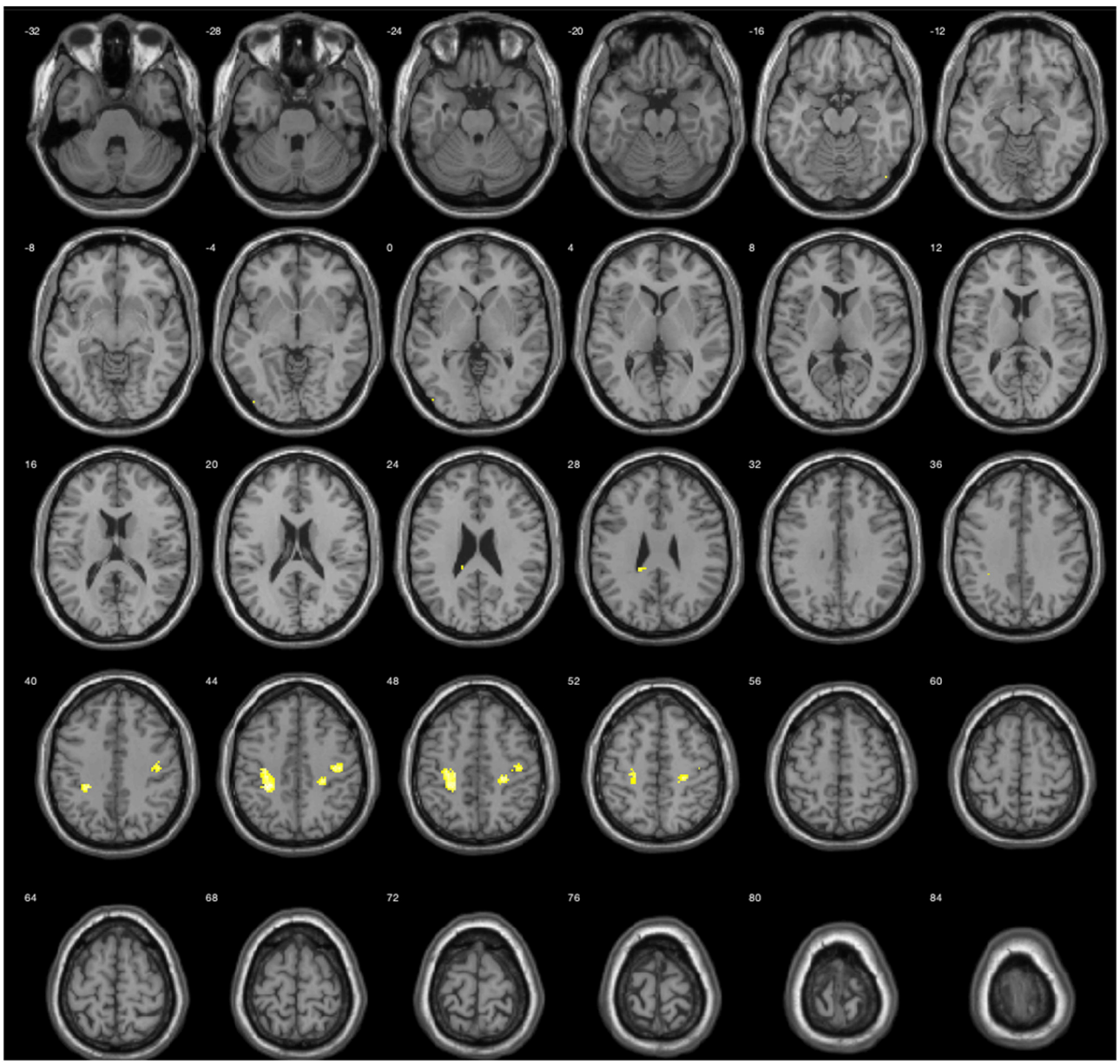

FIGURE 3 | Average activation maps resulting from group analysis, showing the increase of neural activation in hyperopic defocus relative to clear focus state. Color scale indicates score significance level.

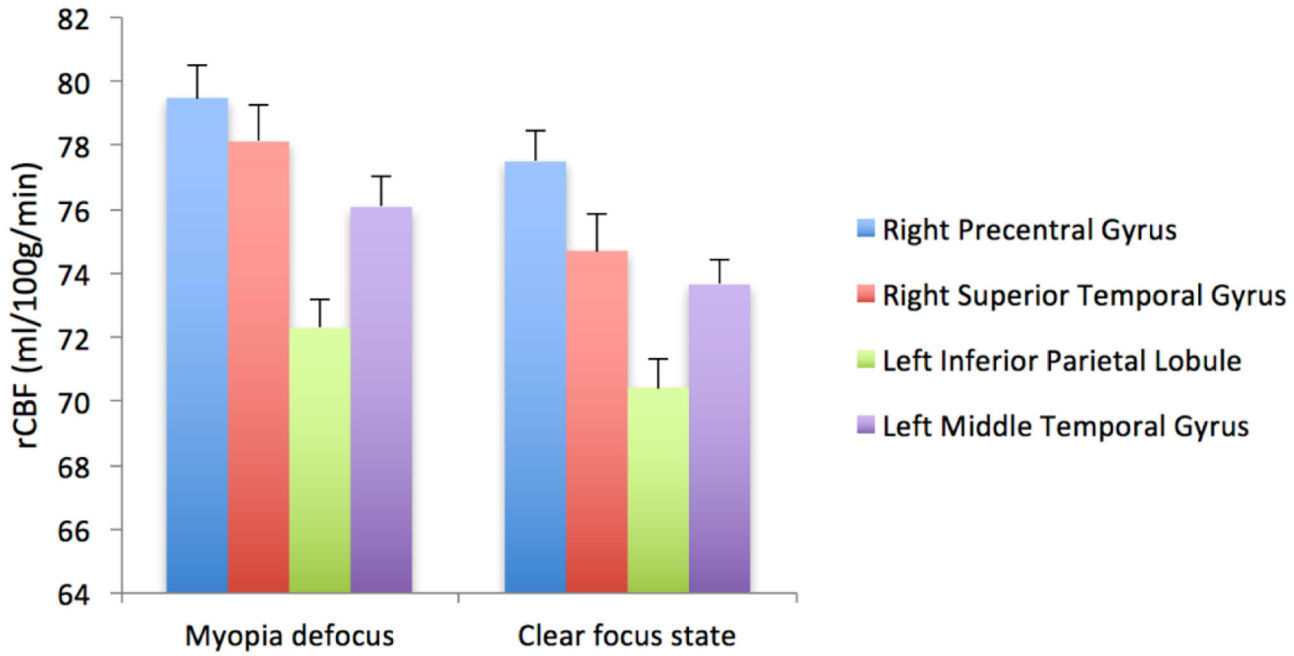

FIGURE 4 | The rCBF signal intensity (ml/100 g/min) change in four ROI averaged over 41 subjects (error bars represent SEM).

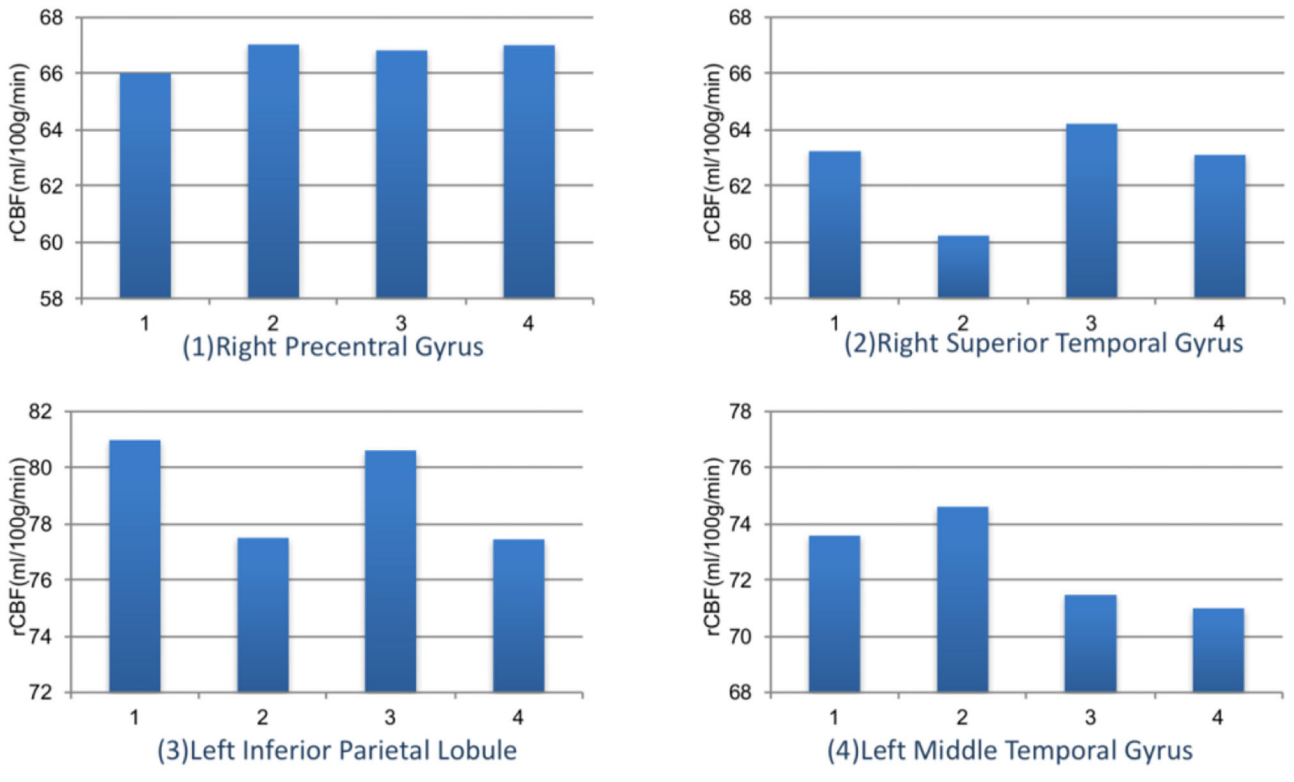

FIGURE 5 | The rCBF signal intensity (ml/100 g/min) changes in four ROIs among different refractive groups. Group 1: emmetropia, Group 2: low myopia, Group 3: moderate myopia, and Group 4: high myopia.

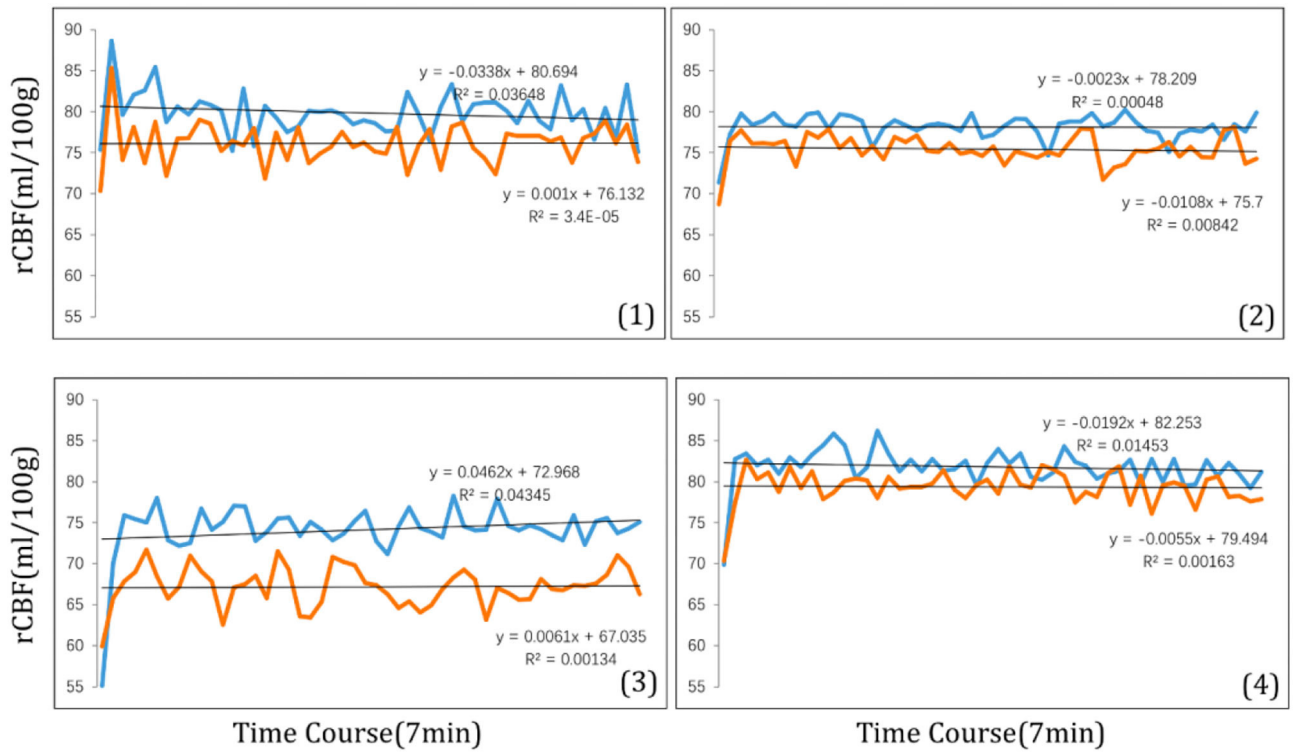

FIGURE 6 | The time course of rCBF signal intensity (ml/100 g) within 7 min in four ROI: (1) right precentral gyrus; (2) right superior temporal; (3) left inferior parietal lobule; (4) left middle temporal gyrus. The blue curve stands for myopic defocus, orange curve stands for clear focus.

not affect form-deprivation myopia (Wildsoet and Wallman, 1995; Dillingham et al., 2013). The experiment results showed an interaction between lens-induced myopia and CNS, and the set point of the emmetropization was recalibrated after the optic nerve was cut off (Wildsoet, 2003). Additionally, ocular structure altered quickly after the eyeball received the defocus signal. The depth of the vitreous chamber and the choroidal thickness had compensatory change when myopic defocus is imposed on the eye of a human. In this compensatory change, the axial length of the eye was slightly shortened, thereby becoming hyperopic (Read et al., 2010; Chakraborty et al., 2012), suggesting eyes can quickly detect and respond to defocus signals (Zhu et al., 2005). Adaptation experiments in humans showed that myopic defocus could improve vision to a certain extent and if the human is continuously exposed to myopic defocus stimulation, their ability to distinguish and identify objects will gradually improve. Even though the impact of spectacle-wearing on myopia progression has been documented in quite a several clinical studies, the under-correction effect on myopia progression remains controversial (Smith, 2013; Li et al., 2015). The effect of myopic defocus signal is stronger than that of hyperopic defocus signal. Recent studies have found that 2-h myopic defocus stimulation per day can inhibit ocular elongation (Nickla et al., 2017). Transitory myopic defocus stimulation can compensate for the myopic effect caused by long-time hyperopic defocus stimulation (Zhu et al., 2003).

Furthermore, it has been discovered that brain structure changes in patients with high myopia due to abnormal sensory input. The study of Guo (Li et al., 2012). found that the density of white matter in the brain was higher in patients with high myopia than in healthy controls, while there was no difference in the density of gray matter. The connection between the visual cortex and the visual connecting region is enhanced under the influence of visual awareness. These pieces of evidence indicated that to better collect and integrate visual signals, the brains of high myopia patients developed an adaptive compensatory change to enhance the functional connection between the visual cortex and the related visual regions. The finding that changes only occur on white matter in the brain suggests that late-onset eye disease affects the structure of the brain in different ways. This is because the volume of gray matter is in a stable state in adulthood, while the development of white matter continues for a lifetime due to its close relation to functional training. The study of Guo (Zhai et al., 2016) further explored the functional connectivity density (FCD) in patients with high myopia, which found that FCD in the left inferior temporal gyrus (ITG), supramarginal gyrus (SMG), and rostrolateral prefrontal cortex (rlPFC) was lower than those of healthy controls. Uncorrected VA is related to the long-range FCD of rlPFC. It is worth noticing that the left ITG is related to the ability of the ventral visual pathway to identify objects. In animal experiments, if the function of the ITG region is damaged, the attention filter function can be compromised

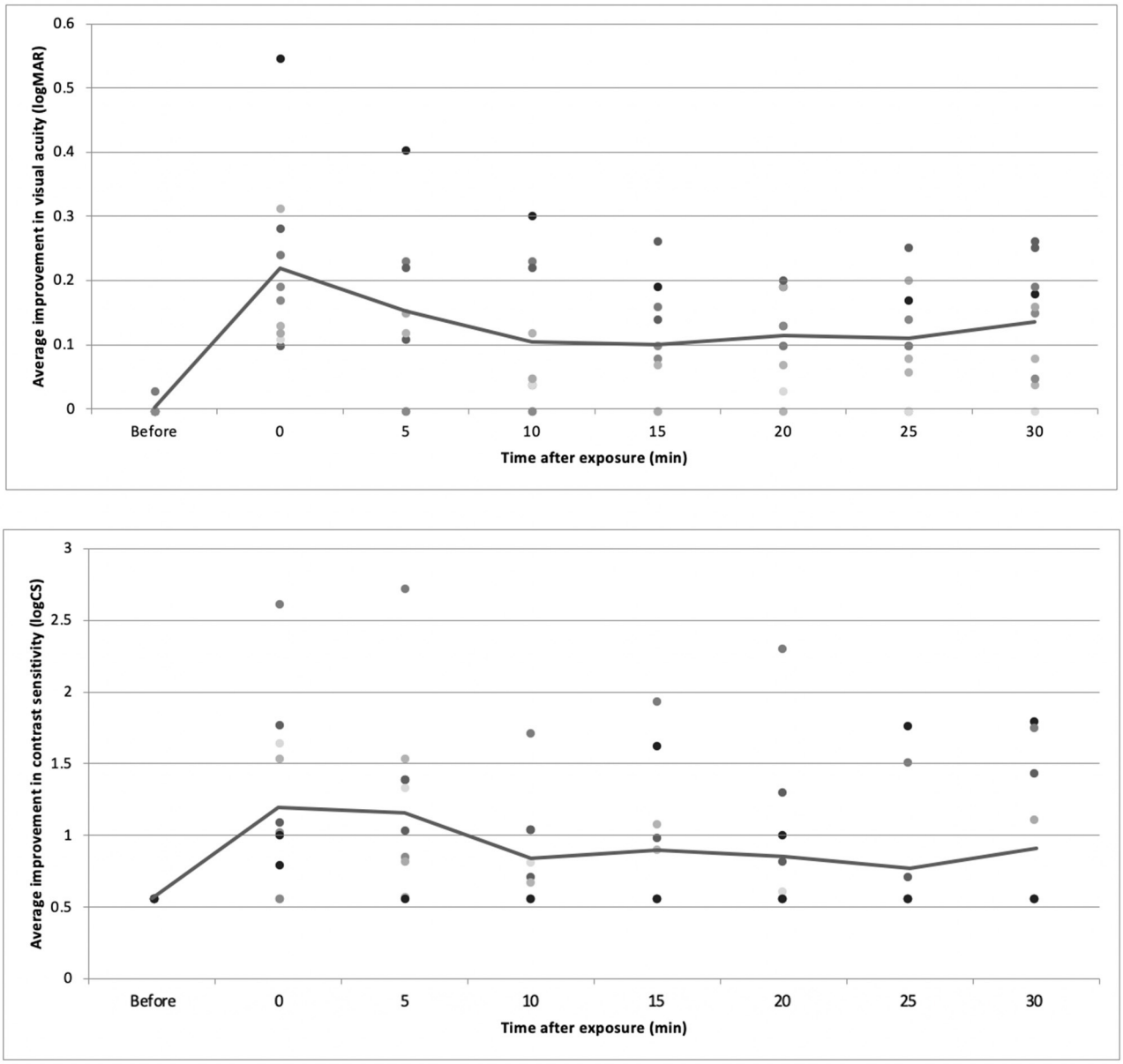

FIGURE 7 | The average change of VA and CS over time.

(Zhang et al., 2011). The damage of SMG is associated with visual attention deficit (Perry and Zeki, 2000; Corbetta and Shulman, 2002), including spatial and locating attention. This means that the visual attention regulation function of high myopia patients is abnormal. The visual experience affects sensory cortex function because of its plasticity (Kaas et al., 1990; Chino et al., 1992; Gilbert and Wiesel, 1992; Chino, 1995; Lewis and Maurer, 2005). Although the moderate myopic defocuses stimulation may slow the myopia progression, we should note that visual deprivation must be avoided because there are multiple sensitive periods during which experience can influence visual development (Blakemore and Cooper, 1970; Lewis and Maurer, 2005).

The retinal defocus mechanism of myopia has been considered to be mainly regulated locally, while some scholars believed the possibility that the defocus mechanism involves brain regulation. The current study validated the hypothesis: the adaptive change and the improvement of visual function induced by myopic defocus may be associated with functional changes in CNS. The right precentral gyrus locates at Brodmann44 and controls both ocular and somatic movement (Iacoboni et al., 1997). Saccade occurs when the visual stimulation is mainly composed of low or high spatial frequency components (Burr et al., 1994), and uncorrected myopia will lead to increased saccadic eye movement (Ghasia and Shaikh, 2015). The function

of ocular movement is to shift the visual attention to fix on features that are of particular interest at the scene, and this function is strongly related to visual attention. The left middle temporal locates at Brodmann21 and is related to distance recognition. The right superior temporal gyrus locates at Brodmann22 and is associated with the ability to identify the object in the ventral visual pathway. In the animal experiment, if this area is damaged, the attention filtering function will be compromised (Zhang et al., 2011). The left inferior parietal lobule locates at Brodmann40 and is also related to visual attention (Goldberg et al., 2002). The attention function network locates in the parietal region and is a feedback source that acts on the "top-down" signal pathway in the visual cortex (Pessoa et al., 2003). The attention function can enhance the perceived sensitivity visual stimulation recognition while reducing the surrounding interference. Attention plays a key role in processing audio and visual stimulation. For example, when we receive a large amount of visual information from the external environment, the irrelevant signal that fails to draw attention will not be processed by the visual system. In addition, from the perspective of perception, this type of signal will not reach the consciousness level (Lavie, 1995). A previous study in an experiment of Reinhart revealed the possibility of improving VA through CNS, which showed that 20 min of transcranial direct-current stimulation (tDCS) to the visual cortex could improve VA by 15%, and the improvement was accompanied by changes in CS at high spatial frequencies (Reinhart et al., 2016). It could be an inspiration for future study targeting the impact of the tDCS on the attention and recognition functional region of the brain. The increasing rCBF caused by myopic defocus indicated a potential way of therapeutic training on myopia.

Through establishing a control group and using the same visual pattern, the brain function signals were compared under the myopic defocus visual stimulation and clear focus visual stimulation. It was found that myopic defocus visual stimulation can lead to more increase in attention and awareness function, suggesting myopic defocus visual stimulation activated stronger advanced central visual processing function. This method excluded the attentional function caused by the visual signal. One of the limitations of this study is that it only proves that the cerebral functional changes when receiving a visual signal, which does not constitute sufficient evidence to confirm that this change of function may cause ocular changes and molecular signal transduction changes. However, several studies have shown that there will be rapid and slight ocular changes and visual function improvement when the eye receives a myopic defocus signal. The future study will focus on ratifying the causal-effect relationship between the ocular changes and brain function changes by further exploring the "top-down" neural pathway in the brain. In addition, the limited number of subjects in each refractive group attributed to the failure to identify whether there are statistically significant differences between the sub-group of refractive error. In the future, we will expand the sample size to further verify whether the difference does exist based on our current exploratory analysis.

CONCLUSION

With the ASL technique of event-related-fMRI, the study found that myopic defocus visual stimulation induced the function and perfusion increase in the right precentral gyrus, right superior temporal gyrus, left inferior parietal lobule, and left middle temporal gyrus. The abovementioned cerebral regions were related to oculomotor response, attention and awareness, contemplating distance, and recognition of the image. The study on the relationship between CNS and myopia will help us understand the changes in CNS induced by refractive correction, suggesting the potential role of adult brain function training and brain plasticity in the mechanism of myopic defocus.

DATA AVAILABILITY STATEMENT

The raw data supporting the conclusions of this article will be made available by the authors, without undue reservation.

ETHICS STATEMENT

The studies involving human participants were reviewed and approved by Institutional Review Board of Beijing MRI Center for Brain Research. The patients/participants provided their written informed consent to participate in this study.

AUTHOR CONTRIBUTIONS

NW and S-ML contributed to acquisition of funding, collection of data, and general supervision of the research group. BW contributed to design, data analysis, and revision of the manuscript. M-TK contributed to design, collection of data, analysis of results, and drafting of the manuscript. A-RR contributed to design, data analysis, and drafting of the manuscript. MY helped to the manuscript revision. JG, XL, and JD contributed to the collection of data. All authors contributed to the article and approved the submitted version.

FUNDING

Young Elite Scientists Sponsorship Program by CAST (YESS) (2018QNRC001); Beijing Natural Science Foundation (JQ20029); the Capital Health Research and Development Special Grant (2020-2-1081); Beijing Talents Fund (2016000021223ZK28); and the National Natural Science Foundation of China (82071000).

ACKNOWLEDGMENTS

All functional magnetic resonance imaging (fMRI) examinations and fMRI image analysis were performed by the State Key Laboratory of Brain and Cognitive Science, Institute of Biophysics, Chinese Academy of Sciences. The content in this article has been presented at ARVO 2017 as Hot topic.

REFERENCES

Benaventeperez, A., Nour, A., and Troilo, D. (2012). The effect of simultaneous negative and positive defocus on eye growth and development of refractive state in marmosets. *Invest. Ophthalmol. Vis. Sci.* 53, 6479–6487. doi: 10.1167/iovs.12-9822

Benaventepérez, A., Nour, A., and Troilo, D. (2014). Axial eye growth and refractive error development can be modified by exposing the peripheral retina to relative myopic or hyperopic defocus. *Invest. Ophthalmol. Vis. Sci.* 55:6765. doi: 10.1167/iovs.14-14524

Blakemore, C., and Cooper, G. F. (1970). Development of the brain depends on the visual environment. *Nature* 228:477–478. doi: 10.1038/228477a0

Burr, D. C., Morrone, M. C., and Ross, J. (1994). Selective suppression of the magnocellular visual pathway during saccadic eye movements. *Nature* 371, 511–513. doi: 10.1038/371511a0

Chakraborty, R., Read, S. A., and Collins, M. J. (2012). Monocular myopic defocus and daily changes in axial length and choroidal thickness of human eyes. *Exp. Eye Res.* 103, 47–54. doi: 10.1016/j.exer.2012.08.002

Chino, Y. M. (1995). Adult plasticity in the visual system. *Can. J. Biochem. Physiol.* 73, 1323–1338. doi: 10.1139/y95-187

Chino, Y. M., Kaas, J. H., Smith, E. L., Langston, A. L., and Cheng, H. (1992). Rapid reorganization of cortical maps in adult cats following restricted deafferentation in retina. *Vision Res.* 32, 789–796. doi: 10.1016/0042-6989(92)90021-A

Corbetta, M., and Shulman, G. L. (2002). Control of goal-directed and stimulus-driven attention in the brain. *Nat. Rev. Neurosci.* 3:201. doi: 10.1038/nrn755

Dillingham, C. M., Guggenheim, J. A., and Erichsen, J. T. (2013). Disruption of the centrifugal visual system inhibits early eye growth in chicks. *Invest. Ophthalmol. Vis. Sci.* 54, 3632–3643. doi: 10.1167/iovs.12-11548

Dillingham, C. M., Guggenheim, J. A., and Erichsen, J. T. (2016). The effect of unilateral disruption of the centrifugal visual system on normal eye development in chicks raised under constant light conditions. *Brain Struct. Funct.* 222, 1–16. doi: 10.1007/s00429-016-1279-9

Ghasia, F. F., and Shaikh, A. G. (2015). Uncorrected myopic refractive error increases microsaccade amplitude. *Invest. Ophthalmol. Vis. Sci.* 56, 2531–2535. doi: 10.1167/iovs.14-15882

Gilbert, C. D., and Wiesel, T. N. (1992). Receptive field dynamics in adult primary visual cortex. *Nature* 356:150. doi: 10.1038/356150a0

Goldberg, M. E., Bisley, J., Powell, K. D., Gottlieb, J., and Kusunoki, M. (2002). The role of the lateral intraparietal area of the monkey in the generation of saccades and visuospatial attention. *Ann. N. Y. Acad. Sci.* 956, 205–215. doi: 10.1111/j.1749-6632.2002.tb02820.x

Hung, L. F., Wallman, J., and Smith, E. L. (2000). Vision-dependent changes in the choroidal thickness of macaque monkeys. *Invest. Ophthalmol. Vis. Sci.* 41, 1259–1269. doi: 10.1073/pnas.0601030103

Iacoboni, M., Woods, R. P., Lenzi, G. L., and Mazziotta, J. C. (1997). Merging of oculomotor and somatomotor space coding in the human right precentral gyrus. *Brain* 120, 1635–1645. doi: 10.1093/brain/120.9.1635

Kaas, J. H., Krubitzer, L. A., Chino, Y. M., Langston, A. L., Polley, E. H., and Blair, N. (1990). Reorganization of retinotopic cortical maps in adult mammals after lesions of the retina. *Science* 248:229. doi: 10.1126/science.2326637

Lavie, N. (1995). Perceptual load as a necessary condition for selective attention. *J. Exp. Psychol.* 21:451. doi: 10.1037/0096-1523.21.3.451

Lewis, T. L., and Maurer, D. (2005). Multiple sensitive periods in human visual development: evidence from visually deprived children. *Dev. Psychobiol.* 46:163. doi: 10.1002/dev.20055

Li, Q., Guo, M., Dong, H., Zhang, Y., Fu, Y., and Yin, X. (2012). Voxel-based analysis of regional gray and white matter concentration in high myopia. *Vision Res.* 58:45. doi: 10.1016/j.visres.2012.02.005

Li, S. Y., Li, S. M., Zhou, Y. H., Liu, L. R., Li, H., Kang, M. T., et al. (2015). Effect of undercorrection on myopia progression in 12-year-old children. *Graefes Arch. Clin. Exp. Ophthalmol.* 253, 1363–1368. doi: 10.1007/s00417-015-3053-8

McFadden, S. A., Tse, D. Y., Bowrey, H. E., Leotta, A. J., Lam, C. S., Wildsoet, C. F., et al. (2014). Integration of defocus by dual power Fresnel lenses inhibits myopia in the mammalian eye. *Invest. Ophthalmol. Vis. Sci.* 55, 908–917. doi: 10.1167/iovs.13-11724

Mon-Williams, M., Tresilian, J. R., Strang, N. C., Kochhar, P., and Wann, J. P. (1998). Improving vision: neural compensation for optical defocus. *Proc. Biol. Sci.* 265, 71–77. doi: 10.1098/rspb.1998.0266

Nickla, D. L., Thai, P., Zanzerkia Trahan, R., and Totonelly, K. (2017). Myopic defocus in the evening is more effective at inhibiting eye growth than defocus in the morning: Effects on rhythms in axial length and choroid thickness in chicks. *Exp. Eye Res.* 154:104. doi: 10.1016/j.exer.2016.11.012

Norton, T. T., and Amedo, A. O. (2006). Effectiveness of hyperopic defocus, minimal defocus, or myopic defocus in competition with a myopiagenic stimulus in tree shrew eyes. *Invest. Ophthalmol. Vis. Sci.* 47:4687. doi: 10.1167/iovs.05-1369

Perry, R. J., and Zeki, S. (2000). The neurology of saccades and covert shifts in spatial attention: an event-related fMRI study. *Brain* 123:2273. doi: 10.1093/brain/123.11.2273

Pessoa, L., Kastner, S., and Ungerleider, L. G. (2003). Neuroimaging studies of attention: from modulation of sensory processing to top-down control. *J. Neurosci.* 23, 3990–3998. doi: 10.1523/JNEUROSCI.23-10-03990.2003

Read, S. A., Collins, M., and Sander, B. (2010). Human optical axial length changes in response to defocus. *Invest. Ophthalmol. Vis. Sci.* 51, 6262–6269. doi: 10.1167/iovs.10-5457

Reinhart, R. M., Xiao, W., McClenahan, L. J., and Woodman, G. F. (2016). Electrical stimulation of visual cortex can immediately improve spatial vision. *Curr. Biol.* 26, 1867–1872. doi: 10.1016/j.cub.2016.05.019

Sawides, L., Marcos, S., Ravikumar, S., Thibos, L., Bradley, A., and Webster, M. (2010). Adaptation to astigmatic blur. *J. Vis.* 10:22. doi: 10.1167/10.12.22

Smith, E. L. (2013). Optical treatment strategies to slow myopia progression: effects of the visual extent of the optical treatment zone. *Exp. Eye Res.* 114, 77–88. doi: 10.1016/j.exer.2012.11.019

Wallman, J., Wildsoet, C., Xu, A., Gottlieb, M. D., Nickla, D. L., Marran, L., et al. (1995). Moving the retina: choroidal modulation of refractive state. *Vision Res.* 35, 37–50. doi: 10.1016/0042-6989(94)E0049-Q

Wallman, J., and Winawer, J. (2004). Homeostasis of eye growth and the question of myopia. *Neuron* 43, 447–468. doi: 10.1016/j.neuron.2004.08.008

Webster, M. A., Georgeson, M. A., and Webster, S. M. (2002). Neural adjustments to image blur. *Nat. Neurosci.* 5, 839–840. doi: 10.1038/nn906

Wildsoet, C., and Wallman, J. (1995). Choroidal and scleral mechanisms of compensation for spectacle lenses in chicks. *Vision Res.* 35, 1175–1194. doi: 10.1016/0042-6989(94)00233-C

Wildsoet, C. F. (1997). Active emmetropization–evidence for its existence and ramifications for clinical practice. *Ophthalmic Physiol. Opt.* 17, 279–290. doi: 10.1046/j.1475-1313.1997.97000033.x

Wildsoet, C. F. (2003). Neural pathways subserving negative lens-induced emmetropization in chicks-Insights from selective lesions of the optic nerve and ciliary nerve. *Curr. Eye Res.* 27, 371–385. doi: 10.1076/ceyr.27.6.371.18188

Zhai, L., Li, Q., Wang, T., Dong, H., Peng, Y., Guo, M., et al. (2016). Altered functional connectivity density in high myopia. *Behav. Brain Res.* 303, 85–92. doi: 10.1016/j.bbr.2016.01.046

Zhang, Y., Meyers, E. M., Bichot, N. P., Serre, T., Poggio, T. A., Desimone, R., et al. (2011). Object decoding with attention in inferior temporal cortex. *Proc. Natl. Acad. Sci. U.S.A.* 108, 8850–8855. doi: 10.1073/pnas.1100999108

Zhu, X., McBrien, N. A., Smith, E. L., Troilo, D., and Wallman, J. (2013). Eyes in various species can shorten to compensate for myopic defocus. *Invest. Ophthalmol. Vis. Sci.* 54, 2634–2644. doi: 10.1167/iovs.12-10514

Zhu, X., Park, T. J., and Wallman, J. (2005). In a matter of minutes, the eye can know which way to grow. *Invest. Ophthalmol. Vis. Sci.* 46, 2238–2241. doi: 10.1167/iovs.04-0956

Zhu, X., Winawer, J. A., and Wallman, J. (2003). Potency of myopic defocus in spectacle lens compensation. *Invest. Ophthalmol. Vis. Sci.* 44:2818. doi: 10.1167/iovs.02-0606

Conflict of Interest: The authors declare that the research was conducted in the absence of any commercial or financial relationships that could be construed as a potential conflict of interest.

The handling editor declared a shared affiliation with several of the authors M-TK, JG, MY, XL, S-ML, and NW at time of review.

Publisher's Note: All claims expressed in this article are solely those of the authors and do not necessarily represent those of their affiliated organizations, or those of the publisher, the editors and the reviewers. Any product that may be evaluated in this article, or claim that may be made by its manufacturer, is not guaranteed or endorsed by the publisher.

frontiers in Neuroscience

ORIGINAL RESEARCH
published: 01 October 2021
doi: 10.3389/fnins.2021.712256

Altered Brain Functional Connectivity at Resting-State in Patients With Non-arteritic Anterior Ischemic Optic Neuropathy

Pengbo Zhao[1], Han Lv[2], Pengde Guo[3], Yan Su[1], Ming Liu[3], Yan Wang[3], Haiqin Hua[3] and Shaohong Kang[3]*

[1] Department of Ophthalmology, Dongfang Hospital, Beijing University of Chinese Medicine, Beijing, China, [2] Department of Radiology, Beijing Friendship Hospital, Capital Medical University, Beijing, China, [3] Department of Radiology, Dongfang Hospital, Beijing University of Chinese Medicine, Beijing, China

OPEN ACCESS

Edited by:
Emilia Iannilli, University at Albany, United States

Reviewed by:
Hong Zhang, Nanjing Medical University, China
Chao Zhang, The Affiliated Hospital of Xuzhou Medical University, China
Feng Liu, Tianjin Medical University General Hospital, China

***Correspondence:**
Pengde Guo
guopengde1898@163.com

Specialty section:
This article was submitted to Perception Science, a section of the journal Frontiers in Neuroscience

Received: *20 May 2021*
Accepted: *09 September 2021*
Published: *01 October 2021*

Citation:
Zhao P, Lv H, Guo P, Su Y, Liu M, Wang Y, Hua H and Kang S (2021) Altered Brain Functional Connectivity at Resting-State in Patients With Non-arteritic Anterior Ischemic Optic Neuropathy. Front. Neurosci. 15:712256. doi: 10.3389/fnins.2021.712256

Purpose: To investigate the possible changes in functional connectivity (FC) in patients with non-arteritic anterior ischemic optic neuropathy (NAION) using resting-state functional MRI (fMRI).

Methods: Thirty-one NAION patients and 31 healthy controls were recruited and underwent resting-state fMRI scans. Regions of interest (ROIs) were defined as bilateral Brodmann's area 17 (BA17). FC analysis was performed between the ROIs and the rest of the brain regions, and the between group comparisons of FC were performed. We conducted correlation analysis between the FC changes and the clinical variables in NAION patients.

Results: Compared with healthy controls, patients with NAION showed significantly decreased FC between the left BA17 and the right inferior frontal gyrus, left caudate nucleus. As for the right BA17, patients exhibited significantly increased FC with the left olfactory gyrus and decreased FC with the right superior frontal gyrus (SFG), right insula. Moreover, FC values between the right insula and the right BA17 were positively correlated with the right side of mean sensitivity in the central visual field ($r = 0.52$, $P < 0.01$) and negatively correlated with the right side of mean defect in the central visual field ($r = -0.55$, $P < 0.01$).

Conclusion: Our study indicated that patients with NAION showed significantly abnormal functional reorganization between the primary visual cortex and several other brain regions not directly related to visual function, which supports that NAION may not only be an ophthalmic disease but also a neuro-ophthalmological disease.

Keywords: non-arteritic anterior ischemic optic neuropathy, functional connectivity, resting state, functional magnetic resonance imaging, neural plasticity

INTRODUCTION

Non-arteritic anterior ischemic optic neuropathy (NAION) is the second most common type of optic neuropathy, with an annual incidence of 2.3–10.2 cases per 100,000 people in the United States (Johnson and Arnold, 1994; Hattenhauer et al., 1997) and 6.25 cases per 100,000 people in China (Xu et al., 2007). Typically, NAION is characterized by sudden, painless unilateral loss of vision (Miller and Arnold, 2015). Although the pathogenesis and pathophysiology of NAION remain undetermined, the lesions are thought to result from infarction of the short posterior ciliary arteries (vessels that supply the anterior portion of the optic nerve head) (Knox et al., 2000), which results in degeneration of retinal ganglion cells, followed by loss of their axonal structure (Zhang et al., 2010).

Previous studies of NAION have mainly concentrated on its pathophysiology, clinical characteristics, prevention, and treatment (Katz and Trobe, 2015; Qin et al., 2015; Berry et al., 2017; Keren et al., 2017). In general, studies concerning the structural and functional plasticity of the brain in cases of NAION are rare because conventional magnetic resonance imaging (MRI) provides little information pertaining to the lesion. Functional MRI (fMRI), a non-invasive neuroimaging technique, has made it possible to explore neural plasticity in NAION. The fMRI has been widely used to study changes in brain function in several eye-related diseases (Burton et al., 2004; Wang et al., 2008, 2021; Shao et al., 2015; Li et al., 2016; van Kemenade et al., 2017; Huang et al., 2018; Min et al., 2018; Xu et al., 2019). Additionally, several fMRI studies have demonstrated abnormal spontaneous brain activity in patients with NAION (Aguirregomozcorta et al., 2011; Guo et al., 2019, 2020).

Functional connectivity (FC) measures the degree of synchrony of the BOLD time-series between different brain regions (Tononi et al., 1994; Liu et al., 2015, 2017; Lv et al., 2018). However, few studies have provided information regarding the FC changes in NAION patients. The primary visual cortex is the first step in cortical visual processing, and its degree of activation is closely related to optic nerve damage that occurs in eye-related diseases. Previous studies have found FC alterations within the primary visual cortex in cases of primary angle-closure glaucoma (Wang et al., 2021), strabismus (Zhu et al., 2018), and amblyopia (Dai et al., 2019). In addition, another study has demonstrated that NAION not only damages the retinal ganglion cells and reduces optic nerve integrity, but also damages the visual cortex (Wang et al., 2011). A previous fMRI study found that activation in the bilateral occipital cortex was decreased after stimulating the affected eye in patients with NAION than after stimulating the eyes of healthy controls (Aguirregomozcorta et al., 2011). These findings indicate that NAION might be related to functional changes within the primary visual cortex. However, it remains unclear whether there are FC changes between the primary visual cortex and the other cortical regions in NAION. Here, we hypothesized that there may be significant changes in FC between the primary visual cortex and other cortical regions in NAION, and the changes would be consistent with the visual network pathology observed in patients with NAION.

MATERIALS AND METHODS

Participants

Thirty-one patients with NAION (20 males and 11 females) who visited the ophthalmology Department at Dong Fang Hospital affiliated with Beijing University of Chinese Medicine were enrolled in the study according to the following inclusion criteria: (1) a typical clinical history of sudden, painless, and monocular visual loss or successive bilateral visual loss; (2) receival of standardized treatment and evaluation at our hospital; and (3) no history of coronary artery disease, hypertension, sleep disorders, or drug addiction. The exclusion criteria were as follows: (1) systemic features suggesting optic neuritis, giant cell arteritis, posterior ischemic optic neuropathy, or a history of optic tumor or other ocular disease; (2) symptoms of neurological disorders, mental disorders, or the inability or unwillingness to cooperate; and (3) abnormal function in the liver or kidney. In addition, 31 healthy controls (HCs) matched for age and gender were recruited according to the following criteria: (1) no history of ocular disease or symptoms of neurological disease; and (2) visual acuity $>$ 1.0 on the vision chart. All participants underwent a vision acuity test, intraocular pressure measurement, a central visual field test, optical coherence tomography to measure retinal nerve-fiber layer thickness, and MRI scanning.

Imaging Data Acquisition

All participants were scanned by a 1.5 Tesla MRI scanner (Intera Achieva System, Royal Philips, Amsterdam, Netherlands) with an eight-channel head coil. The participants were asked to wear sponge earplugs and a black blinder and to refrain from thinking about anything during the scans. The functional data were obtained using an echo planar imaging (EPI) pulse sequence with each scan. Thirty-five axial slices were acquired with the following parameters: repetition time = 3,000 ms, echo time = 30 ms, flip angle = 90°, field of view = 220 mm × 220 mm, matrix = 64 × 64, thickness = 3.6 mm, and gap = 0.72 mm, 100 time points. The total scan time was 300 s. Furthermore, high-resolution structural images (3D BRAVO) were acquired with the following parameters: matrix = 256 × 256, field of view = 256 mm × 256 mm, thickness = 1.0 mm, number of excitations = 2, repetition time = 6.5 ms, echo time = 3.2 ms, and flip angle = 8°, number of slices = 160.

Functional Magnetic Resonance Imaging Data Processing

All data were analyzed using the Data Processing Assistant for Resting State fMRI (DPARSF)[1], which is based on Statistical Parametric Mapping version 8 (SPM8)[2] and the Resting-State fMRI Data Analysis Toolkit (REST)[3], and was implemented in MATLAB 2014a (Mathworks, Natick, MA, United States). The following preprocessing steps were employed: the first 10 volumes were removed because of signal equilibrium and

[1]http://www.rfmri.org/DPARSF_V2_3

[2]https://www.fil.ion.ucl.ac.uk/spm/

[3]http://www.restfmri.net/forum/REST_V1.8

participants take time to adapt to the scanning environment; after that, slice timing and head motion correction were performed. Participants with head movements greater than 1.5 mm along any axis (x, y, or z) or greater than 1.5° in any direction were excluded (four patients were removed from data analysis for this reason). Next, based on the standard stereotaxic coordinate system, the corrected fMRI images were spatially normalized to a Montreal Neurological Institute (MNI) template brain; each voxel was resampled to isotropic 3 mm × 3 mm × 3 mm. The covariates (whole-brain head motion parameters, cerebrospinal fluid signal, and white matter signal) were removed after that. Then, linear trends in the time courses were removed and temporally bandpass filtered (0.01–0.08 Hz) to reduce the effect of physiological high-frequency respiration and cardiac noise, and low-frequency drift; finally, the images were smoothed with a full-width-at-half-maximum Gaussian kernel of 4 mm × 4 mm × 4 mm.

The primary visual cortex, known as Brodmann's area 17 (BA17), is the core area of visual processing in the brain. A previous study reported that the activation in bilateral primary visual cortex was altered in patients with NAION (Aguirregomozcorta et al., 2011). Therefore, we defined the region of interest (ROI) as bilateral BA17 according to the WFU-atlas (Maldjian et al., 2003, 2004) and previous studies (Ding et al., 2013; Zhu et al., 2018). Each ROI was a sphere with a radius of 5 mm. The FC value was determined by the Pearson's correlation coefficient of the time series of each ROI and other gray matter voxels. To improve the normal distribution, the correlation coefficients of r values were converted to z values by applying Fisher's r-to-z conversion. The final fMRI results were presented by REST software and BrainNet Viewer.[4]

Statistical Analysis

Two-sample *t*-tests were used to detect the differences in FC values between the two groups of participants, with gender, age, and duration of disease as covariates ($P < 0.05$, corrected for multiple comparisons using a false discovery rate).

Independent-sample *t*-tests were used to compare the clinical data between patients with NAION and HCs using SPSS 17.0 software (SPSS Inc., Chicago, IL) ($P < 0.05$, uncorrected). Pearson's linear correlation analyses were used to assess the relationships between the mean FC values of brain regions with statistical difference and clinical parameters in NAION patients ($P < 0.05$, uncorrected). Furthermore, the receiver operating characteristic (ROC) curve method was performed to classify different FC values between NAION patients and HCs ($P < 0.05$, uncorrected).

RESULTS

Demographic and Clinical Data

Table 1 shows the demographic and clinical data for the NAION patients and HCs. We found significant differences in vision acuity ($P < 0.01$), thickness of the retinal nerve-fiber layer ($P < 0.01$), intraocular pressure ($P < 0.01$), and the size of the central visual field ($P < 0.01$). No significant differences were found between groups in participant age.

TABLE 1 | Demographic and clinical characteristics of the NAION patients and HCs.

	NAION (*n* = 31)	HCs (*n* = 31)	*t*-value	*P*-value
Age, years	52.74 ± 11.29	50.97 ± 8.20	0.71	0.48
Gender, male/female	20/11	20/11	NA	NA
Duration of illness (years)	6.00 ± 1.12	NA	NA	NA
VA-right	0.53 ± 0.40	1.08 ± 0.17	–7.14	0.00
VA-left	0.57 ± 0.40	1.10 ± 0.17	–6.75	0.00
RNFL-right (μm)	73.00 ± 23.25	97.58 ± 8.24	–5.55	0.00
RNFL-left (μm)	79.03 ± 28.51	97.80 ± 6.91	–3.56	0.00
IOP-right	14.61 ± 2.38	13.10 ± 1.27	3.16	0.02
IOP-left	15.35 ± 2.03	13.68 ± 1.62	3.60	0.00
CVF				
MD-right	12.76 ± 9.30	0.86 ± 1.33	7.05	0.00
MD-left	10.47 ± 9.05	0.92 ± 1.28	5.82	0.00
MS-right	13.83 ± 9.23	26.96 ± 1.42	–7.83	0.00
MS-left	16.79 ± 9.04	26.89 ± 1.29	–6.16	0.00

NAION, non-arteritic anterior ischemic optic neuropathy; HCs, healthy controls; NA, not applicable; VA, vision acuity; RNFL, retinal nerve fiber layer thickness; IOP, intraocular pressure; CVF, central vision field; MD, mean defect; MS, mean sensitivity.

The Brain Areas With Functional Connectivity Differences Between the Non-arteritic Anterior Ischemic Optic Neuropathy Patients and Healthy Controls

The FC distribution maps for each group are shown in **Figures 1**, **2** for the left and right BA17, respectively. Compared with HCs, patients with NAION exhibited significantly decreased FC between the left BA17 and the right inferior frontal gyrus (IFG), and left caudate nucleus (**Figure 1** and **Table 2**). Moreover, patients also showed significantly increased FC between the right BA17 and the left olfactory gyrus and significantly decreased FC between the right BA17 and the right SFG, and right insula (**Figure 2** and **Table 2**).

Correlations Between the Clinical Data and Brain Functional Changes in Non-arteritic Anterior Ischemic Optic Neuropathy Patients

In the study, we calculated Pearson correlation coefficients between the mean FC values of the brain regions with statistical difference and the clinical data in patients with NAION. The decreased FC values in the right insula were positively correlated with the right side of mean sensitivity (MS) in the central field of vision ($r = 0.52$, $P < 0.01$) and negatively correlated with the right side of mean defect (MD) in the

[4]https://www.nitrc.org/projects/bnv/

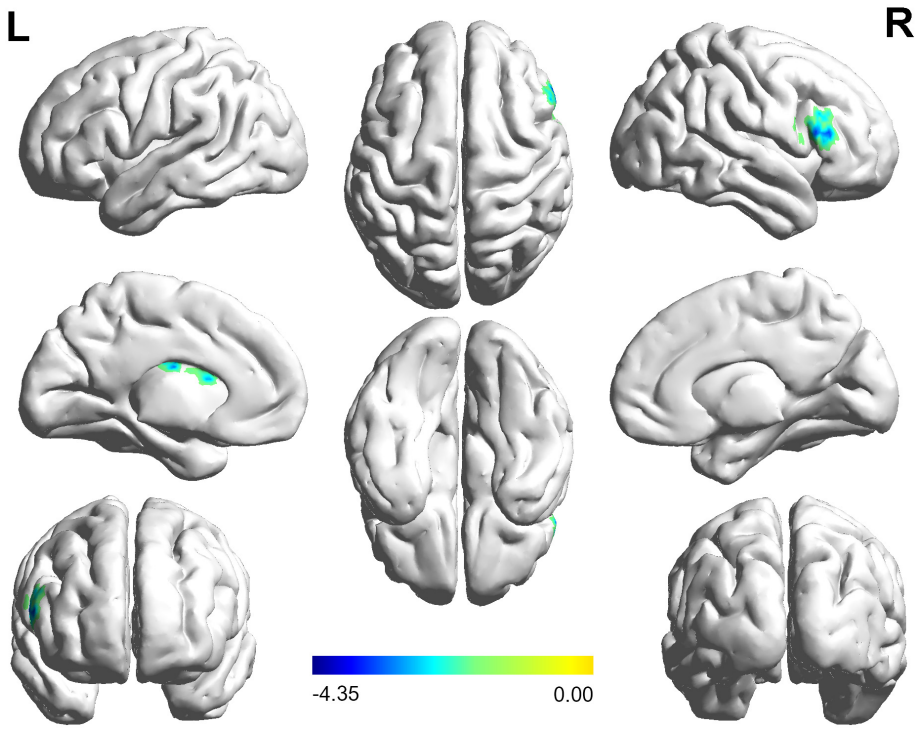

FIGURE 1 | The brain regions with significant FC changes in NAION patients when the left BA17 was used as the seed region. FC, functional connectivity; NAION, non-arteritic anterior ischemic optic neuropathy; BA, Brodmann's area.

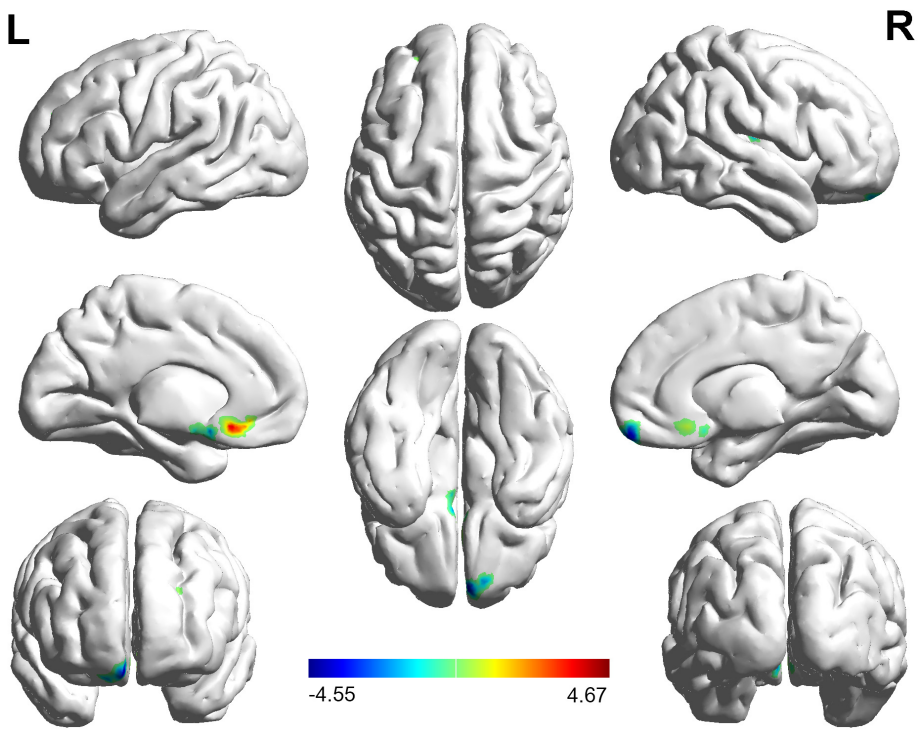

FIGURE 2 | The brain regions with significant FC changes in NAION patients when the right BA17 was used as the seed region. FC, functional connectivity; NAION, non-arteritic anterior ischemic optic neuropathy; BA, Brodmann's area.

TABLE 2 | The brain regions with statistically different FC values between the NAION patients and HCs.

Brain region	Hemisphere	Peak MNI (mm)			Peak *T*-value	Cluster size
		x	y	z		
Left BA17 as ROI						
IFG	R	63	15	21	–4.38	28
Caudate nucleus	L	–12	–9	21	–3.97	22
Right BA17 as ROI						
SFG	R	6	60	–18	–4.55	16
Olfactory gyrus	L	–3	24	–12	4.67	8
Insula	R	42	–15	15	–3.28	18

Two-sample t-test was used to determine the differences between NAION patients and HCs. The threshold was set with P < 0.05, corrected for multiple comparisons by the false discovery rate.
FC, functional connectivity; NAION, non-arteritic anterior ischemic optic neuropathy; HCs, healthy controls; MNI, Montreal Neurological Institute; BA, Brodmann's area; ROI, region of interest; IFG, inferior frontal gyrus; SFG, superior frontal gyrus; L, left; R, right.

central field of visual ($r = -0.55$, $P < 0.01$) (**Figure 3**) when the ROI was the right BA17. No significant correlations were found between mean FC values of any brain regions and the gender, duration of illness, vision acuity, intraocular pressure, or the thickness of the retinal nerve-fiber layer (all $P \geq 0.01$).

The Brain Functional Changes in Non-arteritic Anterior Ischemic Optic Neuropathy Patients as Diagnostic Indicators

The areas under the curve (AUC) of FC values in brain regions with statistical difference were as follows (**Figure 4**): right IFG (0.76, $P < 0.001$, 95% confidence interval (CI): 0.64–0.88), left caudate nucleus (0.71, $P < 0.001$, 95% CI: 0.58–0.84), right SFG (0.80, $P < 0.001$, 95% CI: 0.69–0.91), left olfactory gyrus (0.77, $P < 0.001$, 95% CI: 0.66–0.89), right insula (0.66, $P < 0.05$, 95% CI: 0.52–0.79). The AUC of the FC values in the brain regions associated with the primary visual cortex (including right IFG, right SFG, left olfactory gyrus, and left caudate nucleus) was 0.90 ($P < 0.001$, 95% CI: 0.82–0.97).

DISCUSSION

In this study, applied seed-based FC analysis, we found significant FC changes in NAION patients compared with HCs. When the left BA17 was the seed region, we found that FC with the right IFG, left caudate nucleus was decreased in patients with NAION. In contrast, when the right BA17 was the seed region, we observed that FC with the right SFG, right insula was decreased in the patients, but that FC with the left olfactory gyrus was increased.

The frontal lobe, located anterior to the central sulcus and above the lateral fissure, is the most complex part of the brain. The IFG has been associated with emotional and cognitive empathy (Shamay-Tsoory et al., 2009), offer quality (de Berker et al., 2019), and attentional control (Hampshire et al., 2010). Previous studies have found that a number of optic disease lead to the IFG dysfunction, including optic neuritis (Sun et al., 2020), anisometropic amblyopia (Lin et al., 2012), strabismus and amblyopia (Shao et al., 2019), and primary angle-closure glaucoma (Chen et al., 2019). Moreover, in a previous study, our team found decreased amplitude of low-frequency fluctuation (ALFF) in the right IFG of patients with NAION (Guo et al., 2019). We hypothesize that these results may reflect the loss of eye motion, reduced cognition, and ongoing dysfunction in the neural networks of these patients. Because of these deficits, patients receive poor visual information about what they are seeing. In support of this theory, the present study found decreased FC between the left BA17 and the right IFG in patients with NAION. In addition, the loss of visual input from the eye diminished activity in corresponding parts of the visual cortex. A previous study has demonstrated that patients with NAION exhibit reduced activation in the occipital cortex when stimulating the affected eye (Aguirregomozcorta et al., 2011). Thus, the decreased FC between BA17 and IFG might reflect compensatory inhibition in patients with NAION that reduces the influence of the poor visual information. In addition to the IFG, many studies have also shown that optic diseases are associated with dysfunction in the SFG (Min et al., 2018; Xu et al., 2019; Wang et al., 2021). The SFG occupies one-third of the frontal lobe and is thought to be the main premotor area (Peng et al., 2021). It plays roles in working memory presentation of visual space (Leavitt et al., 2018), and is also related to acute social stress (Chang and Yu, 2019), cognitive control (Tully et al., 2014), and self-consciousness (Hsieh et al., 2011). One study reported increased ALFF in the right SFG of patients with strabismus and amblyopia (Min et al., 2018). Xu et al. (2019) observed that patients with corneal ulcer demonstrated significantly increased regional homogeneity values in bilateral SFG. The abnormal activity in the SFG might reflect a strengthening of networks in patients with visual loss. Interesting, decreased FC between the BA17 and the right SFG was observed in patients with high-tension glaucoma (Wang et al., 2021). In the present study, we found that the FC values between the right BA17 and the right SFG was decreased in patients. This may indicate an impaired functional network between the SFG and the primary visual areas. Though lacking a detailed statistical analysis, we can speculate that the decreased FC can partially explain the unusual mental state reported in several patients with NAION. In addition, we speculate that NAION might influence brain executive functions and the functional integration of visual information.

The insula plays a critical role in emotion processing (Paulus et al., 2005). Additionally, it is involved in the feeling of anxiety (Paulus and Stein, 2006), as well as threat recognition and conscious urges (Craig, 2002; Lerner et al., 2009). Abnormal brain activity in the insula is also associated with diseases of the eyes, such as glaucoma (Chen et al., 2019), monocular blindness (Shao et al., 2018), and optic neuritis (Shao et al., 2015). Shao et al. (2018) found that patients with monocular blindness in the

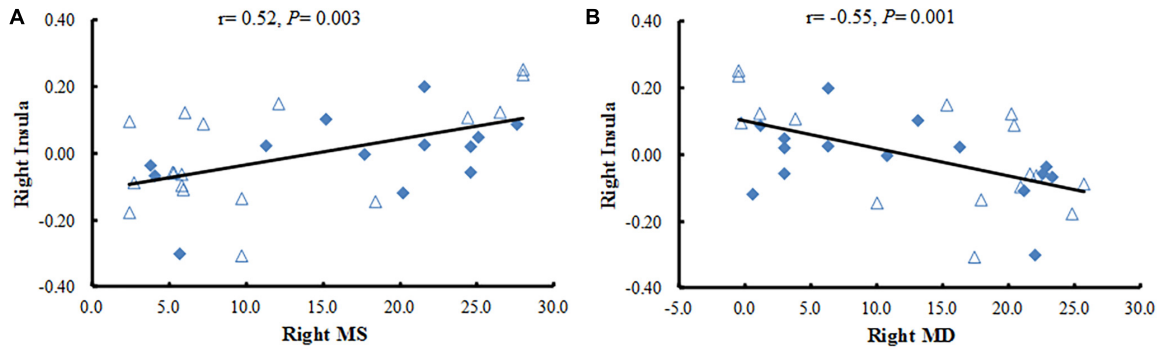

FIGURE 3 | Correlation analysis between the FC values in brain regions with significant differences and clinical variables. **(A)** The Pearson correlation shows a positive association between the mean FC values in the right insula and the right side of MS in NAION patients. **(B)** The Pearson correlation reveals a negative association between the mean FC values in the right insula and the right MD in NAION patients. FC, functional connectivity; NAION, non-arteritic anterior ischemic optic neuropathy; MS, mean sensitivity; MD, mean defect.

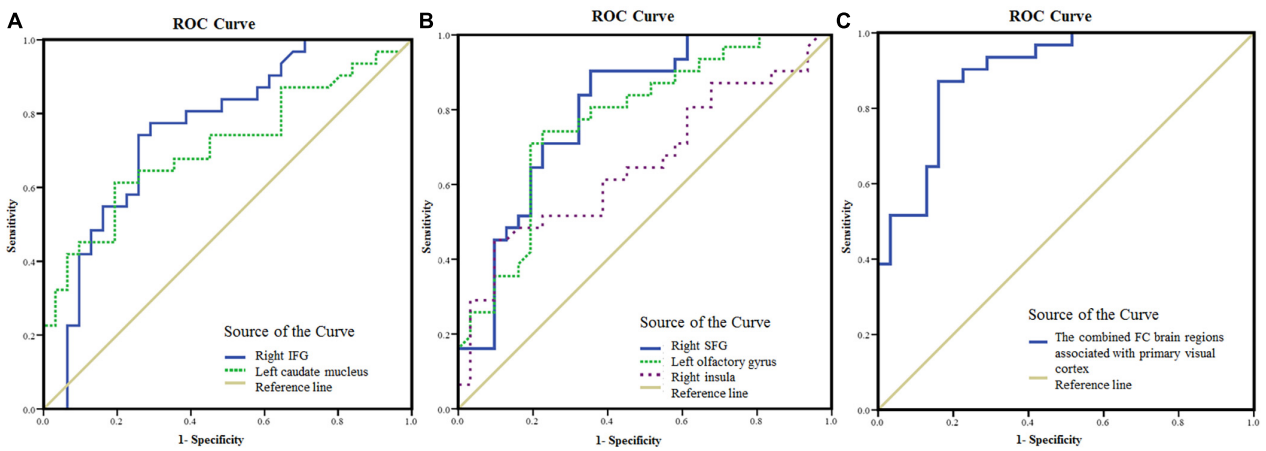

FIGURE 4 | The mean FC values in the brain areas with significant differences between NAION patients and HCs as diagnostic indicators. **(A)** ROC curve analysis of the mean FC values in the right IFG and left caudate nucleus, respectively, for differentiating NAION patients from HCs when the left BA17 was used as the seed region. **(B)** ROC curve analysis of the mean FC values in the right SFG and left olfactory gyrus, respectively, for differentiating NAION patients from HCs when the right BA17 was used as the seed region. **(C)** ROC curve analysis of the combination of the four brain areas (including the right IFG, right SFG, left olfactory gyrus, and left caudate nucleus) for differentiating NAION patients from HCs. FC, functional connectivity; NAION, non-arteritic anterior ischemic optic neuropathy; HCs, healthy controls; BA, Brodmann's area; IFG, inferior frontal gyrus; SFG, superior frontal gyrus; ROC, receiver operating characteristic.

left eye showed increased voxel-mirrored homotopic connectivity in the insula. However, our results in the current study showed that the FC values between the right BA17 and the right insula was decreased in patients with NAION, which is contrary to what other studies have found (Shao et al., 2015, 2018; Chen et al., 2019). Our new results provide further support for our previous finding that ALFF in patients with NAION is abnormal (Guo et al., 2019). NAION is an acute clinical symptom. It is characterized by sudden, painless unilateral loss of vision, which easily sparks emotional reactions. However, many patients had experienced NAION for several years (average duration, 6.00 $\pm$ 1.12 years) before visiting our hospital, and they might have become used to their condition. Thus, the decreased FC with the insula that we observed might reflect an inhibitory effort in patients with NAION to suppress their strong emotions. Meanwhile, we found that the FC values between the right insula and the right BA17 were positively correlated with right side of MS (r = 0.52, P < 0.01) and negatively correlated with right side of MD (r = −0.55, P < 0.01). Both MS and MD are key components of the central field of vision, and are important clinical parameters for assessing the severity of ophthalmological lesions; smaller MS and larger MD indicate more severe the damage. Thus, our current results may reflect ongoing damage and the severity in NAION. Furthermore, these correlations may suggest that the severity of ipsilateral damage in the eye extends down through visual-associated cortex. Thus, the more damage is observed in MS and MD, the more we can assume dysfunction in the ipsilateral insula.

The caudate nucleus is a part of the basal ganglia that is involved in a range of functions. The nucleus is thought to play an important role in the regulation of cortical excitability and sensory processing (Villablanca, 2010). Furthermore, the

nucleus has afferent, efferent, and loop connectivity with the anterior insula cortex and orbitofrontal gyrus (McGeorge and Faull, 1989). Cai et al. (2015) found that patients with primary angle-closure glaucoma demonstrated increased degree centrality in the left anterior cingulate cortex and caudate. They thought that this finding was related to altered proprioception and somatosensory processing. In addition, the caudate nucleus also plays an important role in processing spatial visual information (Gombköto et al., 2011). Our current results showed that the FC values between the left BA17 and the left caudate nucleus was decreased in the patients with NAION. These results may provide direct evidence that NAION is associated with dysfunction of the caudate nucleus. We think that the decreased FC might reflect neural plasticity that compensates for NAION-related deficits and helps prevent secondary damage.

Interestingly, in addition to the decreased FC reported above, we also found increased FC between the right BA17 and the left olfactory gyrus in the patients with NAION. To compensate for the lack of vision, individuals with early onset blindness often experience enhancements in their remaining senses, including the sense of smell. At the same time, the visual cortex can undergo remodeling so that it can receive and process non-visual inputs (Araneda et al., 2016). Gagnon et al. (2015) found that congenitally blind individuals demonstrated enhanced olfaction compared with sighted controls. The enhanced olfactory function can also develop in optically related diseases. Gugleta et al. (2010) found that patients with primary open-angle glaucoma showed alterations in olfaction. Although the pathogenesis is different, the visual impairment in patients with NAION or primary open-angle glaucoma is secondary. Indeed, research into whether the disease leads to olfactory disorders is lacking. Therefore, our current finding could represent an instance of brain plasticity in which the pathway between the visual cortex and olfactory cortex are strengthened. Thus, we speculate that the increased FC between the right BA17 and the left olfactory gyrus may be a compensatory response to the impaired vision in NAION.

In previous studies (Zhu et al., 2018; Jiang et al., 2019; Su et al., 2020), ROC analyses were successfully used to discriminate ocular disease from HCs. In the present study, ROC analysis was applied to identify patients with NAION. The AUC denotes a relatively good accuracy at values over 0.80. Our results indicated a moderate ability to discriminate patients with NAION from controls using the FC values in the brain areas with statistical difference. Although some regions, including the right IFG, right SFG, left olfactory gyrus, and left caudate nucleus, are located in the non-visual cortex, they functionally connect with the primary visual cortex. Therefore, these regions were visually relevant areas. The AUC value was 0.90 when the above regions were combined. Therefore, the results in the present study indicate that the combination of FC values in these regions may serve as a potential biomarker for distinguishing patients with NAION from HCs.

This study has several limitations. First, neuropsychological tests were not performed in the present study. This was because NAION can be accompanied by strong emotional states in some patients, which might influence the accuracy of the tests. Second, the present study included patients in whom both eyes were affected, but at different times. It is difficult to recruit patients who have only one affected eye because follow-up can occur years after the first eye is affected. Further research is required to examine this issue in more detail. Third, the number of NAION patients in the study was small. The accuracy of the results would be improved with larger sample sizes in future studies.

CONCLUSION

Patients with NAION showed significant changes in functional connections between the primary visual cortex and several other brain regions not directly related to visual function. The FC changes in these areas shed light on the neural plasticity in NAION patients and could act as a possible biomarker for distinguishing patients with NAION from HCs. These findings support that NAION may be a neuro-ophthalmological disease.

DATA AVAILABILITY STATEMENT

The original contributions presented in the study are included in the article/supplementary material, further inquiries can be directed to the corresponding author/s.

ETHICS STATEMENT

The studies involving human participants were reviewed and approved by the Medical Research Ethics Committee and Institutional Review Board of Dong Fang Hospital affiliated with Beijing University of Chinese Medicine, Beijing, China (No. JDF-IRB-2015031102). The patients/participants provided their written informed consent to participate in this study. Written informed consent was obtained from the individual(s) for the publication of any potentially identifiable images or data included in this article.

AUTHOR CONTRIBUTIONS

PG conceived the study, participated in the design, and wrote most of the manuscript. PZ and YS recruited patients and collected their clinical data. HL analyzed and interpreted the data. ML scanned the participants. YW, HH, and SK organized the database and carried out the statistical analysis. All authors read and approved the final manuscript.

FUNDING

This work was supported by the Fundamental Research Funds for the Central Universities (grant Nos. 2015-JYB-JSMS107; 2019-JYB-JS-111; and 2020-JYB-ZDGG-120).

REFERENCES

Aguirregomozcorta, M., Mancini, L., Jenkins, T. M., Hickman, S. J., Ciccarelli, O., and Plant, G. T. (2011). A longitudinal functional MRI study of non-arteritic anterior ischaemic optic neuropathy patients. *J. Neurol. Neurosurg. Psychiatry* 82, 905–913. doi: 10.1136/jnnp.2009.194563

Araneda, R., Renier, L. A., Rombaux, P., Cuevas, I., and De Volder, A. G. (2016). Cortical plasticity and olfactory function in early blindness. *Front. Syst. Neurosci.* 10:75. doi: 10.3389/fnsys.2016.00075

Berry, S., Lin, W. V., Sadaka, A., and Lee, A. G. (2017). Nonarteritic anterior ischemic optic neuropathy: cause, effect, and management. *Eye Brain* 9, 23–28. doi: 10.2147/EB.S125311

Burton, H., Sinclair, R. J., and McLaren, D. G. (2004). Cortical activity to vibrotactile stimulation: an fMRI study in blind and sighted individuals. *Hum. Brain Mapp.* 23, 210–228. doi: 10.1002/hbm.20064

Cai, F., Gao, L., Gong, H., Jiang, F., Pei, C., Zhang, X., et al. (2015). Network centrality of resting-state fMRI in primary angle-closure glaucoma before and after surgery. *PLoS One* 10:e0141389. doi: 10.1371/journal.pone.0141389 doi: 10.1371/journal.pone.0141389

Chang, J., and Yu, R. (2019). Acute social stress modulates coherence regional homogeneity. *Brain Imaging Behav.* 13, 762–770. doi: 10.1007/s11682-018-9898-9

Chen, L., Li, S., Cai, F., Wu, L., Gong, H., Pei, C., et al. (2019). Altered functional connectivity density in primary angle-closure glaucoma patients at resting-state. *Quant. Imaging Med. Surg.* 9, 603–614. doi: 10.21037/qims.2019.04.13

Craig, A. D. (2002). How do you feel? Interoception: the sense of the physiological condition of the body. *Nat. Rev. Neurosci.* 3, 655–666. doi: 10.1038/nrn894

Dai, P., Zhang, J., Wu, J., Chen, Z., Zou, B., Wu, Y., et al. (2019). Altered spontaneous brain activity of children with unilateral amblyopia: a resting state fMRI study. *Neural Plast.* 2019:3681430. doi: 10.1155/2019/3681430

de Berker, A. O., Kurth-Nelson, Z., Rutledge, R. B., Bestmann, S., and Dolan, R. J. (2019). Computing value from quality and quantity in human decision-making. *J. Neurosci.* 39, 163–176. doi: 10.1523/JNEUROSCI.0706-18.2018

Ding, K., Liu, Y., Yan, X., Lin, X., and Jiang, T. (2013). Altered functional connectivity of the primary visual cortex in subjects with amblyopia. *Neural Plast.* 2013:612086. doi: 10.1155/2013/612086

Gagnon, L., Ismaili, A. R., Ptito, M., and Kupers, R. (2015). Superior orthonasal but not retronasal olfactory skills in congenital blindness. *PLoS One* 10:e0122567. doi: 10.1371/journal.pone.0122567

Gombköto, P., Rokszin, A., Berényi, A., Braunitzer, G., Utassy, G., Benedek, G., et al. (2011). Neuronal code of spatial visual information in the caudate nucleus. *Neuroscience* 182, 225–231. doi: 10.1016/j.neuroscience.2011.02.048

Gugleta, K., Kochkorov, A., Katamay, R., Husner, A., Welge-Lüssen, A., Flammer, J., et al. (2010). Olfactory function in primary open-angle glaucoma patients. *Klin. Monbl. Augenheilkd.* 227, 277–279. doi: 10.1055/s-0029-1245198

Guo, P. D., Zhao, P. B., Lv, H., Man, F. Y., Su, Y., Zhao, J., et al. (2019). Abnormal spontaneous brain activity in patients with non-arteritic anterior ischemic optic neuropathy detected using functional magnetic resonance imaging. *Chin. Med. J.* 132, 741–743. doi: 10.1097/CM9.0000000000000134

Guo, P., Zhao, P., Lv, H., Su, Y., Liu, M., Chen, Y., et al. (2020). Abnormal regional spontaneous neural activity in nonarteritic anterior ischemic optic neuropathy: a resting-state functional MRI study. *Neural Plast.* 2020:8826787. doi: 10.1155/2020/8826787

Hampshire, A., Chamberlain, S. R., Monti, M. M., Duncan, J., and Owen, A. M. (2010). The role of the right inferior frontal gyrus: inhibition and attentional control. *Neuroimage* 50, 1313–1319. doi: 10.1016/j.neuroimage.2009.12.109

Hattenhauer, M. G., Leavitt, J. A., Hodge, D. O., Grill, R., and Gray, D. T. (1997). Incidence of nonarteritic anterior ischemic optic neuropathy. *Am. J. Ophthalmol.* 123:103. doi: 10.1016/S0002-9394(14)70999-7

Hsieh, C. W., Wu, J. H., Hsieh, C. H., Wang, Q. F., and Chen, J. H. (2011). Different brain network activations induced by modulation and nonmodulation laser acupuncture. *Evid. Based Complement Alternat. Med.* 2011:951258. doi: 10.1155/2011/951258

Huang, X., Zhou, F. Q., Dan, H. D., and Shen, Y. (2018). Abnormal intrinsic brain activity in individuals with peripheral vision loss because of retinitis pigmentosa using amplitude of low-frequency fluctuations. *Neuroreport* 29, 1323–1332. doi: 10.1097/WNR.0000000000001116

Jiang, F., Yu, C., Zuo, M. J., Zhang, C., Wang, Y., Zhou, F. Q., et al. (2019). Frequency-dependent neural activity in primary angle-closure glaucoma. *Neuropsychiatr. Dis. Treat.* 15, 271–282. doi: 10.2147/NDT.S187367 doi: 10.2147/NDT.S187367

Johnson, L. N., and Arnold, A. C. (1994). Incidence of nonarteritic and arteritic anterior ischemic optic neuropathy. population-based study in the state of Missouri and Los Angeles County, California. *J. Neuroophthalmol.* 14, 38–44. doi: 10.1097/00041327-199403000-00011

Katz, D. M., and Trobe, J. D. (2015). Is there treatment for nonarteritic anterior ischemic optic neuropathy. *Curr. Opin. Ophthalmol.* 26, 458–463. doi: 10.1097/ICU.0000000000000199

Keren, S., Zanolli, M., and Dotan, G. (2017). Visual outcome following bilateral non-arteritic anterior ischemic optic neuropathy: a systematic review and meta-analysis. *BMC Ophthalmol.* 17:155. doi: 10.1186/s12886-017-0543-y

Knox, D. L., Kerrison, J. B., and Green, W. R. (2000). Histopathologic studies of ischemic optic neuropathy. *Trans. Am. Ophthalmol. Soc.* 98, 203–20.

Leavitt, M. L., Pieper, F., Sachs, A. J., and Martinez-Trujillo, J. C. (2018). A quadrantic bias in prefrontal representation of visual-mnemonic space. *Cereb. Cortex* 28, 2405–2421. doi: 10.1093/cercor/bhx142

Lerner, A., Bagic, A., Hanakawa, T., Boudreau, E. A., Pagan, F., Mari, Z., et al. (2009). Involvement of insula and cingulate cortices in control and suppression of natural urges. *Cereb. Cortex* 19, 218–223. doi: 10.1093/cercor/bhn074

Li, Q., Bai, J., Zhang, J., Gong, Q., and Liu, L. (2016). Assessment of cortical dysfunction in patients with intermittent exotropia: an fMRI study. *PLoS One* 11:e0160806. doi: 10.1371/journal.pone.0160806

Lin, X., Ding, K., Liu, Y., Yan, X., Song, S., and Jiang, T. (2012). Altered spontaneous activity in anisometropic amblyopia subjects: revealed by resting-state FMRI. *PLoS One* 7:e43373. doi: 10.1371/journal.pone.0043373

Liu, F., Guo, W., Fouche, J. P., Wang, Y., Wang, W., Ding, J., et al. (2015). Multivariate classification of social anxiety disorder using whole brain functional connectivity. *Brain Struct. Funct.* 220, 101–115. doi: 10.1007/s00429-013-0641-4

Liu, F., Wang, Y., Li, M., Wang, W., Li, R., Zhang, Z., et al. (2017). Dynamic functional network connectivity in idiopathic generalized epilepsy with generalized tonic-clonic seizure. *Hum. Brain Mapp.* 38, 957–973. doi: 10.1002/hbm.23430

Lv, H., Wang, Z., Tong, E., Williams, L. M., Zaharchuk, G., Zeineh, M., et al. (2018). Resting-state functional MRI: everything that nonexperts have always wanted to know. *Am. J. Neuroradiol.* 39, 1390–1399. doi: 10.3174/ajnr.A5527

Maldjian, J. A., Laurienti, P. J., and Burdette, J. H. (2004). Precentral gyrus discrepancy in electronic versions of the talairach atlas. *Neuroimage* 21, 450–455. doi: 10.1016/j.neuroimage.2003.09.032

Maldjian, J. A., Laurienti, P. J., Kraft, R. A., and Burdette, J. H. (2003). An automated method for neuroanatomic and cytoarchitectonic atlas-based interrogation of fMRI data sets. *Neuroimage* 19, 1233–1239. doi: 10.1016/s1053-8119(03)00169-1

McGeorge, A. J., and Faull, R. L. (1989). The organization of the projection from the cerebral cortex to the striatum in the rat. *Neuroscience* 29, 503–537. doi: 10.1016/0306-4522(89)90128-0

Miller, N. R., and Arnold, A. C. (2015). Current concepts in the diagnosis, pathogenesis and management of nonarteritic anterior ischaemic optic neuropathy. *Eye* 29, 65–79. doi: 10.1038/eye.2014.144

Min, Y. L., Su, T., Shu, Y. Q., Liu, W. F., Chen, L. L., Shi, W. Q., et al. (2018). Altered spontaneous brain activity patterns in strabismus with amblyopia patients using amplitude of low-frequency fluctuation: a resting-state fMRI study. *Neuropsychiatr. Dis. Treat.* 14, 2351–2359. doi: 10.2147/NDT.S171462

Paulus, M. P., and Stein, M. B. (2006). An insular view of anxiety. *Biol. Psychiatry* 60, 383–387. doi: 10.1016/j.biopsych.2006.03.042

Paulus, M. P., Feinstein, J. S., Castillo, G., Simmons, A. N., and Stein, M. B. (2005). Dose-dependent decrease of activation in bilateral amygdala and insula by lorazepam during emotion processing. *Arch. Gen. Psychiatry* 62, 282–288. doi: 10.1001/archpsyc.62.3.282

Peng, Z. Y., Liu, Y. X., Li, B., Ge, Q. M., Liang, R. B., Li, Q. Y., et al. (2021). Altered spontaneous brain activity patterns in patients with neovascular glaucoma using amplitude of low-frequency fluctuations: a functional magnetic resonance imaging study. *Brain Behav.* 11:e02018. doi: 10.1002/brb3.2018

Qin, Y., Yuan, W., Deng, H., Xiang, Z., Yang, C., Kou, X., et al. (2015). Clinical efficacy observation of acupuncture treatment for nonarteritic anterior ischemic optic neuropathy. *Evid. Based Complement Alternat. Med.* 2015:713218. doi: 10.1155/2015/713218

Shamay-Tsoory, S. G., Aharon-Peretz, J., and Perry, D. (2009). Two systems for empathy: a double dissociation between emotional and cognitive empathy in inferior frontal gyrus versus ventromedial prefrontal lesions. *Brain* 132, 617–627. doi: 10.1093/brain/awn279

Shao, Y., Bao, J., Huang, X., Zhou, F. Q., Ye, L., Min, Y. L., et al. (2018). Comparative study of interhemispheric functional connectivity in left eye monocular blindness versus right eye monocular blindness: a resting-state functional MRI study. *Oncotarget* 9, 14285–14295. doi: 10.18632/oncotarget.24487

Shao, Y., Cai, F. Q., Zhong, Y. L., Huang, X., Zhang, Y., Hu, P.-H., et al. (2015). Altered intrinsic regional spontaneous brain activity in patients with optic neuritis: a resting-state functional magnetic resonance imaging study. *Neuropsychiatr. Dis. Treat.* 11, 3065–3073. doi: 10.2147/NDT.S92968

Shao, Y., Li, Q. H., Li, B., Lin, Q., Su, T., Shi, W. Q., et al. (2019). Altered brain activity in patients with strabismus and amblyopia detected by analysis of regional homogeneity: a resting-state functional magnetic resonance imaging study. *Mol. Med. Rep.* 19, 4832–4840. doi: 10.3892/mmr.2019.10147

Su, T., Yuan, Q., Liao, X. L., Shi, W. Q., Zhou, X. Z., Lin, Q., et al. (2020). Altered intrinsic functional connectivity of the primary visual cortex in patients with retinal vein occlusion: a resting-state fMRI study. *Quant. Imaging Med. Surg.* 10, 958–969. doi: 10.21037/qims.2020.03.24

Sun, M., Zhou, H., Xu, Q., Yang, M., Xu, X., Zhou, M., et al. (2020). Differential patterns of interhemispheric functional connectivity between AQP4-optic neuritis and MOG-optic neuritis: a resting-state functional MRI study. *Acta Radiol.* 62, 776–783. doi: 10.1177/0284185120940250

Tononi, G., Sporns, O., and Edelman, G. M. (1994). A measure for brain complexity: relating functional segregation and integration in the nervous system. *Proc. Natl. Acad. Sci. U.S.A.* 91, 5033–5037. doi: 10.1073/pnas.91.11.5033

Tully, L. M., Lincoln, S. H., Liyanage-Don, N., and Hooker, C. I. (2014). Impaired cognitive control mediates the relationship between cortical thickness of the superior frontal gyrus and role functioning in schizophrenia. *Schizophr. Res.* 152, 358–364. doi: 10.1016/j.schres.2013.12.005

van Kemenade, B. M., Arikan, B. E., Kircher, T., and Straube, B. (2017). The angular gyrus is a supramodal comparator area in action-outcome monitoring. *Brain Struct. Funct.* 222, 3691–3703. doi: 10.1007/s00429-017-1428-9

Villablanca, J. R. (2010). Why do we have a caudate nucleus. *Acta Neurobiol. Exp.* 70, 95–105.

Wang, B., Yan, T., Zhou, J., Xie, Y., Qiu, J., Wang, Y., et al. (2021). Altered fMRI-derived functional connectivity in patients with high-tension glaucoma. *J. Neuroradiol.* 48, 94–98. doi: 10.1016/j.neurad.2020.03.001

Wang, K., Jiang, T., Yu, C., Tian, L., Li, J., Liu, Y., et al. (2008). Spontaneous activity associated with primary visual cortex: a resting-state FMRI study. *Cereb. Cortex* 18, 697–704. doi: 10.1093/cercor/bhm105

Wang, M. Y., Qi, P. H., and Shi, D. P. (2011). Diffusion tensor imaging of the optic nerve in subacute anterior ischemic optic neuropathy at 3T. *Am. J. Neuroradiol.* 32, 1188–1194. doi: 10.3174/ajnr.A2487

Xu, L., Wang, Y., and Jonas, J. B. (2007). Incidence of nonarteritic anterior ischemic optic neuropathy in adult Chinese: the Beijing eye study. *Eur J Ophthalmol.* 17, 459–460. doi: 10.1177/112067210701700335

Xu, M. W., Liu, H. M., Tan, G., Su, T., Xiang, C. Q., Wu, W., et al. (2019). Altered regional homogeneity in patients with corneal ulcer: a resting-state functional MRI study. *Front. Neurosci.* 13:743. doi: 10.3389/fnins.2019.00743

Zhang, C., Guo, Y., Slater, B. J., Miller, N. R., and Bernstein, S. L. (2010). Axonal degeneration, regeneration and ganglion cell death in a rodent model of anterior ischemic optic neuropathy (rAION). *Exp. Eye Res.* 91, 286–292. doi: 10.1016/j.exer.2010.05.021

Zhu, P. W., Huang, X., Ye, L., Jiang, N., Zhong, Y. L., Yuan, Q., et al. (2018). Altered intrinsic functional connectivity of the primary visual cortex in youth patients with comitant exotropia: a resting state fMRI study. *Int. J. Ophthalmol.* 11, 668–673.

Conflict of Interest: The authors declare that the research was conducted in the absence of any commercial or financial relationships that could be construed as a potential conflict of interest.

Publisher's Note: All claims expressed in this article are solely those of the authors and do not necessarily represent those of their affiliated organizations, or those of the publisher, the editors and the reviewers. Any product that may be evaluated in this article, or claim that may be made by its manufacturer, is not guaranteed or endorsed by the publisher.

frontiers in Neuroscience

ORIGINAL RESEARCH
published: 05 October 2021
doi: 10.3389/fnins.2021.752419

Cerebral Blood Flow Difference Between Acute and Chronic Tinnitus Perception: A Perfusion Functional Magnetic Resonance Imaging Study

Jinghua Hu[1†], Jin-Jing Xu[1†], Song'an Shang[2], Huiyou Chen[2], Xindao Yin[2], Jianwei Qi[1] and Yuanqing Wu[1*]*

[1] Department of Otolaryngology, Nanjing First Hospital, Nanjing Medical University, Nanjing, China, [2] Department of Radiology, Nanjing First Hospital, Nanjing Medical University, Nanjing, China

Purpose: The central nervous mechanism of acute tinnitus is different from that of chronic tinnitus, which may be related to the difference of cerebral blood flow (CBF) perfusion in certain regions. To verify this conjecture, we used arterial spin labeling (ASL) perfusion magnetic resonance imaging (MRI) in this study to compare the CBF alterations of patients with acute and chronic tinnitus.

Methods: The current study included patients with chronic tinnitus (n = 35), acute tinnitus (n = 30), and healthy controls (n = 40) who were age-, sex-, and education-matched. All participants underwent MRI scanning and then ASL images were obtained to measure CBF of the entire brain and analyze the differences between groups as well as the correlations with tinnitus characteristics.

Results: The chronic tinnitus group showed increased z-CBF in the right superior temporal gyrus (STG) and superior frontal gyrus (SFG) when compared with the acute tinnitus patients. Further connectivity analysis found enhanced CBF connectivity between the right STG and fusiform gyrus (FG), the right SFG and left middle occipital gyrus (MOG), as well as the right parahippocampal gyrus (PHG). Moreover, in the chronic tinnitus group, the tinnitus handicap questionnaire (THQ) score was positively correlated with the normalized z-CBF of right STG (r = 0.440, p = 0.013).

Conclusion: Our results confirmed that the CBF changes in some brain regions were different between acute and chronic tinnitus patients, which was correlated with certain tinnitus characteristics. This is of great value to further research on chronicity of tinnitus, and ASL has a promising application in the measurement of CBF.

Keywords: cerebral blood flow, tinnitus perception, magnetic resonance imaging, arterial spin labeling, perfusion

OPEN ACCESS

Edited by:
Han Lv,
Capital Medical University, China

Reviewed by:
Xin Huang,
Jiangxi Provincial People's Hospital, China
Zhenyu Xiong,
University of Texas Southwestern Medical Center, United States

***Correspondence:**
Yuanqing Wu
cnnxdd@163.com
Jianwei Qi
Qjw70818@163.com

[†] These authors have contributed equally to this work

Specialty section:
This article was submitted to Perception Science, a section of the journal Frontiers in Neuroscience

Received: *03 August 2021*
Accepted: *30 August 2021*
Published: *05 October 2021*

Citation:
Hu J, Xu J-J, Shang S, Chen H, Yin X, Qi J and Wu Y (2021) Cerebral Blood Flow Difference Between Acute and Chronic Tinnitus Perception: A Perfusion Functional Magnetic Resonance Imaging Study. Front. Neurosci. 15:752419. doi: 10.3389/fnins.2021.752419

INTRODUCTION

Tinnitus is the perception of an auditory sensation without a corresponding external sound stimulus (Biswas et al., 2019). It is a global problem with a prevalence of about 10%–15% in adults worldwide (Henry et al., 2020). A unified classification system for tinnitus has not been realized. In the "A multidisciplinary European guideline for tinnitus: diagnostics, assessment, and treatment"

published in 2019, tinnitus is divided into acute tinnitus (duration ≤ 3 months), subacute tinnitus (duration < 3 months), and chronic tinnitus (duration ≥ 6 months) (Cima et al., 2019). Clinical assessments of tinnitus including objective and subjective assessments showed different clinical features between acute and chronic tinnitus, such as tinnitus loudness, frequency, and tinnitus-related mood disorders (Wallhäusser-Franke et al., 2017). A recent longitudinal study found that 18.4% of acute tinnitus patients had complete remission of tinnitus within 6 months. There was no change in tinnitus characteristics in patients with their tinnitus persistent (Vielsmeier et al., 2020). However, the exact mechanism of the chronization of tinnitus remains a mystery.

In recent years, there have been many neuroimaging techniques used to study the central nervous mechanism of tinnitus like electroencephalography (EEG), magnetoencephalography (MEG), and functional magnetic resonance imaging (fMRI) (Nathan et al., 2005; Han et al., 2018; Berlot et al., 2020; Chen et al., 2021). It seems that the auditory system may play a basic role in tinnitus generation (Møller, 2007). Meanwhile, some non-auditory areas, such as prefrontal, parietal, and limbic regions, are closely related to tinnitus maintenance, severity, the accompanying emotional disorder, and cognitive impairment (Chen et al., 2017b, 2018; Zimmerman et al., 2019). However, most studies have analyzed chronic or acute tinnitus independently. The specific differences of neural mechanism between the acute and chronic tinnitus as well as the mechanism of transformation from acute to chronic tinnitus are rarely investigated. Vanneste et al. (2011) detected enhanced neural activity in the right auditory cortex in chronic tinnitus compared with recent-onset tinnitus using the EEG approach. A latest EEG study compared acute and chronic tinnitus, which found differences in neural activity and connectivity in many regions. It was found that a non-auditory brain region, especially parahippocampus gyrus, plays a key role in the transition from acute to chronic tinnitus (Lan et al., 2021). Therefore, we suggest that chronization of tinnitus is a complex mechanism involving multiple networks.

Besides structural and functional brain alterations, positron emission tomography (PET) and single photo emission computed tomography (SPECT) studies confirmed abnormal cerebral blood flow (CBF) of patients with tinnitus (Lanting et al., 2009; Ueyama et al., 2015). It was found that regional CBF in tinnitus patients was lower in DMN regions and higher in memory and emotional networks (Ueyama et al., 2015). Reyes et al. (2002) used SPECT and found that changes in tinnitus loudness can cause significant CBF changes in the auditory cortex of the temporal lobe. So, the abnormal CBF in tinnitus may be related to the tinnitus sound stimulations, but we do not know if it has anything to do with the duration of the stimulus.

Arterial spin labeling (ASL) is another technique to investigate brain hemodynamic changes. Different from PET and SPECT, ASL is a completely non-invasive method without using invasive radioactive tracers (Ferré et al., 2013). Moreover, ASL could provide reproducible and reliable quantitative measurements of cerebral perfusion non-invasively (Telischak et al., 2015). In terms of quantitative measurement of CBF, ASL is more advantageous than blood oxygen level-dependent MRI (BOLD-MRI) (Detre and Wang, 2002; Kim et al., 2019). ASL has been used to quantify CBF alterations in many diseases, such as Parkinson's disease (Barzgari et al., 2019) and Alzheimer's disease (Zhang et al., 2017). Recently, a few researches used ASL to study CBF alterations in tinnitus patients (Li X. et al., 2020; Li et al., 2021). However, the objects of these studies were pulsatile tinnitus patients, which is different from subjective tinnitus in symptoms, etiology, mechanism, and so on (Pegge et al., 2017). Some recent studies have explored the regional CBF alterations in subjective tinnitus patients with other complications, such as diabetes (Xia et al., 2020) or migraine (Xu et al., 2021). However, no studies have evaluated the role of CBF in tinnitus chronization mechanisms so far. The regional CBF can be used to reflect the neural activity in local brain regions. When different brain regions cooperate to complete a certain function, regional CBF may change synchronously (Li F. et al., 2020). Therefore, CBF connectivity is also an important indicator, which is similar to the structural and functional connectivity.

Based on the above, the current study used ASL technology to calculate and compare CBF changes of acute and chronic tinnitus patients. We hypothesized that different CBF patterns may exist in different stages of tinnitus chronization. A further study on the mechanism of tinnitus chronicity may be of great help to provide a new imaging perspective for early diagnosis and prognosis evaluation.

MATERIALS AND METHODS

This study was approved by the Research Ethics Committee of the Nanjing Medical University. All the subjects signed written informed consent before participating in the study.

Participants

From May 2018 to January 2020, we recruited 30 acute tinnitus patients (duration < 1 month, 11.0 ± 6.9 days) and 35 chronic tinnitus patients (duration > 6 months, 46.1 ± 39.4 months) from the Department of Otolaryngology and 40 healthy examinees as healthy controls (HC) in Nanjing First Hospital of Nanjing Medical University. All subjects were 20–70 years old, right-handed, and completed at least 8 years of education. All tinnitus patients presented bilateral subjective tinnitus without obvious causes. None of them had received any form of tinnitus treatment (including medication, acupuncture, and electrical stimulation) before entering the study.

All subjects were tested by puretone audiometry (PTA) to determine the hearing thresholds at the frequencies of 0.25, 0.5, 1, 2, 4, and 8 kHz. Normal hearing means hearing thresholds < 25 dB and mild hearing loss means hearing thresholds between 26 and 40 dB (Olaosun and Ogundiran, 2013). All HC and most tinnitus patients had normal hearing. Only a few cases of tinnitus patients had mild sensorineural hearing loss. There were no significant differences among acute tinnitus patients, chronic tinnitus patients, and HC in auditory thresholds (**Figure 1**).

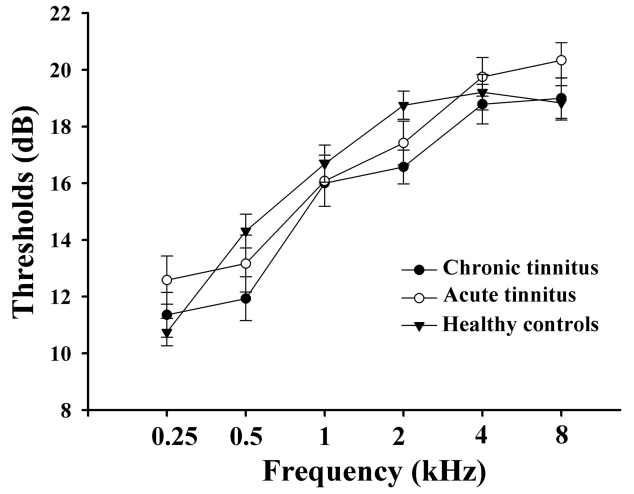

FIGURE 1 | Mean hearing thresholds of the chronic tinnitus, acute tinnitus, and healthy controls. Data are presented as mean ± SEM.

TABLE 1 | Demographic and clinical characteristics of all subjects.

	Chronic tinnitus (n = 35)	Acute tinnitus (n = 30)	Healthy controls (n = 40)	p value
Age (year)	51.11±11.38	49.73±12.17	45.10±11.04	0.064[a]
Education (year)	12.26±2.84	12.80±3.68	12.73±2.51	0.719[a]
Gender (male/female)	10/25	14/16	15/25	0.322[b]
SAS	40.80±5.60	37.93±6.16	38.08±5.72	0.073[a]
SDS	41.46±6.21	40.50±5.48	41.03±4.54	0.777[a]
THQ score	53.24±13.94	47.45±15.27	–	0.115[c]
PTA of left ear (dB HL)	15.26±2.86	16.22±2.91	16.71±2.77	0.089[a]
PTA of right ear (dB HL)	16.50±2.64	16.89±3.48	16.65±2.41	0.857[a]
Mean PTA of both ears (dB HL)	15.61±2.05	16.56±2.80	16.68±1.80	0.086[a]

Data are expressed as Mean ± SD.
[a] The p values are obtained by using one-way analysis of variance.
[b] The p values are obtained by using χ 2 test.
[c] The p values are obtained by using a two-sample t test.
SAS, Self-Rating Anxiety Scale; SDS, Self-Rating Depression Scale; THQ, tinnitus handicap questionnaire; PTA, puretone audiometry.

All the patients filled in the following questionnaires: (1) the Iowa version Tinnitus handicap questionnaire (THQ) (Kuk et al., 1990) to assess the severity of tinnitus; (2) the Self-Rating Depression Scale (SDS) for self-rated depression status; (3) the Self-Rating Anxiety Scale (SAS) for self-rated anxiety status; and (4) the Mini-Mental State Examination (MMSE) to assess the cognitive function. A MMSE score of < 26 indicates cognitive impairment, which is one of the exclusion criteria. None of the participants in this study had depression, anxiety, and mild cognitive impairment according to these tests above.

Participants were also excluded in the current study if they have the following conditions: (1) hyperacusis [detected by the Hyperacusis Questionnaire (Khalfa et al., 2002)]; (2) objective tinnitus, pulsatile tinnitus, Meniere's diseases, history of use of ototoxic drugs, or ear surgery and other major ear diseases; (3) bad habits that may affect the nervous system (e.g., severe smoking, alcoholism, and drug addiction), neurological or psychiatric illness such as serious insomnia, brain injury, schizophrenia, and Alzheimer's disease, Parkinson's disease, and peripheral neuropathy; (4) major medical illness such as cancer, blood system diseases, and thyroid dysfunction; and (5) contraindications for MRI such as heart pacemakers, artificial heart valves, aneurysm clips, metal objects in the body, and claustrophobia. The characteristics of the acute tinnitus and chronic tinnitus patients and HC are shown in **Table 1**.

Magnetic Resonance Imaging Measurements

During the MRI scan, the subjects kept their eyes closed, stayed awake and remained still, and avoided thinking about anything in particular. We used foam padding to reduce the head motion, and none of subjects in this study was excluded because of excessive head motion (with over 2.0 mm translation or 2.0° rotation in any direction). We also used earplugs (Hearos Ultimate Softness Series, United States) to reduce the perception of the scanner noise, and they could attenuate the noise by approximately 32 dB, according to the manufacturer's data.

Imaging was performed on a 3.0-T MRI scanner (Ingenia, Philips Medical Systems, Netherlands) with an 8-channel receiver array head coil. Imaging parameters are as follows: (1) A three-dimensional turbo fast echo (3D-TFE) T1-weighted imaging (T1WI) sequence with high resolution for structural images: acquisition matrix = 256 × 256, field of view (FOV) = 256 × 256 mm^2, repetition time (TR)/echo time (TE) = 8.1/3.7 ms, flip angle (FA) = 8°, slices = 170, thickness = 1 mm, gap = 0 mm. The structural sequence scanning time totaled 5 min and 29 s. (2) A 3D-pseudocontinuous arterial spin labeling (pCASL) sequence for ASL-CBF images: TR = 4,000 ms; TE = 11 ms; post-label delay = 2,000 ms; FA = 90°; slice thickness = 4 mm with 10% gap; FOV = 240 × 240 mm^2; matrix = 64 × 64; 24 axial slices, label duration = 1,650 ms. The ASL sequence scanning time totaled 4 min and 8 s.

Data Processing and Cerebral Blood Flow Analysis

We used ASL data processing toolbox (ASLtbx) (Wang et al., 2008) and statistical parameter mapping software 12 (SPM12) to process MRI data. The pCASL data were processed to generate CBF map and quantitative CBF was calculated on this basis (Xu et al., 2010). The images were rearranged and adjusted to correct head movement. After non-linear transformation, the CBF images of 40 HC subjects were co-registered with the PET template in the Montreal Neurological Institute (MNI) space. The average co-registered CBF images of the HC came to be the MNI-standard CBF template. Each CBF image of acute and chronic tinnitus patients was co-registered to this MNI-standard CBF template (voxel size was 1.5 mm × 1.5 mm × 1.5 mm) and then was spatially smoothed with a Gaussian kernel [width at half maximum (FWHM) is 8 mm]. Normalization CBF map was obtained by dividing the

CBF per voxel by the average CBF across the entire brain (Aslan and Lu, 2010).

Gray Matter Volume Calculation

The gray matter volume (GMV) calculation was performed by using SPM12. The structural images were tissue classified in a standard uniform segmentation model and the cerebral tissues can be segmented into gray matter (GM), white matter (WM), and cerebrospinal fluid. The GM concentration map was initial affine registered to the MNI space (resampled to the voxel size of 1.5 mm × 1.5 mm × 1.5 mm). Then, a non-linear deformation of GM concentration image was carried out. Multiplying the non-linear determinant and GM concentration together results in the GMV of each voxel. Then, all the GMVs were smoothed using a Gaussian kernel of FWHM 10 mm. After spatial pre-processing of the data, the voxel-wised GMV maps were used in the later ASL analysis as covariates.

Cerebral Blood Flow Connectivity Analysis

According to previous studies (Andersson et al., 2000; Xia et al., 2020), the clusters with significant group differences in CBF of tinnitus patients were selected as seed regions of interest (ROIs) including parieto-temporal auditory cortex, frontal paralimbic areas, and posterior cingulate cortex. To determine whether the ROIs have abnormal CBF connectivity, a multiple regression model was used to detect the CBF connectivity between each ROI seed and other voxels in the whole brain for each group. Age, gender, and GMV were included in this model as confounding covariates. The three groups were compared in pairs, and the CBF connectivity maps of each pair were combined to form a spatial mask to which the CBF of each voxel of each ROI was then correlated. For each pair of voxels, the slopes of CBF correlation reflect the difference in CBF connectivity between groups. A two-sample *t*-test was established within the spatial mask of the CBF connectivity map of ROI to analyze the differences in CBF connectivity between each ROI and all the other voxels in the brain so that we obtain a voxel map that shows significantly different CBF connectivity among acute tinnitus patients, chronic tinnitus patients, and HC subjects for each ROI. Multiple comparisons were corrected using the false discovery rate (FDR) correction (significance set at $p < 0.01$).

Statistical Analyses

Statistical analyses were performed using the SPSS software (version 20.0; SPSS, Chicago, IL, United States). One-way analysis of variance (ANOVA) was used to compare the differences in demographic information and clinical measures among three groups. A *post hoc* test was used for comparison between the tinnitus and HC groups (*t*-test for means and χ^2 test for proportions). Significance level was set at $p < 0.05$. For normalized CBF, the discrete sequence was Z transformed and the result was expressed as z-CBF. To extract regions that were significantly different in z-CBF between groups, a VBM analysis and two-sample *t*-test were used to perform group comparisons between the tinnitus and HC group. For CBF connectivity, a two-sample *t*-test was performed to extract areas with significantly different CBF connectivity between two groups. The results were corrected by age, gender, education level, and GMV and represented in the MNI coordinate system. The statistical value of the *t*-test was expressed as *T*-value and was corrected by FDR correction (significance threshold was set as $p < 0.01$).

In order to compute the correlations between the tinnitus characteristics and abnormal CBF as well as CBF connectivity, Pearson's correlation based on ROI analysis was performed (age, gender, education level, and GMV as the correction factors). $p < 0.05$ was set as the significance threshold.

RESULTS

Normalized Cerebral Blood Flow Differences Between Groups

Figure 2 and **Table 2** show brain regions with different normalized CBF between groups. It turned out that z-CBF increased in the right superior temporal gyrus (STG) and superior frontal gyrus (SFG) of chronic tinnitus patients, when compared with the acute tinnitus subjects. Increased z-CBF in the right middle temporal gyrus (MTG) and left SFG was observed in the chronic tinnitus group compared to that in the HC group. Furthermore, acute tinnitus patients showed higher z-CBF in the left STG compared to the HC group. Moreover, no significant differences of GM and WM volumes among chronic tinnitus, acute tinnitus patients, and healthy controls were observed.

Cerebral Blood Flow Connectivity Differences Between Groups

Figure 3 and **Table 3** depicted the group differences on CBF connectivity. When making a comparison with acute tinnitus, the chronic tinnitus group exhibited enhanced CBF connectivity between the seed ROI of the right STG and fusiform gyrus (FG). Moreover, it was observed in chronic tinnitus patients that the CBF connectivity aggrandized between the seed ROI of the right SFG and left middle occipital gyrus (MOG) as well as right parahippocampal gyrus (PHG). CBF connections between the seed ROI of the left STG and right FG were increased in chronic tinnitus patients compared to the HC group. There were no significant differences in CBF connectivity in seed of the right MTG and left SFG between groups.

Relationship Between z- Cerebral Blood Flow and Clinical Characteristics

Figure 4 illustrates the correlations between the z-CBF alteration and the tinnitus characteristics. Compared with acute tinnitus, the THQ score was significantly positively related with the z-CBF of the right STG in chronic tinnitus patients ($r = 0.440$, $p = 0.013$) but not in acute tinnitus patients ($r = 0.361$, $p > 0.05$). Besides, compared with HC, the THQ score was positively correlated with the z-CBF of the right MTG in chronic tinnitus patients ($r = 0.426$, $p = 0.017$). Finally, the z-CBF and CBF connectivity in

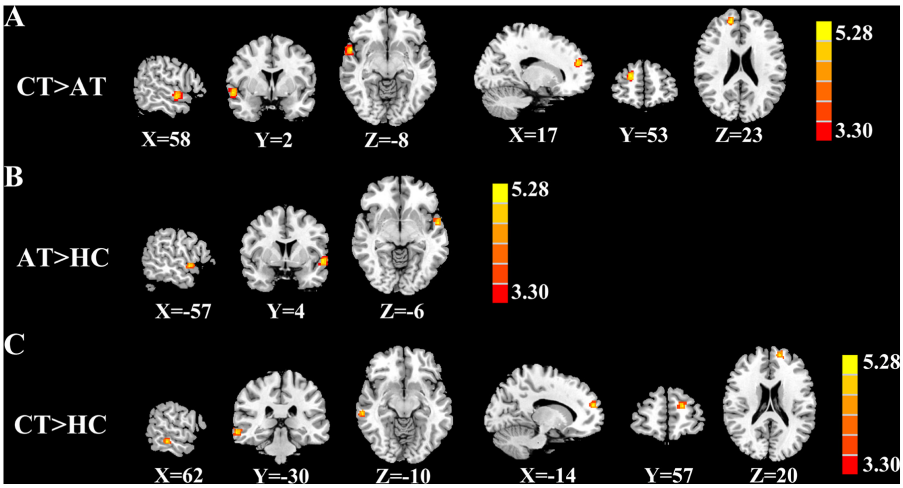

FIGURE 2 | Significant CBF differences among the chronic tinnitus (CT), acute tinnitus (AT), and healthy controls (HC). **(A)** Compared to AT, CT showed increased z-CBF in the right superior temporal gyrus (STG), and right superior frontal gyrus (SFG). **(B)** Compared to HC, AT showed higher z-CBF in the left STG. **(C)** Compared to HC, CT showed increased z-CBF in right middle temporal gyrus (MTG) and left SFG. Significant thresholds were corrected using FDR criterion and set at $p < 0.01$.

other brain regions was not significantly correlated with specific tinnitus characteristics.

DISCUSSION

In this study, ASL-MRI was firstly used to compare the CBF perfusion differences between acute and chronic tinnitus. In comparison to the acute tinnitus group, the chronic tinnitus patients showed different CBF mainly in the STG, SFG, and MTG. Further ROI analysis exhibited that CBF connectivity was enhanced between the right STG and FG, right SFG and PHG, as well as the left MOG. In addition, in the chronic tinnitus group, there were positive correlations between THQ score and increased CBF in ROIs of temporal gyrus.

TABLE 2 | Brain regions with significant group differences in normalized CBF with GMV correction.

Brain regions	BA	Peak MNI coordinates x, y, z (mm)	Peak *T* value	Cluster size (voxels)
CT>AT				
R_STG	22	58, 2, −8	4.405	163
R_SFG	10	17, 53, 23	5.588	455
AT>HC				
L_STG	22	−57, 4, −6	4.984	231
CT>HC				
R_MTG	21	62, −30, −10	4.488	325
L_SFG	10	−14, 57, 20	4.499	142

Thresholds were set at a corrected p< 0.01 corrected by FDR criterion. MNI, Montreal Neurological Institute; CT, chronic tinnitus; AT, acute tinnitus; HC, healthy control; STG, superior temporal gyrus; SFG, superior frontal gyrus; MTG, middle temporal gyrus; L, left; R, right.

The Temporal Gyrus

Compared to the acute tinnitus group, chronic tinnitus patients had increased z-CBF in the right STG. As part of the auditory cortex, the STG is critical for high-order auditory processing of speech by encoding phonetic features (Yi et al., 2019). It is believed that tinnitus is caused by an abnormal GM structure and neural activity of the central auditory cortex (Aldhafeeri et al., 2012; Chen et al., 2015a,c; Cai et al., 2019). Several researchers have also found increased CBF in the temporal auditory cortex of tinnitus patients using PET and SPECT (Andersson et al., 2000; Ueyama et al., 2015). However, the correlation between this change and tinnitus remains to be proved. Similar to our results, in the EEG study of Vanneste et al., increased neural electrical activity was found in the right auditory cortex in chronic tinnitus relative to recent-onset tinnitus (Vanneste et al., 2011). According to the tinnitus model proposed by Eggermont and Roberts (2004), the initial signal of ringing in the ears is due to abnormal nerve activity of auditory nerve fibers caused by peripheral auditory pathway injury. The abnormal neural activity causes other auditory neuron hyperactivity, which has a similar edge frequency. If the abnormity persists, the auditory cortex will reorganize in response to the change, mimicking the response to normal acoustic stimuli. That is why chronic tinnitus can lead to central alterations (Eggermont, 2003). It was found that in tinnitus patients in the resting state without external sound stimulation, the α activity of neurons in the temporal cortex was reduced. The longer the duration of tinnitus, the less variability of this α activity (Schlee et al., 2014). This reflects a reduced adaptation of the auditory cortex to persistent tinnitus. Therefore, we hypothesize that long-term abnormal auditory stimuli lead to changes in the auditory cortex, which are different from those in the acute phase, including an increase of CBF.

Moreover, the right FG and left MOG were found to have enhanced CBF connectivity to the right STG and SFG of chronic

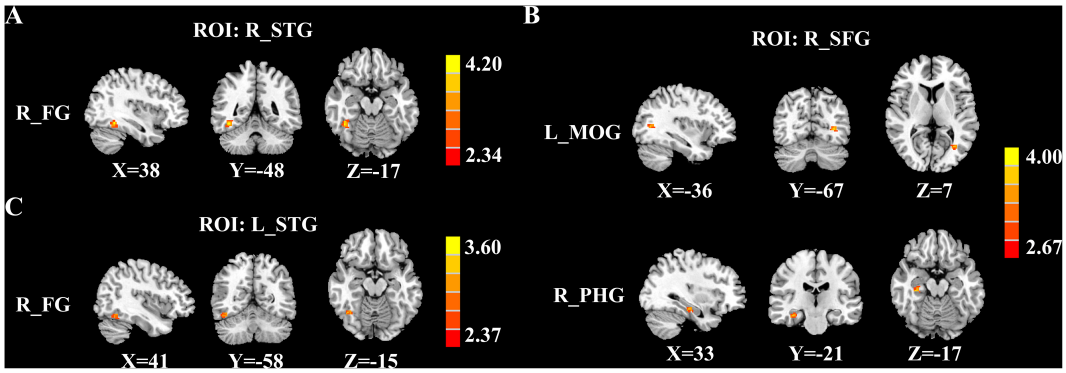

FIGURE 3 | Significant group differences in CBF connectivity among the chronic tinnitus (CT), acute tinnitus (AT), and healthy controls (HC). **(A)** Compared with AT patients, CT patients exhibited increased CBF connectivity between the right superior temporal gyrus (STG) and the right fusiform gyrus (FG). **(B)** Compared with AT patients, CT patients also showed increased CBF connectivity between the right superior frontal gyrus (SFG) and the left middle occipital gyrus (MOG) as well as the right parahippocampal gyrus (PHG). **(C)** Compared with HC, the CT patients showed increased CBF connectivity between the left STG and the right FG. Significant thresholds were corrected using FDR criterion and set at $p < 0.01$.

tinnitus brain in comparison to acute tinnitus. The FG is located in the ventral temporal cortex. FG and the visual area of the MOG belong to the visual center, which participates in advanced visual processing (Weiner and Zilles, 2016). Both visual and auditory processing engage the attention networks. Burton et al. (2012) found that in patients with annoying tinnitus, the functional activity of the visual cortex, including the occipital lobe and the temporoparietal junction, was negatively correlated with that of the auditory cortex. It means that when the blood oxygen activity increased in the auditory area, the activity of the visual area decreased, and vice versa. This may reflect an adaptation mechanism of the tinnitus brain: to focus attention on non-auditory tasks to reduce the salience of tinnitus sound. We hypothesized that during the acute phase of tinnitus, the brain is in a compensatory state and can make these adaptations above. However, when tinnitus signals exist for a long time and take up too much attention processing resources, tinnitus patients need to mobilize more attention during visual processing. So, a decompensated change happens and the attention network is widely active. This may explain our results showing increased CBF connectivity between the auditory-visual attention networks in patients with chronic tinnitus. Husain et al. (2015) compared central differences in processing auditory and visual attention in chronic tinnitus patients. They found that when tinnitus patients were in the visual modality, attention and short-term memory networks were more responsive, suggesting that tinnitus sufferers are more likely to be distracted than normal people when processing visual signals and thus become aware of their tinnitus (Husain et al., 2015). These results suggest that using attention demanding tasks to divert attention away from tinnitus may help reduce the severity of tinnitus (Searchfield et al., 2007).

In addition, the functional connectivity between STG and limbic area, cerebellum, and thalamus was found to be abnormal in chronic tinnitus, which was correlated with tinnitus-related characteristics including tinnitus-related emotional disorders, tinnitus severity, and tinnitus duration (Zhang et al., 2015; Chen et al., 2017b; Feng et al., 2018). These results demonstrated the important role of the auditory cortex in tinnitus. Therefore, we suggest that changes in CBF and CBF connectivity in the auditory region of the temporal gyrus may be involved in the chronicity of tinnitus. We also observed different CBF values in bilateral temporal gyrus of tinnitus brain, with enhanced CBF in the right STG, while no significant difference in the left STG. There is no clear evidence of a link between this asymmetry and tinnitus characteristics so far. However, some scholars believe that the hemisphere asymmetry of activity in the auditory cortex is a general characteristic of the normal brain unrelated to tinnitus brain (Geven et al., 2014).

TABLE 3 | Brain regions with significant group differences in CBF connectivity.

ROI	Brain regions	BA	Peak MNI coordinates x, y, z (mm)	Peak *T* value	Voxels
R_STG	R_FG	37	38, −48, −17	4.276	157
R_SFG	L_MOG	19	−36, −67, 7	3.738	172
	R_PHG	36	33, −21, −17	3.571	107
L_STG	R_FG	37	41, −58, −15	3.475	112

Thresholds were set at a corrected p<0.01 corrected by FDR criterion. ROI, region of interest; MNI, Montreal Neurological Institute; STG, superior temporal gyrus; FG, fusiform gyrus; SFG, superior frontal gyrus; MOG, middle occipital gyrus; PHG, parahippocampal gyrus; L, left; R, right.

The Frontal Gyrus

Increased z-CBF in the right SFG was observed in the chronic tinnitus group compared to the acute tinnitus group. The SFG is a vital component of the auditory connection cortex, which takes part in processing multi-sensory signals, including auditory perception. Therefore, SFG may also be involved in the perception of tinnitus (Melloni et al., 2007; Chen et al., 2014). According to Chen et al., the bilateral SFG presented stronger network centrality, which suggested that the prefrontal cortex, especially SFG, is the major cortical hub of the tinnitus

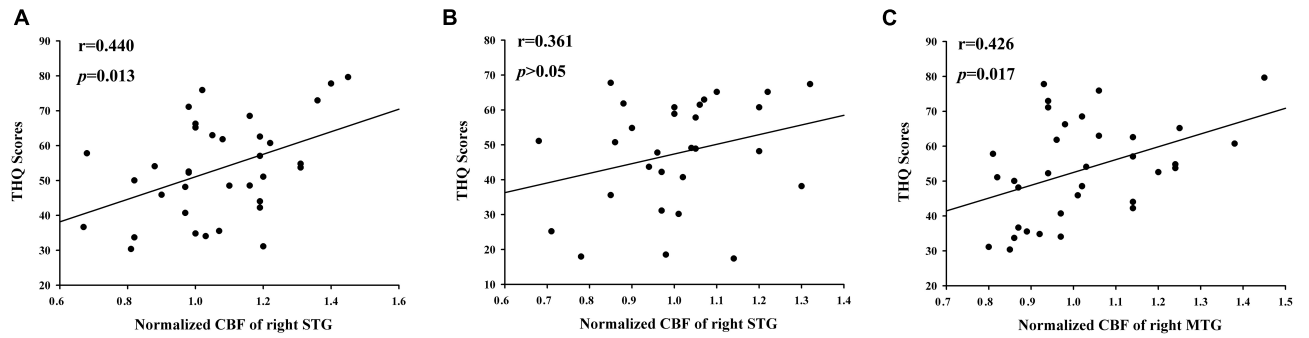

FIGURE 4 | The significant correlations between the CBF changes and the tinnitus characteristics. The THQ score was positively correlated with the normalized z-CBF of the right STG in chronic tinnitus patients ($r = 0.440$, $p = 0.013$) **(A)**, but not in acute tinnitus patients ($r = 0.361$, $p > 0.05$) **(B)**. Compared with HC, the THQ score was positively correlated with the normalized z-CBF of the right MTG in chronic tinnitus patients ($r = 0.426$, $p = 0.017$) **(C)**.

model (Chen et al., 2016). What is more, they found that tinnitus duration was significantly correlated with the increased amplitude of low-frequency fluctuation (ALFF) in SFG. ALFF is an indicator to reflect the intention of neural activity when the brain is in resting state. This result suggested that SFG could play a specific role in chronicity of tinnitus (Chen et al., 2015b).

The prefrontal part of the SFG is one of the ingredients of the default mode network (DMN), which was proved to be responsible for memory, emotion, and intrinsic control networks (Raichle, 2015). Decreased functional connectivity (FC) within the DMN may be vulnerable to chronic tinnitus patients with cognitive impairment (Chen et al., 2018). Schmidt et al. (2017) revealed decreased correlations between the DMN and the precuneus in long-term tinnitus when compared to recent-onset tinnitus (who had tinnitus for >6 months but <1 year) so that DMN–precuneus decoupling can be responsible for tinnitus persistent perception and a potential marker of chronic tinnitus (Schmidt et al., 2017).

Prefrontal cortex (PFC) also plays a basic role in the frontostriatal circuit, which is a top-down gating system involved in the brain "reward" mechanism (McGinty and Grace, 2009). This circuit is also associated with cognitive functions including regulation of attention tasks and learning. For example, the striatum is responsible for rapid "stimulus response" to the learning content, while the PFC is responsible for memory and storage (Antzoulatos and Miller, 2011). Thompson and Neugebauer (2019) suggested that this system plays an important role in the central nervous mechanism of chronic pain. It is believed that both chronic pain and tinnitus are sensory disorders. They are highly similar in their central mechanisms, among which the frontostriatal circuit may be the key (Rauschecker et al., 2015; Xu et al., 2019).

The Limbic System

Our study showed enhanced CBF connectivity between the right SFG and PHG in chronic tinnitus patients. PHG is one of the key structures of the limbic system. Previous studies have shown abnormal changes in the structure, neural activity, and CBF of the PHG in tinnitus patients (Laureano et al., 2014; Chen et al., 2017a; Schmidt et al., 2018). Actually, the auditory and memory/limbic networks are closely interconnected in the perception of sound (Ćurčić-Blake et al., 2017). In a tinnitus model proposed by Rauschecker et al., the initial tinnitus was caused by the impairment of the auditory pathway, and the limbic system can prevent tinnitus signals from reaching the auditory cortex, thereby eliminating tinnitus (Rauschecker et al., 2010). Dysfunction of the limbic system affects this elimination mechanism, leading to persistent perception of tinnitus.

Meanwhile, the PHG plays a central role in memory recollection by sending information from the hippocampus to the related areas (Diederen et al., 2010). De Ridder et al. (2006) suggested that tinnitus memory was constantly updated due to the abnormal continuous activity of the PHG, which contributed to the dysfunction of tinnitus adaptation mechanism and finally led to the maintenance of tinnitus. Lan et al. (2021) found that the abnormal brain regions of acute tinnitus patients were mainly concentrated in the auditory cortex, while chronic tinnitus involved a larger brain network, in which the PHG showed significantly enhanced connectivity. This is similar to our result. All these results highlight that the PHG may be a very vital region to distinguish acute tinnitus from chronic tinnitus.

In addition to memory function, abnormalities in the structure and function of the PHG may be associated with the development of emotion disorders (Almeida et al., 2009). Jastreboff (1990) proposed that whether tinnitus patients develop negative emotions such as depression and anxiety depends on whether the limbic system is involved in central changes. Depression and anxiety, in turn, modulate the structural effects of tinnitus brain and further aggravate tinnitus by enhancing the detection and perception of tinnitus through specific patterns (Besteher et al., 2019). The PHG also plays an important role in the formation and maintenance of bound information (Luck et al., 2010). In this way, tinnitus patients are more likely to bundle some uncomfortable symptoms with tinnitus, which further increases the anxiety and fear of tinnitus. This is obviously more conducive to the elimination of tinnitus. Although the interaction mode between tinnitus and negative emotions is not completely clear, it is certain that the long-term perception of tinnitus is related to the memory and emotion mechanism mediated by the limbic system.

Cerebral Blood Flow Connectivity

Cerebral blood flow connectivity changes in tinnitus patients are firstly reported in the current study. CBF of different brain regions is not independent, which can reflect the changes of neuronal activity. Synchronous changes of CBF connectivity may occur in areas of the same functional network (Havsteen et al., 2018; Jaganmohan et al., 2021). The changes in CBF connectivity were explored in a variety of neurological diseases, such as Alzheimer's disease (Zheng et al., 2019) and Parkinson's disease (Shang et al., 2021). The majority of the differences between ASL and BOLD-FC networks were observed within the brain areas constituting the corresponding networks. In general, BOLD networks showed a stronger overall level of FC, with the exception of higher FC in several specific regions of CBF networks (Jann et al., 2015).

Limitations

Several inevitable limitations must be acknowledged in this study. First, our sample size was moderate, which may limit the generalization of our results. Second, all subjects wore earplugs during the MRI scan, but the noise of the scanner is inevitable. This may affect the metabolism degree of attention network. Furthermore, the definition of acute and chronic tinnitus has not reached a uniform standard. Although the "Clinical Practice Guideline: Tinnitus" published in the United States in 2014 and the "A multidisciplinary European guideline for tinnitus: diagnostics, assessment, and treatment" published in 2019 both recommend that chronic tinnitus should last longer than 6 months, some studies used different standards such as 3 months (Besteher et al., 2019) and 4 years (Vanneste et al., 2011). Different classification criteria may have different results. Finally, we did not use longitudinal follow-up study in this study. If tinnitus patients were followed up regularly and grouped studies were conducted according to the outcome of the condition, the results might be more convincing. These limitations should be taken into consideration in further research.

CONCLUSION

In summary, chronic tinnitus is different from acute tinnitus with increased CBF and CBF connectivity in several auditory and non-auditory brain regions. Multiple brain networks, including cognition, attention, emotion, and memory networks may be involved in the chronicity of tinnitus. Our study investigated the different brain neural mechanisms between acute and chronic tinnitus and emphasizes the potential use of ASL and CBF properties in the tinnitus field, which may bring us a better understanding of the neuropathological mechanisms underlying tinnitus chronicity.

DATA AVAILABILITY STATEMENT

The original contributions presented in the study are included in the article/supplementary material, further inquiries can be directed to the corresponding authors.

ETHICS STATEMENT

The studies involving human participants were reviewed and approved by Research Ethics Committee of the Nanjing Medical University. The patients/participants provided their written informed consent to participate in this study.

AUTHOR CONTRIBUTIONS

JH and J-JX designed the experiment, analyzed the data, and drafted the manuscript for the work. SS and HC helped to acquire the clinical and fMRI data. XY helped to revise the manuscript critically for important intellectual content. JQ and YW did the financial support, review, and final approval of the manuscript to be published. All authors have read and approved the final manuscript.

FUNDING

This work was supported by the Medical Science and Technology Development Foundation of Nanjing Department of Health (No. ZKX20037), Natural Science Foundation of Jiangsu Province (No. BK20211008), and 333 High-level Talents Training Project of Jiangsu Province (No. BRA2019122).

REFERENCES

Aldhafeeri, F. M., Mackenzie, I., Kay, T., Alghamdi, J., and Sluming, V. (2012). Neuroanatomical correlates of tinnitus revealed by cortical thickness analysis and diffusion tensor imaging. *Neuroradiology* 54, 883–892. doi: 10.1007/s00234-012-1044-6

Almeida, J. R. C., Mechelli, A., Hassel, S., Versace, A., Kupfer, D. J., and Phillips, M. L. (2009). Abnormally increased effective connectivity between parahippocampal gyrus and ventromedial prefrontal regions during emotion labeling in bipolar disorder. *Psychiatry Res.* 174, 195–201. doi: 10.1016/j.pscychresns.2009.04.015

Andersson, G., Lyttkens, L., Hirvelä, C., Furmark, T., Tillfors, M., and Fredrikson, M. (2000). Regional cerebral blood flow during tinnitus: a PET case study with lidocaine and auditory stimulation. *Acta Otolaryngol.* 120, 967–972. doi: 10.1080/00016480050218717

Antzoulatos, E. G., and Miller, E. K. (2011). Differences between neural activity in prefrontal cortex and striatum during learning of novel abstract categories. *Neuron* 71, 243–249. doi: 10.1016/j.neuron.2011.05.040

Aslan, S., and Lu, H. (2010). On the sensitivity of ASL MRI in detecting regional differences in cerebral blood flow. *Magn. Reson. Imaging* 28, 928–935. doi: 10.1016/j.mri.2010.03.037

Barzgari, A., Sojkova, J., Maritza, D. N., Pozorski, V., Okonkwo, O. C., Starks, E. J., et al. (2019). Arterial spin labeling reveals relationships between resting cerebral perfusion and motor learning in Parkinson's disease. *Brain Imaging Behav.* 13, 577–587. doi: 10.1007/s11682-018-9877-1

Berlot, E., Arts, R., Smit, J., George, E., Gulban, O. F., Moerel, M., et al. (2020). A 7 Tesla fMRI investigation of human tinnitus percept in cortical and subcortical auditory areas. *NeuroImage* 25:102166. doi: 10.1016/j.nicl.2020.102166

Besteher, B., Gaser, C., Ivanšić, D., Guntinas-Lichius, O., Dobel, C., and Nenadić, I. (2019). Chronic tinnitus and the limbic system: reappraising brain structural effects of distress and affective symptoms. *Neuroimage* 24:101976. doi: 10.1016/j.nicl.2019.101976

Biswas, R., Lugo, A., Gallus, S., Akeroyd, M. A., and Hall, D. A. (2019). Standardized questions in English for estimating tinnitus prevalence and severity, hearing difficulty and usage of healthcare resources, and their translation into 11 European languages. *Hear. Res.* 377, 330–338. doi: 10.1016/j.heares.2019.02.008

Burton, H., Wineland, A., Bhattacharya, M., Nicklaus, J., Garcia, K. S., and Piccirillo, J. F. (2012). Altered networks in bothersome tinnitus: a functional connectivity study. *BMC Neurosci.* 13:3. doi: 10.1186/1471-2202-13-3

Cai, W. W., Li, Z. C., Yang, Q. T., and Zhang, T. (2019). Abnormal spontaneous neural activity of the central auditory system changes the functional connectivity in the tinnitus brain: a resting-state functional MRI study. *Front. Neurosci.* 13:1314. doi: 10.3389/fnins.2019.01314

Chen, Q., Lv, H., Chen, Y. C., Song, J. J., and Wang, Z. (2021). Editorial: neuroimaging approaches to the study of tinnitus and hyperacusis. *Front. Neurosci.* 15:700670. doi: 10.3389/fnins.2021.700670

Chen, Y. C., Feng, Y., Xu, J. J., Mao, C. N., Xia, W., Ren, J., et al. (2016). Disrupted brain functional network architecture in chronic tinnitus patients. *Front. Aging Neurosci.* 8:174. doi: 10.3389/fnagi.2016.00174

Chen, Y. C., Li, X., Liu, L., Wang, J., Lu, C. Q., Yang, M., et al. (2015a). Tinnitus and hyperacusis involve hyperactivity and enhanced connectivity in auditory-limbic-arousal-cerebellar network. *Elife* 4:e06576.

Chen, Y. C., Zhang, J., Li, X. W., Xia, W., Feng, X., Qian, C., et al. (2015c). Altered intra- and interregional synchronization in resting-state cerebral networks associated with chronic tinnitus. *Neural Plast.* 2015:475382.

Chen, Y. C., Xia, W., Luo, B., Muthaiah, V. P., Xiong, Z., Zhang, J., et al. (2015b). Frequency-specific alternations in the amplitude of low-frequency fluctuations in chronic tinnitus. *Front. Neural Circuits* 9:67. doi: 10.3389/fncir.2015.00067

Chen, Y. C., Xia, W., Chen, H., Feng, Y., Xu, J. J., Gu, J. P., et al. (2017b). Tinnitus distress is linked to enhanced resting-state functional connectivity from the limbic system to the auditory cortex. *Hum. Brain Mapp.* 38, 2384–2397. doi: 10.1002/hbm.23525

Chen, Y. C., Wang, F., Wang, J., Bo, F., Xia, W., Gu, J. P., et al. (2017a). Resting-state brain abnormalities in chronic subjective tinnitus: a meta-analysis. *Front. Hum. Neurosci.* 11:22. doi: 10.3389/fnhum.2017.00022

Chen, Y. C., Zhang, H., Kong, Y., Lv, H., Cai, Y., Chen, H., et al. (2018). Alterations of the default mode network and cognitive impairment in patients with unilateral chronic tinnitus. *Quant. Imaging Med. Surg.* 8, 1020–1029. doi: 10.21037/qims.2018.11.04

Chen, Y. C., Zhang, J., Li, X. W., Xia, W., Feng, X., Gao, B., et al. (2014). Aberrant spontaneous brain activity in chronic tinnitus patients revealed by resting-state functional MRI. *Neuroimage Clin.* 6, 222–228.

Cima, R., Mazurek, B., Haider, H., Kikidis, D., Lapira, A., Noreña, A., et al. (2019). A multidisciplinary European guideline for tinnitus: diagnostics, assessment, and treatment. *HNO* 67(Suppl. 1), 10–42. doi: 10.1007/s00106-019-0633-7

Ćurčić-Blake, B., Ford, J. M., Hubl, D., Orlov, N. D., Sommer, I. E., Waters, F., et al. (2017). Interaction of language, auditory and memory brain networks in auditory verbal hallucinations. *Prog. Neurobiol.* 148, 1–20. doi: 10.1016/j.pneurobio.2016.11.002

De Ridder, D., Fransen, H., Francois, O., Sunaert, S., Kovacs, S., and Van De Heyning, P. (2006). Amygdalohippocampal involvement in tinnitus and auditory memory. *Acta OtoLaryngol.* 126, 50–53. doi: 10.1080/03655230600895580

Detre, J. A., and Wang, J. (2002). Technical aspects and utility of fMRI using BOLD and ASL. *Clin. Neurophysiol.* 113, 621–634. doi: 10.1016/s1388-2457(02)00038-x

Diederen, K. M., Neggers, S. F., Daalman, K., Blom, J. D., Goekoop, R., Kahn, R. S., et al. (2010). Deactivation of the parahippocampal gyrus preceding auditory hallucinations in schizophrenia. *Am. J. Psychiatry* 167, 427–435. doi: 10.1176/appi.ajp.2009.09040456

Eggermont, J. J. (2003). Central tinnitus. *Auris Nasus Larynx* 30, 7–12. doi: 10.1016/s0385-8146(02)00122-0

Eggermont, J. J., and Roberts, L. E. (2004). The neuroscience of tinnitus. *Trends Neurosci.* 27, 676–682.

Feng, Y., Chen, Y. C., Lv, H., Xia, W., Mao, C. N., Bo, F., et al. (2018). Increased resting-state cerebellar-cerebral functional connectivity underlying chronic tinnitus. *Front. Aging Neurosci.* 10:59. doi: 10.3389/fnagi.2018.00059

Ferré, J. C., Bannier, E., Raoult, H., Mineur, G., Carsin-Nicol, B., and Gauvrit, J. Y. (2013). Arterial spin labeling (ASL) perfusion: techniques and clinical use. *Diagn. Interv. Imaging* 94, 1211–1223. doi: 10.1016/j.diii.2013.06.010

Geven, L. I., De Kleine, E., Willemsen, A. T. M., and Van Dijk, P. (2014). Asymmetry in primary auditory cortex activity in tinnitus patients and controls. *Neuroscience* 256, 117–125. doi: 10.1016/j.neuroscience.2013.10.015

Han, Q., Zhang, Y., Liu, D., Wang, Y., Feng, Y., Yin, X., et al. (2018). Disrupted local neural activity and functional connectivity in subjective tinnitus patients: evidence from resting-state fMRI study. *Neuroradiology* 60, 1193–1201. doi: 10.1007/s00234-018-2087-0

Havsteen, I., Damm Nybing, J., Christensen, H., and Christensen, A. F. (2018). Arterial spin labeling: a technical overview. *Acta Radiol.* 59, 1232–1238. doi: 10.1177/0284185117752552

Henry, J. A., Reavis, K. M., Griest, S. E., Thielman, E. J., Theodoroff, S. M., Grush, L. D., et al. (2020). Tinnitus: an epidemiologic perspective. *Otolaryngol. Clin. North Am.* 53, 481–499.

Husain, F. T., Akrofi, K., Carpenter-Thompson, J. R., and Schmidt, S. A. (2015). Alterations to the attention system in adults with tinnitus are modality specific. *Brain Res.* 1620, 81–97. doi: 10.1016/j.brainres.2015.05.010

Jaganmohan, D., Pan, S., Kesavadas, C., and Thomas, B. (2021). A pictorial review of brain arterial spin labelling artefacts and their potential remedies in clinical studies. *Neuroradiol. J.* 34, 154–168. doi: 10.1177/1971400920977031

Jann, K., Gee, D. G., Kilroy, E., Schwab, S., Smith, R. X., Cannon, T. D., et al. (2015). Functional connectivity in BOLD and CBF data: similarity and reliability of resting brain networks. *Neuroimage* 106, 111–122. doi: 10.1016/j.neuroimage.2014.11.028

Jastreboff, P. J. (1990). Phantom auditory perception (tinnitus): mechanisms of generation and perception. *Neurosci. Res.* 8, 221–254. doi: 10.1016/0168-0102(90)90031-9

Khalfa, S., Dubal, S., Veuillet, E., Perez-Diaz, F., Jouvent, R., and Collet, L. (2002). Psychometric normalization of a hyperacusis questionnaire. *ORL* 64, 436–442. doi: 10.1159/000067570

Kim, J. H., Choi, D. S., Park, S. E., Choi, H. C., Koh, E. H., and Kim, S. H. (2019). Preoperative localization of the sensorimotor cortex and measurement of tumor perfusion in a single acquisition using ASL technique. *J. Clin. Neurosci.* 59, 367–371. doi: 10.1016/j.jocn.2018.10.098

Kuk, F. K., Tyler, R. S., Russell, D., and Jordan, H. (1990). The psychometric properties of a tinnitus handicap questionnaire. *Ear Hear.* 11, 434–445. doi: 10.1097/00003446-199012000-00005

Lan, L., Li, J., Chen, Y., Chen, W., Li, W., Zhao, F., et al. (2021). Alterations of brain activity and functional connectivity in transition from acute to chronic tinnitus. *Hum. Brain Mapp.* 42, 485–494. doi: 10.1002/hbm.25238

Lanting, C. P., De Kleine, E., and Van Dijk, P. (2009). Neural activity underlying tinnitus generation: results from PET and fMRI. *Hear. Res.* 255, 1–13. doi: 10.1016/j.heares.2009.06.009

Laureano, M. R., Onishi, E. T., Bressan, R. A., Castiglioni, M. L. V., Batista, I. R., Reis, M. A., et al. (2014). Memory networks in tinnitus: a functional brain image study. *PLoS One* 9:e87839. doi: 10.1371/journal.pone.0087839

Li, F., Lu, L., Shang, S. A., Chen, H., Wang, P., Haidari, N. A., et al. (2020). Cerebral blood flow and its connectivity deficits in mild traumatic brain injury at the acute stage. *Neural Plast.* 2020, 1–10. doi: 10.1155/2020/2174371

Li, X., Zhao, P., Qiu, X., Ding, H., Lv, H., Yang, Z., et al. (2020). Lateralization effects on cerebral blood flow in patients with unilateral pulsatile tinnitus measured With arterial spin labeling. *Front. Hum. Neurosci.* 14:497. doi: 10.3389/fnhum.2020.591260

Li, X., Zhao, P., Qiu, X., Lv, H., Ding, H., Yang, Z., et al. (2021). Altered cerebral blood flow in patients with unilateral venous pulsatile tinnitus: an arterial spin labeling study. *Br. J. Radiol.* 94:20200990. doi: 10.1259/bjr.20200990

Luck, D., Danion, J.-M., Marrer, C., Pham, B.-T., Gounot, D., and Foucher, J. (2010). The right parahippocampal gyrus contributes to the formation and maintenance of bound information in working memory. *Brain Cogn.* 72, 255–263. doi: 10.1016/j.bandc.2009.09.009

McGinty, V., and Grace, A. (2009). Activity-dependent depression of medial prefrontal cortex inputs to accumbens neurons by the basolateral amygdala. *Neuroscience* 162, 1429–1436. doi: 10.1016/j.neuroscience.2009.05.028

Melloni, L., Molina, C., Pena, M., Torres, D., Singer, W., and Rodriguez, E. (2007). Synchronization of neural activity across cortical areas correlates with conscious perception. *J. Neurosci.* 27, 2858–2865. doi: 10.1523/jneurosci.4623-06.2007

Møller, A. R. (2007). "The role of neural plasticity in tinnitus," in *Progress in Brain Research*, eds B. Langguth, G. Hajak, T. Kleinjung, A. Cacace, and A. R. Møller (Amsterdam: Elsevier), 37–544. doi: 10.1016/s0079-6123(07)66003-8

Nathan, W., Stephan, M., Marcus, M., Katalin, D., and Thomas, E. (2005). Tinnitus perception and distress is related to abnormal spontaneous brain activity as measured by magnetoencephalography. *PLoS Med.* 2:e153. doi: 10.1371/journal.pmed.0020153

Olaosun, A. O., and Ogundiran, O. (2013). Hearing loss and the elderly-a primer. *Population* 3, 171–175.

Pegge, S.a.H, Steens, S. C. A., Kunst, H. P. M., and Meijer, F. J. A. (2017). Pulsatile tinnitus: differential diagnosis and radiological work-up. *Curr. Radiol. Rep*. 5:5.

Raichle, M. E. (2015). The brain's default mode network. *Annu. Rev. Neurosci.* 38, 433–447.

Rauschecker, J. P., Leaver, A. M., and Muhlau, M. (2010). Tuning out the noise: limbic-auditory interactions in tinnitus. *Neuron* 66, 819–826. doi: 10.1016/j.neuron.2010.04.032

Rauschecker, J. P., May, E. S., Maudoux, A., and Ploner, M. (2015). Frontostriatal gating of tinnitus and chronic pain. *Trends Cogn. Sci.* 19, 567–578. doi: 10.1016/j.tics.2015.08.002

Reyes, S. A., Salvi, R. J., Burkard, R. F., Coad, M. L., Wack, D. S., Galantowicz, P. J., et al. (2002). Brain imaging of the effects of lidocaine on tinnitus. *Hear. Res.* 171, 43–50. doi: 10.1016/s0378-5955(02)00346-5

Schlee, W., Schecklmann, M., Lehner, A., Kreuzer, P. M., Vielsmeier, V., Poeppl, T. B., et al. (2014). Reduced variability of auditory alpha activity in chronic tinnitus. *Neural Plast.* 2014:436146.

Schmidt, S. A., Carpenter-Thompson, J., and Husain, F. T. (2017). Connectivity of precuneus to the default mode and dorsal attention networks: a possible invariant marker of long-term tinnitus. *Neuroimage Clin.* 16, 196–204. doi: 10.1016/j.nicl.2017.07.015

Schmidt, S. A., Zimmerman, B., Bido Medina, R. O., Carpenter-Thompson, J. R., and Husain, F. T. (2018). Changes in gray and white matter in subgroups within the tinnitus population. *Brain Res.* 1679, 64–74. doi: 10.1016/j.brainres.2017.11.012

Searchfield, G. D., Morrison-Low, J., and Wise, K. (2007). "Object identification and attention training for treating tinnitus," in *Progress in Brain Research*, eds B. Langguth, G. Hajak, T. Kleinjung, A. Cacace, and A. R. Møller (Amsterdam: Elsevier), 441–460. doi: 10.1016/s0079-6123(07)66043-9

Shang, S., Wu, J., Zhang, H., Chen, H., Cao, Z., Chen, Y. C., et al. (2021). Motor asymmetry related cerebral perfusion patterns in Parkinson's disease: an arterial spin labeling study. *Hum. Brain Mapp.* 42, 298–309. doi: 10.1002/hbm.25223

Telischak, N. A., Detre, J. A., and Zaharchuk, G. (2015). Arterial spin labeling MRI: clinical applications in the brain. *J. Magn. Reson. Imaging* 41, 1165–1180. doi: 10.1002/jmri.24751

Thompson, J. M., and Neugebauer, V. (2019). Cortico-limbic pain mechanisms. *Neurosci. Lett.* 702, 15–23. doi: 10.1016/j.neulet.2018.11.037

Ueyama, T., Donishi, T., Ukai, S., Yamamoto, Y., Ishida, T., Tamagawa, S., et al. (2015). Alterations of regional cerebral blood flow in tinnitus patients as assessed using single-photon emission computed tomography. *PLoS One* 10:e0137291. doi: 10.1371/journal.pone.0137291

Vanneste, S., Van De Heyning, P., and De Ridder, D. (2011). The neural network of phantom sound changes over time: a comparison between recent-onset and chronic tinnitus patients. *Eur. J. Neurosci.* 34, 718–731. doi: 10.1111/j.1460-9568.2011.07793.x

Vielsmeier, V., Santiago Stiel, R., Kwok, P., Langguth, B., and Schecklmann, M. (2020). From acute to chronic tinnitus: pilot data on predictors and progression. *Front. Neurol.* 11:997. doi: 10.3389/fneur.2020.00997

Wallhäusser-Franke, E., D'amelio, R., Glauner, A., Delb, W., Servais, J. J., Hörmann, K., et al. (2017). Transition from acute to chronic tinnitus: predictors for the development of chronic distressing tinnitus. *Front. Neurol.* 8:605. doi: 10.3389/fneur.2017.00605

Wang, Z., Aguirre, G. K., Rao, H., Wang, J., Fernández-Seara, M. A., Childress, A. R., et al. (2008). Empirical optimization of ASL data analysis using an ASL data processing toolbox: ASLtbx. *Magn. Reson. Imaging* 26, 261–269. doi: 10.1016/j.mri.2007.07.003

Weiner, K. S., and Zilles, K. (2016). The anatomical and functional specialization of the fusiform gyrus. *Neuropsychologia* 83, 48–62. doi: 10.1016/j.neuropsychologia.2015.06.033

Xia, W., Cui, J., Luo, Y., Xu, J. J., Chen, H., Yin, X., et al. (2020). Glucose control has an impact on cerebral blood flow alterations in chronic tinnitus patients. *Front. Neurosci.* 14:623520. doi: 10.3389/fnins.2020.623520

Xu, G., Rowley, H. A., Wu, G., Alsop, D. C., Shankaranarayanan, A., Dowling, M., et al. (2010). Reliability and precision of pseudo-continuous arterial spin labeling perfusion MRI on 3.0 T and comparison with 15O-water PET in elderly subjects at risk for Alzheimer's disease. *NMR Biomed.* 23, 286–293. doi: 10.1002/nbm.1462

Xu, J. J., Cui, J. L., Feng, Y., Yong, W., Chen, H. Y., Chen, Y. C., et al. (2019). Chronic tinnitus exhibits bidirectional functional dysconnectivity in frontostriatal circuit. *Front. Neurosci.* 13:1299. doi: 10.3389/fnins.2019.01299

Xu, Z. G., Xu, J. J., Chen, Y. C., Hu, J., Wu, Y., and Xue, Y. (2021). Aberrant cerebral blood flow in tinnitus patients with migraine: a perfusion functional MRI study. *J. Headache Pain* 22:61.

Yi, H. G., Leonard, M. K., and Chang, E. F. (2019). The encoding of speech sounds in the superior temporal gyrus. *Neuron* 102, 1096–1110. doi: 10.1016/j.neuron.2019.04.023

Zhang, J., Chen, Y. C., Feng, X., Yang, M., Liu, B., Qian, C., et al. (2015). Impairments of thalamic resting-state functional connectivity in patients with chronic tinnitus. *Eur. J. Radiol.* 84, 1277–1284. doi: 10.1016/j.ejrad.2015.04.006

Zhang, N., Gordon, M. L., and Goldberg, T. E. (2017). Cerebral blood flow measured by arterial spin labeling MRI at resting state in normal aging and Alzheimer's disease. *Neurosci. Biobehav. Rev.* 72, 168–175. doi: 10.1016/j.neubiorev.2016.11.023

Zheng, W., Cui, B., Han, Y., Song, H., Li, K., He, Y., et al. (2019). Disrupted regional cerebral blood flow, functional activity and connectivity in Alzheimer's disease: a combined ASL perfusion and resting state fMRI study. *Front. Neurosci.* 13:738. doi: 10.3389/fnins.2019.00738

Zimmerman, B. J., Abraham, I., Schmidt, S. A., Baryshnikov, Y., and Husain, F. T. (2019). Dissociating tinnitus patients from healthy controls using resting-state cyclicity analysis and clustering. *Netw. Neurosci.* 3, 67–89. doi: 10.1162/netn_a_00053

Conflict of Interest: The authors declare that the research was conducted in the absence of any commercial or financial relationships that could be construed as a potential conflict of interest.

frontiers in Human Neuroscience

ORIGINAL RESEARCH
published: 08 October 2021
doi: 10.3389/fnhum.2021.754234

Abnormal Low-Frequency Oscillations Reflect Abnormal Eye Movement and Stereovision in Patients With Comitant Exotropia

*Juan Chen†, Han Jin†, Yu-Lin Zhong and Xin Huang**

Department of Ophthalmology, Jiangxi Provincial People's Hospital Affiliated to Nanchang University, Nanchang, China

OPEN ACCESS

Edited by:
Yu-Chen Chen,
Nanjing Medical University, China

Reviewed by:
Chao Liu,
Shandong University, China
Liting Chen,
The First Affiliated Hospital of Nanchang University, China
Vijaya Prakash Krishnan Muthaiah,
University at Buffalo, United States

***Correspondence:**
Xin Huang
2017103020035@whu.edu.cn

†These authors have contributed equally to this work

Specialty section:
This article was submitted to Sensory Neuroscience, a section of the journal Frontiers in Human Neuroscience

Received: *06 August 2021*
Accepted: *09 September 2021*
Published: *08 October 2021*

Citation:
Chen J, Jin H, Zhong Y-L and Huang X (2021) Abnormal Low-Frequency Oscillations Reflect Abnormal Eye Movement and Stereovision in Patients With Comitant Exotropia. Front. Hum. Neurosci. 15:754234. doi: 10.3389/fnhum.2021.754234

Background: Patients with comitant exotropia (CE) are accompanied by abnormal eye movements and stereovision. However, the neurophysiological mechanism of impaired eye movements and stereovision in patient with CE is still unclear.

Purpose: The purpose of this study is to investigate spontaneous neural activity changes in patients with CE using the amplitude of low-frequency fluctuation (ALFF) method and the machine learning method.

Materials and Methods: A total of 21 patients with CE and 21 healthy controls (HCs) underwent resting-state magnetic resonance imaging scans. The ALFF and fractional amplitude of low-frequency fluctuation (fALFF) values were chosen as classification features using a machine learning method.

Results: Compared with the HC group, patients with CE had significantly decreased ALFF values in the right angular (ANG)/middle occipital gyrus (MOG)/middle temporal gyrus (MTG) and bilateral supplementary motor area (SMA)/precentral gyrus (PreCG). Meanwhile, patients with CE showed significantly increased fALFF values in the left putamen (PUT) and decreased fALFF values in the right ANG/MOG. Moreover, patients with CE showed a decreased functional connectivity (FC) between the right ANG/MOG/MTG and the bilateral calcarine (CAL)/lingual (LING) and increased FC between the left PUT and the bilateral cerebellum 8/9 (CER 8/9). The support vector machine (SVM) classification reaches a total accuracy of 93 and 90% and the area under the curve (AUC) of 0.93 and 0.90 based on ALFF and fALFF values, respectively.

Conclusion: Our result highlights that patients with CE had abnormal brain neural activities including MOG and supplementary motor area/PreCG, which might reflect the neural mechanism of eye movements and stereovision dysfunction in patients with CE. Moreover, ALFF and fALFF could be sensitive biomarkers for distinguishing patients with CE from HCs.

Keywords: concomitant exotropia, ALFF, fALFF, functional magnetic resonance imaging, support vector machine, machine learning

INTRODUCTION

Comitant exotropia (CE) is a common eye movement disorder, characterized by ocular deviation and impaired stereovision function. The prevalence of exotropia is 1.0% of all children (Govindan et al., 2005). There are several risk factors for the occurrence of strabismus including genetics (Maconachie et al., 2013), amblyopia (Shapira et al., 2018), and refractive error (Zhu et al., 2015). At present, strabismus surgery is an effective treatment for patients with strabismus. However, stereovision was not established in some patients with exotropia after surgery (Sturm et al., 2011). Thus, the pathological neural mechanism of impaired stereovision in patients with CE is still poorly understood.

Binocular vision is common to humans. Binocular processing primarily emerges when neurons receiving input from the two eyes converge onto common cells in the primary visual cortex (Basgoze et al., 2018). Binocular vision plays an important role in stereoscopic vision. Moreover, Hou et al. (2020) reported that binocular interactions share a common gain control mechanism in the striate and extra-striate cortex. Patients with strabismus with impaired stereovision were associated with brain activity changes. Chen and Tarczy-Hornoch (2011) found that the patients with strabismus had decreased cortical activity in the primary visual cortex. Meanwhile, Shi et al. (2019) demonstrated that patients with constant exotropia had higher regional homogeneity (ReHo) values in the second visual cortex. Yan et al. (2019) demonstrated that strabismus showed increased functional connectivity (FC) between the primary visual cortex and the frontal eye field. In addition, patients with strabismus are also accompanied by cerebral structural changes. Yan et al. (2010) found that patients with CE showed lower fractional anisotropy values in the middle occipital gyrus (MOG) and supramarginal gyrus. However, these existing studies were mainly focused on the visual cortex changes in the strabismus. Whether whole spontaneous brain activity changes in patients with CE is still poorly understood.

The low-frequency oscillations (LFO) (0.01–0.08 Hz) on blood oxygen level-dependent (BOLD) imaging play an important role in various neurophysiological activities including vision (Chan et al., 2017) and cognition (van Kerkoerle et al., 2014). The amplitude of low-frequency fluctuation (ALFF) is a reliable and sensitive functional MRI (fMRI) method to quantify the total power of LFO within a specific frequency range (Zou et al., 2008). In contrast to the task MRI method, this technique does not require the participants to perform any task during scanning.

Thus, this study aimed to determine whether patients with CE were associated with intrinsic brain activity dysfunction using ALFF and fALFF methods. Meanwhile, the seed-based FC method was applied to calculate time series correlation based on different ALFF and fALFF regions. Moreover, machine learning techniques (e.g., support vector machine, SVM) were applied to assess whether ALFF and fALFF values could be sensitivity biomarkers to distinguish patients with CE from healthy controls (HCs). Our findings might reflect neural mechanisms of eye movement disorder and impaired stereovision in patients with CE.

MATERIALS AND METHODS

Participants

A total of 21 patients (15 males/6 females, mean age: 15.80 ± 2.46 years) with CE and 21 age- and sex-matched HCs (15 males/6 females, mean age: 16.00 ± 2.68 years) were recruited from Jiangxi Provincial People's Hospital Affiliated to Nanchang University. The diagnostic criteria of patients with CE were as follows: (1) CE, exodeviation angles between 15Δ and 80Δ, and (2) without a history of strabismus surgery.

The exclusion criteria of individuals with CE in this study were as follows: (1) additional ocular-related complications (e.g., cataract, glaucoma, high myopia, or optic neuritis), (2) sensory exotropia and fixed exotropia, and (3) comitant exotropia were associated with amblyopia.

All HCs met the following criteria: (1) no ocular diseases (e.g., myopia, cataracts, glaucoma, optic neuritis, or retinal degeneration), (2) binocular visual acuity ≥ 1.0, and (3) no ocular surgical history.

MRI Acquisition

MRI scanning was performed on a 3-Tesla magnetic resonance scanner (Discovery MR 750W system; GE Healthcare, Milwaukee, WI, USA) with an eight-channel head coil with the following parameters: repetition time/echo time (TR/TE)

TABLE 1 | Demographics and visual measurements between the two groups.

Condition	CE group	HC group	T-values	P-values
Gender (male/female)	(15/6)	(15/6)	N/A	N/A
Comitant category	congenital exotropia	N/A	N/A	N/A
Age (years)	15.80 ± 2.46	16.00 ± 2.68	−0.240	0.812
Handedness	21 R	21 R	N/A	N/A
BCVA-OD	1.12 ± 0.27	1.05 ± 0.23	0.899	0.374
BCVA-OS	1.18 ± 0.26	1.08 ± 0.21	1.305	0.199

Independent t-test for the other normally distributed continuous data (means ± SD).
CE, comitant exotropia; HC, healthy control.

= 2,000/25 ms, thickness = 3.0 mm, gap = 1.2 mm, acquisition matrix = 64 × 64, flip angle = 90°, field of view = 240 mm^2 × 240 mm^2, voxel size = 3.6 mm^3 × 3.6 mm^3 × 3.6 mm^3, and 35 axial slices. All subjects underwent MRI scanning with their eyes closed without falling asleep.

fMRI Data Processing

All preprocessing was performed using the toolbox for Data Processing and Analysis of Brain Imaging (DPABI, http://www.rfmri.org/dpabi) (Yan et al., 2016), and the following steps were followed (Yin et al., 2017): (1) remove first 10 volumes. (2)

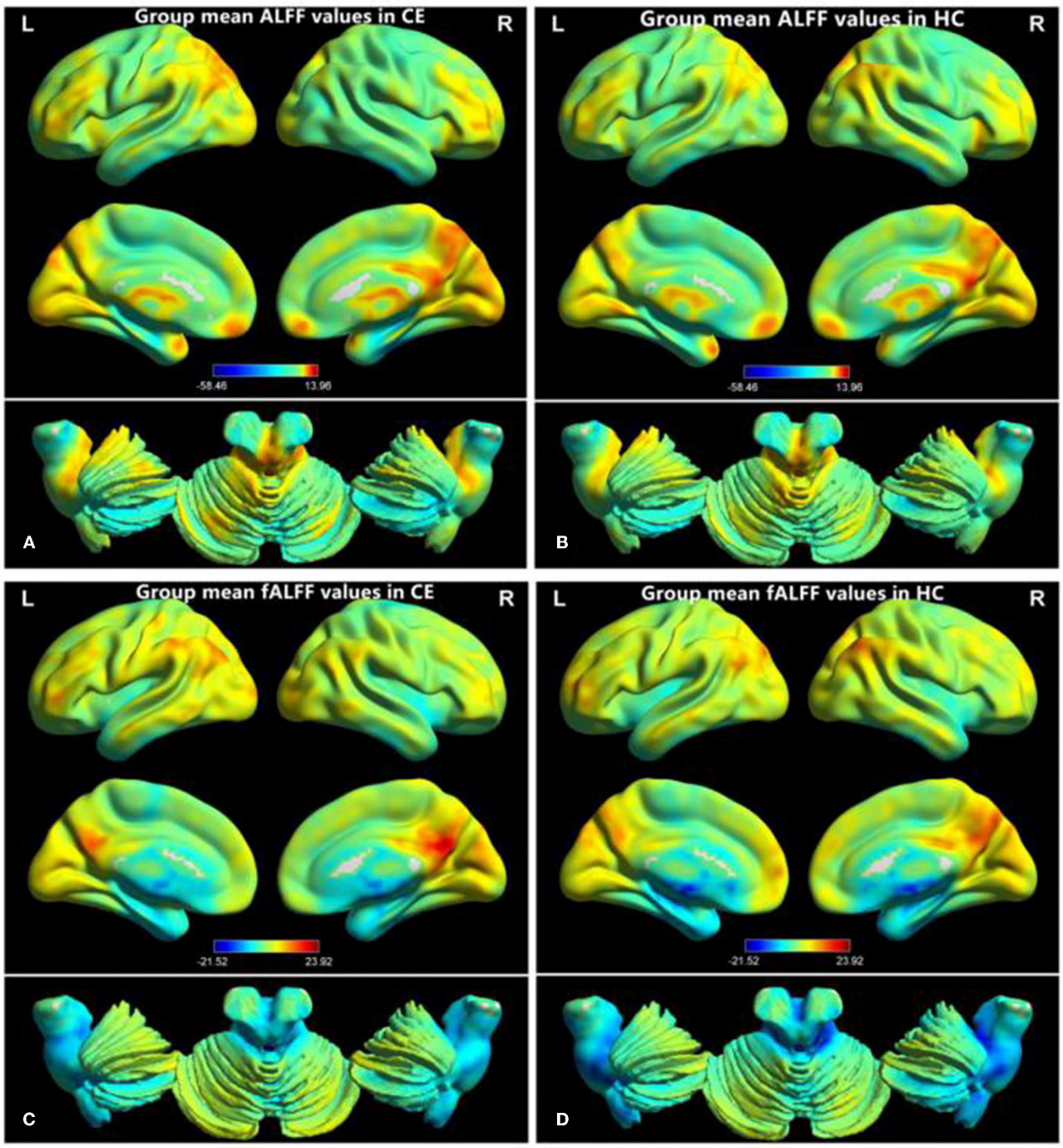

FIGURE 1 | Distribution patterns of ALFF and fALFF were observed at the group level in CE and HC. Within-group mean ALFF maps within the CE **(A)** and HCs **(B)** within-group mean fALFF maps within the CE **(C)** and HCs **(D)**. ALFF, amplitude of low-frequency fluctuation; fALFF, fractional amplitude of low-frequency fluctuation; CE, comitant exotropia; HC, healthy control.

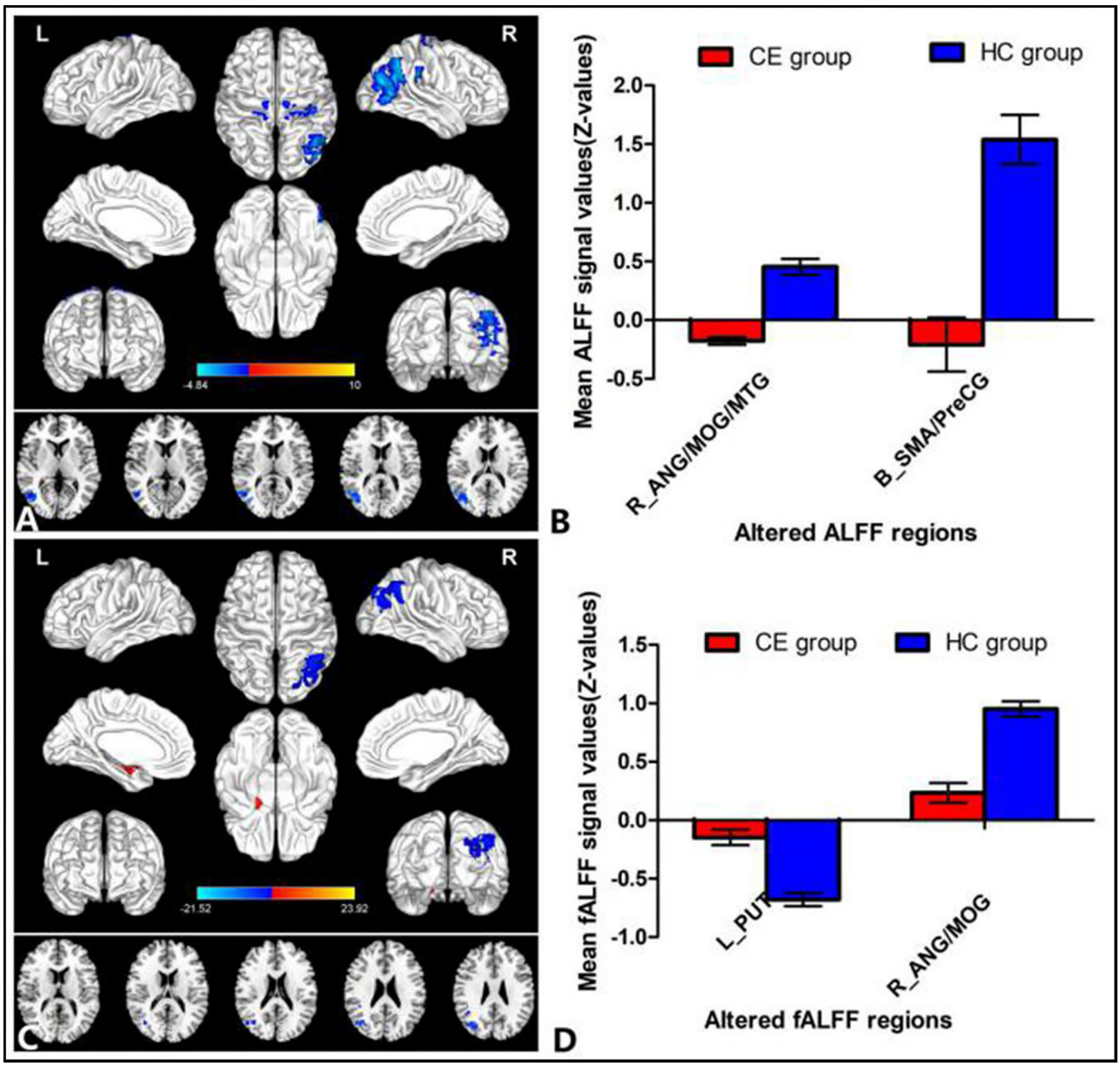

FIGURE 2 | Group comparisons of the ALFF and fALFF between the CE and HCs. Significantly different ALFF was found between the two groups. **(A)** Significantly different fALFF were found between the two groups. **(C)** The blue areas denote lower ALFF and fALFF values, and the red areas denote increased ALFF and fALFF values. The mean values of altered ALFF/fALFF values are shown in a histogram **(B,D)**. ALFF, amplitude of low-frequency fluctuation; fALFF, fractional amplitude of low-frequency fluctuation; CE, comitant exotropia; HC, healthy control; ANG, angular; MOG, middle occipital gyrus; MTG, middle temporal gyrus; SMA, supplementary motor area; PreCG, precentral gyrus; PUT, putamen; R, right; L, left.

Slice timing effects and motion-corrected. (3) Individual 3D-BRAVO images were registered to the mean fMRI data, and normalized data (in Montreal Neurological Institute [MNI] 152 space) were re-sliced at a resolution of 3 mm^3 × 3 mm^3 × 3 mm^3. (4) Spatial smoothing by convolution with an isotropic Gaussian kernel of 6 mm × 6 mm × 6 mm full width at half maximum. (5) Linear regression analysis was used to regress out several covariates [six head motion parameters, mean framewise displacement (FD), global brain signal, and averaged signal from white matter signal, and cerebrospinal fluid) (6). Data with linear trend were removed, and temporal band-pass was filtered (0.01–0.08 Hz). Fisher's *r*-to-*z* transformation was used to acquire an approximate normal distribution and help to reduce the impacts of individual variations on group statistical comparisons.

ALFF and fALFF Analyses

To calculate ALFF, we converted the smoothed signal of each voxel from the time domain to frequency domain *via* fast Fourier transform (FFT) to obtain the power spectrum. The fALFF value was computed as the ratio of the power in the specific frequency band to that of the whole detected frequency range for suppressing nonspecific signals in the rs-fMRI data.

Seed-Based Resting-State FC Analysis

To further detect the altered functional networks behind the impaired ALFF and fALFF. The regions of interest (ROIs) were selected as seeds for the whole-brain FC analysis from the significant results of fALFF and ALFF images from the comparison of patients with CE and HCs. The correlation analysis of time course was performed between the spherical seed region (6 mm) and each voxel of the whole brain for each subject.

Ophthalmic Examination

All participants underwent several examinations including best-corrected visual acuity (BCVA), exodeviation angle, ocular motility, fusional control score, Worth 4-dot test, and Titmus stereopsis test.

Statistical Analysis

The independent sample *t*-test was used to investigate the clinical features between the two groups.

The one-sample *t*-test was conducted to assess the group mean of zALFF and zfALFF maps. The two-sample *t*-test was used to compare the two group differences in the zALFF and zfALFF maps using the Gaussian random field (GRF) method that was used to correct for multiple comparisons and regressed covariates of age and sex and FD (two-tailed, voxel-level $P < 0.01$, GRF correction, cluster-level $P < 0.05$). The two-sample t-test was used to compare the two group differences in the FC maps.

SVM Analysis

The SVM algorithm was performed using the Pattern Recognition for Neuroimaging Toolbox (PRoNTo) software Cyclotron Research Centre, University of Liège, Belgium (Schrouff et al., 2013). The following steps were followed: (1) the ALFF and fALFF maps served as a classification feature. (2) Then, the leave-one-out cross-validation (LOOCV) technique was used to perform SVM classifier validation. For classification, two classes were defined (patient group and HC group) and processed using a soft-margin hyper-parameter approach. The soft-margin parameters take the values 0.01, 0.1, 1, 10, 100, and 1,000 in the SVM classifier in the current version of PRoNTo, which make the model obtain the maximum interval hyperplane with the minimum classification error, and then, selected the soft-margin parameter with the lowest total error rate as the final parameter for each cycle of the cross-validation. (3) For classification, the permutation test was applied to assess the statistical significance of the total accuracy of this classification (Liu et al., 2012). The total accuracy, specificity, sensitivity, and area under the receiver operating characteristic curve (AUC) were determined to assess the classification performance of the machine learning model.

RESULTS

Clinical Measurements

There were no differences in age and gender and best-corrected visual acuity between the two groups ($P > 0.05$; **Table 1**).

ALFF and fALFF Differences

The group means of ALFF and fALFF maps of the CE and HC are shown in **Figures 1A–D**. Compared with the HC group, patients with CE showed significantly decreased ALFF values in the right angular (ANG)/MOG/middle temporal gyrus (MTG) and bilateral supplementary motor area (SMA)/precentral gyrus (PreCG) (**Figure 2A**; **Table 2**). Meanwhile, patients with CE showed significantly increased fALFF values in the left putamen (PUT) and decreased fALFF values in the right ANG/MOG (**Figure 2C**; **Table 2**). The mean values of altered ALFF maps were shown with a histogram (**Figure 2B**). The mean values of altered fALFF maps were shown with a histogram (**Figure 2D**).

FC Differences

Patients with CE showed a decreased FC between the right ANG/MOG/MTG and the bilateral calcarine (CAL)/lingual (LING) (**Figure 3A**; **Table 3**) and increased FC between the left PUT and the bilateral cerebellum 8/9 (CER 8/9) (**Figure 3B**; **Table 3**). The mean values of altered FC maps were shown with a histogram (**Figures 3A,B**).

TABLE 2 | Different ALFF values between the two groups.

Condition	Brain regions	BA	Peak *T*-scores	MNI coordinates (*x*, *y*, *z*)	Cluster size (voxels)
Different ALFF values					
CE<HC	R_ANG/MOG/MTG	19, 40	−4.378	48, −75, 24	528
CE<HC	B_SMA/PreCG	3, 4	−4.8378	21, −24, 78	303
Different fALFF values					
CE>HC	L_PUT	-	4.461	−24, −9, 6	144
CE<HC	R_ANG/MOG	19, 40	−4.5814	30, −84, 33	340

The statistical threshold was set at the voxel level with P < 0.01 for multiple comparisons using Gaussian random field theory.
ALFF, amplitude of low-frequency fluctuation; CE, comitant exotropia; HC, healthy control; ANG, angular; MOG, middle occipital gyrus; MTG, middle temporal gyrus; SMA, supplementary motor area; PreCG, precentral gyrus; PUT, putamen; R, right; L, left; B, bilateral.

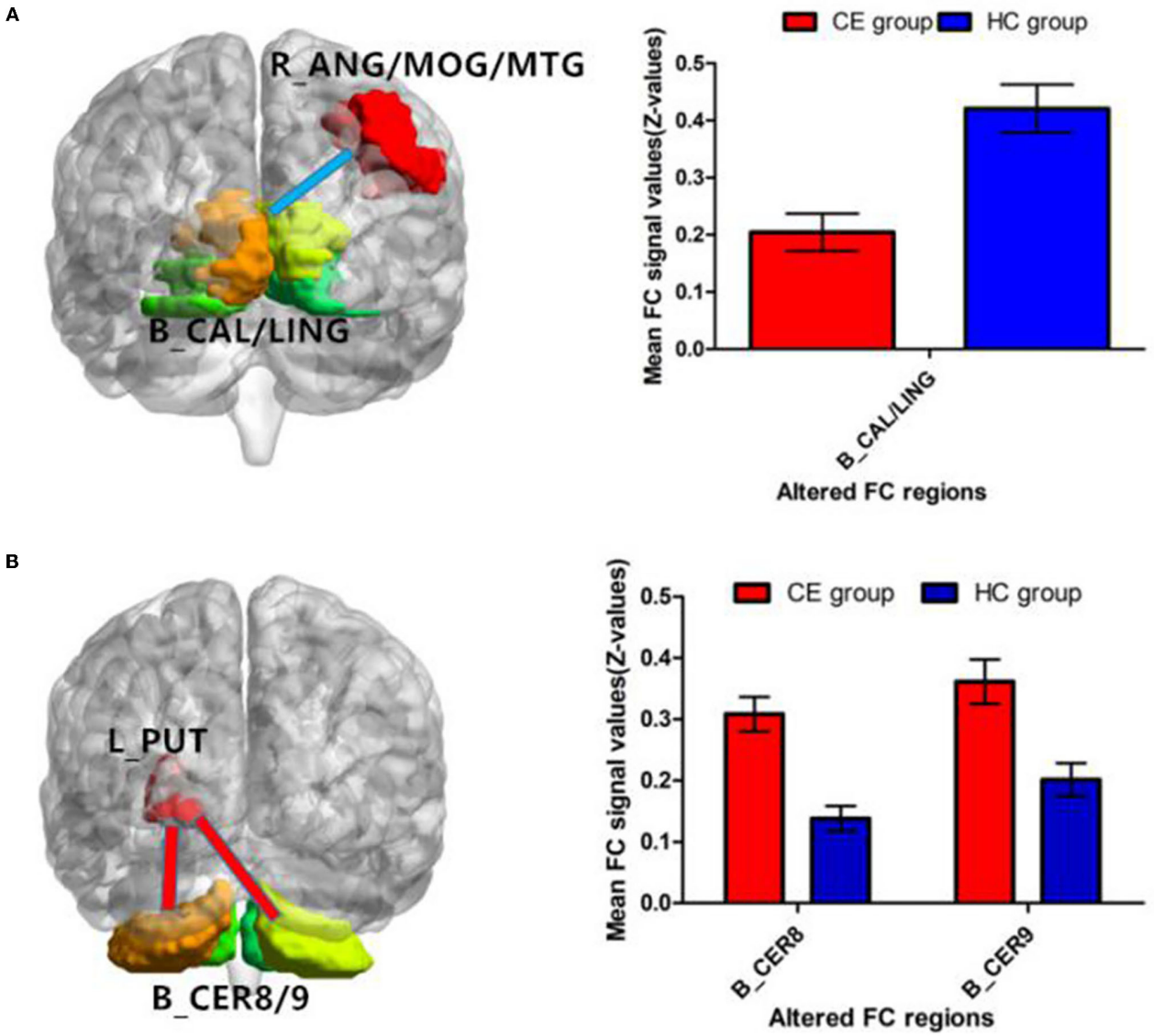

FIGURE 3 | Significant z-FC map differences seeded as ROI in different ALFF/fALFF regions between the two groups. The cool color indicates decreased z-FC values. The warm color indicates increased z-FC values. Significantly different FC values seeded as ROI in R-ANG/MOG/MTG **(A)** and L-PUT **(B)**. ALFF, amplitude of low-frequency fluctuation; fALFF, fractional amplitude of low-frequency fluctuation; ROI, region of interests; FC, functional connectivity; CE, comitant exotropia; HC, healthy control; ANG, angular; MOG, middle occipital gyrus; MTG, middle temporal gyrus; CAL, calcarine; LING, lingual; PUT, putamen; CER, cerebellum.

SVM Classification Results

The SVM classification reaches a total accuracy of 93%. The AUC of the classification model was 0.93 based on ALFF (**Figure 4**). The SVM classification reaches a total accuracy of 90%. The AUC of the classification model was 0.90 based on fALFF (**Figure 5**).

DISCUSSION

The purpose of this study was to investigate the spontaneous neural activity changes in patients with CE. Compared with the HC group, patients with CE showed significantly decreased ALFF values in the right ANG/MOG/MTG and bilateral SMA/PreCG. Meanwhile, patients with CE showed significantly increased fALFF values in the left PUT and decreased fALFF values in the right ANG/MOG. Moreover, patients with CE showed a decreased FC between the right ANG/MOG/MTG and the bilateral calcarine (CAL)/lingual (LING) and increased FC between the left PUT and the bilateral CER 8/9. Furthermore, the SVM classification reaches a total accuracy of 93 and 90% and the AUC of 0.93 and 0.90 based on ALFF and fALFF values, respectively.

TABLE 3 | Different functional connectivity (FC) values between the two groups.

Condition	Brain regions	BA	Peak *T*-scores	MNI coordinates (*x*, *y*, *z*)	Cluster size (voxels)
Seed in R-ANG/MOG/MTG					
CE<HC	B_CAL/LING	17, 18	−4.205	−12, −102, −12	1,092
Seed in L-PUT					
CE>HC	B_CER8	–	4.5664	6, −63, −36	1,209
CE>HC	B_CER9	–	3.332	−33, −60, −24	91

The statistical threshold was set at the voxel level with $P < 0.01$ for multiple comparisons using Gaussian random field theory.
ALFF, amplitude of low-frequency fluctuation; CE, comitant exotropia; HC, healthy control; ANG, angular; MOG, middle occipital gyrus; MTG, middle temporal gyrus; CAL, calcarine; LING, lingual; PUT, putamen; CER, cerebellum; R, right; L, left; B, bilateral.

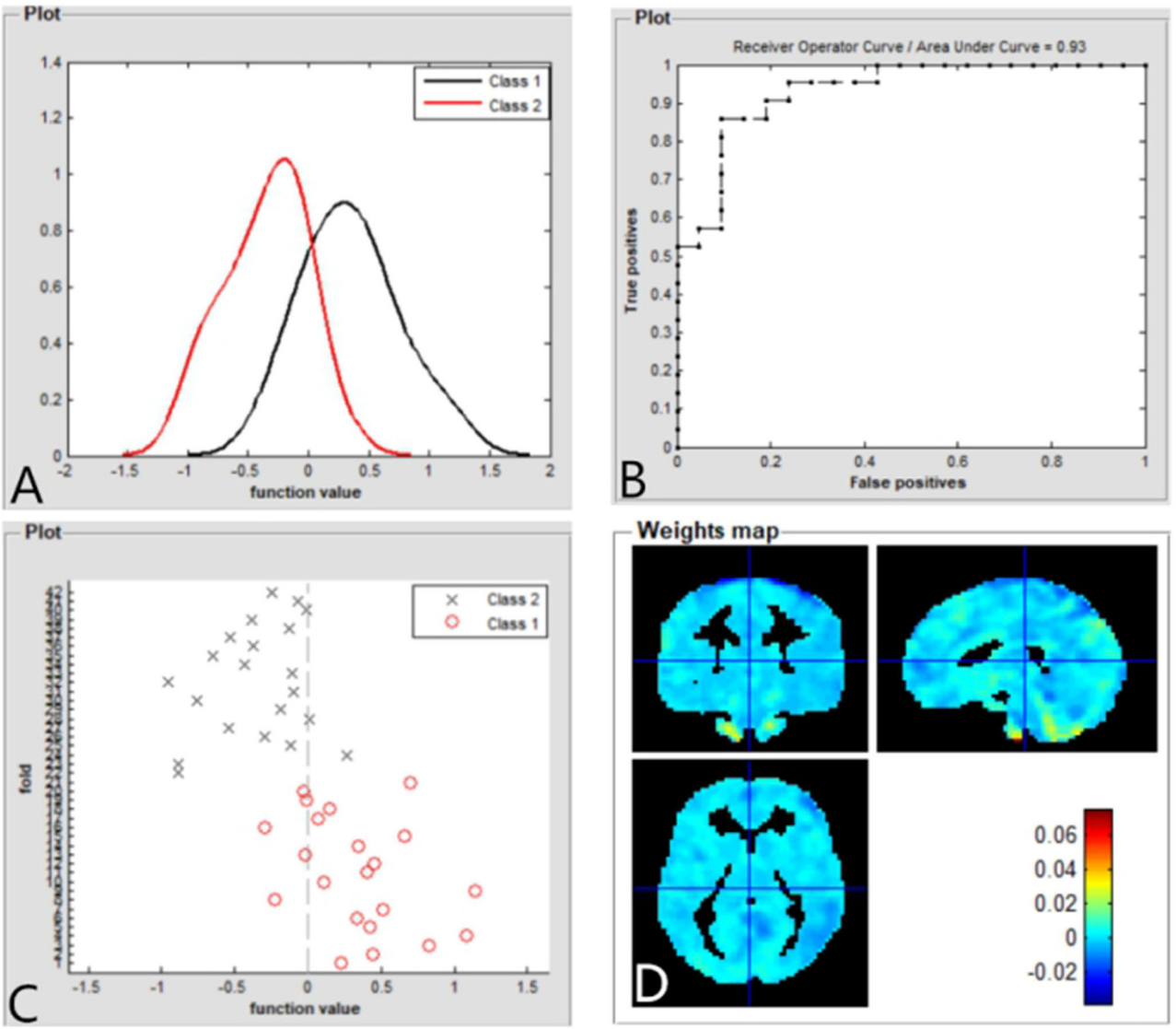

FIGURE 4 | Based on ALFF values, distribution of function values of the two groups (class 1: patient group; class 2: HC group) **(A)**; the ROC curve of the classifier, and the AUC was 0.93 **(B)**; function values of the two groups (class 1: CE group; class 2: HC group) **(C)**; and weight maps for SVM models **(D)**. ALFF, amplitude of low-frequency fluctuation; ROC, receiver operator characteristic; AUC, areas under the curve; CE, comitant exotropia; HC, healthy control; SVM, support vector machine.

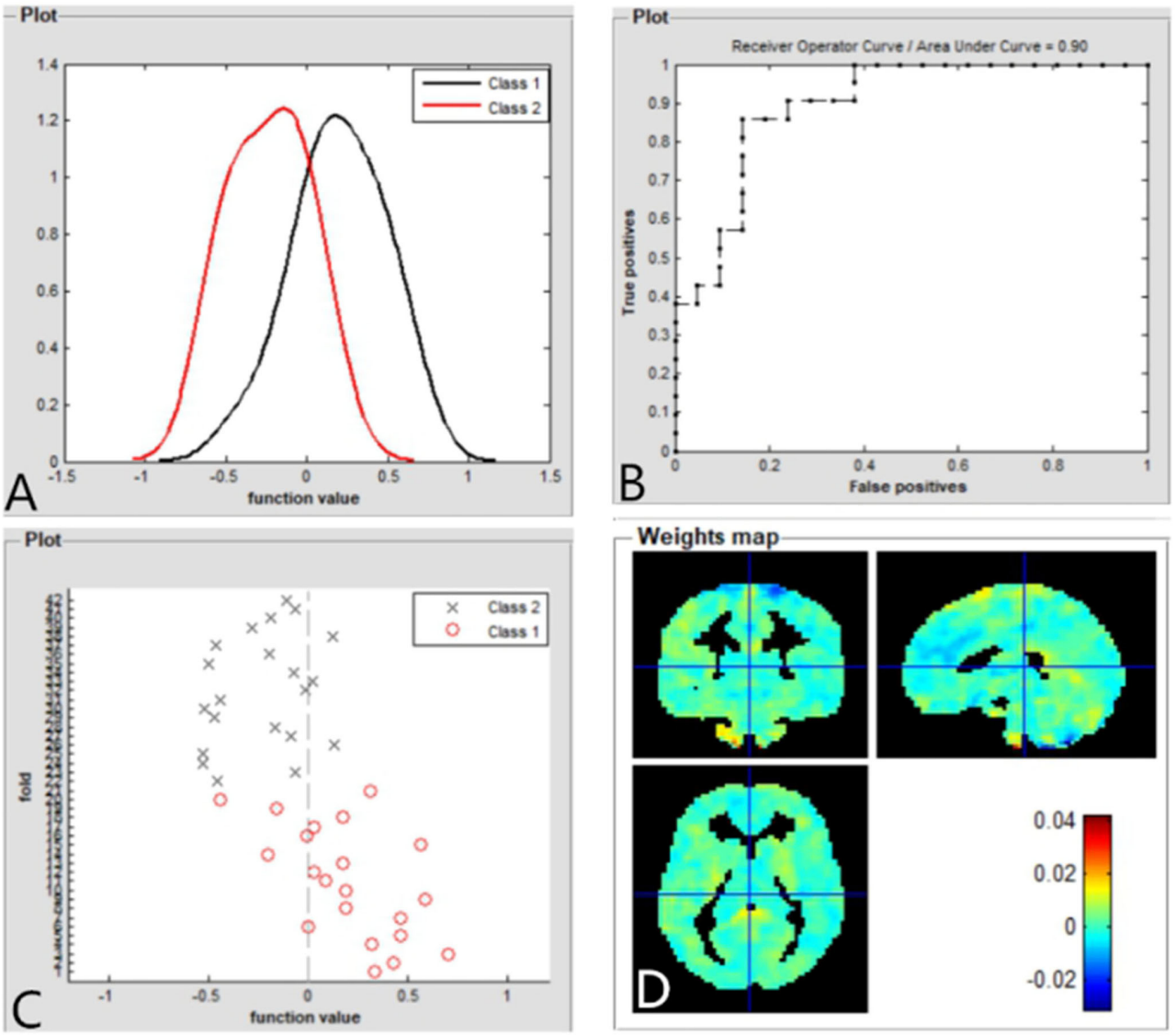

FIGURE 5 | Based on fALFF values, distribution of function values of the two groups (class 1: patient group; class 2: HC group) **(A)**; the ROC curve of the classifier, and the AUC was 0.90 **(B)**; function values of the two groups (class 1: patient group; class 2: HC group) **(C)**; weight maps for SVM models **(D)**. fALFF, fractional amplitude of low-frequency fluctuation; ROC, receiver operator characteristic; AUC, areas under curve; CE, comitant exotropia; HC, healthy controls; SVM, support vector machine.

An important finding is that patients with CE had significantly decreased ALFF values in the bilateral SMA/PreCG. The SMA/PreCG regions are important motor control-related brain functions. SMA is involved in the saccadic task and eye movement control (O'Driscoll et al., 1995; Campos et al., 2005). In addition, the supplementary eye field is located in SMA, which plays an important role in eye movement control and goal-directed behavior (Parton et al., 2007; Stuphorn, 2015). The frontal eye field is located in PreCG. Previous studies have revealed that the PreCG plays an important role in eye movement control (Blanke et al., 2000; Amiez and Petrides, 2009). Thus, we speculated that the significantly decreased ALFF values in the SMA/PreCG regions might contribute to the eye movement disorders in patients with CE.

In addition, another interesting finding is that patients with CE showed significantly decreased ALFF and fALFF values in the right ANG/MOG/MTG. Previous studies have identified a number of visual areas responsive to disparity-defined depth (Brouwer et al., 2005). Gonzalez et al. (2005) demonstrated that the parietal-occipital-temporal junction plays an important role in the processing of stereoscopic information. Meanwhile, previous studies demonstrated that middle temporal (MT) neurons showed a stronger ability of MT neurons to signal binocular disparity in moving vs. stationary random-dot

stereograms, presence of disparity-sensitive cells in MT+ and that these neurons can detect surface orientation on the basis of disparity gradients (Nguyenkim and DeAngelis, 2003; Palanca and DeAngelis, 2003). Consistent with these findings, we speculated that the significantly decreased ALFF and fALFF values in the right ANG/MOG/MTG regions might contribute to the binocular and stereoscopic vision disorders in patients with CE.

Furthermore, patients with CE showed a decreased FC between the right ANG/MOG/MTG and the bilateral calcarine (CAL)/lingual (LING) and increased FC between the left PUT and the bilateral CER 8/9. Previous studies have identified that functional connections between the visual cortices contribute to the formation of stereovision (Freeman, 1996; Nasr et al., 2016; Abed Rabbo et al., 2018). Thus, the decreased FC between the right ANG/MOG/MTG and the bilateral CAL/LING might reflect the impaired binocular and stereoscopic vision in individuals with CE.

In this study, the SVM classification reaches a total accuracy of 93 and 90% and the AUC of 0.93 and 0.90 based on ALFF and fALFF values, respectively. Thus, ALFF and fALFF maps might be sensitive biomarkers for discriminating those groups.

Some limitations should be mentioned in this study. First, the sample size is small. Second, BOLD signals can be influenced by physiological noise, which might be a bad influence on the result of ALFF values. Third, the patients with CE showed different strabismus angles, which might be reflecting the consistency of ALFF results.

CONCLUSION

Our results highlight that patient with CE had abnormal brain neural activities including MOG and supplementary motor area/PreCG, which might reflect the neural mechanism of eye movements and stereovision dysfunction in patients with CE. Moreover, ALFF and fALFF could be sensitive biomarkers for distinguishing patients with CE from HCs.

DATA AVAILABILITY STATEMENT

The raw data supporting the conclusions of this article will be made available by the authors, without undue reservation.

ETHICS STATEMENT

The studies involving human participants were reviewed and approved by Medical Ethics Committee of the Jiangxi Provincial People's Hospital. Written informed consent to participate in this study was provided by the participants' legal guardian/next of kin.

AUTHOR CONTRIBUTIONS

XH, JC, and HJ contributed to data collection, statistical analyses, and wrote the manuscript. XH, JC, HJ, and Y-LZ designed the protocol and contributed to the MRI analysis. XH and JC designed this study, oversaw all clinical aspects of study conduct, and manuscript preparation. All authors contributed to the study and approved the submitted version.

REFERENCES

Abed Rabbo, F., Koch, G., Lefevre, C., and Seizeur, R. (2018). Stereoscopic visual area connectivity: a diffusion tensor imaging study. *Surg. Radiol. Anat.* 40, 1197–1208. doi: 10.1007/s00276-018-2076-3

Amiez, C., and Petrides, M. (2009). Anatomical organization of the eye fields in the human and non-human primate frontal cortex. *Prog. Neurobiol.* 89, 220–230. doi: 10.1016/j.pneurobio.2009.07.010

Basgoze, Z., Mackey, A. P., and Cooper, E. A. (2018). Plasticity and adaptation in adult binocular vision. *Curr. Biol.* 28, R1406–R1413. doi: 10.1016/j.cub.2018.10.024

Blanke, O., Spinelli, L., Thut, G., Michel, C. M., Perrig, S., Landis, T., et al. (2000). Location of the human frontal eye field as defined by electrical cortical stimulation: anatomical, functional and electrophysiological characteristics. *Neuroreport* 11, 1907–1913. doi: 10.1097/00001756-200006260-00021

Brouwer, G. J., van Ee, R., and Schwarzbach, J. (2005). Activation in visual cortex correlates with the awareness of stereoscopic depth. *J. Neurosci.* 25, 10403–10413. doi: 10.1523/JNEUROSCI.2408-05.2005

Campos, M., Breznen, B., Bernheim, K., and Andersen, R. A. (2005). Supplementary motor area encodes reward expectancy in eye-movement tasks. *J. Neurophysiol.* 94, 1325–1335. doi: 10.1152/jn.00022.2005

Chan, R. W., Leong, A. T. L., Ho, L. C., Gao, P. P., Wong, E. C., Dong, C. M., et al. (2017). Low-frequency hippocampal-cortical activity drives brain-wide resting-state functional MRI connectivity. *Proc. Natl. Acad. Sci. U. S. A.* 114, E6972–E6981. doi: 10.1073/pnas.1703309114

Chen, V. J., and Tarczy-Hornoch, K. (2011). Functional magnetic resonance imaging of binocular interactions in visual cortex in strabismus. *J. Pediatr. Ophthalmol. Strabismus* 48, 366–374. doi: 10.3928/01913913-20101118-01

Freeman, R. D. (1996). Studies of functional connectivity in the developing and mature visual cortex. *J. Physiol. Paris* 90, 199–203. doi: 10.1016/S0928-4257(97)81423-4

Gonzalez, F., Relova, J. L., Prieto, A., and Peleteiro, M. (2005). Evidence of basal temporo-occipital cortex involvement in stereoscopic vision in humans: a study with subdural electrode recordings. *Cereb. Cortex* 15, 117–122. doi: 10.1093/cercor/bhh114

Govindan, M., Mohney, B. G., Diehl, N. N., and Burke, J. P. (2005). Incidence and types of childhood exotropia: a population-based study. *Ophthalmology* 112, 104–108. doi: 10.1016/j.ophtha.2004.07.033

Hou, C., Nicholas, S. C., and Verghese, P. (2020). Contrast normalization accounts for binocular interactions in human striate and extra-striate visual cortex. *J. Neurosci.* 40, 2753–2763. doi: 10.1523/JNEUROSCI.2043-19.2020

Liu, F., Guo, W., Yu, D., Gao, Q., Gao, K., Xue, Z., et al. (2012). Classification of different therapeutic responses of major depressive disorder with multivariate pattern analysis method based on structural MR scans. *PLoS One* 7:e40968. doi: 10.1371/journal.pone.0040968

Maconachie, G. D., Gottlob, I., and McLean, R. J. (2013). Risk factors and genetics in common comitant strabismus: a systematic review of the literature. *JAMA Ophthalmol.* 131, 1179–1186. doi: 10.1001/jamaophthalmol.2013.4001

Nasr, S., Polimeni, J. R., and Tootell, R. B. (2016). Interdigitated color- and disparity-selective columns within human visual cortical areas V2 and V3. *J. Neurosci.* 36, 1841–1857. doi: 10.1523/JNEUROSCI.3518-15.2016

Nguyenkim, J. D., and DeAngelis, G. C. (2003). Disparity-based coding of three-dimensional surface orientation by macaque middle temporal neurons. *J. Neurosci.* 23, 7117–7128. doi: 10.1523/JNEUROSCI.23-18-07117.2003

O'Driscoll, G. A., Alpert, N. M., Matthysse, S. W., Levy, D. L., Rauch, S. L., and Holzman, P. S. (1995). Functional neuroanatomy of antisaccade eye movements investigated with positron emission tomography. *Proc. Natl. Acad. Sci. U. S. A.* 92, 925–929. doi: 10.1073/pnas.92.3.925

Palanca, B. J., and DeAngelis, G. C. (2003). Macaque middle temporal neurons signal depth in the absence of motion. *J. Neurosci.* 23, 7647–7658. doi: 10.1523/JNEUROSCI.23-20-07647.2003

Parton, A., Nachev, P., Hodgson, T. L., Mort, D., Thomas, D., Ordidge, R., et al. (2007). Role of the human supplementary eye field in the control of saccadic eye movements. *Neuropsychologia* 45, 997–1008. doi: 10.1016/j.neuropsychologia.2006.09.007

Schrouff, J., Rosa, M. J., Rondina, J. M., Marquand, A. F., Chu, C., Ashburner, J., et al. (2013). PRoNTo: pattern recognition for neuroimaging toolbox. *Neuroinformatics* 11, 319–337. doi: 10.1007/s12021-013-9178-1

Shapira, Y., Machluf, Y., Mimouni, M., Chaiter, Y., and Mezer, E. (2018). Amblyopia and strabismus: trends in prevalence and risk factors among young adults in Israel. *Br. J. Ophthalmol.* 102, 659–666. doi: 10.1136/bjophthalmol-2017-310364

Shi, H., Wang, Y., Liu, X., Xia, L., Chen, Y., Lu, Q., et al. (2019). Cortical alterations by the abnormal visual experience beyond the critical period: a resting-state fMRI Study on constant exotropia. *Curr. Eye Res.* 44, 1386–1392. doi: 10.1080/02713683.2019.1639767

Stuphorn, V. (2015). The role of supplementary eye field in goal-directed behavior. *J. Physiol. Paris* 109, 118–128. doi: 10.1016/j.jphysparis.2015.02.002

Sturm, V., Menke, M. N., Knecht, P. B., and Schoffler, C. (2011). Long-term follow-up of children with acute acquired concomitant esotropia. *J AAPOS* 15, 317–320. doi: 10.1016/j.jaapos.2011.03.018

van Kerkoerle, T., Self, M. W., Dagnino, B., Gariel-Mathis, M. A., Poort, J., van der Togt, C., et al. (2014). Alpha and gamma oscillations characterize feedback and feedforward processing in monkey visual cortex. *Proc. Natl. Acad. Sci. U. S. A.* 111, 14332–14341. doi: 10.1073/pnas.1402773111

Yan, C. G., Wang, X. D., Zuo, X. N., and Zang, Y. F. (2016). DPABI: data processing and analysis for (Resting-State) brain imaging. *Neuroinformatics* 14, 339–351. doi: 10.1007/s12021-016-9299-4

Yan, X., Lin, X., Wang, Q., Zhang, Y., Chen, Y., Song, S., et al. (2010). Dorsal visual pathway changes in patients with comitant extropia. *PLoS One* 5:e10931. doi: 10.1371/journal.pone.0010931

Yan, X., Wang, Y., Xu, L., Liu, Y., Song, S., Ding, K., et al. (2019). Altered functional connectivity of the primary visual cortex in adult comitant strabismus: a resting-state functional MRI study. *Curr. Eye Res.* 44, 316–323. doi: 10.1080/02713683.2018.1540642

Yin, S., Liu, L., Tan, J., Ding, C., Yao, D., and Chen, A. (2017). Attentional control underlies the perceptual load effect: evidence from voxel-wise degree centrality and resting-state functional connectivity. *Neuroscience* 362, 257–264. doi: 10.1016/j.neuroscience.2017.08.055

Zhu, H., Yu, J. J., Yu, R. B., Ding, H., Bai, J., Chen, J., et al. (2015). Association between childhood strabismus and refractive error in Chinese preschool children. *PLoS One* 10:e0120720. doi: 10.1371/journal.pone.0120720

Zou, Q. H., Zhu, C. Z., Yang, Y., Zuo, X. N., Long, X. Y., Cao, Q. J., et al. (2008). An improved approach to detection of amplitude of low-frequency fluctuation (ALFF) for resting-state fMRI: fractional ALFF. *J. Neurosci. Methods* 172, 137–141. doi: 10.1016/j.jneumeth.2008.04.012

Conflict of Interest: The authors declare that the research was conducted in the absence of any commercial or financial relationships that could be construed as a potential conflict of interest.

Publisher's Note: All claims expressed in this article are solely those of the authors and do not necessarily represent those of their affiliated organizations, or those of the publisher, the editors and the reviewers. Any product that may be evaluated in this article, or claim that may be made by its manufacturer, is not guaranteed or endorsed by the publisher.

frontiers in Neuroscience

ORIGINAL RESEARCH
published: 11 October 2021
doi: 10.3389/fnins.2021.749824

Proficiency in Using Level Cue for Sound Localization Is Related to the Auditory Cortical Structure in Patients With Single-Sided Deafness

Ja Hee Kim[1,2†], Leeseul Shim[2†], Junghwa Bahng[3] and Hyo-Jeong Lee[1,2]*

[1] Department of Otorhinolaryngology-Head and Neck Surgery, Hallym University College of Medicine, Chuncheon, South Korea, [2] Laboratory of Brain & Cognitive Sciences for Convergence Medicine, Hallym University College of Medicine, Anyang, South Korea, [3] Department of Audiology and Speech-Language Pathology, Hallym University of Graduate Studies, Seoul, South Korea

Spatial hearing, which largely relies on binaural time/level cues, is a challenge for patients with asymmetric hearing. The degree of the deficit is largely variable, and better sound localization performance is frequently reported. Studies on the compensatory mechanism revealed that monaural level cues and monoaural spectral cues contribute to variable behavior in those patients who lack binaural spatial cues. However, changes in the monaural level cues have not yet been separately investigated. In this study, the use of the level cue in sound localization was measured using stimuli of 1 kHz at a fixed level in patients with single-sided deafness (SSD), the most severe form of asymmetric hearing. The mean absolute error (MAE) was calculated and related to the duration/age onset of SSD. To elucidate the biological correlate of this variable behavior, sound localization ability was compared with the cortical volume of the parcellated auditory cortex. In both SSD patients (n = 26) and normal controls with one ear acutely plugged (n = 23), localization performance was best on the intact ear side; otherwise, there was wide interindividual variability. In the SSD group, the MAE on the intact ear side was worse than that of the acutely plugged controls, and it deteriorated with longer duration/younger age at SSD onset. On the impaired ear side, MAE improved with longer duration/younger age at SSD onset. Performance asymmetry across lateral hemifields decreased in the SSD group, and the maximum decrease was observed with the most extended duration/youngest age at SSD onset. The decreased functional asymmetry in patients with right SSD was related to greater cortical volumes in the right posterior superior temporal gyrus and the left planum temporale, which are typically involved in auditory spatial processing. The study results suggest that structural plasticity in the auditory cortex is related to behavioral changes in sound localization when utilizing monaural level cues in patients with SSD.

Keywords: hearing loss, unilateral hearing loss, sound localization, neuronal plasticity, gray matter volume

OPEN ACCESS

Edited by:
Jae-Jin Song, Seoul National University Bundang Hospital, South Korea

Reviewed by:
James W. Dias, Medical University of South Carolina, United States
I-Hui Hsieh, National Central University, Taiwan

***Correspondence:**
Hyo-Jeong Lee
hyojlee@hallym.ac.kr

† These authors have contributed equally to this work and share first authorship

Specialty section:
This article was submitted to Perception Science, a section of the journal Frontiers in Neuroscience

Received: *30 July 2021*
Accepted: *20 September 2021*
Published: *11 October 2021*

Citation:
Kim JH, Shim L, Bahng J and Lee H-J (2021) Proficiency in Using Level Cue for Sound Localization Is Related to the Auditory Cortical Structure in Patients With Single-Sided Deafness. Front. Neurosci. 15:749824. doi: 10.3389/fnins.2021.749824

Abbreviations: AI, asymmetry index; GM volume, gray matter volume; MAE, mean absolute error; MRI, magnetic resonance imaging; NC, normal control; nCV, normalized cortical volume; PT, planum temporale; PTA, pure-tone average; SSD, single-sided deafness; STG, superior temporal gyrus.

INTRODUCTION

Unilateral loss of hearing deteriorates sound localization ability, which relies largely on binaural time and level differences in the sound source that reaches the two ears. Loss of binaural time/level cues results in poor localization performance, which is a significant behavioral deficit in patients with asymmetric hearing (Kumpik and King, 2019; Snapp and Ausili, 2020). However, reported data also show considerable variability in the degree to which localization accuracy is affected by monaural hearing, suggesting the adaptive contribution of the monaural level cues and monaural pinna cues, which normally play a minor role. For example, relatively good localization has been found in some adults with various degrees of unilateral hearing loss, whereas others cannot localize at all (Slattery and Middlebrooks, 1994; Van Wanrooij, 2004; Shub et al., 2008; Agterberg et al., 2012; Firszt et al., 2017; Pastore et al., 2020). The variable impact of hearing loss on localization ability, even in individuals with unilateral sensorineural single-sided deafness (SSD), indicates that hearing loss in the poorer ear alone does not eradicate the potential to localize sound. Instead, this variability suggests that malleable processes in higher-level structures occur naturally to improve localization accuracy. Deprived of binaural difference cues, the adaptive change in SSD would rely on increased proficiency of using remaining monaural spatial cues. Monaural level cues are primarily used over monaural spectral shape cues (Shub et al., 2008; Pastore et al., 2020). Although inherently ambiguous, the monaural level cue can serve as a valid cue to azimuth because the learned sound will appear louder when presented on the better-hearing side (Agterberg et al., 2012). A sound source located on the impaired hearing side is attenuated by the subject's head when reaching the hearing ear side. The degree of attenuation varies according to the azimuthal location relative to the intact ear. This level cue by head shadowing would be unreliable if the source level varies frequently, but it serves as an essential localization cue in a familiar environment. Considering the high prevalence of high-frequency hearing loss, considerable patients with asymmetric hearing might rely on monaural level cues rather than the monaural spectral cues based on high-frequency information. Reflecting the high variability of localization performance and the diversity of the audiologic profile, clinical factors that contribute to improved auditory spatial ability have only been reported in a few studies; longer duration of SSD (Liu et al., 2018; Nelson et al., 2019) and younger age at SSD onset (Firszt et al., 2017; Nelson et al., 2019) have been associated with better localization performance.

Although adaptive changes in localization performance have been reported repeatedly, the neural correlates associated with functional changes have not yet been clearly addressed. Different auditory spatial cues are separately processed in the lower brainstem and are integrated in the higher subcortex or above. Across the auditory neural pathway, functional changes that improve localization performance occur at a higher level, where cue integration takes place and enables the reweighting of spatial cues. The auditory cortex plays a crucial role in auditory spectrotemporal analysis, and functional neuroimaging studies (Pavani et al., 2002; Deouell et al., 2007; Ahveninen et al., 2014; Callan et al., 2015) and lesion studies (Zatorre and Penhune, 2001; Zündorf et al., 2014) have indicated that it is essential for sound localization. Functional magnetic resonance imaging (MRI) studies have shown that sound localization processing has a particular activating effect on areas of the posterior auditory cortex, such as the planum temporale (PT) (van der Zwaag et al., 2011; van der Heijden et al., 2018, 2019). While each auditory cortex preferentially responds to sound location in the contralateral hemifield, right hemispheric dominance (Zatorre and Penhune, 2001; Zündorf et al., 2014; Callan et al., 2015) and the role of interhemispheric connection (Briley et al., 2013; Derey et al., 2016) have been reported. The auditory cortex also has a feedback/feedforward connection to the higher-order cortices that is associated with top-down attentional modulation of auditory spatial ability (van der Heijden et al., 2018, 2019). Meanwhile, neuroanatomical characteristics of the auditory cortex, such as the change of gray matter volume (GM volume), have shown to be associated with certain types of hearing loss (Cardin, 2016). For example, structural changes in the gray matter in the auditory cortex have been found for patients with mild-to-moderate hearing loss (Husain et al., 2011), high-frequency hearing loss (Eckert et al., 2012, 2019), and unilateral hearing loss (Yang et al., 2014; Heggdal et al., 2020). Yet, the evidence for the structural changes relating to auditory performance in sound localization is limited.

In the present study, sound localization ability using monaural level cues was evaluated in 26 patients with SSD and compared with those from acute plugged controls (n = 23) to examine the behavioral change in auditory spatial ability in the SSD group. In the SSD group, clinical factors were analyzed to determine whether the duration of SSD/age at SSD onset was related to behavioral changes. To examine the biological substrate in the auditory cortex associated with behavioral adaptation, the GM volume was measured in the parcellated regions of the bilateral auditory cortices and compared to the changes in localization performance using monaural level cues in the SSD group.

MATERIALS AND METHODS

Participants

Demographic and clinical information for all subjects is provided in **Table 1**. Twenty-six patients who had severe to profound unilateral sensorineural hearing loss (M:F = 12:14; age mean ± SD = 42.7 ± 11.4 years old) participated in the study. Fifteen patients had unilateral hearing loss in their left ear (SSD-L), whereas eleven had hearing loss in their right ear (SSD-R). The inclusion criterion was severe to profound hearing loss in one ear [pure-tone average (PTA) ≥ 70 dB HL] and 30 dB HL or better in the other ear (Vincent et al., 2015; Van de Heyning et al., 2016). Pure tone audiometry was performed at the range of frequencies from 125 to 8000 Hz, and the averaged 4-tone thresholds at 500, 1000, 2000, and 4000 Hz produced PTA. Patients were included only when the duration of severe to profound hearing loss was more than 1 month. Causes of unilateral hearing loss were congenital hearing loss, sudden sensorineural hearing loss, and progressive sensorineural

hearing loss in 4, 13, and 9 patients, respectively. For those with a history of progressive hearing loss, the onset and duration of hearing loss were defined based on the time when their hearing loss reached the level of severe hearing loss. When analyzing sound localization performance, the two SSD groups were pooled (details are presented in section "Results") and subdivided into three subgroups according to their duration of SSD ($SSD_{<7\ years}$: 0.17–7 years of SSD, $SSD_{10-29\ years}$: 10–29 years of SSD, and $SSD_{43-46\ years}$: 43–46 years of SSD).

Twenty-three healthy subjects (M:F = 11:12; age mean ± SD = 41.7 ± 12.0 years) with normal hearing (PTA less than 25 dB HL in both ears) without a history of hearing problems served as the normal control (NC) group. The participants were matched to the SSD group in terms of the hearing threshold in the intact ear, sex, and age.

All participants were right-handed. Subjects were excluded if they had any neurological/neuropsychiatric history or took any related medication. Medical history including diabetes, hypertension, and any condition that contraindicated MRI scanning were also exclusion criteria.

This study protocol was approved by the Institutional Review Board of the Hallym University Sacred Heart Hospital (Anyang, South Korea) (IRB No. 2018-02-019-002).

Sound Localization Test

A sound localization test was performed using a DHA-8 apparatus (Directional Hearing Evaluator 8, Interacoustics, Denmark) that assesses a person's ability to identify the source location of a sound. Eight speakers were used in the experiment with two speakers in the front and rear of the subject (at 0° and 180°) and three additional speakers on each side of the individual, separated by 45°. All speakers were mounted at head level and labeled no. 1 to no. 8 (**Figure 1**).

As auditory stimuli, a 1 kHz warble tone at 40 dB SL was presented using GSI 61 Audiometry (Grason-Stadler, MN, United States). The duration of the sound presentation was 3 s, with an approximate 5 s interstimulus interval. Five trials from each of eight loudspeakers were presented in random order, and a total of 40 trials were tested per subject. Presentation® software (Neurobehavioral System, Albany, CA, United States) was used to randomize trials and to record responses.

The subjects were seated in the center of the sound booth and a chair facing the loudspeaker at 0° azimuth (front) and at 1 m from the speakers in any direction. Prior to the test, a training session composed of randomized trials of three presentations per speaker was conducted. Subjects answered the sound source by the number of speakers using their own voice. Participants were asked not to move their head in the course of the experiment. The response angle was averaged for five trials per speaker. To calculate the mean absolute error (MAE), the absolute difference between the response speaker and stimulus speaker was averaged for five trials per speaker, meaning smaller values indicated better sound localization. An asymmetry index (AI) was calculated to reflect performance discrepancies between the good- and poor-hearing sides. AI was defined as a relative difference in weighted angle differences between good- and poor-ear sides using the following equation:

$$\mathrm{AI} = \frac{(\text{Poor} - \text{ear speaker}: \ 225^\circ + 2 \times 270^\circ + 315^\circ) - (\text{Good} - \text{ear speaker}: \ 45^\circ + 2 \times 90^\circ + 135^\circ)}{(\text{Poor} - \text{ear speaker}: \ 225^\circ + 2 \times 270^\circ + 315^\circ) + (\text{Good} - \text{ear speaker}: \ 45^\circ + 2 \times 90^\circ + 135^\circ)}$$

This index may span from −1 to 1. When this index approaches zero, it means that the sound localization performance is similar across the good- vs. poor-hearing ear sides. When the good-hearing side markedly outperformed the poor-hearing side, the AI was approximately 1.

The SSD group was tested *via* the intact ear. In the NC group, a simulation experiment was conducted to compare the results with those of the SSD group. The right ear was covered with an earmuff and subjected to narrowband noise

TABLE 1 | Demographic characteristics of the groups.

	SSD-L (*n* = 15)	SSD-R (*n* = 11)	NC (*n* = 23)	*p*-Value
Age (years)	38.9 ± 12.1	46.1 ± 9.1	41.7 ± 11.9	0.929
Sex (M/F)	8/8	4/7	11/12	0.707
Age at onset of SSD (years)	24.3 ± 14.4	24.9 ± 20.0	–	0.755
Duration of SSD (years)	14.5 ± 12.8	21.1 ± 20.2	–	0.716
Good-ear PTA (dB HL)	14.0 ± 12.6	13.8 ± 9.6	10.0 ± 7.2 (Lt)	0.357
Poor-ear PTA (dB HL)	108.2 ± 15.5	104.0 ± 19.3		0.936

SSD-L and SSD-R denote patient groups with single-sided deafness in the left and right ears, respectively.
NC, normal control group; M, male; F, female; dB HL, dB hearing level.

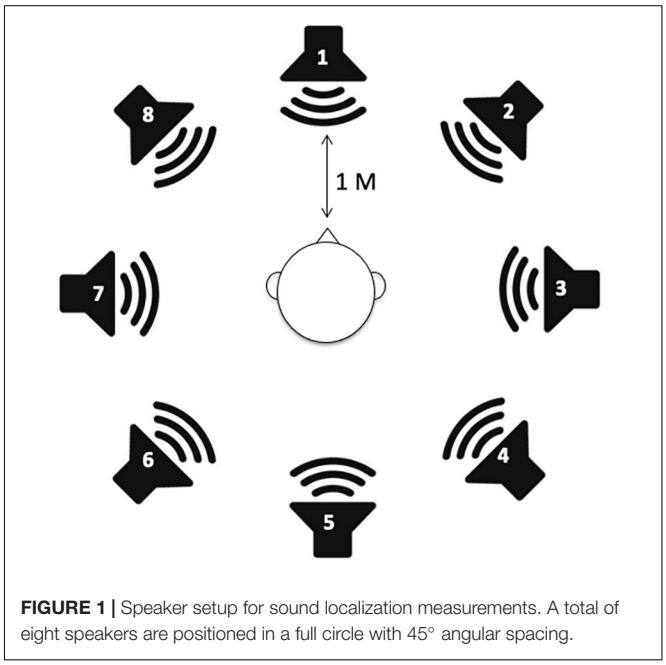

FIGURE 1 | Speaker setup for sound localization measurements. A total of eight speakers are positioned in a full circle with 45° angular spacing.

(centered at 1 kHz) for masking using an insert earphone (ER3-A, Etymotic Research Inc. Elk grove village, IL, United States), which prevented auditory stimuli from being processed by the covered right ear. The narrowband noise for the masking was provided through an audiometer at 20 dB SL for frequencies above 1 kHz (AudioStar Pro; GSI Grason-Stadler, Eden Prairie, MN, United States).

Structural Analysis of the Auditory Cortex

Structural Magnetic Resonance Imaging

High-resolution 3D-T1 weighted images were obtained using a 3T MRI scanner (Philips, Amsterdam, Netherlands) in both the SSD and NC groups. A 3D-gradient fast field echo sequence was applied with repetition time (TR) = 9.3 ms, echo time (TE) = 4.6 ms, field angle of field of view (FOV) = 230 × 230 mm, and matrix size = 230 × 200. The slice thickness was 1.0 mm, for a total of 160 slices without gaps.

Image Preprocessing

The cortical volume of the gray matter was generated using voxel-based morphometry (VBM) with the Dartel toolbox running within SPM8 (Statistical Parametric Mapping[1]) implemented in MATLAB version R2009a (MathWorks Inc., Natick, MA, United States) (Ashburner and Friston, 2000; Good et al., 2001). First, the 3-D T1 image of each participant was segmented into gray matter, white matter, and cerebrospinal fluid using a unified tissue segmentation procedure after image intensity nonuniformity correction. Flow fields and a series of template images were generated and used to modulate the spatially normalized brain volume to Montreal Neurological Institute (MNI) space by nonaffine warping. Eventually, a modulated gray matter image was obtained for each subject to detect differences in cortical volume.

Normalized Cortical Volume in the Parcellated Auditory Cortex

Three regions of interest (ROIs) per hemisphere (a total of six ROIs) were extracted from the Harvard-Oxford cortical and subcortical structural atlases using the FSL anatomy toolbox.[2] The ROIs encompassing auditory regions were the anterior part of the superior temporal gyrus (STG), posterior part of the STG, and PT. These ROIs were binarized and registered to the individual's anatomical space. Additionally, a gray matter mask was applied to transformed ROIs to extract distinct anatomical indices. Finally, to correct for variation in brain size across the individuals, normalized cortical volume (nCV), which represents the GM volume of the predefined ROIs divided by whole-brain volume, was calculated for each ROI.

Statistical Analysis

Statistical analyses were conducted with R using the ppcor, jmv, dunn.test, and WRS2 packages (Kim, 2015; Mair and Wilcox, 2020; Selker et al., 2020). A normality test was performed using Shapiro–Wilk's test. Group differences in age and sex distribution were tested using one-way ANOVA and Fisher's exact test, respectively. In the NC group, PTA across the right and left ears was compared using a paired *t*-test. Between the two SSD groups, the age at SSD onset, the duration of SSD, and PTA in the poor-hearing ear were compared using the Wilcoxon rank sum test. The PTA in the good-hearing ear was compared across the two SSD groups and the acutely plugged NC group (left ear) using the Kruskal–Wallis test.

To analyze sound localization test results, response angles and MAE were analyzed to test the group differences and speaker directions effect (with interaction), using robust ANOVA for mixed design provided by WRS2 package. Nonparametric repeated-measures ANOVA tested the stimulation direction effect on the MAE across groups. The Wilcoxon rank sum test was used to compare the AI values and the MAE in each direction between the NC and SSD groups. For comparison across NC and SSD subgroups, the Kruskal–Wallis test was performed with Dunn's *post hoc* test with the *p*-value adjusted by the Benjamini–Hochberg method. Nonparametric partial correlation analyses were carried out between sound localization performances (MAE and AI) and clinical factors (age at SSD onset and duration of SSD), controlling for age.

When analyzing cortical structure, two SSD groups were analyzed separately, considering the innate structural/functional asymmetry of the brain. The nCV in each ROI was compared across groups using robust one-way ANOVA based on trimmed means. A nonparametric partial correlation was used to examine whether the nCV extracted from six ROIs was related to the age at onset of SSD, duration of SSD, and AI, controlling for age at the time of the experiment.

RESULTS

Demographic Characteristics

Across the three groups, age [$F(2,46) = 1.273$, $p = 0.290$] and sex distribution (Fisher's exact test, $p = 0.707$) were not significantly different. PTA in the good (tested) ear was also not different across the three groups [$\chi^2(2) = 2.062$, $p = 0.357$]. Between the two SSD groups (SSD-R vs. SSD-L), there were no significant differences in PTA in the poor ear (Wilcoxon rank sum test, $p = 0.936$), duration of SSD ($p = 0.716$) or age at onset of SSD ($p = 0.755$).

When the two SSD groups were pooled, the duration of SSD was negatively correlated with the age at onset of SSD ($r_s = -0.793$, $n = 26$, $p < 0.001$), but the age at the time of the experiment was related to neither the duration ($p = 0.271$) nor the age at onset of SSD ($p = 0.101$). When the two SSD groups were separately tested, a negative correlation between age at onset and duration of SSD was significant in both SSD groups (SSD-R: $r_s = -0.834$, $p = 0.001$; SSD-L: $r_s = -0.606$, $p = 0.017$). The age at the time of the experiment was significantly related to the age at onset of SSD in the SSD-L group only (SSD-R: $p = 0.422$; SSD-L: $r_s = 0.581$, $p = 0.023$) but was not related to the duration of SSD in either group (SSD-R: $p = 0.705$, SSD-L: $p = 0.334$).

[1] www.fil.ion.ucl.ac.uk/spm

[2] https://fsl.fmrib.ox.ac.uk/fsl/fslwiki/Atlases

In the NC group, PTA from both ears was not different [$t(22) = 1.464$, $p = 0.157$].

Behavioral Results

When the localization test results of the SSD-L group were flipped to match the good-/poor-hearing side with those of the SSD-R group, the response angle was different across stimulation directions, whereas no differences were found for groups. A mixed design ANOVA results showed no significant interaction between stimulation direction and group [robust ANOVA for mixed design; stimulation direction: $F(7,11.1) = 26.8$, $p < 0.001$; group: $F(1,13.7) = 0.6$, $p = 0.447$; stimulation direction × group: $F(7,11.1) = 1.42$, $p = 0.288$]. Therefore, all data reported here were standardized such that negative angular or stimulus values represent the impaired (plugged) ear side and positive values represent the intact (open) ear side. The pooled data from the SSD group were compared with those from the NC group (the right ear was covered and masked to simulate SSD-R).

Sound Localization Performance

The sound localization performance of all individuals in the NC and SSD groups is provided in **Figure 2**. The results of the simulated NC group revealed that although all responses from the intact ear side (+45°, +90°, and +135°) were on the same hemifield (**Figure 2A**), the responses from the acutely plugged ear were more diverse. The SSD patients variably responded to stimuli from the good-hearing sides, and some patients even responded to the opposite hemifield with stimuli from the good-hearing side (**Figure 2B**). A robust ANOVA for mixed design was examined the effect of group and stimulation angles on behavioral performances. Results showed a significant effect of the stimulation angles, with no effects for the group and interaction [stimulation direction: $F(7,19.9) = 13.7$, $p < 0.001$; group: $F(1,19.8) = 3.2$, $p = 0.087$; stimulation direction × group: $F(7,19.9) = 1.98$, $p = 0.109$]. When the SSD group was divided into three subgroups by the duration of SSD (**Figure 2B**), stimulation angle and its interaction with subgroup showed significant effects, whereas group differences did not [robust ANOVA for mixed design; stimulation direction: $F(7,3.9) = 19.3$, $p = 0.007$; subgroup: $F(2,3.9) = 5.27$, $p = 0.078$; stimulation direction × subgroup: $F(14,3.8) = 14.3$, $p = 0.012$].

Both the NC and SSD groups showed a clear response bias toward the intact side. While 37.5% of the stimuli were provided on the good-hearing side (three out of eight speakers), 68.2 and 67.3% of responses were recorded on this hemifield in the plugged NC and SSD groups, respectively. However, in the impaired side of the SSD subgroup with a very long duration of SSD (43–46 years), bias toward the intact ear side was not apparent, of whom three out of five responded with the correct hemifield to stimuli from three speakers on the poor-hearing side (**Figure 2B**, black triangles).

Mean absolute error values between the stimulation angle and response angle were grouped in four directions (front, back, good-ear side, and poor-ear side) and compared between groups (**Table 2** and **Figure 3**). When comparing the NC and SSD groups, the MAE values in the four directions were significantly different across stimulation angles, and interaction was significant; however the group effect was not significant [robust ANOVA for mixed design; group: $F(1,24.3) = 0$, $p = 0.967$; stimulation direction: $F(3,21.3) = 41.3$, $p < 0.001$; stimulation direction × group: $F(3,21.3) = 3.7$, $p = 0.028$]. When comparing each direction separately, the simulated NC group showed significantly better performance (smaller angle difference) than the SSD group for the good-hearing side only (**Table 2**). On the other three directions, the performances were not significant among groups (Wilcoxon rank sum test; good-hearing side: $p = 0.008$; poor-hearing side: $p = 0.196$; front: $p = 0.212$; and back: $p = 0.150$). In the NC group, MAE values were significantly different across source directions [$\chi^2(3) = 25.6$, $p < 0.001$, **Figure 3A**, left panel], with a smaller error on the good-hearing side than on all three other sides ($p < 0.001$). In the SSD group (**Figure 3A**, right panel), MAE values were also significantly different across directions [$\chi^2(3) = 28.6$, $p < 0.001$]; the MAE for the good-hearing side was significantly better than that for the poor ($p = 0.001$) and front ($p < 0.001$) directions but was not better than that for the back direction ($p = 0.234$), for which the MAE was also smaller (better) than that for the poor-hearing ($p = 0.036$) and front ($p < 0.001$) directions. When MAE values were further analyzed across the NC group and three SSD subgroups with different durations of SSD (**Figure 3B**), MAE values were significantly different across source directions [$F(3,41.9) = 43.7$, $p < 0.001$] and interacted with the group [$F(9,33.6) = 5.4$, $p < 0.001$], but the group effect was not significant [$F(3,30.0) = 0.2$, $p = 0.875$]. In the *post hoc* comparison, the group difference was significant only in the good-hearing direction [$\chi^2(3) = 10.4$, $p = 0.015$], with a significantly smaller MAE in the NC group over two SSD subgroups with over 10 years of SSD (NC vs. $SSD_{10-29\ years}$: $p = 0.018$, NC vs. $SSD_{43-46\ years}$: $p = 0.035$). Similar to the NC group, the $SSD_{<7\ years}$ group showed the best MAE on the good-hearing side compared with all three other directions [$\chi^2(3) = 13.6$, $p = 0.004$; good vs. poor: $p < 0.001$; good vs. front: $p < 0.001$; good vs. back: $p = 0.048$], but in the other two subgroups with over 10 years of SSD, MAE values on the good-hearing side were not significantly superior to the MAE values on the poor-hearing side and back ($p > 0.05$) (**Figure 3B**).

The AI values were calculated in each group to represent the difference in sound localization performance between good- and poor-hearing sides (**Table 2**). AI values were significantly smaller in the SSD group than in the NC group (Wilcoxon rank sum test, $p = 0.046$), meaning that localization performance between the good- and poor-hearing sides was more symmetric in the SSD group than in the acutely plugged controls. When further compared between the NC group and SSD subgroups, AI values differed significantly across groups [Kruskal–Wallis $\chi^2(3) = 9.2$, $p = 0.027$], with significantly smaller AI values in the $SSD_{43-46\ years}$ group than in the NC group ($p = 0.042$) and $SSD_{<7\ years}$ group ($p = 0.033$).

Localization Performance and Clinical Factors

In the SSD group, a partial correlation analysis was performed to examine whether the age at onset or the duration of SSD affected the sound localization performance. While MAE values in the front and back directions were not related to either the duration

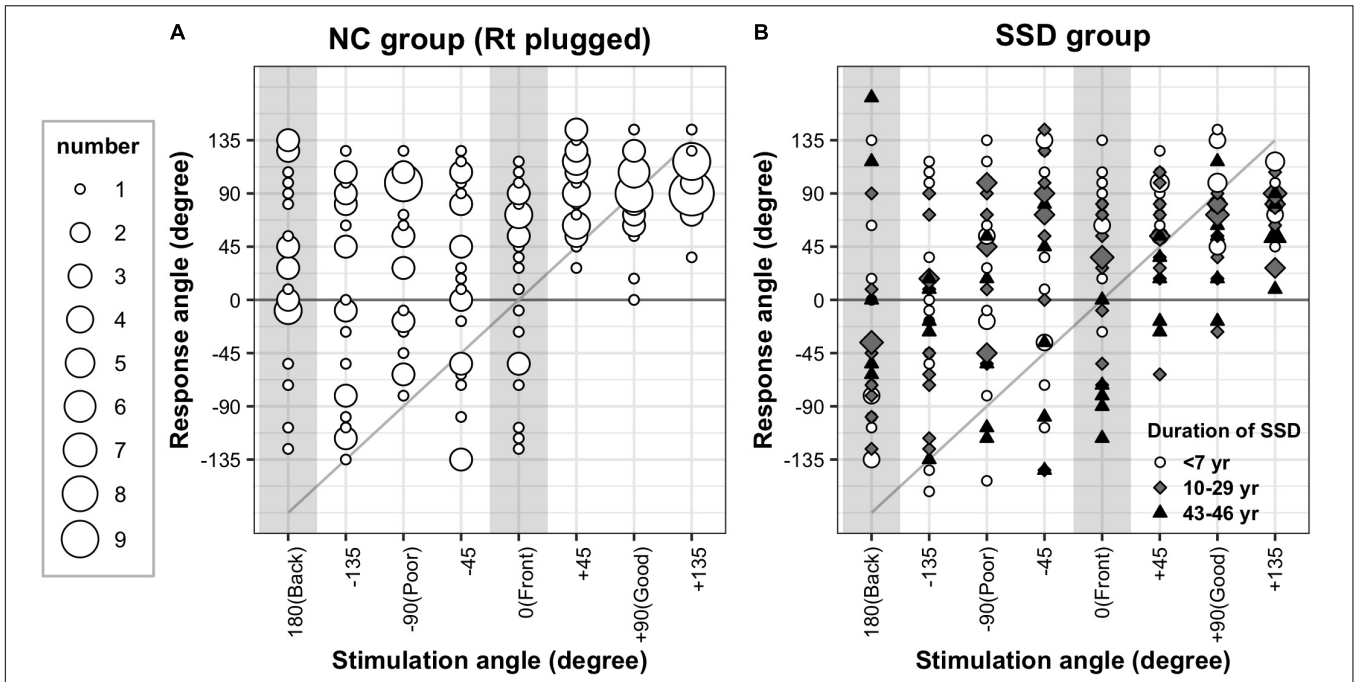

FIGURE 2 | Sound localization test results. Response angles were plotted by stimulation angle in the acutely plugged NC **(A)** and SSD **(B)** groups. Both groups showed response bias toward the intact (open) ear side. Upon all responses, 68.2 and 67.3% were recorded on the intact ear side in the simulated NC and SSD groups, respectively.

TABLE 2 | Mean absolute error values in four directions and asymmetry index values in the SSD and NC groups (mean ± SD).

	Mean absolute error (|stimulus – response|, degree)				AI
Group	**Good-hearing side (45°, 90°, 135°)**	**Poor-hearing side (−45°, −90°, −135°)**	**Front (0°)**	**Back (180°)**	
NC (left only, n = 23)	42.8 ± 16.6	105.0 ± 42.3	97.4 ± 41.4	92.3 ± 45.7	0.42 ± 0.28
SSD (n = 26)	60.1 ± 23.1**	94.5 ± 32.1	112.0 ± 25.5	72.0 ± 32.5	0.26 ± 0.30*
$SSD_{<7\ years}$ (n = 11)	49.1 ± 17.7	108.0 ± 29.9	108.0 ± 31.9	81.0 ± 41.4	0.41 ± 0.24
$SSD_{10-29\ years}$ (n = 10)	67.2 ± 23.6*	90.0 ± 32.4	118.0 ± 20.5	70.2 ± 19.8	0.20 ± 0.35
$SSD_{43-46\ years}$ (n = 5)	70.2 ± 26.8*	73.8 ± 27.7	112.0 ± 20.7	55.8 ± 29.4	0.02 ± 0.14*

SSD, single-sided deafness; NC, normal control; AI, asymmetry index.
The symbols "" and "**" denote statistically significant differences ($p < 0.05$ and $p < 0.01$, respectively) from the NC group.*

or age at onset of SSD ($p > 0.05$), MAE values from the poor-hearing side showed a significant correlation with both factors (**Figure 4A**). In cases of SSD onset at a younger age, localization ability was better (smaller angle difference) on the poor-hearing side ($r_s = 0.439$, $p = 0.028$). On the good-hearing side, a negative trend showing worse performance with SSD onset at a younger age was found ($p = 0.124$). As expected with the strong negative correlation between onset age and duration of SSD, a reverse relationship was found with the duration of SSD. When the duration of SSD increased, localization performance improved on the poor-hearing side ($r_s = -0.527$, $p = 0.007$), and tended to deteriorate on the good-hearing side ($r_s = 0.358$, $p = 0.079$). As a result, the difference in sound localization ability between the good- and poor-hearing sides was the largest when the duration of SSD was the shortest (and the age onset of SSD was the latest), and the performance asymmetry between the good- and poor-hearing sides decreased as the duration of SSD increased (and with a younger age of SSD onset). This change in performance asymmetry was confirmed with the analysis of AI in this group. The AI value was smallest when the onset age of SSD was the youngest ($p = 0.036$, $r_s = 0.421$, **Figure 4B**, left panel) and the duration of the SSD was the longest ($p = 0.018$, $r_s = -0.470$, **Figure 4B**, right panel).

Auditory Cortex and Asymmetry Index

For analyses of the cortical structural indices, the SSD-R and SSD-L groups were not pooled considering the inherent structural/functional asymmetry of the brain. Across the SSD-R, SSD-L, and NC groups, there was no significant difference in nCV in any of the six ROIs (one-way ANOVA on trimmed means, $p > 0.05$). In both the SSD-R and SSD-L groups, nCV in all six ROIs did not reveal a significant relationship with either the onset age of SSD or duration of SSD (nonparametric partial correlation controlling age, $p > 0.05$). In the SSD-R group, greater volumes

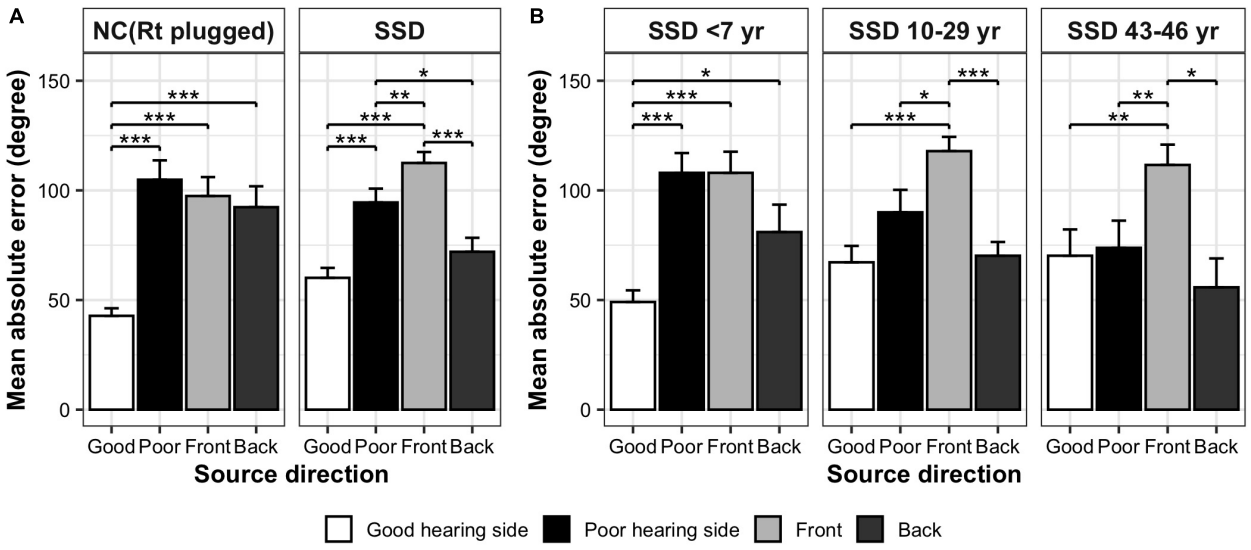

FIGURE 3 | Comparison of MAE values in four directions (mean ± SE). **(A)** NC (acutely plugged) group and SSD group. **(B)** SSD subgroups with different duration of SSD. ***$p < 0.001$; **$p < 0.01$; *$p < 0.05$.

in the right posterior STG ($r_s = -0.855$, $p = 0.002$) and the left PT ($r_s = -0.765$, $p = 0.010$) were associated with smaller AI values (**Figure 5**), whereas the aging effect was removed. In other words, the greater the GM volume of these regions, the more symmetric the localization performance between the impaired and intact hearing sides in this group. In the SSD-L group and NC group, nCV was not related to AI in any of the six ROIs.

DISCUSSION

Auditory Source Localization Using Level Cues Improved on the Deaf Ear Side and Deteriorated on the Intact Ear Side in Single-Sided Deafness Patients

Changes in sound localization behavior in the SSD group observed in the present study can be summarized as follows: (1) In the SSD group, localization ability using level cues on the intact ear side was worse than that in the acutely plugged controls (**Table 2**) and tended to deteriorate with longer duration of SSD. (2) On the impaired ear side of the SSD group, localization performance improved with longer duration/younger age onset of SSD (**Figure 4A**). (3) As a result, functional asymmetry between intact and impaired sides decreased in the SSD group, and the maximum decrease was observed with the longest duration/the youngest age onset of SSD (**Table 2** and **Figure 4B**).

For binaural listeners, interaural time and level differences are the two most reliable sources for azimuthal localization, and monaural spectral cues play an auxiliary role, such as discriminating sources in the cone of confusion (Risoud et al., 2018). The monaural spectral cue is generated by the filtering action of the pinna (and head and torso) and composed of high-frequency information. This head-related transfer function is specific to each individual, as the morphology of the body and the pinna varies greatly between individuals. Monaural listeners also heavily rely on monaural level cues, which are generally ignored by binaural listeners (Van Wanrooij, 2004). When the sound source originates from the deaf side, the perceived intensity relates to its azimuth, as the subject's head attenuates the perceived sound level. Adaptation of this level cue can be measured when the stimulus level is fixed (Van Wanrooij, 2004). Using a 1 kHz sound at a fixed stimulus level, the localization performance measured in this study can reflect the monaural strategy of sound localization using level cues.

On the intact ear side, both the SSD and simulated NC groups showed clear response bias toward the intact (open) ear side (**Figure 2**), but the MAE values were significantly smaller in the NC group with simulated hearing loss (**Table 2**). The decreased performance in the SSD group on this side seemed to be associated with SSD experience, a finding supported by the tendency toward increased MAE with increased SSD duration (**Figure 4A**, right side). The effect of SSD experience was clear on the side with impaired hearing, a finding supported by significant correlations with clinical factors. Their MAE was the best (smallest) when the duration of SSD was the longest or the age at the onset of SSD was the youngest. The AI was calculated by combining the behavioral changes on the intact and impaired sides that changed in opposite ways to represent both factors as a single measure. As expected, **Figure 4A** shows that the functional asymmetry between the intact and impaired sides decreased with a longer duration/earlier age at the onset of SSD, with a moderate correlation (**Figure 4B**). A longer duration of SSD (Slattery and Middlebrooks, 1994; Liu et al., 2018), a younger age at the onset of SSD (Firszt et al., 2015, 2017), and both together (Nelson et al., 2019) have been previously associated with improved localization ability in SSD patients. In recent studies that measured localization behavior in SSD

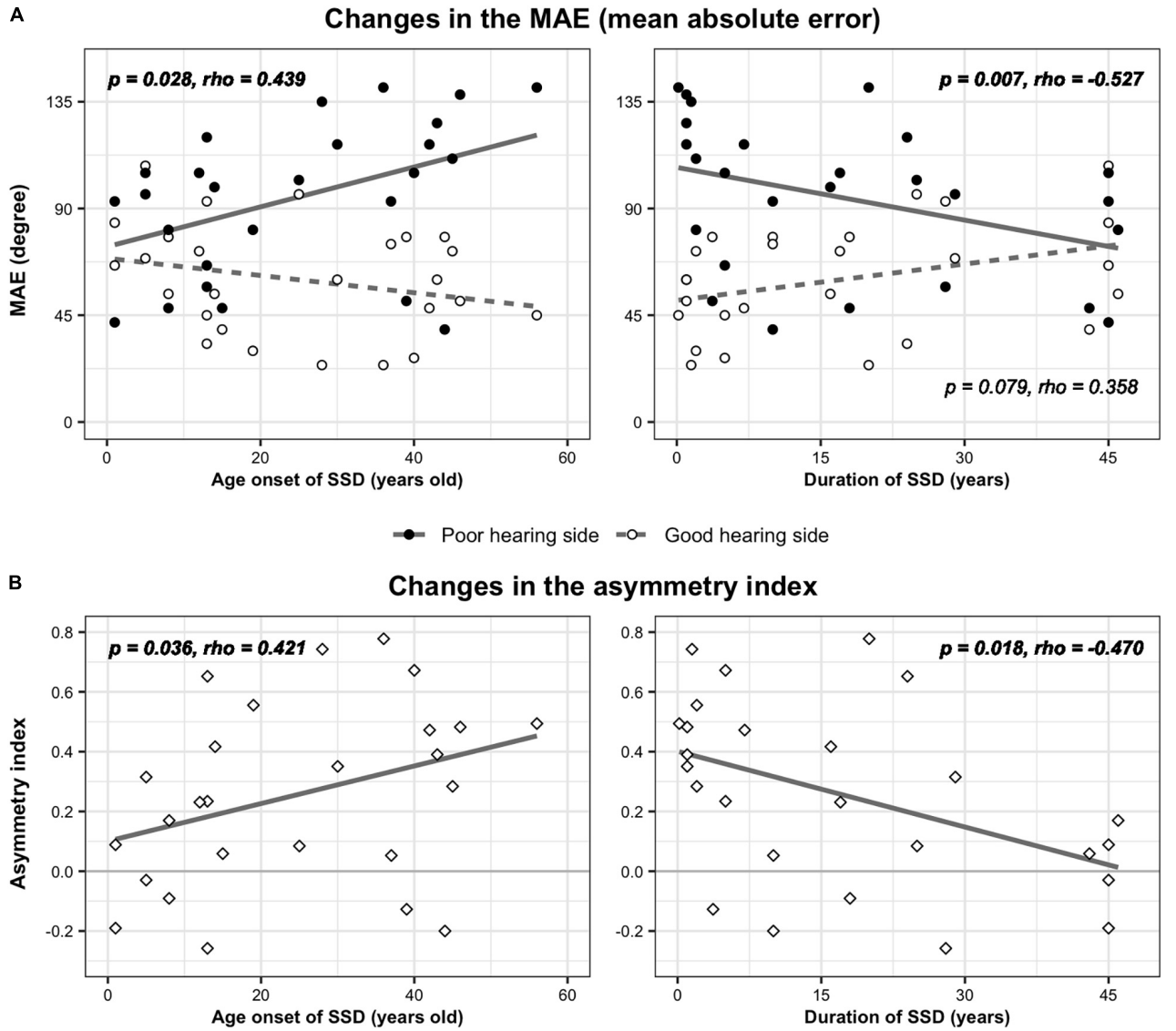

FIGURE 4 | Changes in localization parameters with age of SSD onset and SSD duration. **(A)** MAE values of three speakers on the good- and poor-hearing sides were plotted as a function of onset age (left) and duration (right) of SSD. **(B)** The asymmetry index, which represents the relative difference in weighted MAE values between the good- and poor-hearing sides, was also plotted by the onset age (left) and duration (right) of SSD.

patients, those with the best localization performance were those who had more symmetrical abilities on the intact/impaired sides (Agterberg et al., 2012; Nelson et al., 2019). The results of this study replicate those of previous studies showing that auditory spatial strategy changes to help patients cope with single-sided hearing, which attenuates binaural difference cues. However, the magnitude and quality of change varies according to the testing method, the stimuli used, and the audiologic profile of subjects. Behavioral changes are related to the duration and/or onset of unilateral hearing. Overall, the findings suggest adaptive changes in behavior in response to prolonged experience with unilateral hearing and/or developmental plasticity. The demographic profile of our patient cohort did not allow us to differentiate the effects of those two clinical variables. This should be further addressed in future studies with a greater number of patients.

Gray Matter Volume in the Posterior Part of the Auditory Cortex Is Associated With Auditory Spatial Abilities in Right Single-Sided Deafness Patients

To pursue the biological substrate that grounds the above observed behavioral changes, the cortical structure of the parcellated auditory cortex was compared to the behavioral performance in the SSD group. The AI was used as a composite index representing behavioral changes across impaired and intact sides. Right and left SSDs were separately analyzed considering

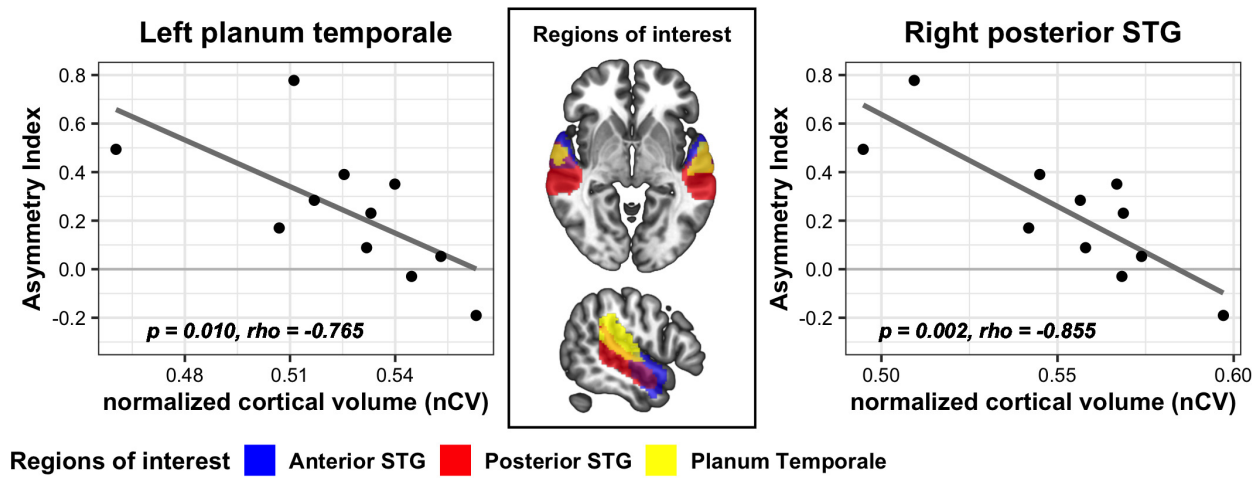

FIGURE 5 | Significant correlation between nCV and AI values in two ROIs of the SSD-R group. STG, superior temporal gyrus.

the functional/structural asymmetry of the auditory cortex. As a result, the GM volume in the right posterior STG and the left PT were strongly related to the AI in the right SSD patients; a greater volume in those areas was related to more symmetric localization performance between the good-/poor-hearing sides.

Auditory spatial processing is mediated by the dorsal stream of the cortical auditory pathway. From the primary auditory cortex, the dorsal stream is directed posteriorly *via* the PT and dorsally to the inferior parietal lobule, premotor cortex, and dorsolateral prefrontal cortex, the latter of which is involved in top-down modulation to the primary and nonprimary auditory regions (van der Heijden et al., 2019). The posterior auditory cortex, including the PT, has been traditionally implicated in spatial processing, especially to the sound source in the contralateral hemisphere (Ahveninen et al., 2014; Callan et al., 2015; van der Heijden et al., 2018).

Compared to bilateral deafness, SSD is a more recent focus of dedicated research, and less is known about neuroplasticity following unilateral hearing loss (Vanderauwera et al., 2020). Although the overall number of studies is small and the audiologic profiles included are diverse, neural changes associated with asymmetric hearing have been observed in both functional and structural domains and are related to clinical/audiologic variables such as the duration of SSD (Yang et al., 2014; Wang et al., 2016), age at SSD onset (Lee et al., 2020), severity of hearing impairment (Wang et al., 2016; Xie et al., 2019), and side (Khosla et al., 2003; Burton et al., 2012; Zhang et al., 2016; Heggdal et al., 2019; Xie et al., 2019; Han et al., 2021). However, findings are scarce regarding how the observed neuroplasticity in asymmetric hearing is related to binaural auditory performance, such as sound localization ability. In one recent fMRI study of subjects with varying degrees of asymmetric hearing loss (Vannson et al., 2020), changes in auditory localization ability were associated with neural plasticity in the posterior auditory cortex, where structural correlation with localization performance was also observed in this study. Neuroimaging studies with sound localization tasks have not yet been reported, and neuroplasticity related to auditory spatial performance changes should be further elucidated with consideration of clinical variables such as the degree, duration, and onset of hearing asymmetry.

This study found cortical structural changes in relation to auditory spatial behavior in the SSD-R group only. Ear-specific neuroplasticity in patients with asymmetric hearing has been reported, yet the findings are controversial. Recent neuroimaging studies have shown a clear impact of the deafness side, with a greater degree of neural plasticity for right-sided hearing loss (Cañete et al., 2019; Heggdal et al., 2020; Han et al., 2021). On the other hand, others reported more extensive neurofunctional reorganization in individuals with left-sided hearing loss (Khosla et al., 2003; Hanss et al., 2009; Zhang et al., 2016). In a series of studies, Zhang et al. (2018a,b) have found different patterns of changes in resting-state connectivity as a function of side of hearing loss. Taken together, previous literature indicates that neuroplastic changes can vary depending on the neural indices applied to measure and the way to examine behavioral performance. In our study, we measured auditory spatial ability, which is known to be dominantly processed in the right hemisphere. Thus, we assumed that in the SSD-R group, auditory input would be efficiently delivered to the right auditory cortex *via* the intact left ear. Accordingly, the relatively preserved sensory input might incur more extensive structural changes in the auditory cortex in this group.

The behavioral changes in auditory spatial ability related to the experience of asymmetric hearing have motivated the development of sound localization training programs and devices for patients with asymmetric hearing loss (Firszt et al., 2015; Fletcher and Zgheib, 2020). A recent study with an animal model reported a specific role of auditory cortical plasticity in sound localization training (Bajo et al., 2019). Improved knowledge regarding the behavioral implications of neuroplasticity in the human auditory cortex would help to improve the effectiveness of those rehabilitative options.

CONCLUSION

In SSD patients, sound localization ability changes in relation to the onset/duration of SSD and prolonged experience/earlier onset of SSD were related to a more symmetric performance of using the monaural level cue across the intact and impaired sides. A significant structural correlation of the posterior auditory region to the adaptive behavioral change in sound localization suggests that neuroplasticity occurs in the cortical areas for auditory spatial processing in subjects who suffer from deficits in function due to asymmetric auditory input.

DATA AVAILABILITY STATEMENT

The raw data supporting the conclusions of this article is available from the corresponding author on reasonable request.

ETHICS STATEMENT

The studies involving human participants were reviewed and approved by the Institutional Review Board of the Hallym University Sacred Heart Hospital. The patients/participants provided their written informed consent to participate in this study.

AUTHOR CONTRIBUTIONS

JHK and H-JL contributed to the conception and design of the study. JHK and LS collected and analyzed the data. H-JL and JB contributed to the final version of the manuscript. All authors discussed the result and contributed to writing the manuscript.

FUNDING

This study was supported by the Basic Science Research Program through the National Research Foundation of Korea funded by the Korean Government (NRF-2019R1A2B5B01070129); a Center for Women in Science, Engineering and Technology (WISET) grant funded by the Ministry of Science and ICT (MSIT) under the Program for Returners into R&D (WISET-2020-470) and the Hallym University Research Fund.

REFERENCES

Agterberg, M. J. H., Snik, A. F. M., Hol, M. K. S., Van Wanrooij, M. M., and Van Opstal, A. J. (2012). Contribution of monaural and binaural cues to sound localization in listeners with acquired unilateral conductive hearing loss: improved directional hearing with a bone-conduction device. *Hear. Res.* 286, 9–18. doi: 10.1016/j.heares.2012.02.012

Ahveninen, J., Kopčo, N., and Jääskeläinen, I. P. (2014). Psychophysics and neuronal bases of sound localization in humans. *Hear. Res.* 307, 86–97. doi: 10.1016/j.heares.2013.07.008

Ashburner, J., and Friston, K. J. (2000). Voxel-based morphometry—the methods. *Neuroimage* 11, 805–821. doi: 10.1006/nimg.2000.0582

Bajo, V. M., Nodal, F. R., Korn, C., Constantinescu, A. O., Mann, E. O., Boyden, E. S., et al. (2019). Silencing cortical activity during sound-localization training impairs auditory perceptual learning. *Nat. Commun.* 10:3075. doi: 10.1038/s41467-019-10770-4

Briley, P. M., Kitterick, P. T., and Summerfield, A. Q. (2013). Evidence for opponent process analysis of sound source location in humans. *JARO* 14, 83–101. doi: 10.1007/s10162-012-0356-x

Burton, H., Firszt, J. B., Holden, T., Agato, A., and Uchanski, R. M. (2012). Activation lateralization in human core, belt, and parabelt auditory fields with unilateral deafness compared to normal hearing. *Brain Res.* 1454, 33–47. doi: 10.1016/j.brainres.2012.02.066

Callan, A., Callan, D., and Ando, H. (2015). An fMRI study of the ventriloquism effect. *Cereb. Cortex* 25, 4248–4258. doi: 10.1093/cercor/bhu306

Cañete, O. M., Purdy, S. C., Brown, C. R. S., Neeff, M., and Thorne, P. R. (2019). Impact of unilateral hearing loss on behavioral and evoked potential measures of auditory function in adults. *J. Am. Acad. Audiol.* 30, 564–578. doi: 10.3766/jaaa.17096

Cardin, V. (2016). Effects of aging and adult-onset hearing loss on cortical auditory regions. *Front. Neurosci.* 10:199. doi: 10.3389/fnins.2016.00199

Deouell, L. Y., Heller, A. S., Malach, R., D'Esposito, M., and Knight, R. T. (2007). Cerebral responses to change in spatial location of unattended sounds. *Neuron* 55, 985–996. doi: 10.1016/j.neuron.2007.08.019

Derey, K., Valente, G., de Gelder, B., and Formisano, E. (2016). Opponent coding of sound location (Azimuth) in planum temporale is robust to sound-level variations. *Cereb. Cortex* 26, 450–464. doi: 10.1093/cercor/bhv269

Eckert, M. A., Cute, S. L., Vaden, K. I., Kuchinsky, S. E., and Dubno, J. R. (2012). Auditory cortex signs of age-related hearing loss. *JARO* 13, 703–713. doi: 10.1007/s10162-012-0332-5

Eckert, M. A., Vaden, K. I., and Dubno, J. R. (2019). Age-related hearing loss associations with changes in brain morphology. *Trends Hear.* 23:233121651985726. doi: 10.1177/2331216519857267

Firszt, J. B., Reeder, R. M., Dwyer, N. Y., Burton, H., and Holden, L. K. (2015). Localization training results in individuals with unilateral severe to profound hearing loss. *Hear. Res.* 319, 48–55. doi: 10.1016/j.heares.2014.11.005

Firszt, J. B., Reeder, R. M., and Holden, L. K. (2017). Unilateral hearing loss: understanding speech recognition and localization variability–implications for cochlear implant candidacy. *Ear Hear.* 38, 159–173. doi: 10.1097/aud.0000000000000380

Fletcher, M. D., and Zgheib, J. (2020). Haptic sound-localisation for use in cochlear implant and hearing-aid users. *Sci. Rep.* 10:14171. doi: 10.1038/s41598-020-70379-2

Good, C. D., Johnsrude, I. S., Ashburner, J., Henson, R. N. A., Friston, K. J., and Frackowiak, R. S. J. (2001). A voxel-based morphometric study of ageing in 465 normal adult human brains. *Neuroimage* 14, 21–36. doi: 10.1006/nimg.2001.0786

Han, J.-H., Lee, J., and Lee, H.-J. (2021). Ear-specific hemispheric asymmetry in unilateral deafness revealed by auditory cortical activity. *Front. Neurosci.* 15:698718. doi: 10.3389/fnins.2021.698718

Hanss, J., Veuillet, E., Adjout, K., Besle, J., Collet, L., and Thai-Van, H. (2009). The effect of long-term unilateral deafness on the activation pattern in the auditory cortices of French-native speakers: influence of deafness side. *BMC Neurosci.* 10:23. doi: 10.1186/1471-2202-10-23

Heggdal, P. O. L., Aarstad, H. J., Brännström, J., Vassbotn, F. S., and Specht, K. (2019). An fMRI-study on single-sided deafness: spectral-temporal properties and side of stimulation modulates hemispheric dominance. *Neuroimage* 24:101969. doi: 10.1016/j.nicl.2019.101969

Heggdal, P. O. L., Larsen, K. S., Brännström, J., Aarstad, H. J., and Specht, K. (2020). Reduced grey- and white matter volumes due to unilateral hearing loss following treatment for vestibular schwannoma. *Heliyon* 6:e05658. doi: 10.1016/j.heliyon.2020.e05658

Husain, F. T., Medina, R. E., Davis, C. W., Szymko-Bennett, Y., Simonyan, K., Pajor, N. M., et al. (2011). Neuroanatomical changes due to hearing loss and chronic tinnitus: a combined VBM and DTI study. *Brain Res.* 1369, 74–88. doi: 10.1016/j.brainres.2010.10.095

Khosla, D., Ponton, C. W., Eggermont, J. J., Kwong, B., Dort, M., and Vasama, J.-P. (2003). Differential ear effects of profound unilateral deafness on the adult human central auditory system. *JARO* 4, 235–249. doi: 10.1007/s10162-002-3014-x

Kim, S. (2015). ppcor: an R package for a fast calculation to semi-partial correlation coefficients. *Commun. Stat. Appl. Methods* 22, 665–674. doi: 10.5351/CSAM.2015.22.6.665

Kumpik, D. P., and King, A. J. (2019). A review of the effects of unilateral hearing loss on spatial hearing. *Hear. Res.* 372, 17–28. doi: 10.1016/j.heares.2018.08.003

Lee, H.-J., Smieja, D., Polonenko, M. J., Cushing, S. L., Papsin, B. C., and Gordon, K. A. (2020). Consistent and chronic cochlear implant use partially reverses cortical effects of single sided deafness in children. *Sci. Rep.* 10:21526. doi: 10.1038/s41598-020-78371-6

Liu, Y.-W., Cheng, X., Chen, B., Peng, K., Ishiyama, A., and Fu, Q.-J. (2018). Effect of tinnitus and duration of deafness on sound localization and speech recognition in noise in patients with single-sided deafness. *Trends Hear.* 22:233121651881380. doi: 10.1177/2331216518813802

Mair, P., and Wilcox, R. (2020). Robust statistical methods in R using the WRS2 package. *Behav. Res.* 52, 464–488. doi: 10.3758/s13428-019-01246-w

Nelson, E., Reeder, R. M., Holden, L. K., and Firszt, J. B. (2019). Front- and rear-facing horizontal sound localization results in adults with unilateral hearing loss and normal hearing. *Hear. Res.* 372, 3–9. doi: 10.1016/j.heares.2018.03.016

Pastore, M. T., Natale, S. J., Clayton, C., Dorman, M. F., Yost, W. A., and Zhou, Y. (2020). Effects of head movements on sound-source localization in single-sided deaf patients with their cochlear implant on versus off. *Ear Hear.* 41, 1660–1674. doi: 10.1097/AUD.0000000000000882

Pavani, F., Macaluso, E., Warren, J. D., Driver, J., and Griffiths, T. D. (2002). A common cortical substrate activated by horizontal and vertical sound movement in the human brain. *Curr. Biol.* 12, 1584–1590. doi: 10.1016/S0960-9822(02)01143-0

Risoud, M., Hanson, J.-N., Gauvrit, F., Renard, C., Lemesre, P.-E., Bonne, N.-X., et al. (2018). Sound source localization. *Eur. Ann. Otorhinolaryngol. Head Neck Dis.* 135, 259–264. doi: 10.1016/j.anorl.2018.04.009

Selker, R., Love, J., and Dropmann, D. (2020). *jmv: The "jamovi" Analyses*. Available online at: https://CRAN.R-project.org/package=jmv (accessed June 30, 2020).

Shub, D. E., Carr, S. P., Kong, Y., and Colburn, H. S. (2008). Discrimination and identi?cation of azimuth using spectral shapea). *J. Acoust. Soc. Am.* 124:10.

Slattery, W. H., and Middlebrooks, J. C. (1994). Monaural sound localization: acute versus chronic unilateral impairment. *Hear. Res.* 75, 38–46. doi: 10.1016/0378-5955(94)90053-1

Snapp, H. A., and Ausili, S. A. (2020). Hearing with one ear: consequences and treatments for profound unilateral hearing loss. *J. Clin. Med.* 9:1010. doi: 10.3390/jcm9041010

Van de Heyning, P., Távora-Vieira, D., Mertens, G., Van Rompaey, V., Rajan, G. P., Müller, J., et al. (2016). Towards a unified testing framework for single-sided deafness studies: a consensus paper. *Audiol. Neurotol.* 21, 391–398. doi: 10.1159/000455058

van der Heijden, K., Rauschecker, J. P., de Gelder, B., and Formisano, E. (2019). Cortical mechanisms of spatial hearing. *Nat. Rev. Neurosci.* 20, 609–623. doi: 10.1038/s41583-019-0206-5

van der Heijden, K., Rauschecker, J. P., Formisano, E., Valente, G., and de Gelder, B. (2018). Active sound localization sharpens spatial tuning in human primary auditory cortex. *J. Neurosci.* 38, 8574–8587. doi: 10.1523/JNEUROSCI.0587-18.2018

van der Zwaag, W., Gentile, G., Gruetter, R., Spierer, L., and Clarke, S. (2011). Where sound position influences sound object representations: a 7-T fMRI study. *Neuroimage* 54, 1803–1811. doi: 10.1016/j.neuroimage.2010.10.032

Van Wanrooij, M. M. (2004). Contribution of head shadow and pinna cues to chronic monaural sound localization. *J. Neurosci.* 24, 4163–4171. doi: 10.1523/JNEUROSCI.0048-04.2004

Vanderauwera, J., Hellemans, E., and Verhaert, N. (2020). Research insights on neural effects of auditory deprivation and restoration in unilateral hearing loss: a systematic review. *J. Clin. Med.* 9:812. doi: 10.3390/jcm9030812

Vannson, N., Strelnikov, K., James, C. J., Deguine, O., Barone, P., and Marx, M. (2020). Evidence of a functional reorganization in the auditory dorsal stream following unilateral hearing loss. *Neuropsychologia* 149:107683. doi: 10.1016/j.neuropsychologia.2020.107683

Vincent, C., Arndt, S., Firszt, J. B., Fraysse, B., Kitterick, P. T., Papsin, B. C., et al. (2015). Identification and evaluation of cochlear implant candidates with asymmetrical hearing loss. *Audiol. Neurotol.* 20, 87–89. doi: 10.1159/000380754

Wang, X., Xu, P., Li, P., Wang, Z., Zhao, F., Gao, Z., et al. (2016). Alterations in gray matter volume due to unilateral hearing loss. *Sci. Rep.* 6:25811. doi: 10.1038/srep25811

Xie, X., Liu, Y., Han, X., Liu, P., Qiu, H., Li, J., et al. (2019). Differences in intrinsic brain abnormalities between patients with left- and right-sided long-term hearing impairment. *Front. Neurosci.* 13:206. doi: 10.3389/fnins.2019.00206

Yang, M., Chen, H.-J., Liu, B., Huang, Z.-C., Feng, Y., Li, J., et al. (2014). Brain structural and functional alterations in patients with unilateral hearing loss. *Hear. Res.* 316, 37–43. doi: 10.1016/j.heares.2014.07.006

Zatorre, R. J., and Penhune, V. B. (2001). Spatial localization after excision of human auditory cortex. *J. Neurosci.* 21, 6321–6328. doi: 10.1523/JNEUROSCI.21-16-06321.2001

Zhang, G.-Y., Yang, M., Liu, B., Huang, Z.-C., Li, J., Chen, J.-Y., et al. (2016). Changes of the directional brain networks related with brain plasticity in patients with long-term unilateral sensorineural hearing loss. *Neuroscience* 313, 149–161. doi: 10.1016/j.neuroscience.2015.11.042

Zhang, Y., Mao, Z., Feng, S., Liu, X., Zhang, J., and Yu, X. (2018a). Monaural-driven functional changes within and beyond the auditory cortical network: evidence from long-term unilateral hearing impairment. *Neuroscience* 371, 296–308. doi: 10.1016/j.neuroscience.2017.12.015

Zhang, Y., Mao, Z., Feng, S., Wang, W., Zhang, J., and Yu, X. (2018b). Convergent and divergent functional connectivity patterns in patients with long-term left-sided and right-sided deafness. *Neurosci. Lett.* 665, 74–79. doi: 10.1016/j.neulet.2017.11.050

Zündorf, I. C., Karnath, H.-O., and Lewald, J. (2014). The effect of brain lesions on sound localization in complex acoustic environments. *Brain* 137, 1410–1418. doi: 10.1093/brain/awu044

Conflict of Interest: The authors declare that the research was conducted in the absence of any commercial or financial relationships that could be construed as a potential conflict of interest.

frontiers in Human Neuroscience

ORIGINAL RESEARCH
published: 12 November 2021
doi: 10.3389/fnhum.2021.707014

Effect of Emissary Vein on Hemodynamics of the Transverse-Sigmoid Sinus Junction

Xiaoyu Qiu[1†], Pengfei Zhao[1†], Xiaoshuai Li[1], Heyu Ding[1], Han Lv[1], Zhenxia Mu[2], Xiaofei Xue[2], Shusheng Gong[3], Zhenghan Yang[1], Bin Gao[2] and Zhenchang Wang[1]**

[1] Department of Radiology, Beijing Friendship Hospital, Capital Medical University, Beijing, China, [2] Faculty of Environment and Life, Beijing University of Technology, Beijing, China, [3] Department of Otolaryngology Head and Neck Surgery, Beijing Friendship Hospital, Capital Medical University, Beijing, China

Objective: To investigate the effect of the blood flow direction and afflux location of emissary veins (EVs) on the hemodynamics of the transverse-sigmoid sinus (TS-SS) junction.

Methods: A patient-specific geometric model was constructed using computed tomography venography (CTV) and 4D flow MR data from a venous pulsatile tinnitus (PT) patient. New EV models were assembled with the afflux at the superior, middle and inferior portions of the SS from the original model, and inlet and outlet directions were applied. Computational fluid dynamics (CFD) simulation was performed to analyze the wall pressure and flow pattern of the TS-SS junction in each condition.

Results: Compared to the model without EVs, the wall pressure was greatly increased in models with inlet flow and greatly decreased in models with outlet flow. The more closely the EV approached the TS-SS, the larger the pressure in models with inlet flow, and the smaller the pressure in models with outlet flow. The flow streamline in the lateral part of the TS-SS junction was smooth in all models. The streamlines in the medial part were regular spirals in outlet models and chaotic in inlet models. The streamlines showed no obvious changes regardless of afflux location. The velocity at the TS-SS junction of inlet models were uniform, medium-low flow rate, while in control and outlet models were the lateral high flow rate and the central low flow rate.

Conclusion: The flow direction and afflux location of EVs affect the hemodynamics of the TS-SS junction, which may influence the severity of PT.

Keywords: pulsatile tinnitus, emissary veins, medical imaging, computational fluid dynamics, hemodynamics

OPEN ACCESS

Edited by:
Jae-Jin Song, Seoul National University Bundang Hospital, South Korea

Reviewed by:
R. Shane Tubbs, Tulane University, United States
Sang-Yeon Lee, Seoul National University Hospital, South Korea

***Correspondence:**
Bin Gao
gaobin@bjut.edu.cn
Zhenchang Wang
cjr.wzhch@vip.163.com

[†] *These authors have contributed equally to this work*

Specialty section:
This article was submitted to Sensory Neuroscience, a section of the journal Frontiers in Human Neuroscience

Received: *08 May 2021*
Accepted: *05 October 2021*
Published: *12 November 2021*

Citation:
Qiu X, Zhao P, Li X, Ding H, Lv H, Mu Z, Xue X, Gong S, Yang Z, Gao B and Wang Z (2021) Effect of Emissary Vein on Hemodynamics of the Transverse- Sigmoid Sinus Junction. Front. Hum. Neurosci. 15:707014. doi: 10.3389/fnhum.2021.707014

INTRODUCTION

Pulsatile tinnitus (PT) is a bothersome and not infrequent condition with vascular origins; this condition, mostly occurs in childbearing women. After a rigorous examination, venous origins are most commonly found (Lyu et al., 2018). In recent years, the newly treatable causes, innovative therapeutic procedures and possible mechanisms of venous PT have attracted a great deal of

attention. The transverse-sigmoid sinus (TS-SS) junction has been reported as the most commonly involved site in venous PT. Recent studies have implied that venous PT may be generated by a combination of multiple vascular, skeletal and pressure factors (Eisenman et al., 2018). The roles of TS stenosis (Hewes et al., 2020), SS diverticulum (Lansley et al., 2017), venous outflow dominance, SS wall dehiscence (Zhao et al., 2016) and increased intracranial pressure (Funnell et al., 2018; Onder, 2018) have been well investigated. Increased wall pressure and a turbulent flow pattern at the TS-SS junction are thought to be associated with venous PT (Amans et al., 2018; Li et al., 2018; Mu et al., 2020), which implies that any procedure changing the hemodynamics in this area may alleviate or worsen the sound.

Emissary veins (EVs) are valveless channels between the dural venous sinuses and extracranial venous structures, although most of EVs are inflow, bidirectional flow and turbulence are possible under an increase in intracranial pressure (Mortazavi et al., 2012; Reardon and Raghavan, 2016). Most reports concerning EVs relate to the possibility of intraoperative iatrogenic bleeding (Ozen and Sahin, 2020). Three EVs communicate with the TS-SS junction or SS: the mastoid EV (MEV), the petrosquamosal sinus and the posterior condylar EV. These veins are found in more than 80% (Pekcevik et al., 2014; Gulmez Cakmak et al., 2019; Ozen and Sahin, 2020), 11.1% (Pekala et al., 2018), and 76.5% (Pekcevik et al., 2014) of the population, respectively, and their diameter varies from less than 1 mm to more than 5 mm. All three have been reported as causes of PT (Lambert and Cantrell, 1986; Lee et al., 2013; Liu et al., 2013), and the sound may be totally eliminated after ligation. However, the curative effect of EV ligation against PT is not stable in clinical practice. To our knowledge, studies on this topic are rare, and all of them are case reports. The roles of EVs in the occurrence of PT have not been investigated. It is important to explore which types of EVs may benefit from ligation for PT.

We speculate that EVs may result in the occurrence of PT. On the one hand, an abnormally enlarged EV may itself cause PT when presenting with both strong blood flow and a dehiscent wall along the mastoid air cells; on the other hand, it is more often for EVs to act as one of the most important factors to result in PT by changing the hemodynamics at the TS-SS junction (Kao et al., 2017). The effect of EVs may mainly depend on the direction and velocity of their blood flow and the location of the afflux. Thus, it is important to identify the roles of these factors in the changes on hemodynamics at the TS-SS junction to predict the effect of ligation.

Computational fluid dynamics (CFD) is an emerging technique to simulate hemodynamics in venous PT patients (Kao et al., 2017; Amans et al., 2018; Tian et al., 2019; Mu et al., 2020). This method utilizes computational processing to perform numerical analysis of fluid flow within three- dimensional (3D) models. These models can replicate patient-specific vascular segments by importing real geometrical information obtained by computed tomography venography (CTV) or magnetic resonance venography (MRV) into finite element analysis software (Markl et al., 2012).

CTV has been usually used to capture real vascular morphology (Narvid et al., 2011; Zhao et al., 2016), and 4D flow MR has the ability to capture accurate blood flow velocity and complex blood flow patterns *in vivo* (Kweon et al., 2016; Amans et al., 2018; Li et al., 2018). Through the combination of imaging examination and CFD analysis of individual finite element models, the simulation flow field can be visualized pictorially, and complex hemodynamic characteristics can be determined. However, CTV combined MR 4D-flow have not been adapted in CFD analysis.

In this study, based on CTV images and 4D flow MR velocity data of a patient with PT, 7 semipersonalized models were established, including an original model without EVs, 3 inlet EVs in the superior, middle and inferior portions of the SS, and 3 outlet EVs in the superior, middle and inferior portions of the SS. Steady-state CFD was used to investigate the hemodynamic effects of EV-related factors at the TS-SS junction. The wall pressure distribution, velocity streamlines and velocity difference at the TS-SS junction were calculated to assess the hemodynamic changes in the blood flow direction and afflux location of EVs at that junction. In this study, semi personalized simulation digital models were constructed based on multimodal image data to explore the influence of the EVs location and blood flow direction on the hemodynamics of TS-SS junction, so as to predict the possible role of EVs in PT.

MATERIALS AND METHODS

Participant

Research ethics board approval was obtained in our institution. This study was based on a 22-year-old female who presented with a 2-year history of left-sided PT. The symptom was eliminated by compressing the ipsilateral jugular vein. The results of physical examination and otoscopic and audiometric evaluation were unremarkable. CTV showed an enlarged left MEV about 2 mm in diameter, ipsilateral upstream TS stenosis and SS wall dehiscence. PT was not relieved after ligation of the MEV.

Imaging Features

Patient-specific raw CTV images were obtained using a 256-slice spiral CT scanner (Philips Medical Systems, Netherlands); the CTV data consisted of 231 slices acquired before ligation (512 × 512 pixels, 0.625 mm slice thickness) in Digital Imaging and Communications in Medicine format. Iodinated non-ionic contrast material was applied to display the lumens of the TS, SS, jugular vein, and large MEV on CTV images.

The patient underwent MRV and a 4D flow scan with a 3.0 T MR scanner (Philips, Ingenia, Netherlands). All visualization, assessment and interpretation of 4D flow data were performed using dedicated GT Flow 2.2.15 software (GyroTools, Switzerland).

Vascular Model Construction

CTV image files were imported into MIMICS 20.0 software (Materialise, Belgium) to construct a 3D model of the left TS

to jugular bulb containing the EV as original model, which was used to compare with the 3D model post-processed by 4D flow to verify the accuracy of CFD simulation; then a "ligation" model without EV was constructed as the control subject. Based on control subject, three new 20-cm-long and 2-mm-diameter EV models were built using Solidworks 2016 software (Dassault Systemes, United States). Due to the irregular shape of the patient's real EV, there might be additional confounding factors; therefore, semipersonalized EV models with regular shapes were simulated to control unrelated variables. The new finite element models were assembled at the superior, middle and inferior portions of SS, and the direction were set to inflow (group 1) and outflow (group 2). The presence of superior, middle, and inferior inlet EVs and the presence of superior, middle, inferior outlet EVs were named cases 1–6, respectively. Through image segmentation and 3D model creation, geometric models were obtained. The models were smoothed using Freeform and Geomagic software (Geomagic, United States). After processing, the surface geometries were saved in standard tessellation language format.

Computational Models and Simulations

The standard tessellation language format files were imported into Fluent 2019 R1 (ANSYS, Inc., Cecil Township, Pennsylvania, United States) for meshing; high quality polyhedral 3D meshing was successfully created. In order to confirm the adaptive grid size, the wall pressure was used as the criterion for the grid-independence test. The area of wall pressure was located at the TS-SS junction (**Figure 1**). A grid with less than 5% pressure error was considered acceptable. A maximum of 1013699 elements were developed, which was a sufficient number for this study. The element size of each case was set to a maximum of 0.2 mm. Four boundary layers were generated to resolve the flow field at the fluid-wall interface. The venous wall was assumed to be rigid and a no-slip boundary condition was applied. The blood was assumed to be a laminar and incompressible Newtonian fluid with a density of 1050 kg/m^3 and a viscosity of 0.0035 Pa/s. The constant inlet section was located at the TS of the model, and the boundary condition used the real blood flow velocity of 45 cm/s at the TS measured by 4D flow; the constant outlet was located at the jugular bulb, and the boundary condition was set to an absolute pressure of 0 pa. In the original model, since the real blood flow in the EV was observed as the outflow direction in 4D flow, the boundary condition was set to the real velocity of −20 cm/s measured by 4D flow. According to the flow directions prescribed by the study design, when the distal newly built EVs were used as inlets or outlets, the boundary conditions were ± 20 cm/s, respectively. The Navier-Stokes formula, solved with Fluent 2019 R1, was used as the governing equation for calculations. Based on the simulation results, several flow parameters were calculated and color-coded according to magnitude and distribution to evaluate the effects of model hemodynamics quantitatively. These parameters included wall pressure distribution, wall maximum pressure (P_{max}), wall average pressure (P_{avg}), velocity streamlines and distribution, maximum velocity (V_{max}) and average velocity (V_{avg}). The original model simulation only needed to obtain the velocity streamline, which was used to compare with the 4D flow results.

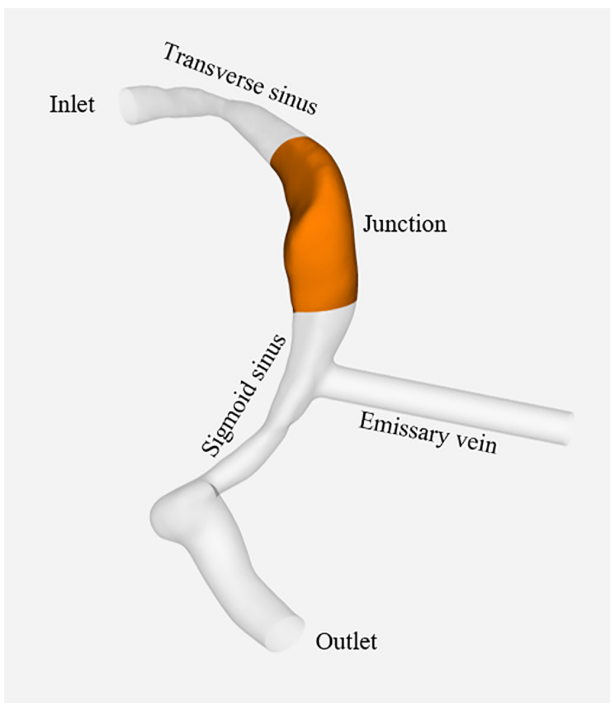

FIGURE 1 | Positions of inlet, TS, TS-SS junction, SS, EV, and outlet.

RESULTS

Comparison of Original Model Computational Fluid Dynamics Simulation and 4D Flow Results

Comparing the velocity streamline of the real 4D flow MR postprocessing model of the patient collected in this study with the streamline model obtained by CFD simulation, it was found that the blood flow pattern and velocity were consistent (**Figure 2**), which confirmed the accuracy of CFD simulation *in vivo* blood flow state. Therefore, the follow-up results of this study can be considered as reliable.

The Control Subject

The CFD simulation results of the control subject, which can be compared with the results of cases 1–6, are shown in **Figures 3D,H**. The pressure at the TS-SS junction area was lower than the pressure upstream of the transverse sinus stenosis and was higher at the lateral wall of the TS-SS junction, especially at the dome (**Figures 3D,H**). The shape of the streamlines was smoother on the lateral side, compared to regular spiral on the medial side. The overall flow pattern at the junction area was regular (**Figure 4D**). The velocity distribution illustrated that the velocity at the junction area was significantly slower than the velocity in the TS stenosis. The flow velocity on the lateral side

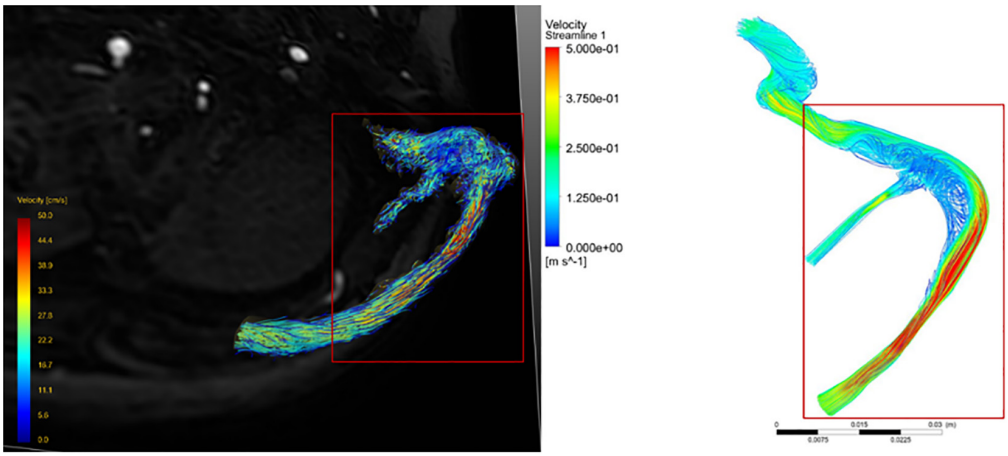

FIGURE 2 | Comparison of velocity streamline obtained from 4D flow MR post-processing with that simulated by CFD.

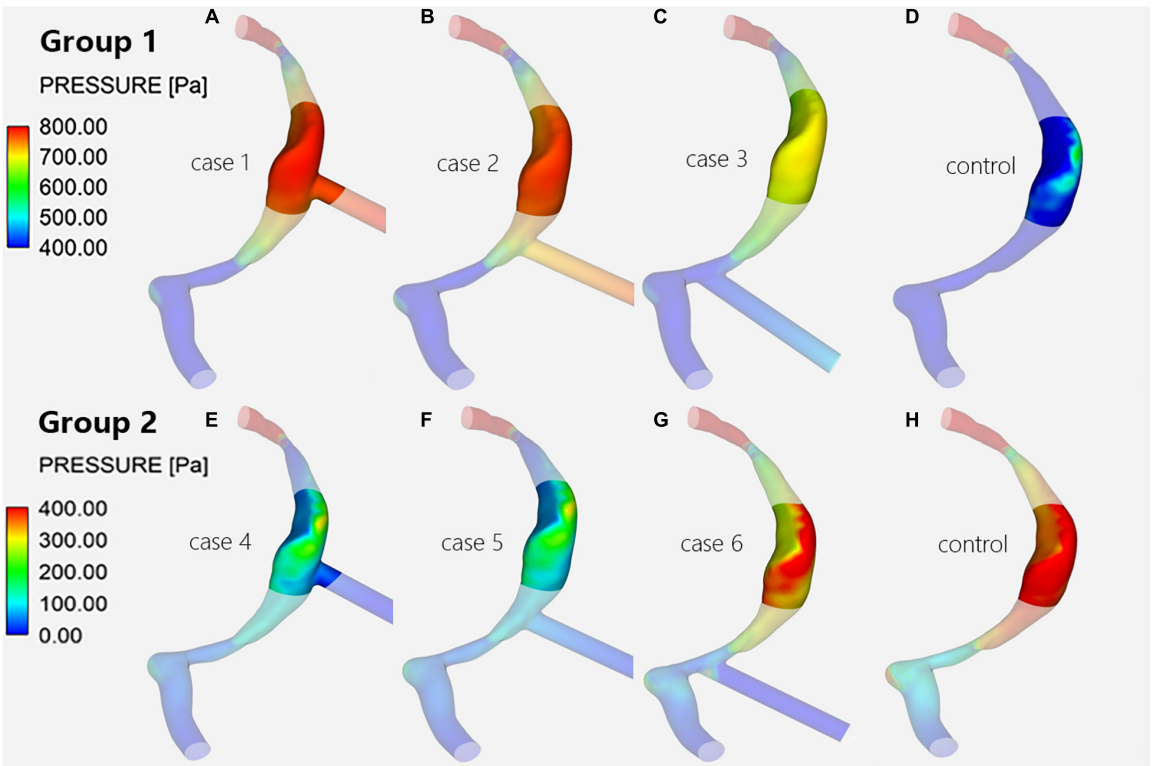

FIGURE 3 | Wall pressure distribution of the TS-SS junction. The upper row shows the wall pressure distribution of models with inlet EVs **(A–C)** and without EVs **(D)** in group 1; the lower row shows that of models with outlet EVs **(E–G)** and without EVs **(H)** in group 2.

of the junction area was faster than the velocity on the medial side (**Figure 5D**).

Wall Pressure Changes at the Transverse-Sigmoid Sinus Junction

When there was influent blood flow in the EVs, whether they were located at the superior, middle, or inferior portion of the SS, the wall pressures of group 1 at the junction were higher than those of the control subject, with the difference being most notable at the lateral wall (**Figures 3A–D**); when there was reverse flow, the pressures of group 2 were lower than those of the control subject, but the pressures was still higher at the dome of the lateral wall than at the medial wall at the TS-SS junction (**Figures 3E–H**).

In group 1, the pressures at the TS-SS junction decreased gradually as the EVs moved down, but they were higher than

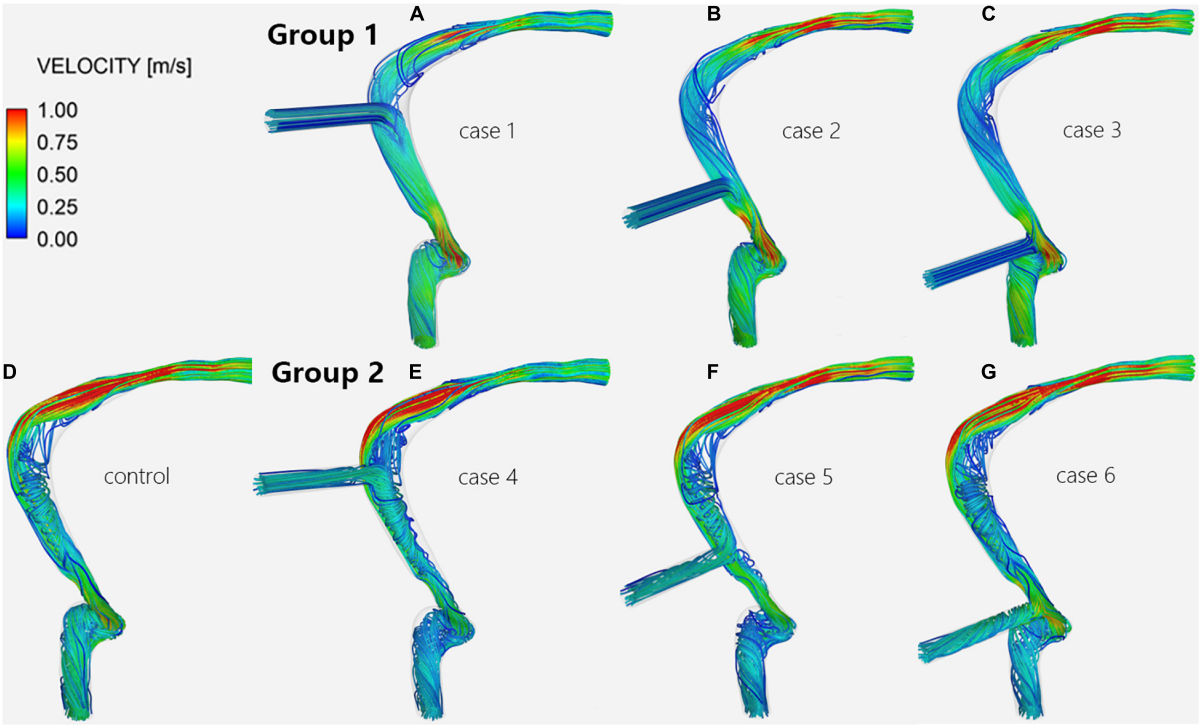

FIGURE 4 | Velocity streamlines of the TS-SS junction. The upper row shows the velocity streamlines of inlet EVs **(A–C)** in group 1; the lower row shows those of models without EVs **(D)** and with outlet EVs **(E–G)** in group 2.

those of the control subject (**Figures 3A–D**). Conversely, in group 2, as the EV position moved down, the pressures at the TS-SS junction increased, but they were lower than those of the control subject (**Figures 3E–H**). Again, the highest pressures were always at the dome of the TS-SS junction. **Figure 6** illustrates the P_{avg} on the junction area, and the quantitative P_{max} and P_{avg} are shown in **Table 1**.

Blood Flow Patterns at the Transverse-Sigmoid Sinus Junction

Regardless of whether the EVs were inlets or outlets, the blood flow patterns of cases 1–6 compared with the control subject showed that the streamlines in the lateral part of the TS-SS junction area were all smooth (**Figure 4**). The streamlines of group 1 in the medial part were slightly disordered (**Figures 4A–C**), while those of group 2 were regular spirals similar to the control subject (**Figures 4E–G**).

In group 1, the changes in blood flow velocity distribution at the TS-SS junction showed little change, but they were different from those of the control subject, and the flow velocities were relatively uniform, medium-low flow rate (**Figures 5A–D**). In group 2, the flow velocity changes at the TS-SS junction were similar to those of the control subject, group 2 had higher flow velocities in the lateral and medial parts than lower velocities in the central part, similar to the control subject (**Figures 5D–G**). The overall flow velocity of TS-SS junction in group 1 was lower than that in group 2. **Figure 7** indicates the difference in V_{avg} in each case. The quantitative data on V_{max} and V_{avg} are also shown in **Table 1**.

DISCUSSION

This study is the first to comprehensively explore the effect of EV on the hemodynamics of the TS-SS junction. Finite element analysis, a powerful simulation tool in biomechanics (Miller, 2009), was used to show the influence of the flow direction and afflux location of EVs on the hemodynamics of the TS-SS junction. Previous studies of the hemodynamics of venous PT mostly used CTV or digital subtraction angiography to construct CFD models (Kao et al., 2017; Amans et al., 2018; Tian et al., 2019; Mu et al., 2020). To evaluate the effects of EVs in different locations and different flow directions on the hemodynamics of the TS-SS junction, we included CTV combined with 4D flow images from a venous PT patient to construct a highly simulated CFD model. In previous studies, data on the inlet blood flow of the TS, which we consider important for the results, were mostly assigned subjectively. In this study, 4D flow MR was used to obtain the true velocity at the entrance and to compare the flow pattern with the initial model to improve the reliability of the results.

As our subject, we chose a patient with the most common features of venous PT, such as ipsilateral TS stenosis (Han et al., 2017; Lansley et al., 2017; Eisenman et al., 2018; Hewes et al., 2020), distention of the TS-SS junction (Hsieh and Wang, 2020),

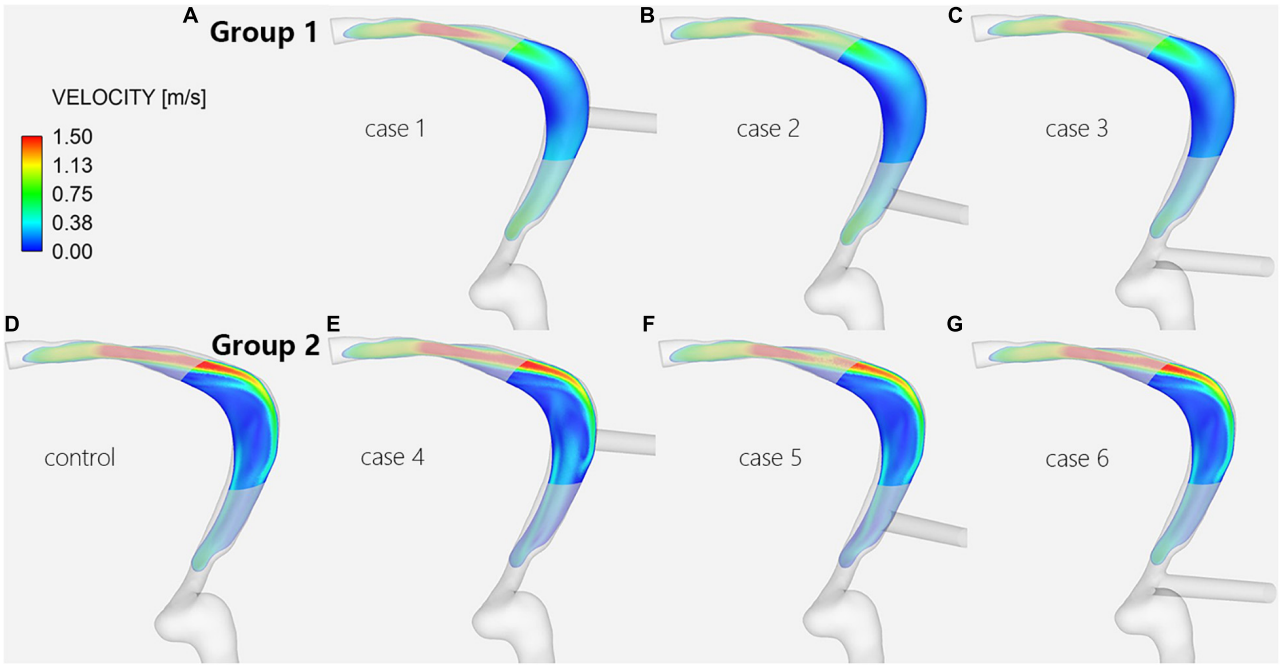

FIGURE 5 | Velocity distribution of the TS-SS junction. The upper row shows the velocity distribution of inlet EVs **(A–C)** in group 1; the lower row shows those of models without EVs **(D)** and with outlet EVs **(E–G)** in group 2.

SS wall dehiscence (Dong et al., 2015; Mundada et al., 2015; Eisenman et al., 2018), and ipsilateral EV (Dong et al., 2015), so that the study would reflect common clinical situations. The diameter of the EVs was set to 2 mm instead of a much larger size for the same reason. The location was set to three different positions to simulate the afflux locations of the petrosquamous sinus, MEV and posterior condylar EV. Bidirectional blood flow was permitted because the EVs are valveless. In addition, we assumed that the faster the velocity, the more remarkable the abovementioned effects would be; therefore, this important factor was not specifically investigated here.

Pressure change has been reported as an important indicator affecting PT (Mu et al., 2020). Our results showed that the flow directions of EVs may significantly affect the pressure of the TS-SS junction. We concluded that the EV flow direction must be considered when choosing the ligation operation. If there is strong blood flow from an EV into the SS, ligation may be helpful to alleviate the sound. Otherwise, this treatment will be not only worthless but also harmful. For example, ligation may increase the risk of intracranial hypertension and associated serious neurological injury if the blood flow blocked by the ligation cannot be compensated (Zhao et al., 2016). When an EV acts as an inlet, the vessel wall at the TS-SS junction is subjected to the impact of blood flow from at least two directions, including one from the TS and another from the EV, which may increase the pressure. Under these circumstances, EV ligation is equivalent to reducing the blood flow into the SS, and the pressure is reliably reduced as well. In contrast, When an EV is the outlet, as a collateral drainage vein pathway, it can prevent any increase in upstream resistance, thus affecting the overall upstream pressure gradient and limiting the increase in blood pressure (Levitt et al., 2016). Therefore, after ligation, the area of the downstream outlet decreases, which will definitely increase the pressure at the SS. In addition, when the EV is inlet, the higher the EV position is, the closer it is to the TS-SS junction, and the greater the blood flow impact from both sides of TS and EV, so the higher the pressure is. The ligation effect may be better at this time.

TS venous flow sharply turned at the TS-SS junction, affecting the lumen and inducing an evident vortex at the TS-SS junction (Shin et al., 2019). Our findings suggested that the blood flow patterns at the junction in all models had smooth streamlines on the lateral side. The angle between the TS and SS influences the distribution of the flow field; therefore, the difference in the flow

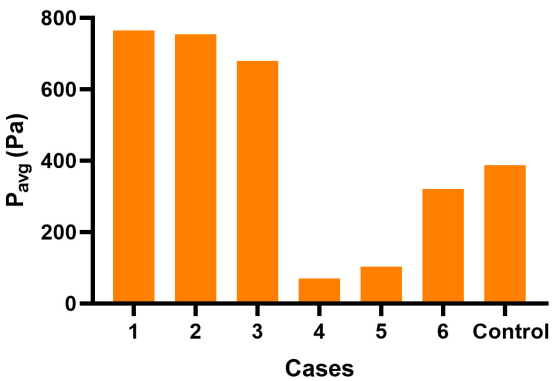

FIGURE 6 | Wall P_{avg} at the junction area in each case.

TABLE 1 | Quantitative data on wall pressures and velocities.

Case	Model	P_{max}(Pa)	P_{avg}(Pa)	V_{max}(cm/s)	V_{avg}(cm/s)
Control	No EV	593.6	386.7	148.6	25.7
1	s-in	791.2	764.8	63.3	18.2
2	m-in	780.1	754.3	69.0	16.9
3	i-in	706.9	679.3	70.6	16.7
4	s-out	307.1	70.1	150.0	26.6
5	m-out	304.3	103.1	147.1	25.3
6	i-out	521.0	320.1	149.6	25.3

※ *s, superior; m, middle; i, inferior; in, inlet; out, outlet;* P_{max}*, wall maximum pressure;* P_{avg}*, wall average pressure;* V_{max}*, maximum velocity;* V_{avg}*, average velocity.*

field may be caused by the different shapes of individual vessels. In this case, because of the angle between the TS and SS, the blood flow from the TS is concentrated on the lateral side, while the flow velocity on the medial side is relatively low. Our results also suggested that the flow velocity in the inlet group was much lower than in the outlet group and the control subject. The reason may be associated with that the EV inlet blood flow opposes the TS inlet blood flow, and the kinetic energy is transformed into potential energy according to mass conservation, resulting in increased wall pressure and decreased flow velocity. And in the inlet group, EV blood flowed into the SS, the normal lateral high-speed blood flow band disappeared after impact, replaced by a relatively uniform, slightly increased flow velocity distribution in central of the TS-SS junction. The medial part of EV models with outlet EVs or without EVs is a regular spiral flow, which may be related to the swirling flow of blood under normal circumstances (Ha et al., 2015); the irregular flow on the medial side of inlet EV models may be caused by the collision of opposite blood flow, which would cause the normal swirling flow to disappear and be replaced with slightly disordered blood flow. It is also concluded that ligation should be considered when the large EV of a PT patient is an inlet.

Unfortunately, in this original case, PT still exists after large EV ligation. Part of the reason is that the EV is located in the middle to inferior portion of the SS, which is a non-negligible distance from the TS-SS junction, and 4D flow MR postprocessing images showed that there was outlet blood flow in the EV. According to the abovementioned research, this kind of EV has little effect on the hemodynamics of the TS-SS junction. Therefore, ligation is not an effective treatment for the patient, which is consistent with the results of the present study.

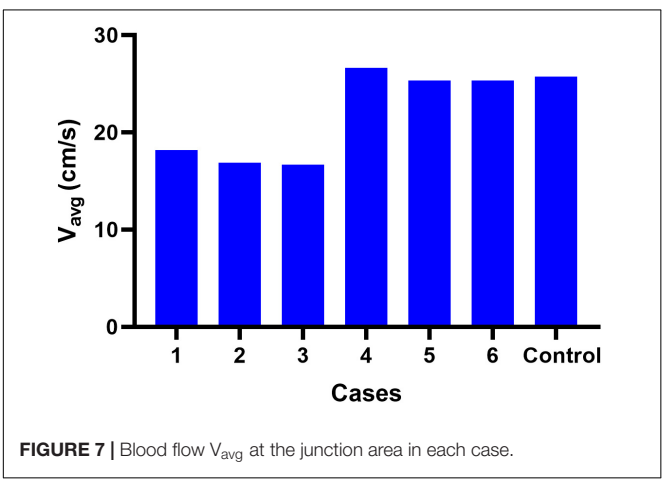

FIGURE 7 | Blood flow V_{avg} at the junction area in each case.

This study has several limitations. First, there is only one case, which is not completely representative, although the most common morphologic and hemodynamic characteristics of EV and TS-SS junction in PT patients were set as numerical boundary conditions. Second, this case is a semi-individual model. The disadvantage of the semipersonalized model is that it cannot fully simulate the characteristics of the original structure and can implement only targeted simulations. The research model requires different EV positions; thus, in order to control other influencing factors, EV models with the same regular shape are established, and the other parts are personalized. Third, because the venous sinus is limited to the skull and dura mater, and is less elastic than an artery, we considered it acceptable to neglect wall elasticity, and the vessel wall of the venous sinus was assumed to be rigid and governed by the no-slip boundary condition (Sforza et al., 2010). Fourth, the results show the influence of the MEV entry distance on the blood flow at the junction, but the relationship between the degree of the effect on blood flow and the distance was not quantified, and the specific orientation of the entry point was not considered. Finally, this study focused only on the effects of different EV positions and flow directions on the hemodynamic of the TS-SS junction. In fact, the EV diameter and internal flow rate can also affect the target area; this influence will be further studied in the future.

CONCLUSION

A specific-patient hemodynamic analysis implies that the flow direction and afflux location of EVs affect the hemodynamics of the TS-SS junction and the severity of PT. The main observation is that when the enlarged EV is located in the superior SS and the blood flow through the EV is positive, the hemodynamic indicators of the TS-SS junction area are markedly worse than in the model without EV. Venous PT patients who have enlarged EVs adjacent to the TS-SS junction and inlet flow are most likely to benefit from ligation. The combined use of imaging technology and CFD simulation to obtain hemodynamic information, such as wall pressure and flow velocity, can provide a more accurate inference regarding the etiology of PT for clinical practice and establish a theoretical basis for subsequent treatment.

DATA AVAILABILITY STATEMENT

The original contributions presented in the study are included in the article/supplementary material, further inquiries can be directed to the corresponding author/s.

ETHICS STATEMENT

The studies involving human participants were reviewed and approved by the Beijing Friendship Hospital, Capital Medical University. The patients/participants provided their written informed consent to participate in this study.

AUTHOR CONTRIBUTIONS

XQ, XL, HD, and HL collected the clinical and imaging data. XQ, ZM, XX, and PZ performed the experiment and drafted the manuscript. ZW and BG designed the study and ensured the questions related to all aspects of the work. PZ, ZY, BG, and ZW gave critical comments on the manuscript. All authors contributed to the article and approved the submitted version.

FUNDING

This study was supported by the National Natural Science Foundation of China (Grant Nos. 61931013 and 81701644) and the Beijing Scholar Program [Grant No. (2015)160].

REFERENCES

Amans, M. R., Haraldsson, H., Kao, E., Kefayati, S., Meisel, K., Khangura, R., et al. (2018). MR venous flow in sigmoid sinus diverticulum. *AJNR Am. J. Neuroradiol.* 39, 2108–2113. doi: 10.3174/ajnr.A5833

Dong, C., Zhao, P. F., Yang, J. G., Liu, Z. H., and Wang, Z. C. (2015). Incidence of vascular anomalies and variants associated with unilateral venous pulsatile tinnitus in 242 patients based on dual-phase contrast-enhanced computed tomography. *Chin. Med. J. (Engl.)* 128, 581–585. doi: 10.4103/0366-6999.151648

Eisenman, D. J., Raghavan, P., Hertzano, R., and Morales, R. (2018). Evaluation and treatment of pulsatile tinnitus associated with sigmoid sinus wall anomalies. *Laryngoscope* 128(Suppl. 2), S1–S13. doi: 10.1002/lary.27218

Funnell, J. P., Craven, C. L., Thompson, S. D., D'Antona, L., Chari, A., Thorne, L., et al. (2018). Pulsatile versus non-pulsatile tinnitus in idiopathic intracranial hypertension. *Acta Neurochir. (Wien)* 160, 2025–2029. doi: 10.1007/s00701-018-3587-8

Gulmez Cakmak, P., Ufuk, F., Yagci, A. B., Sagtas, E., and Arslan, M. (2019). Emissary veins prevalence and evaluation of the relationship between dural venous sinus anatomic variations with posterior fossa emissary veins: MR study. *Radiol. Med.* 124, 620–627. doi: 10.1007/s11547-019-01010-2

Ha, H., Choi, W., Park, H., and Lee, S. J. (2015). Effect of swirling blood flow on vortex formation at post-stenosis. *Proc. Inst. Mech. Eng. H* 229, 175–183. doi: 10.1177/0954411915573065

Han, Y., Yang, Q., Yang, Z., Xia, J., Su, T., Yu, J., et al. (2017). Computational fluid dynamics simulation of hemodynamic alterations in sigmoid sinus diverticulum and ipsilateral upstream sinus stenosis after stent implantation in patients with pulsatile tinnitus. *World Neurosurg.* 106, 308–314. doi: 10.1016/j.wneu.2017.06.168

Hewes, D., Morales, R., Raghavan, P., and Eisenman, D. J. (2020). Pattern and severity of transverse sinus stenosis in patients with pulsatile tinnitus associated with sigmoid sinus wall anomalies. *Laryngoscope* 130, 1028–1033. doi: 10.1002/lary.28168

Hsieh, Y. L., and Wang, W. (2020). Extraluminal sigmoid sinus angioplasty: a pertinent reconstructive surgical method targeting dural sinus hemodynamics to resolve pulsatile tinnitus. *Otol. Neurotol.* 41, e132–e145. doi: 10.1097/MAO.0000000000002464

Kao, E., Kefayati, S., Amans, M. R., Faraji, F., Ballweber, M., Halbach, V., et al. (2017). Flow patterns in the jugular veins of pulsatile tinnitus patients. *J. Biomech.* 52, 61–67. doi: 10.1016/j.jbiomech.2016.12.008

Kweon, J., Yang, D. H., Kim, G. B., Kim, N., Paek, M., Stalder, A. F., et al. (2016). Four-dimensional flow MRI for evaluation of post-stenotic turbulent flow in a phantom: comparison with flowmeter and computational fluid dynamics. *Eur. Radiol.* 26, 3588–3597. doi: 10.1007/s00330-015-4181-6

Lambert, P. R., and Cantrell, R. W. (1986). Objective tinnitus in association with an abnormal posterior condylar emissary vein. *Am. J. Otol.* 7, 204–207.

Lansley, J. A., Tucker, W., Eriksen, M. R., Riordan-Eva, P., and Connor, S. E. J. (2017). Sigmoid Sinus diverticulum. dehiscence, and venous sinus stenosis: potential causes of pulsatile tinnitus in patients with idiopathic intracranial hypertension? *AJNR Am. J. Neuroradiol.* 38, 1783–1788. doi: 10.3174/ajnr.A5277

Lee, S. H., Kim, S. S., Sung, K. Y., and Nam, E. C. (2013). Pulsatile tinnitus caused by a dilated mastoid emissary vein. *J. Korean Med. Sci.* 28, 628–630. doi: 10.3346/jkms.2013.28.4.628

Levitt, M. R., McGah, P. M., Moon, K., Albuquerque, F. C., McDougall, C. G., Kalani, M. Y. S., et al. (2016). Computational modeling of venous sinus stenosis in idiopathic intracranial hypertension. *AJNR Am. J. Neuroradiol.* 37, 1876–1882. doi: 10.3174/ajnr.A4826

Li, Y., Chen, H., He, L., Cao, X., Wang, X., Chen, S., et al. (2018). Hemodynamic assessments of venous pulsatile tinnitus using 4D-flow MRI. *Neurology* 91, e586–e593. doi: 10.1212/WNL.0000000000005948

Liu, Z., Chen, C., Wang, Z., Gong, S., Xian, J., and Liang, X. (2013). Petrosquamosal sinus in the temporal bone as a cause of pulsatile tinnitus: a radiological detection. *Clin. Imaging* 37, 561–563. doi: 10.1016/j.clinimag.2011.12.019

Lyu, A. R., Park, S. J., Kim, D., Lee, H. Y., and Park, Y. H. (2018). Radiologic features of vascular pulsatile tinnitus - suggestion of optimal diagnostic image workup modalities. *Acta Otolaryngol.* 138, 128–134. doi: 10.1080/00016489.2017.1385847

Markl, M., Frydrychowicz, A., Kozerke, S., Hope, M., and Wieben, O. (2012). 4D flow MRI. *J. Magn. Reson. Imaging* 36, 1015–1036. doi: 10.1002/jmri.23632

Miller, K. (2009). The computational biomechanics for medicine workshop series. *Med. Image Anal.* 13:911. doi: 10.1016/j.media.2008.10.002

Mortazavi, M. M., Tubbs, R. S., Riech, S., Verma, K., Shoja, M. M., Zurada, A., et al. (2012). Anatomy and pathology of the cranial emissary veins: a review with surgical implications. *Neurosurgery* 70, 1312–1318. doi: 10.1227/NEU.0b013e31824388f8

Mu, Z., Qiu, X., Zhao, D., Li, X., Fu, M., Liu, Y., et al. (2020). Hemodynamic study on the different therapeutic effects of SSWD resurfacing surgery on patients with pulsatile tinnitus. *Comput. Methods Programs Biomed.* 190:105373. doi: 10.1016/j.cmpb.2020.105373

Mundada, P., Singh, A., and Lingam, R. K. (2015). CT arteriography and venography in the evaluation of pulsatile tinnitus with normal otoscopic examination. *Laryngoscope* 125, 979–984. doi: 10.1002/lary.25010

Narvid, J., Do, H. M., Blevins, N. H., and Fischbein, N. J. (2011). CT angiography as a screening tool for dural arteriovenous fistula in patients with pulsatile tinnitus: feasibility and test characteristics. *AJNR Am. J. Neuroradiol.* 32, 446–453. doi: 10.3174/ajnr.A2328

Onder, H. (2018). Sigmoid sinus dehiscence and suspected idiopathic intracranial hypertension in pulsatile tinnitus? *Neuroradiology* 60, 355–356. doi: 10.1007/s00234-018-2009-1

Ozen, O., and Sahin, C. (2020). Evaluation of the mastoid emissary canals with computerized tomography in patients with chronic otitis media. *J. Neurol. Surg .B Skull Base* 81, 82–87. doi: 10.1055/s-0039-3399518

Pekala, P. A., Rybus, J. J., Stachura, M., Pekala, J. R., Skinningsrud, B., Tubbs, R. S., et al. (2018). Prevalence of petrosquamosal sinus and its clinical significance: radiologic study and meta-analysis. *World Neurosurg.* 111, e616–e623. doi: 10.1016/j.wneu.2017.12.132

Pekcevik, Y., Sahin, H., and Pekcevik, R. (2014). Prevalence of clinically important posterior fossa emissary veins on CT angiography. *J. Neurosci. Rural Pract.* 5, 135–138. doi: 10.4103/0976-3147.131654

Reardon, M. A., and Raghavan, P. (2016). Venous abnormalities leading to tinnitus: imaging evaluation. *Neuroimaging Clin. N. Am.* 26, 237–245. doi: 10.1016/j.nic.2015.12.006

Sforza, D. M., Lohner, R., Putman, C., and Cebral, J. (2010). Hemodynamic analysis of intracranial aneurysms with moving parent arteries: basilar tip aneurysms. *Int. J. Numer. Method Biomed. Eng.* 26, 1219–1227. doi: 10.1002/cnm.1385

Shin, P., Choi, W., Joo, J., and Oh, W. Y. (2019). Quantitative hemodynamic analysis of cerebral blood flow and neurovascular coupling using optical coherence tomography angiography. *J. Cereb. Blood Flow Metab.* 39, 1983–1994. doi: 10.1177/0271678X18773432

Tian, S., Fan, X., Wang, Y., Liu, Z., and Wang, L. (2019). An in vitro experimental study on the relationship between pulsatile tinnitus and the dehiscence/thinness of sigmoid sinus cortical plate. *J. Biomech.* 84, 197–203. doi: 10.1016/j.jbiomech.2018.12.049

Zhao, P., Lv, H., Dong, C., Niu, Y., Xian, J., and Wang, Z. (2016). CT evaluation of sigmoid plate dehiscence causing pulsatile tinnitus. *Eur. Radiol.* 26, 9–14. doi: 10.1007/s00330-015-3827-8

Conflict of Interest: The authors declare that the research was conducted in the absence of any commercial or financial relationships that could be construed as a potential conflict of interest.

frontiers in Neuroscience

ORIGINAL RESEARCH
published: 08 December 2021
doi: 10.3389/fnins.2021.732113

Transverse Sinus Stenosis in Venous Pulsatile Tinnitus Patients May Lead to Brain Perfusion and White Matter Changes

Xiaoshuai Li[1], Ning Xu[1], Xuxu Meng[1], Chihang Dai[1], Xiaoyu Qiu[1], Heyu Ding[1], Han Lv[1], Rong Zeng[2], Jing Xie[2], Pengfei Zhao[1], Zhenghan Yang[1], Shusheng Gong[2]* and Zhenchang Wang[1]**

[1] Department of Radiology, Beijing Friendship Hospital, Capital Medical University, Beijing, China, [2] Department of Otolaryngology Head and Neck Surgery, Beijing Friendship Hospital, Capital Medical University, Beijing, China

Objective: Transverse sinus stenosis (TSS) is associated with various symptoms, but whether it can lead to pathological brain changes is unclear. This study aimed to investigate brain changes in venous pulsatile tinnitus (PT) patients with TSS.

Materials and Methods: In this study, fifty-five consecutive venous PT patients and fifty age- and gender-matched healthy controls (HCs) were investigated. In CT venography, the combined conduit score (CCS) was used to assess the degree of TSS in venous PT patients. Magnetic resonance venography was used to assess TSS in HCs. All the participants had undergone arterial spin labeling and structural MRI scans.

Results: Two patients without TSS and ten HCs with TSS were excluded. Fifty-three venous PT patients with TSS and 40 HCs without TSS were included in this study. All the patients had unilateral cases: 16 on the left and 37 on the right. Based on the CCS, the patients were divided into high-degree TSS (a score of 1–2) ($n = 30$) and low-degree TSS groups (a score of 3–4) ($n = 23$). In the whole brain and gray matter, the patients with high-degree TSS showed decreased cerebral blood flow (CBF) compared with patients with low-degree TSS as well as HCs ($P < 0.05$), and no significant difference in CBF was found in patients with low-degree TSS and HCs ($P > 0.05$). In white matter (WM) regions, the patients with high-degree TSS exhibited decreased CBF relative to the HCs ($P < 0.05$). The incidence of cloud-like WM hyperintensity was significantly higher in the above two patient groups than in the HC group ($P < 0.05$).

Conclusion: TSS in venous PT patients may lead to decreased CBF and cloud-like WM hyperintensity. These neuroimaging findings may provide new insights into pathological TSS in venous PT.

Keywords: transverse sinus stenosis, pulsatile tinnitus, brain perfusion, white matter, arterial spin labeling

OPEN ACCESS

Edited by:
Jiajia Zhu,
First Affiliated Hospital of Anhui Medical University, China

Reviewed by:
Siying Song,
Capital Medical University, China
Hao Ding,
Tianjin Medical University, China

***Correspondence:**
Pengfei Zhao
zhaopengf05@163.com
Shusheng Gong
gongss1962@163.com
Zhenchang Wang
cjr.wzhch@vip.163.com

Specialty section:
This article was submitted to Perception Science, a section of the journal Frontiers in Neuroscience

Received: *28 June 2021*
Accepted: *19 November 2021*
Published: *08 December 2021*

Citation:
Li X, Xu N, Meng X, Dai C, Qiu X, Ding H, Lv H, Zeng R, Xie J, Zhao P, Yang Z, Gong S and Wang Z (2021) Transverse Sinus Stenosis in Venous Pulsatile Tinnitus Patients May Lead to Brain Perfusion and White Matter Changes. Front. Neurosci. 15:732113. doi: 10.3389/fnins.2021.732113

INTRODUCTION

Pulsatile tinnitus (PT) is an auditory perception synchronized with vascular pulsation (Wang et al., 2014). According to the blood vessels of origin, PT is divided into the arterial, venous and arteriovenous types (Hofmann et al., 2013), of which venous PT accounts for 84% of the PT population (Lyu et al., 2018). The sound originates from turbulent flow in the transverse-sigmoid

sinus, which is then perceived by the inner ear (Bae et al., 2015). Transverse sinus stenosis (TSS) is one of the most common anomalies in venous PT, and it is also a clear etiology of this condition. A previous study reported that 84.6% of venous PT patients have varying degrees of bilateral TSS (Hewes et al., 2020). After stent placement, PT can disappear completely (Baomin et al., 2014). With the rapid development of imaging techniques, an increasing number of studies have focused on the relationship between TSS and the central nervous system (Saindane et al., 2014; Morris et al., 2017; Favoni et al., 2019).

The intracranial venous system is a complex three-dimensional structure with greater anatomic variation and asymmetry than the arterial structure (Scott and Farb, 2003). Additionally, the former is susceptible to physiological factors such as posture, breathing, and the hydration status (Werner et al., 2011). Some additional factors, such as enlarged arachnoid granules, septa, and congenital causes, can lead to TSS (Durst et al., 2016), increasing the susceptibility to this venous pathology.

Currently, TSS is the cause of the pathological conditions of venous PT (Baomin et al., 2014) and idiopathic intracranial hypertension (Farb et al., 2003; Carvalho et al., 2017). However, few studies have focused on the neuroimaging characteristics of symptomatic TSS. A previous study used semiquantitative single-photon emission computed tomography (SPECT) to identify decreased brain perfusion and cloud-like white matter (WM) hyperintensity in symptomatic internal jugular vein (IJV) stenosis patients (Zhou et al., 2019). Bai et al. (2019) further found that patients with symptomatic TSS also have cloud-like WM hyperintensity. Ding et al. reported a PT patient with TSS and decreased brain perfusion; after TSS was resolved by stent placement, the hypoperfusion state returned to normal (Ding et al., 2019). These findings indicate that TSS may cause pathological changes in the central nervous system. However, the above studies assessed brain perfusion using SPECT (Ding et al., 2019; Zhou et al., 2019), which is a semiquantitative and invasive technique. Arterial spin labeling (ASL) uses magnetically labeled arterial blood water as an endogenous tracer, which can non-invasively and quantitatively assess brain perfusion (Ha et al., 2019). Additionally, because stent placement requires the long-term use of anticoagulants, sigmoid sinus wall reconstruction is the main surgical treatment for venous PT in clinical practice (Zhao et al., 2016; Eisenman et al., 2018; Hewes et al., 2020) but does not resolve TSS. In the present study, we aimed to quantitatively evaluate brain perfusion changes by ASL and investigate white matter changes in venous PT patients with TSS, possibly helping clinicians better understand such abnormalities and choose treatment options.

MATERIALS AND METHODS

Subjects

This study protocol was approved by local institutional review boards. All the participants offered written informed consent.

Fifty-five consecutive venous PT patients from the Department of Otolaryngology Head and Neck surgery were included in the study between January 2018 and December 2020. All the patients showed pulse-synchronous tinnitus, which disappeared after compression of the ipsilateral internal jugular vein. The age was between 18 and 50 years. These patients had no neurological disorders, such as headache, papilledema, decreased vision, sleep disturbance or memory deterioration. The audiometric and otoscopic examination results were normal. CT arteriography/venography (CTA/V), digital substraction angiography (DSA), and ASL were performed in each patient before treatment. The exclusion criteria for venous PT patients were as follows: (1) systemic diseases such as hypertension, hyperlipidemia, diabetes, and kidney disease; (2) carotid or intracranial artery abnormalities, including congenital malformation, large or small vascular disease and stenosis; (3) IJV stenosis or thrombosis; (4) significant stenosis or hypoplasia of venous sinuses in HCs; (5) neurodegenerative diseases or neuroinflammation; (6) psychiatric or neurological disorders; (7) history of head trauma or tumor; (8) drug and alcohol abuse in the last 3 months; and (9) contraindications for MRI. The Tinnitus Handicap Inventory (THI) score was used to assess the severity of PT.

Fifty age- and gender-matched healthy controls (HCs) were enrolled. The exclusion criteria for HCs were the same as those for venous PT patients above.

Imaging Technique

MR arteriography/venography (MRA/V) of all the participants was performed using a Philips 3.0T MRI unit (Ingenia; Philips Healthcare, Best, Netherlands). The parameters of 3D time of flight (TOF) MRA were as follows: repetition time (TR), 19 ms; echo time (TE), 3.5 ms; flip angle (FA), 18°; field of view (FOV), 200 × 200 mm; matrix, 400 × 256; slice thickness, 1.1 mm, no gap; 156 slices. The parameters of 3D phase-contrast MRV were as follows: TR, 17 ms; TE, 6.2 ms; FA, 10°; FOV, 173 × 173 × 192 mm; velocity encoding, 15 cm/s; matrix, 144 × 108 × 120.

All venous PT patients had undergone CTA/V examination using a 64-slice CT system (Philips, Best, Netherlands) with a bolus tracking program. The parameters for CTA/V were as follows: 300 mAs; 100 kV; collimation, 64 × 0.625 mm; matrix, 512 × 512; and rotation time, 0.75 s; contrast agent (iopamidol, 370 mg/ml iodine; Bracco, Shanghai, China): 1.5 ml/kg, 5 ml/s. Images were reconstructed on a postprocessing workstation with the following parameters: thickness, 1 mm, no gap; standard algorithms (width 700 Hu; level 200 Hu) for soft tissue reconstruction; bone algorithms (width 4,000 Hu; level 700 Hu) for bone reconstruction.

Head MRA/V and cervical Doppler ultrasound were used to exclude intracranial and cervical arteriovenous abnormalities in HCs. In venous PT patients, head CTA/V and DSA were used to assess intracranial and cervical arteries and veins. CTV was used to assess the severity of TSS in venous PT patients. Based on the improvement of the method proposed by Farb et al. (2003), the TSS in venous PT patients was assessed by dividing the cross-sectional area of the most stenotic segment of the transverse sinus by that of the distal superior sagittal sinus (**Figure 1**). The left and right transverse sinuses were independently divided into 0–4

grades as follows: grade 0, discontinuity (gap); grade 1, hypoplasia or severe stenosis (<25%); grade 2, moderate stenosis (25–50%); grade 3, mild stenosis (50–75%); and grade 4, normal (>75%). This method calculates the combined conduit score (CCS) as the sum of right and left scores, which can be used to reflect the overall venous drainage. Normally, the left and right transverse sinuses would reveal a score of 4, and the final CCS would show a score of 8. A transverse sinus is characterized as dominant if its largest cross-sectional area is greater than 150% of that of the smaller side (Li et al., 2021).

All the participants had undergone brain structure and perfusion scans using a GE 3.0T MRI unit (Discovery MR750W; GE, Milwaukee, WI, United States) using an eight-channel phased-array head coil. The structural images included a 3D T1-brain volume (T1-BRAVO) sequence [TR/TE/inversion time (TI), 8.4/3.2/450 ms; slice thickness, 1 mm without gap; FA, 12°; 196 slices], T2-weighted imaging (T2WI: TR/TE, 5,637/130 ms; slice thickness, 6 mm; gap: 7 mm; 20 slices), T2 fluid attenuated inversion recovery (T2 FLAIR: TR/TE/TI, 8,400/88/2,404 ms; slice thickness, 6 mm; gap, 7 mm; FA, 160°; 20 slices) and diffusion-weighted imaging (DWI: TR/TE, 4,880/79 ms; slice thickness, 6 mm; gap, 7 mm; b value: 0, 1,000 s/mm^2; FA, 90°; 20 slices). The perfusion images were acquired using a 3D pseudocontinuous ASL sequence with fast spin-echo acquisition (TR/TE, 4,854/10.7 ms; slice thickness, 4 mm, no gap; number of excitations, 3; postlabel delay, 2,025 ms; FOV, 240 mm × 240 mm; in-plane resolution, 3.37 mm × 3.37 mm; FA, 111°; 36 slices). During the imaging process, the participants were instructed to close their eyes, move as little as possible, stay awake and think of nothing. Earplugs were provided to reduce noise.

Cerebral Blood Flow Calculation

Using a single compartment model, the ASL difference images were calculated after subtracting the label images from the control images. Next, we obtained the cerebral blood flow (CBF) maps from the ASL difference images. The preprocessing of the CBF images was as follows. Statistical Parametric Mapping (SPM8) software was used to normalize the CBF maps to the Montreal Neurological Institute (MNI) space (Zhuo et al., 2017; Guo et al., 2018). Specifically, the CBF images of all the HCs were coregistered to a PET perfusion template in the MNI space to obtain a standard CBF template. We coregistered the CBF images of all HCs and PT patients to this standard CBF template and resampled the data to 2 × 2 × 2 mm. In the data processing and analysis of brain imaging (DPABI) software package, the CBF values (ml/100 g/min) of the gray matter (GM), WM and whole brain in each participant were extracted using specific GM, WM and whole brain masks, respectively.

White Matter Change Evaluation

All the participants had undergone brain structure scans. Based on previous studies (Bai et al., 2019; Zhou et al., 2019), the WM change was defined as bilaterally symmetrical cloud-like hyperintensity in the bilateral centrum semiovale and/or periventricular area on the T2 FLAIR sequence and was evaluated by three neuroradiologists (with 6, 8, and 12 years of experience) blinded to the clinical data. Inconsistent cases reached a consensus through consultation.

Statistical Analysis

Statistical analysis was performed using SPSS software, version 22.0 (IBM, Chicago, IL). Fisher's exact test and two-sample *t*-test were used to explore the differences in the clinical and demographic data between the venous PT patients and HCs. To compare CBF among the three groups, one-way analysis of variance (Bonferroni correction) was used. Chi-squared test was used to compare the difference in the incidence of cloud-like WM hyperintensity among the three groups (Bonferroni correction).

RESULTS

Demographic and Clinical Characteristics

Two venous PT patients without TSS and ten HCs with TSS were excluded. Fifty-three patients and 40 HCs were enrolled in this study. The prevalence of TSS was 96.4% in venous PT patients and 20% in HCs. All the patients had unilateral PT, 16 cases on the left and 37 cases on the right. The mean PT duration was 28.0 ± 23.8 months, and the mean THI score was 50.8 ± 22.2. The patients and HCs were well matched for age (two-sample *t*-test, $P = 0.100$), gender (Fisher's exact test, $P = 1.000$) and body mass index (two-sample *t*-test, $P = 0.416$) (**Table 1**).

Radiological Evaluation

No obvious abnormalities were found in the intracranial arteries and cervical arteriovenous systems of all the participants. The dominance of the transverse sinus in 44 patients was on the symptomatic side, and 9 patients had codominance. Most patients (46/53) had varying degrees of bilateral TSS. The remaining 7 patients had TSS on the PT side and dysplasia of the transverse sinus on the asymptomatic side. Because all the patients had different degrees of unilateral/bilateral TSS, the CCS

TABLE 1 | Characteristics of the venous PT patients and HCs.

	PT (*n* = 53)		HC (*n* = 40)	*P*
Age (year)	35.5 ± 7.0		37.9 ± 6.7	0.100[a]
Gender (male/female)	5/48		3/37	1.000[b]
BMI	23.0 ± 2.5		22.6 ± 2.0	0.416[a]
Side (left/right)	16/37			
PT duration (months)	28.0 ± 23.8			
THI score	50.8 ± 22.2			
TSS degree	High-degree	Low-degree		
CCS	1–2 score	3–4 score		
Number	30	23		

The data are presented as mean ± standard deviation.
PT, pulsatile tinnitus; HC, healthy control; BMI, body mass index; THI, Tinnitus Handicap Inventory; CCS, combined conduit score; TSS, transverse sinus stenosis.
[a] *Two-sample t-test.*
[b] *Fisher's exact test.*

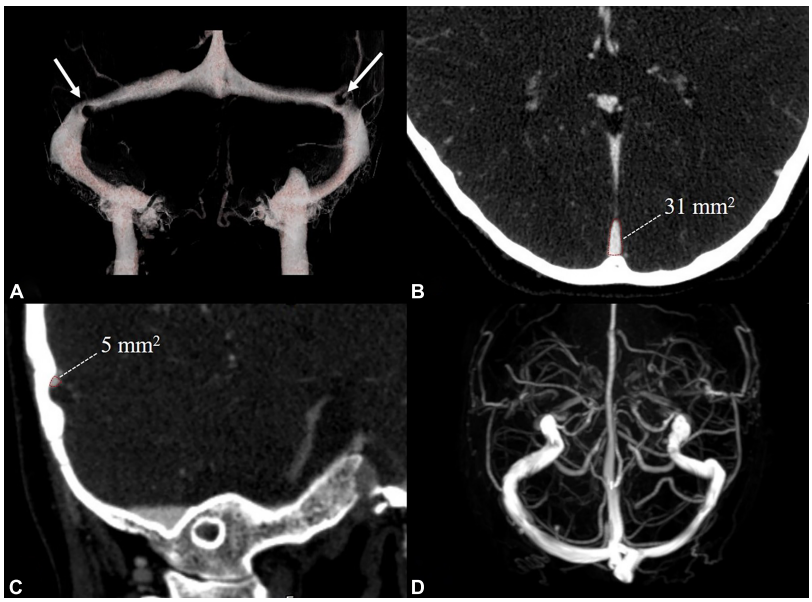

FIGURE 1 | Examples of radiological evaluation in a venous PT patient with TSS and a healthy control. CTV **(A)** showed bilateral TSS in the venous PT patient (white arrow). The cross-sectional area of the distal superior sagittal sinus **(B)** and TSS **(C)** were measured perpendicular to the venous sinus. MRV **(D)** showed no TSS in the healthy control. TSS: transverse sinus stenosis.

ranged from 1 to 4 in all the patients. Based on the CCS, the venous PT patients were divided into a high-degree TSS group (a score of 1–2) (n = 30) and a low-degree TSS group (a score of 3–4) (n = 23) (**Table 1**). MRV revealed no incidental TSS in the HCs (**Figure 1**).

Cerebral Blood Flow Differences Among the Groups

The CBF values of patients with high-degree and low-degree TSS and HCs are exhibited in **Table 2**. Significant differences were found in the CBF value of the whole brain, GM and WM among the three groups (whole brain: P = 0.001; GM: P = 0.002; WM: P = 0.005). In the whole brain and GM, the patients with high-degree TSS showed significantly decreased CBF compared with the HCs (whole brain: 45.68 ± 5.58 ml/100 g/min vs. 51.58 ± 7.29 ml/100 g/min, P = 0.001; GM: 49.08 ± 6.26 ml/100 g/min vs. 55.03 ± 7.91 ml/100 g/min, P = 0.002); the patients with high-degree TSS exhibited significantly decreased CBF relative to compared with those with low-degree TSS (whole brain: 45.68 ± 5.58 ml/100 g/min vs. 50.30 ± 6.03 ml/100 g/min, P = 0.036; GM: 49.08 ± 6.26 ml/100 g/min vs. 54.04 ± 6.45 ml/100 g/min, P = 0.039); no significant difference in CBF was found in patients with low-degree TSS and HCs ($P > 0.05$). In the WM region, the patients with high-degree TSS exhibited significantly decreased CBF compared with that in the HCs (38.80 ± 3.90 ml/100 g/min vs. 42.83 ± 6.03 ml/100 g/min, P = 0.004).

White Matter Change

Cloud-like WM hyperintensity on the T2 FLAIR sequence was observed in 17 of 30 patients with high-degree TSS (56.7%) and 13 of 23 patients with low-degree TSS (56.5%). The incidence of WM change was significantly higher in the above two patient groups than in the HC group (9 of 40; 22.5%; $P < 0.05$) (**Figure 2**).

DISCUSSION

In this study, we investigated brain perfusion and WM changes in venous PT patients with TSS. The results indicated that as the severity of TSS increased and overall venous drainage concomitantly decreased, the CBF values of the GM, WM and whole brain were significantly decreased. Additionally, the incidence of cloud-like WM hyperintensity was significantly higher in patients with TSS than in HCs. These findings confirm that TSS in venous PT patients may lead to pathological brain changes.

TABLE 2 | CBF measurement among the three groups.

	High-degree TSS	Low-degree TSS	HC	P^a
Whole brain CBF (ml/100 g/min)	45.68 ± 5.58	50.30 ± 6.03	51.58 ± 7.29	0.001
GM CBF (ml/100 g/min)	49.08 ± 6.26	54.04 ± 6.45	55.03 ± 7.91	0.002
WM CBF (ml/100 g/min)	38.80 ± 3.90	41.97 ± 4.62	42.83 ± 6.03	0.005

The data are presented as mean ± standard deviation.
TSS, Transverse sinus stenosis; GM, gray matter; WM, white matter; HC, healthy control; CBF, cerebral blood flow.
[a]*One-way analysis of variance.*

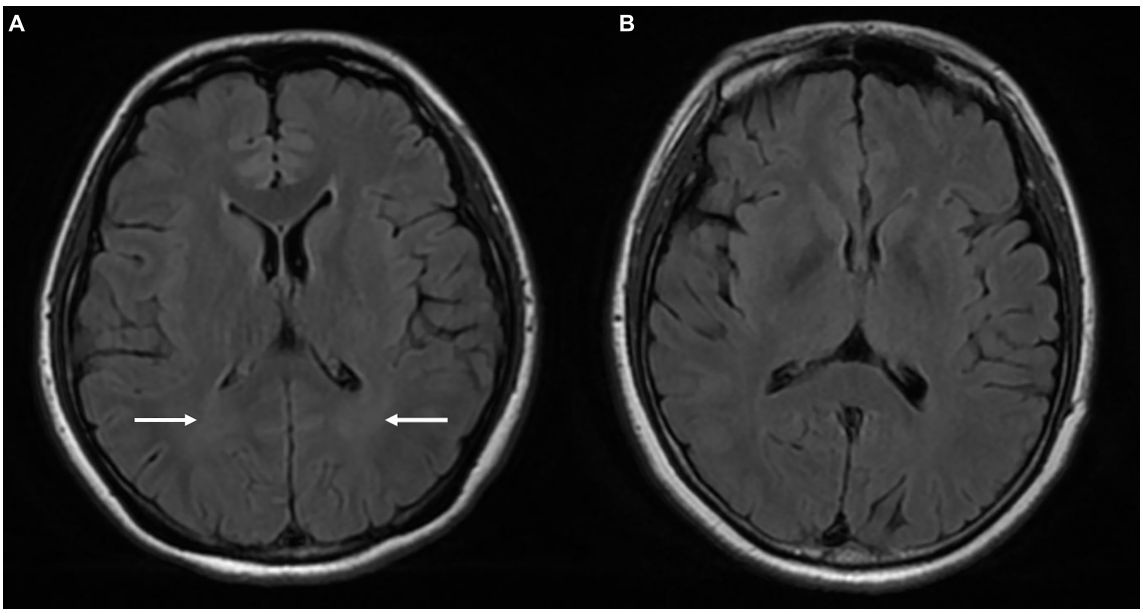

FIGURE 2 | Comparison of the MRI findings between a 33-year-old female patient with TSS **(A)** and a 42-year-old female healthy control **(B)**. Venous PT patient with TSS: T2 FLAIR **(A)** shows symmetrical cloud-like WM hyperintensity in the bilateral periventricular area (white arrow) that was absent in the healthy control **(B)**. PT, pulsatile tinnitus; TSS, transverse sinus stenosis; FLAIR, fluid attenuated inversion recovery; WM, white matter.

Venous PT is related to abnormal hemodynamics caused by different morphological changes (Li et al., 2021), including TSS, sigmoid sinus dehiscence with and without diverticulum, and jugular bulb abnormality (Dong et al., 2015; Kao et al., 2017; Hewes et al., 2020). TSS is one of the most common morphological abnormalities of venous PT and a cause of venous PT. Hewes et al. (2020) found that 84.6% of these patients had different degrees of bilateral TSS. After stent placement, the blood flow pattern became more regular (Han et al., 2017) and the PT disappeared immediately (Baomin et al., 2014). Therefore, TSS plays an essential role in the pathophysiology of venous PT.

Previous studies have reported decreased brain perfusion in patients with extracranial venous drainage disorder (Garaci et al., 2012; Zhou et al., 2019). Moreover, after stent placement or surgical restoration, brain hypoperfusion significantly improved or even disappeared (Zamboni et al., 2016; Zhou et al., 2019). Regarding pathophysiological mechanism, Zhou et al. (2019) believed that cerebral venous outflow disorder may contribute to increased intracranial venous pressure and that long-term venous hypertension reduces brain perfusion and disruption of the intracranial microvasculature. However, the above studies all used invasive examination including single-photon emission computed tomography (SPECT) and dynamic susceptibility contrast (DSC) MRI. Furthermore, these studies used semiquantitative or region-of-interest-based methods to assess CBF; these methods do not provide an accurate and comprehensive reflection of brain perfusion status. In this study, we used the ASL technique to non-invasively and quantitatively evaluate the CBF of the GM, WM and whole brain. Compared with HCs, patients with high-degree TSS showed significantly decreased CBF in the GM, WM and whole brain, demonstrating that TSS can lead to decreased brain perfusion. We also found that the patients with high-degree TSS showed significantly decreased CBF in whole brain and GM compared with the patients with low-degree TSS, and no significant difference was found between the patients with low-degree TSS and the HCs. This finding indicates that only a certain degree of TSS can lead to a significant decrease in brain perfusion. In contrast to the whole brain and GM, no significant difference was found in WM CBF between the patients with low-degree and high-degree TSS. Because the CBF of WM is significantly lower than that of GM under physiological conditions (Puig et al., 2020), we speculate that, in the two PT subgroups, the difference in WM CBF caused by TSS was too small to reach a statistical level.

Previous studies have mainly focused on the effects of aging and arterial diseases including cerebral small vessel disease, large vessel occlusion or stenosis on the WM (Lamar et al., 2010; Fennema-Notestine et al., 2016; Wang et al., 2016; Mistry et al., 2020). Chung et al. (2011) found that more severe age-related WM changes were observed in subjects with IJV reflux. This finding links WM changes with cerebral venous outflow disorder. Subsequently, their study further revealed that compared with patients with negative IJV reflux, the WM changes in Alzheimer's disease (AD) patients with positive IJV reflux showed an increasing trend, indicating that cerebral venous outflow disorder may be involved in forming WM changes in AD patients (Chung et al., 2014). Zhou et al. (2019) found that 95.3% of patients with symptomatic IJV stenosis had bilateral symmetrical cloud-like WM hyperintensity. Bai et al. (2019) further found that cloud-like WM hyperintensity is a common feature of patients with IJV stenosis and patients with TSS.

However, the above two studies did not include a control group for comparative analysis. In the present study, we found that the incidence of cloud-like WM hyperintensity is significantly higher in patients with TSS than in HCs. In contrast to the previous study, the participants in this study were relatively young (venous PT patients: 35.5 ± 7.0 years; HCs: 37.9 ± 6.7 years) and had no history of AD or arterial diseases. Currently, the underlying mechanism of the formation of cloud-like WM hyperintensity remains unclear. Zhou et al. (2019) believed that decreased brain perfusion was usually related to the formation of white matter lesions, particularly deep white matter lesions. We speculate that the relationships among decreased CBF, cloud-like WM hyperintensity, and TSS are as follows: TSS may inhibit the outflow of deoxyhemoglobin-rich venous blood and flow of hemoglobin-rich arterial blood into capillaries. These effects may affect the oxygen exchange between blood and brain tissues, resulting in decreased CBF using the ASL technique; long-term ischemia and hypoxia may lead to the demyelination of WM (Bai et al., 2019; Zhou et al., 2019).

In this study, we used the ASL technique, which uses arterial blood water as endogenous tracer (Binnewijzend et al., 2013), to non-invasively and quantitatively measure CBF. In contrast to traditional perfusion imaging techniques such as SPECT, dynamic contrast-enhanced MRI and DSC MRI, ASL can be used to perform repeated studies on subjects because of the lack of radioactivity and the non-use of exogenous contrast agents. This technique has been widely used in brain tumors, epilepsy, neurodegenerative and cerebrovascular diseases (Haller et al., 2016; Delgado et al., 2018; Barzgari et al., 2019) and provides valuable information for clinicians. Currently, the treatment principle for venous PT with TSS is based on eliminating PT without evaluating the brain perfusion and WM changes. Therefore, the decision to perform sigmoid sinus wall reconstruction or stent implantation does not depend on the presence or absence of brain change. In this study, however, decreased CBF and cloud-like WM hyperintensity in venous PT patients with TSS deserve more attention from clinicians. Appropriate and early intervention may help improve the neuropathological progress of patients.

This study has several limitations. First, because of the limited sample size, the effect of gender on CBF was not investigated. More venous PT patients will be included and grouped by gender. Second, previous studies have found that venous PT and idiopathic intracranial hypertension overlap in demography (Lansley et al., 2017; Hewes et al., 2020), that is, idiopathic intracranial hypertension may be present in venous PT patients. Idiopathic intracranial hypertension may affect brain perfusion (Bicakci et al., 2006). In this study, all the patients had no clinical symptoms of idiopathic intracranial hypertension; thus, lumbar puncture was not performed. Third, other comorbidities, such as diabetes and hypertension, can cause WM signal change (Fennema-Notestine et al., 2016). All the subjects in this study were young and middle-aged (patients: 35.5 ± 7.0 years; HCs: 37.9 ± 6.7 years), and none had systemic diseases such as hypertension, hyperlipidemia, and diabetes. Additionally, this is a cross-sectional study. We will enroll patients after the resolution of TSS and evaluate their neuroimaging characteristics to further verify the influence of TSS on the central nervous system.

CONCLUSION

In summary, we found that TSS in venous PT patients can lead to decreased CBF and cloud-like WM hyperintensity. These representative neuroimaging findings may help understand the pathological TSS in venous PT.

DATA AVAILABILITY STATEMENT

The raw data supporting the conclusions of this article will be made available by the authors, without undue reservation.

ETHICS STATEMENT

The studies involving human participants were reviewed and approved by the Ethics Committee of Beijing Friendship Hospital. The patients/participants provided their written informed consent to participate in this study.

AUTHOR CONTRIBUTIONS

XL, PZ, and ZW: conceptualization. XL and PZ: data curation and methodology. XL: formal analysis, investigation, visualization, software, and writing–original draft. RZ, JX, ZY, SG, and ZW: funding acquisition. HD, HL, XQ, XM, and CD: project administration. ZY, SG, and ZW: resources and supervision. ZW: validation. PZ and ZW: writing–review and editing. All authors contributed to the article and approved the submitted version.

FUNDING

This study was supported by the National Natural Science Foundation of China (Grant No. 61931013) and Beijing Scholars Program (No. [2015] 160).

SUPPLEMENTARY MATERIAL

The Supplementary Material for this article can be found online at: https://www.frontiersin.org/articles/10.3389/fnins.2021.732113/full#supplementary-material

REFERENCES

Bae, S. C., Kim, D. K., Yeo, S. W., Park, S. Y., and Park, S. N. (2015). Single-center 10-year experience in treating patients with vascular tinnitus: diagnostic approaches and treatment outcomes. *Clin. Exp. Otorhinolaryngol.* 8, 7–12. doi: 10.3342/ceo.2015.8.1.7

Bai, C., Xu, Y., Zhou, D., Ding, J., Yang, Q., Ding, Y., et al. (2019). The comparative analysis of non-thrombotic internal jugular vein stenosis and cerebral venous

sinus stenosis. *J. Thromb. Thrombolysis* 48, 61–67. doi: 10.1007/s11239-019-01820-1

Baomin, L., Yongbing, S., and Xiangyu, C. (2014). Angioplasty and stenting for intractable pulsatile tinnitus caused by dural venous sinus stenosis: a case series report. *Otol. Neurotol.* 35, 366–370. doi: 10.1097/MAO.0b013e3182990d52

Barzgari, A., Sojkova, J., Maritza Dowling, N., Pozorski, V., Okonkwo, O. C., Starks, E. J., et al. (2019). Arterial spin labeling reveals relationships between resting cerebral perfusion and motor learning in Parkinson's disease. *Brain Imaging Behav.* 13, 577–587. doi: 10.1007/s11682-018-9877-1

Bicakci, K., Bicakci, S., and Aksungur, E. (2006). Perfusion and diffusion magnetic resonance imaging in idiopathic intracranial hypertension. *Acta Neurol. Scand.* 114, 193–197. doi: 10.1111/j.1600-0404.2006.00702.x

Binnewijzend, M. A., Kuijer, J. P., Benedictus, M. R., van der Flier, W. M., Wink, A. M., Wattjes, M. P., et al. (2013). Cerebral blood flow measured with 3D pseudocontinuous arterial spin-labeling MR imaging in Alzheimer disease and mild cognitive impairment: a marker for disease severity. *Radiology* 267, 221–230. doi: 10.1148/radiol.12120928

Carvalho, G. B., Matas, S. L., Idagawa, M. H., Tibana, L. A., de Carvalho, R. S., Silva, M. L., et al. (2017). A new index for the assessment of transverse sinus stenosis for diagnosing idiopathic intracranial hypertension. *J. Neurointerv. Surg.* 9, 173–177. doi: 10.1136/neurintsurg-2016-012605

Chung, C. P., Beggs, C., Wang, P. N., Bergsland, N., Shepherd, S., Cheng, C. Y., et al. (2014). Jugular venous reflux and white matter abnormalities in Alzheimer's disease: a pilot study. *J. Alzheimers Dis.* 39, 601–609. doi: 10.3233/JAD-131112

Chung, C. P., Wang, P. N., Wu, Y. H., Tsao, Y. C., Sheng, W. Y., Lin, K. N., et al. (2011). More severe white matter changes in the elderly with jugular venous reflux. *Ann. Neurol.* 69, 553–559. doi: 10.1002/ana.22276

Delgado, A. F., De Luca, F., Hanagandi, P., van Westen, D., and Delgado, A. F. (2018). Arterial spin-labeling in children with brain tumor: a meta-analysis. *AJNR Am. J. Neuroradiol.* 39, 1536–1542. doi: 10.3174/ajnr.A5727

Ding, J., Guan, J., Ji, X., and Meng, R. (2019). Cerebral venous sinus stenosis may cause intracranial arterial hypoperfusion. *Clin. Neuroradiol.* 30, 409–411. doi: 10.1007/s00062-019-00833-w

Dong, C., Zhao, P., Yang, J., Liu, Z., and Wang, Z. (2015). Incidence of vascular anomalies and variants associated with unilateral venous pulsatile tinnitus in 242 patients based on dual-phase contrast-enhanced computed tomography. *Chin Med. J. (Engl.)* 128, 581–585. doi: 10.4103/0366-6999.151648

Durst, C. R., Ornan, D. A., Reardon, M. A., Mehndiratta, P., Mukherjee, S., Starke, R. M., et al. (2016). Prevalence of dural venous sinus stenosis and hypoplasia in a generalized population. *J. Neurointerv. Surg.* 8, 1173–1177. doi: 10.1136/neurintsurg-2015-012147

Eisenman, D. J., Raghavan, P., Hertzano, R., and Morales, R. (2018). Evaluation and treatment of pulsatile tinnitus associated with sigmoid sinus wall anomalies. *Laryngoscope* 128 Suppl 2, S1–S13. doi: 10.1002/lary.27218

Farb, R. I., Vanek, I., Scott, J. N., Mikulis, D. J., Willinsky, R. A., Tomlinson, G., et al. (2003). Idiopathic intracranial hypertension: the prevalence and morphology of sinovenous stenosis. *Neurology* 60, 1418–1424. doi: 10.1212/01.wnl.0000066683.34093.e2

Favoni, V., Pierangeli, G., Cirillo, L., Toni, F., Abu-Rumeileh, S., La Morgia, C., et al. (2019). Transverse sinus stenosis in refractory chronic headache patients: an observational study. *Front. Neurol.* 10:1287. doi: 10.3389/fneur.2019.01287

Fennema-Notestine, C., McEvoy, L. K., Notestine, R., Panizzon, M. S., Yau, W. W., Franz, C. E., et al. (2016). White matter disease in midlife is heritable, related to hypertension, and shares some genetic influence with systolic blood pressure. *Neuroimage Clin.* 12, 737–745. doi: 10.1016/j.nicl.2016.10.001

Garaci, F. G., Marziali, S., Meschini, A., Fornari, M., Rossi, S., Melis, M., et al. (2012). Brain hemodynamic changes associated with chronic cerebrospinal venous insufficiency are not specific to multiple sclerosis and do not increase its severity. *Radiology* 265, 233–239. doi: 10.1148/radiol.12112245

Guo, X., Zhu, J., Zhang, N., Zhang, L., Qi, Y., Cai, H., et al. (2018). Altered neurovascular coupling in neuromyelitis optica. *Hum. Brain Mapp.* 40, 976–986. doi: 10.1002/hbm.24426

Ha, J. Y., Choi, Y. H., Lee, S., Cho, Y. J., Cheon, J. E., Kim, I. O., et al. (2019). Arterial spin labeling MRI for quantitative assessment of cerebral perfusion before and after cerebral revascularization in children with moyamoya disease. *Korean J. Radiol.* 20, 985–996. doi: 10.3348/kjr.2018.0651

Haller, S., Zaharchuk, G., Thomas, D. L., Lovblad, K. O., Barkhof, F., and Golay, X. (2016). Arterial spin labeling perfusion of the brain: emerging clinical applications. *Radiology* 281, 337–356. doi: 10.1148/radiol.2016150789

Han, Y., Yang, Q., Yang, Z., Xia, J., Su, T., Yu, J., et al. (2017). Computational fluid dynamics simulation of hemodynamic alterations in sigmoid sinus diverticulum and ipsilateral upstream sinus stenosis after stent implantation in patients with pulsatile tinnitus. *World Neurosurg.* 106, 308–314. doi: 10.1016/j.wneu.2017.06.168

Hewes, D., Morales, R., Raghavan, P., and Eisenman, D. J. (2020). Pattern and severity of transverse sinus stenosis in patients with pulsatile tinnitus associated with sigmoid sinus wall anomalies. *Laryngoscope* 130, 1028–1033. doi: 10.1002/lary.28168

Hofmann, E., Behr, R., Neumann-Haefelin, T., and Schwager, K. (2013). Pulsatile tinnitus: imaging and differential diagnosis. *Deutsch. Arztebl. Int.* 110, 451–458. doi: 10.3238/arztebl.2013.0451

Kao, E., Kefayati, S., Amans, M. R., Faraji, F., Ballweber, M., Halbach, V., et al. (2017). Flow patterns in the jugular veins of pulsatile tinnitus patients. *J. Biomech.* 52, 61–67. doi: 10.1016/j.jbiomech.2016.12.008

Lamar, M., Charlton, R. A., Morris, R. G., and Markus, H. S. (2010). The impact of subcortical white matter disease on mood in euthymic older adults: a diffusion tensor imaging study. *Am. J. Geriatr. Psychiatry* 18, 634–642. doi: 10.1097/JGP.0b013e3181cabad1

Lansley, J. A., Tucker, W., Eriksen, M. R., Riordan-Eva, P., and Connor, S. E. J. (2017). Sigmoid Sinus diverticulum, dehiscence, and venous sinus stenosis: potential causes of pulsatile tinnitus in patients with idiopathic intracranial hypertension? *AJNR Am. J. Neuroradiol.* 38, 1783–1788. doi: 10.3174/ajnr.a5277

Li, X., Qiu, X., Ding, H., Lv, H., Zhao, P., Yang, Z., et al. (2021). Effects of different morphologic abnormalities on hemodynamics in patients with venous pulsatile tinnitus: a four-dimensional flow magnetic resonance imaging study. *J. Magn. Reson. Imaging* 53, 1744–1751. doi: 10.1002/jmri.27503

Lyu, A. R., Park, S. J., Kim, D., Lee, H. Y., and Park, Y. H. (2018). Radiologic features of vascular pulsatile tinnitus - suggestion of optimal diagnostic image workup modalities. *Acta Otolaryngol.* 138, 128–134. doi: 10.1080/00016489.2017.1385847

Mistry, E. A., Mistry, A. M., Mehta, T., Arora, N., Starosciak, A. K., La Rosa, F., et al. (2020). White matter disease and outcomes of mechanical thrombectomy for acute ischemic stroke. *AJNR Am. J. Neuroradiol.* 41, 639–644. doi: 10.3174/ajnr.A6478

Morris, P. P., Black, D. F., Port, J., and Campeau, N. (2017). Transverse sinus stenosis is the most sensitive MR imaging correlate of idiopathic intracranial hypertension. *AJNR Am. J. Neuroradiol.* 38, 471–477. doi: 10.3174/ajnr.a5055

Puig, O., Henriksen, O. M., Vestergaard, M. B., Hansen, A. E., Andersen, F. L., Ladefoged, C. N., et al. (2020). Comparison of simultaneous arterial spin labeling MRI and (15)O-H2O PET measurements of regional cerebral blood flow in rest and altered perfusion states. *J. Cereb. Blood Flow Metab.* 40, 1621–1633. doi: 10.1177/0271678X19874643

Saindane, A. M., Bruce, B. B., Desai, N. K., Roller, L. A., Newman, N. J., and Biousse, V. (2014). Transverse sinus stenosis in adult patients with Chiari malformation type I. *AJR Am. J. Roentgenol.* 203, 890–896. doi: 10.2214/AJR.14.12528

Scott, J. N., and Farb, R. I. (2003). Imaging and anatomy of the normal intracranial venous system. *Neuroimaging Clin. N. Am.* 13, 1–12. doi: 10.1016/s1052-5149(02)00062-x

Wang, G. P., Zeng, R., Liu, Z. H., Liang, X. H., Xian, J. F., Wang, Z. C., et al. (2014). Clinical characteristics of pulsatile tinnitus caused by sigmoid sinus diverticulum and wall dehiscence: a study of 54 patients. *Acta Otolaryngol.* 134, 7–13. doi: 10.3109/00016489.2013.831479

Wang, M., Norman, J. E., Srinivasan, V. J., and Rutledge, J. C. (2016). Metabolic, inflammatory, and microvascular determinants of white matter disease and cognitive decline. *Am. J. Neurodegener. Dis.* 5, 171–177.

Werner, J. D., Siskin, G. P., Mandato, K., Englander, M., and Herr, A. (2011). Review of venous anatomy for venographic interpretation in chronic cerebrospinal venous insufficiency. *J. Vasc. Interv. Radiol.* 22, 1681–1690. doi: 10.1016/j.jvir.2011.08.018

Zamboni, P., Menegatti, E., Cittanti, C., Sisini, F., Gianesini, S., Salvi, F., et al. (2016). Fixing the jugular flow reduces ventricle volume and improves brain perfusion. *J. Vasc. Surg. Venous Lymphat. Disord.* 4, 434–445. doi: 10.1016/j.jvsv.2016.06.006

Zhao, P., Lv, H., Dong, C., Niu, Y., Xian, J., and Wang, Z. (2016). CT evaluation of sigmoid plate dehiscence causing pulsatile tinnitus. *Eur. Radiol.* 26, 9–14. doi: 10.1007/s00330-015-3827-8

Zhou, D., Ding, J., Asmaro, K., Pan, L., Ya, J., Yang, Q., et al. (2019). Clinical characteristics and neuroimaging findings in internal jugular venous outflow disturbance. *Thromb. Haemost.* 119, 308–318. doi: 10.1055/s-0038-1676815

Zhuo, C., Zhu, J., Qin, W., Qu, H., Ma, X., and Yu, C. (2017). Cerebral blood flow alterations specific to auditory verbal hallucinations in schizophrenia. *Br. J. Psychiatry* 210, 209–215. doi: 10.1192/bjp.bp.115.174961

Conflict of Interest: The authors declare that the research was conducted in the absence of any commercial or financial relationships that could be construed as a potential conflict of interest.

The reviewer SS has declared a shared parent affiliation with the authors at the time of the review.

frontiers in Neuroscience

ORIGINAL RESEARCH
published: 16 December 2021
doi: 10.3389/fnins.2021.792264

Aberrant Interhemispheric Functional Connectivity in Diabetic Retinopathy Patients

Song Wan[1†], Wen Qing Xia[2†] and Yu Lin Zhong[1]*

[1] Department of Ophthalmology, Jiangxi Provincial People's Hospital, Nanchang, China, [2] Department of Endocrinology, Nanjing First Hospital, Nanjing Medical University, Nanjing, China

Background: Accumulating lines of evidence demonstrated that diabetic retinopathy (DR) patients trigger abnormalities in brain's functional connectivity (FC), whereas the alterations of interhemispheric coordination pattern occurring in DR are not well understood. Our study was to investigate alterations of interhemispheric coordination in DR patients.

Methods: Thirty-four DR individuals (19 males and 15 females: mean age: 52.97 ± 8.35 years) and 37 healthy controls (HCs) (16 males and 21 females; mean age: 53.78 ± 7.24 years) were enrolled in the study. The voxel-mirrored homotopic connectivity (VMHC) method was conducted to investigate the different interhemispheric FC between two groups. Then, the seed-based FC method was applied to assess the different FCs with region of interest (ROI) in the brain regions of decreased VMHC between two groups.

Results: Compared with HC groups, DR groups showed decreased VMHC values in the bilateral middle temporal gyrus (MTG), lingual/calcarine/middle occipital gyrus (LING/CAL/MOG), superior temporal gyrus (STG), angular (ANG), postcentral gyrus (PosCG), inferior parietal lobule (IPL), and precentral gyrus (PreCG). Meanwhile, altered FC includes the regions of auditory network, visual network, default mode network, salience network, and sensorimotor network. Moreover, a significant positive correlation was observed between the visual acuity-oculus dexter (OD) and zVMHC values in the bilateral LING/CAL/MOG (r = 0.551, p = 0.001), STG (r = 0.426, p = 0.012), PosCG (r = 0.494, p = 0.003), and IPL (r = 0.459, p = 0.006) in DR patients.

Conclusion: Our results highlighted that DR patients were associated with substantial impairment of interhemispheric coordination in auditory network, visual network, default mode network, and sensorimotor network. The VMHC might be a promising therapeutic target in the intervention of brain functional dysfunction in DR patients.

Keywords: diabetic retinopathy, voxel-mirrored homotopic connectivity, functional magnetic resonance imaging, functional network, functional connectivity

OPEN ACCESS

Edited by:
Han Lv,
Capital Medical University, China

Reviewed by:
Tianming Huo,
Wuhan University, China
Hai Jun Li,
Nanchang University, China

****Correspondence:***
Yu Lin Zhong
804722489@qq.com

† These authors have contributed equally to this work

Specialty section:
This article was submitted to Perception Science, a section of the journal Frontiers in Neuroscience

Received: *10 October 2021*
Accepted: *09 November 2021*
Published: *16 December 2021*

Citation:
Wan S, Xia WQ and Zhong YL (2021) Aberrant Interhemispheric Functional Connectivity in Diabetic Retinopathy Patients. Front. Neurosci. 15:792264. doi: 10.3389/fnins.2021.792264

INTRODUCTION

Diabetic retinopathy (DR) is a serious diabetic-related retinal disease (Zhang et al., 2010). The prevalence of DR is 34.6% among diabetes patients worldwide (Yau et al., 2012). The main pathophysiological mechanisms and clinical features of DR are retinal microangiopathy and vision loss. Retinal neurodegeneration is an important pathogenesis of DR and is characterized by glial cell activation and neuronal apoptosis. Furthermore, DR patients were accompanied by cognitive decline. Recently, growing lines of evidence demonstrated that DR is associated with an increased risk of stroke (Hagg et al., 2013; Wong et al., 2020). Accumulating studies demonstrated that DR is closely related to the occurrence of neurodegenerative diseases (Lynch and Abramoff, 2017; Sundstrom et al., 2018). DR patients are at a high risk for neurodegenerative disorder. However, the exact neural mechanisms of neurodegenerative disorder in DR patients remain unclear.

The functional magnetic resonance imaging method provides a new opportunity for non-invasive research on functional and structural changes of brain *in vivo*. Qi et al. (2020) demonstrated that DR had significantly altered brain neural activity changes in the middle occipital gyrus, the left cerebellum, the left inferior temporal gyrus, and the left hippocampus. Dai et al. (2017) reported that DR patients had abnormal functional connectivity (FC) within visual and cognition networks. Meanwhile, Yu et al. (2020) found that the DR group showed different FCs between the V1 and visual-related brain regions. Moreover, Huang et al. (2019) reported that the DR group showed reduction in the efficiency of functional brain network, relative to the healthy control (HC) group. Thus, existing studies are mainly focused on local brain activity and FC in DR patients. The functional architecture of interhemispheric changes in DR patients remains unknown.

Functional homotopy is a basic principle of the brain's intrinsic functional architecture (Biswal et al., 1995). The consistency of interhemispheric FC is closely related to a variety of neurophysiological function. The corpus callosum plays an important role in the interhemispheric FC, and the corpus callosum dysfunction might lead to impaired interhemispheric coordination within large-scale brain networks (Roland et al., 2017; Bartha-Doering et al., 2021). Recently, the voxel-mirrored homotopic connectivity (VMHC) method quantified the resting-state FC between hemispheres to reflect the interhemispheric coordination pattern. Prior neuroimaging studies revealed that diabetes patients showed abnormal interhemispheric FC, which is closely related to cognitive impairment. Cui et al. (2021) reported that diabetes patients had decreased interhemispheric FC between bilateral lingual gyrus and sensorimotor cortex. Zhang et al. (2021) also found that decreased VMHC values within the default mode network and middle temporal gyrus (MTG) might serve as a sensitive biomarker for cognitive decline. The VMHC method has been successfully applied to investigate the interhemispheric FC changes in anisometropic and strabismic amblyopia (Liang et al., 2017), Alzheimer's disease (Wang et al., 2015), and alcohol dependence (Guo et al., 2019). DR is a serious complication of diabetes. Thus, the DR patients may be associated with different VMHC patterns from diabetes

TABLE 1 | Behavioral data between two groups.

	DR group	HC group	*t*-values	*p*-values
Gender (male/female)	19/15	16/21	N/A	N/A
Age (years)	52.97 ± 8.35	53.78 ± 7.24	−0.412	0.681
Duration of diabetes (years)	10.44 ± 6.03	N/A	N/A	N/A
BCVA-OD	0.47 ± 0.27	1.23 ± 0.23	−12.593	<0.001
BCVA-OS	0.44 ± 0.31	1.22 ± 0.23	−12.121	<0.001
HbA1c (%)	7.69 ± 2.44	N/A	N/A	N/A

Behavioral data (means ± SD). DR, diabetic retinopathy; HC, healthy control; N/A, not applicable; BCVA, best corrected visual acuity; OD, oculus dexter; OS, oculus sinister; Hb, glycosylated hemoglobin.

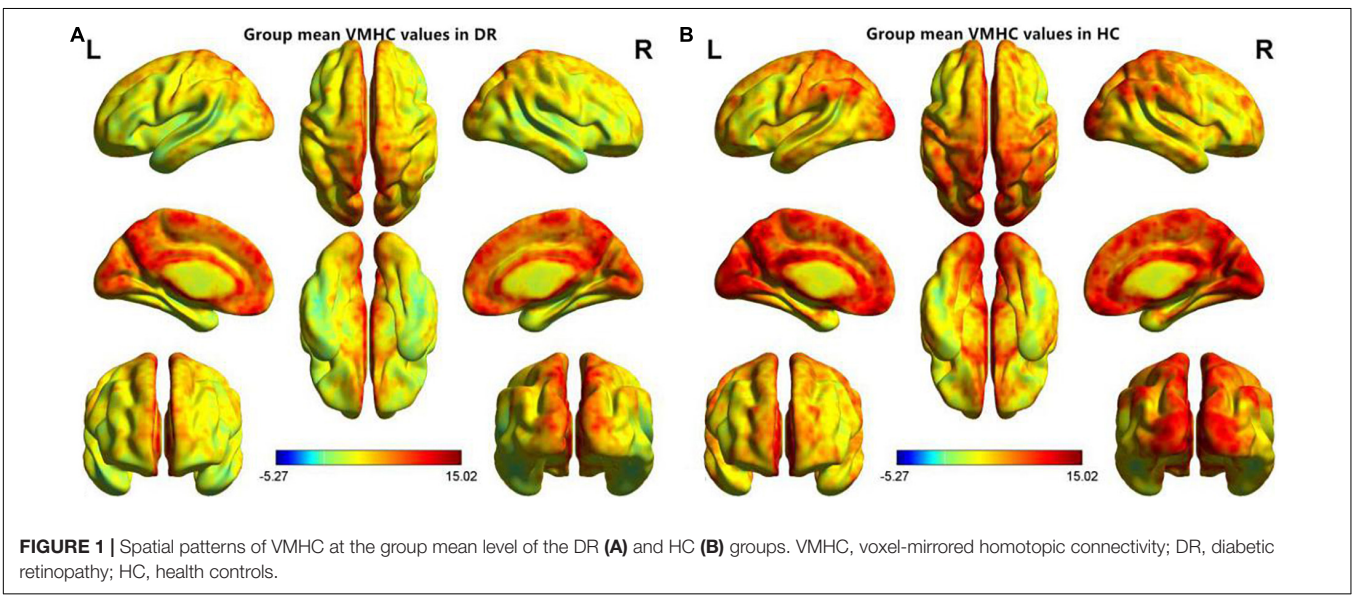

FIGURE 1 | Spatial patterns of VMHC at the group mean level of the DR **(A)** and HC **(B)** groups. VMHC, voxel-mirrored homotopic connectivity; DR, diabetic retinopathy; HC, health controls.

patients without retinopathy. We hypothesized that DR patients may lead to interhemispheric FC changes within cognition-related brain region.

Based on the above assumptions, our study aimed to determine whether DR patients were associated with abnormal interhemispheric FC. Moreover, the seed-based FC method was used to assess the FC between the seed regions (brain regions of different VMHC values between two groups) and whole brain. Our results might shed new light on underlying neural mechanisms of cognitive decline in DR patients.

MATERIALS AND METHODS

Subjects

Thirty-four DR individuals (19 males and 15 females: mean age: 52.97 ± 8.35 years) and 37 HCs (16 males and 21 females; mean age: 53.78 ± 7.24 years) matched for age, sex, and education participated in the study.

The inclusion criteria of DR patients were as follows (Zhang et al., 2010): fasting plasma glucose ≥7.0 mmol/L, random plasma glucose ≥11.1 mmol/L, or 2-h glucose ≥11.1 mmol/L (Yau et al., 2012); the DR patients showed microaneurysms, hard exudates, and retinal hemorrhages.

All HCs met the following criteria (Zhang et al., 2010): fasting plasma glucose <7.0 mmol/L, random plasma glucose <11.1 mmol/L, and HbA1c <6.5% (Yau et al., 2012); no ocular diseases (Wong et al., 2020); binocular visual acuity ≥1.0; and (Hagg et al., 2013) no ocular surgical history.

MRI Parameters

MRI scanning was performed on a 3-T MR scanner (Discovery MR 750W system; GE Healthcare, Milwaukee,

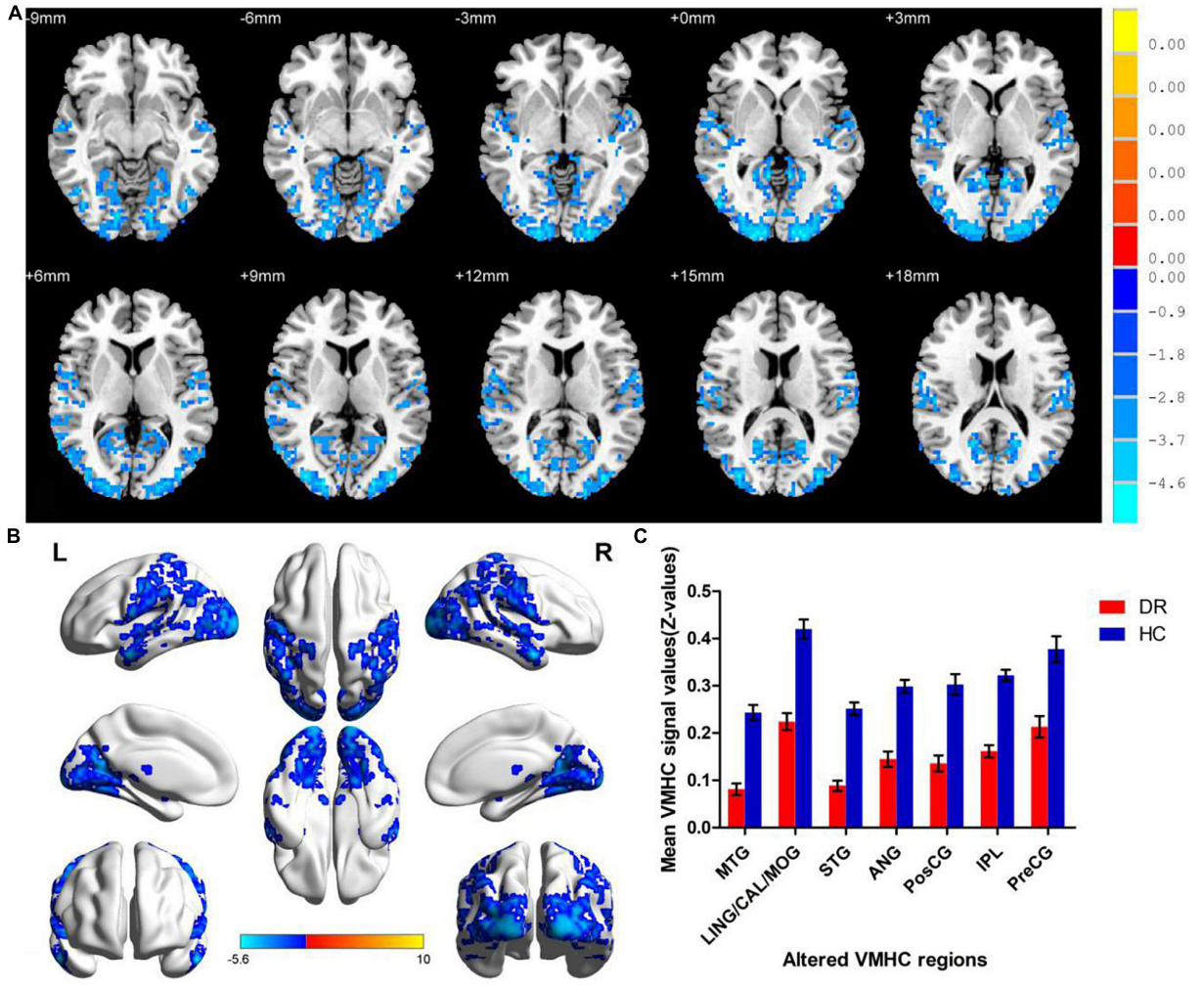

FIGURE 2 | Significant zVMHC maps differences between two groups **(A,B)**. The mean values of altered VMHC values between two groups **(C)**. VMHC, voxel-mirrored homotopic connectivity; DR, diabetic retinopathy; HCs, healthy controls; L, left hemisphere; R, right hemisphere; BA, Brodmann's area. MTG, middle temporal gyrus; LING/CAL/MOG, lingual/calcarine/middle occipital gyrus; STG, superior temporal gyrus; ANG, angular; PosCG, postcentral gyrus; IPL, inferior parietal lobule; PreCG, precentral gyrus.

WI, United States) with an eight-channel head coil. The T1 images have the following parameters: repetition time = 8.5 ms, echo time = 3.3 ms, thickness = 1.0 mm, gap = 0 mm, acquisition matrix = 256 × 256, field of view = 240 mm × 240 mm, and flip angle = 12°; functional images have the following parameters: repetition time = 2,000 ms, echo time = 25 ms, thickness = 3.0 mm, gap = 1.2 mm, acquisition matrix = 64 × 64, field of view = 240 mm × 240 mm, flip angle = 90°, voxel size = 3.6 mm × 3.6 mm × 3.6 mm, and 35 axial slices.

fMRI Scanning Steps

All subjects were asked to keep in the supine position and lay still, close their eyes without moving and falling asleep, and not to think of anything in particular during MRI scanning (Zhang et al., 2010; Yau et al., 2012). Before MRI scanning, we would tell the whole experimental process in detail to all subjects (Wong et al., 2020). To avoid noise, the subjects wore earplugs during MRI scanning.

fMRI Data Preprocessing

The preprocessing of fMRI data was performed with the toolbox for Data Processing & Analysis of Brain Imaging (DPABI[1]) (Yan et al., 2016) with the following steps (Zhang et al., 2010): The whole BOLD pictures of each subjects were removed first 10 points picture and then the remained BOLD picture were slice timing, motion corrected and realigned (Yau et al., 2012); normalized data [in Montreal Neurological Institute (MNI) 152 space] were re-sliced (Wong et al., 2020); regress out several covariates [Friston 24-Parameter Model (Friston et al., 1996) includes six head motion parameters, mean framewise displacement (FD), and global brain signal] (Hagg et al., 2013); data with linear trend were removed, and temporal band pass was filtered (0.01–0.1 Hz).

[1]http://www.rfmri.org/dpabi

TABLE 2 | Significant difference in VMHC between two groups.

Condition/brain regions	BA	Peak *t*-scores	MNI coordinates (*x*, *y*, *z*)	Cluster size (voxels)
DR < HC				
MTG	21	−5.141	±54, 0, −21	50
LING/CAL/MOG	18,19	−5.596	±9, −54, 3	1,144
STG	21	−4.643	±60, −9, −9	300
ANG	39	−4.635	±51, −54, 27	95
PosCG	3	−4.140	±45, −15, 39	130
IPL	40	−4.780	±51, −48, 54	312
PreCG	4	−3.683	±21, −30, 72	43

t: statistical value of peak voxels indicating different VMHC values. VMHC, voxel-mirrored homotopic connectivity; DR, diabetic retinopathy; HCs, healthy controls; MNI, Montreal Neurological Institute; BA, Brodmann's area; MTG, middle temporal gyrus; LING/CAL/MOG, lingual/calcarine/middle occipital gyrus; STG, superior temporal gyrus; ANG, angular; PosCG, postcentral gyrus; IPL, inferior parietal lobule; PreCG, precentral gyrus.

Voxel-Mirrored Homotopic Connectivity Analysis

According to a previous study (Zuo et al., 2010), VMHC was performed using the DPABI toolkit. The VMHC values were computed as the Pearson correlation between every pair of mirrored interhemispheric voxels' time series. All VMHC maps were *z*-transformed with Fisher's *r*-to-*z* transformation.

Resting State Functional Connectivity Analysis

After fMRI data were normalized, the fMRI map was smoothed with a 6-mm full-width-half-maximum Gaussian kernel, several covariates were regressed out, and temporal band pass was filtered (0.01–0.1 Hz). The brain regions of different VMHC values were defined as regions of interest (ROIs). Then, the

TABLE 3 | Significant difference in FC between two groups in the seed-based analysis.

Seeds	Brain regions	BA	Peak *t*-scores	MNI coordinates (*x*, *y*, *z*)	Cluster size (voxels)
R-MTG	L-MTG	21	−5.6356	−54, 0, −21	335
L-MTG	R-MTG	21	−5.9625	54, 0, −21	355
R-LING/CAL/MOG	R-CER	–	4.1144	39, −63, −21	275
	L-PUT	–	3.744	−21, 15, −6	96
	L-CAL	18	−5.6603	−9, −54, 3	466
	R-CAU	–	5.2546	12, 6, 6	224
L-LING/CAL/MOG	B-LING	18	−5.1924	9, −54, 3	599
R-STG	L-MTG	21	−3.8746	−63, −6, −12	163
L-STG	R-TPOsup	38	−4.6008	48, 9, −21	286
	L-PreCG	3	4.2574	−42, −6, 27	96
	L-INS	–	3.7065	−30, 12, 0	65
R-ANG	R-ROL	–	4.1664	60, −3, 12	616
	R-IPL	7	4.5064	18, −45, 51	270
R-PosCG	L-THA	–	4.5859	−6, −6, 0	507
	L-PosCG	4	−5.3769	−57, −15, 18	1,149
	R-PCUN	7	4.4313	15, −63, 42	1,445
L-PosCG	R-LING	18	−3.3128	9, −75, −3	154
	L-ROL	–	−3.6437	−48, 0, 12	70
	L-PosCG	4	−3.8548	−57, −9, 18	187
	R-CUN	19	−3.9295	9, −87, 30	138
	R-PreCG	3	−4.9488	48, −12, 45	481
	L-PCC	–	3.8502	−3, −45, 24	348
R-IPL	R-PosCG	4	4.3822	30, −21, 21	313
L-IPL	L-IFGtriang	–	−4.3103	−33, 24, 27	517
R-PreCG	L-MTG	41	−3.7637	−51, −18, −3	297

t: statistical value of peak voxels indicating different FC values. VMHC, voxel-mirrored homotopic connectivity; DR, diabetic retinopathy; HCs, healthy controls; MNI, Montreal Neurological Institute; BA, Brodmann's area; MTG, middle temporal gyrus; LING/CAL/MOG, lingual/calcarine/middle occipital gyrus; STG, superior temporal gyrus; ANG, angular; PosCG, postcentral gyrus; IPL, inferior parietal lobule; PreCG, precentral gyrus; CER, cerebellum_Crus1; PUT, putamen; CAU, caudate; TPOsup, temporal pole (superior); INS, insula; ROL, rolandic operculum; THA, thalamus; PCUN, precuneus; CUN, cuneus; IFGtriang, inferior frontal gyrus (triangular); L, left; R, right; B, bilateral.

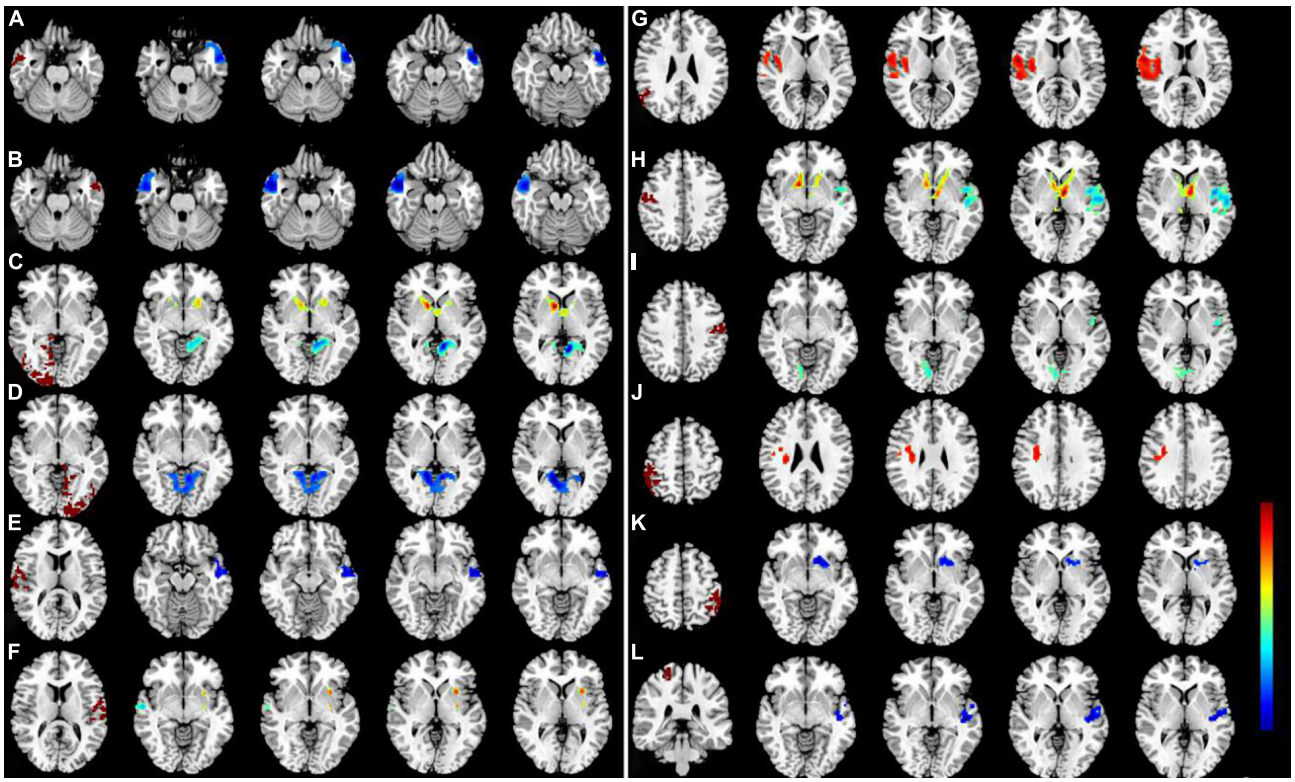

FIGURE 3 | Significant zFC map differences seeded as ROI in different VMHC regions between two groups. Significant different FC values ROI in R-MTG **(A)**, L-MTG **(B)**, R-LING/CAL/MOG **(C)**, R-LING/CAL/MOG **(D)**, R-STG **(E)**, L-STG **(F)**, R-ANG **(G)**, R-PosCG **(H)**, L-PosCG **(I)**, R-IPL **(J)**, L-IPL **(K)**, and R-PreCG **(L)**. VMHC, voxel-mirrored homotopic connectivity; ROI, region of interest; FC, functional connectivity; DR, diabetic retinopathy; HCs, healthy controls; MTG, middle temporal gyrus; LING/CAL/MOG, lingual/calcarine/middle occipital gyrus; STG, superior temporal gyrus; ANG, angular; PosCG, postcentral gyrus; IPL, inferior parietal lobule; PreCG, precentral gyrus.

resting state functional connectivity (RSFC) method was applied to assess the FC between the seed regions and whole brain to obtain FC maps.

Statistical Analysis

The χ^2 test and independent-samples *t*-test were applied to compare behavioral data between two groups.

One-sample *t*-test was conducted to assess intra-group patterns of zVMHC maps between two groups. Two-sample *t*-tests were conducted to assess different zVMHC and zFC between two groups (two-tailed, voxel-wise $p < 0.01$, GRF theory connected, cluster level, $p < 0.05$).

Pearson correlation was performed to investigate the relationship between the zVMHC values and clinical variables in DR groups.

RESULTS

Behavioral Data Comparison

We found the significant difference in best corrected visual acuity (BCVA)-oculus dexter (OD) ($p < 0.001$) and BCVA-oculus sinister (OS) ($p < 0.001$) between two groups. More details are shown in **Table 1**.

Voxel-Mirrored Homotopic Connectivity Differences

Similar spatial patterns of VMHC were found between two groups (**Figure 1**). Compared with HC groups,

TABLE 4 | Receiver operating characteristic curve analysis.

Condition/brain regions		AUC	*p*-values	95% CI
DR < HC	MTG	0.913	$p < 0.001$	0.850–0.976
DR < HC	LING/CAL/MOG	0.895	$p < 0.001$	0.821–0.969
DR < HC	STG	0.952	$p < 0.001$	0.906–0.998
DR < HC	ANG	0.888	$p < 0.001$	0.806–0.969
DR < HC	PosCG	0.837	$p < 0.001$	0.746–0.927
DR < HC	IPL	0.942	$p < 0.001$	0.893–0.991
DR < HC	PreCG	0.799	$p < 0.001$	0.697–0.902

ROC, receiver operating characteristic; CI, confidence interval; AUC, area under the curve; MTG, middle temporal gyrus; LING/CAL/MOG, lingual/calcarine/middle occipital gyrus; STG, superior temporal gyrus; ANG, angular; PosCG, postcentral gyrus; IPL, inferior parietal lobule; PreCG, precentral gyrus.

DR groups showed decreased VMHC values in the bilateral MTG, lingual/calcarine/middle occipital gyrus (LING/CAL/MOG), superior temporal gyrus (STG), angular (ANG), postcentral gyrus (PosCG), inferior parietal lobule (IPL), and precentral gyrus (PreCG) (**Figure 2** and **Table 2**).

Seed-Based Functional Connectivity Differences

We investigated resting-state FC seeded as 14 ROIs (seven per hemisphere) with lower VMHC values between two groups (**Table 3**). This region of altered FC includes the regions of auditory network (MTG and STG), visual network (LING/CAL/MOG), default mode network (ANG and IPL), salience network (insula), and sensorimotor network (PosCG and PreCG) (**Figure 3**).

Receiver Operating Characteristic Curve

The area under curve (AUC) for zVMHC was as follows: DR < HC, for MTG, 0.913; for LING/CAL/MOG, 0.895; for STG, 0.952; for ANG, 0.888; for PosCG, 0.837; for IPL, 0.942; and for PreCG, 0.799 (**Table 4** and **Figure 4**).

Pearson Correlation Analysis

A significant positive correlation was found between the visual acuity-OD and zVMHC values in the bilateral LING/CAL/MOG (r = 0.551, p = 0.001), STG (r = 0.426, p = 0.012), PosCG (r = 0.494, p = 0.003), and IPL (r = 0.459, p = 0.006) in DR patients (**Figure 5**).

DISCUSSION

The VMHC method is a sensitive and high-resolution resting-state fMRI technology, which is applied to assess the FC between two cerebral hemispheres. In our study, we found that DR patients had decreased interhemispheric FC within auditory network, visual network, default mode network, and sensorimotor network. A significant positive correlation was observed between the visual acuity-OD and zVMHC values in the bilateral LING/CAL/MOG (r = 0.551, p = 0.001), STG (r = 0.426, p = 0.012), PosCG (r = 0.494, p = 0.003), and IPL (r = 0.459, p = 0.006) in DR patients.

We found that DR groups showed decreased VMHC values in the LING/CAL/MOG, which was located in the visual network.

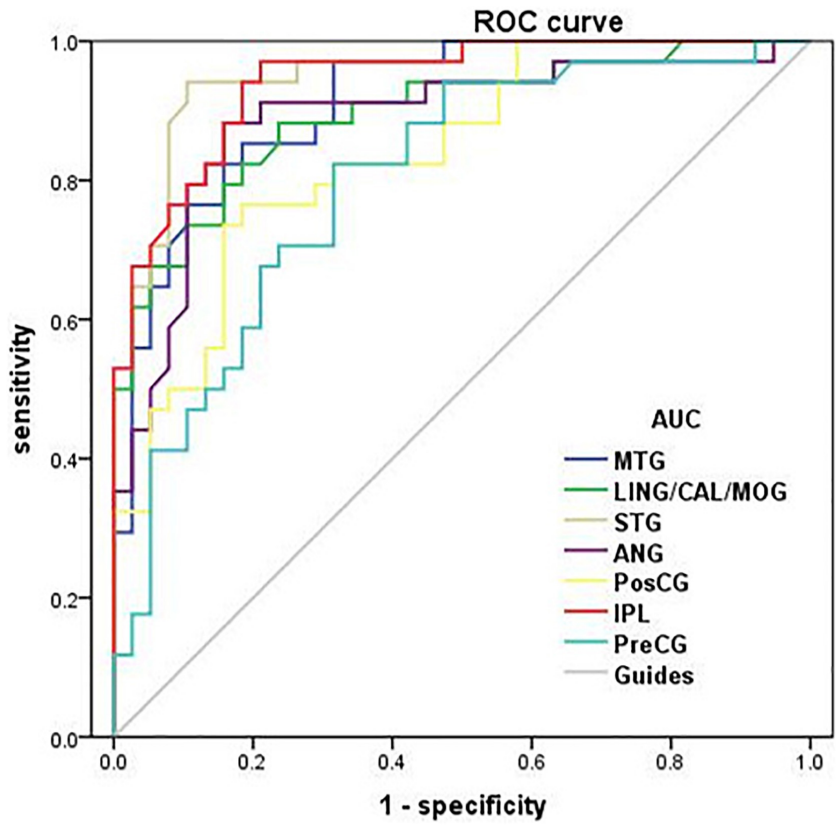

FIGURE 4 | Receiver operating characteristic curve analysis of the mean zVMHC. ROC curve in zVMHC: DR < HC; for MTG, 0.913 (p < 0.001; 95% CI: 0.850–0.976); for LING/CAL/MOG, 0.895; for STG, 0.952; for ANG, 0.888; for PosCG, 0.837; for IPL, 0.942; and for PreCG, 0.799. ROC, receiver operating characteristic; AUC, area under the curve; VMHC, voxel-mirrored homotopic connectivity; DR, diabetic retinopathy; HCs, healthy controls; MTG, middle temporal gyrus; LING/CAL/MOG, lingual/calcarine/middle occipital gyrus; STG, superior temporal gyrus; ANG, angular; PosCG, postcentral gyrus; IPL, inferior parietal lobule; PreCG, precentral gyrus.

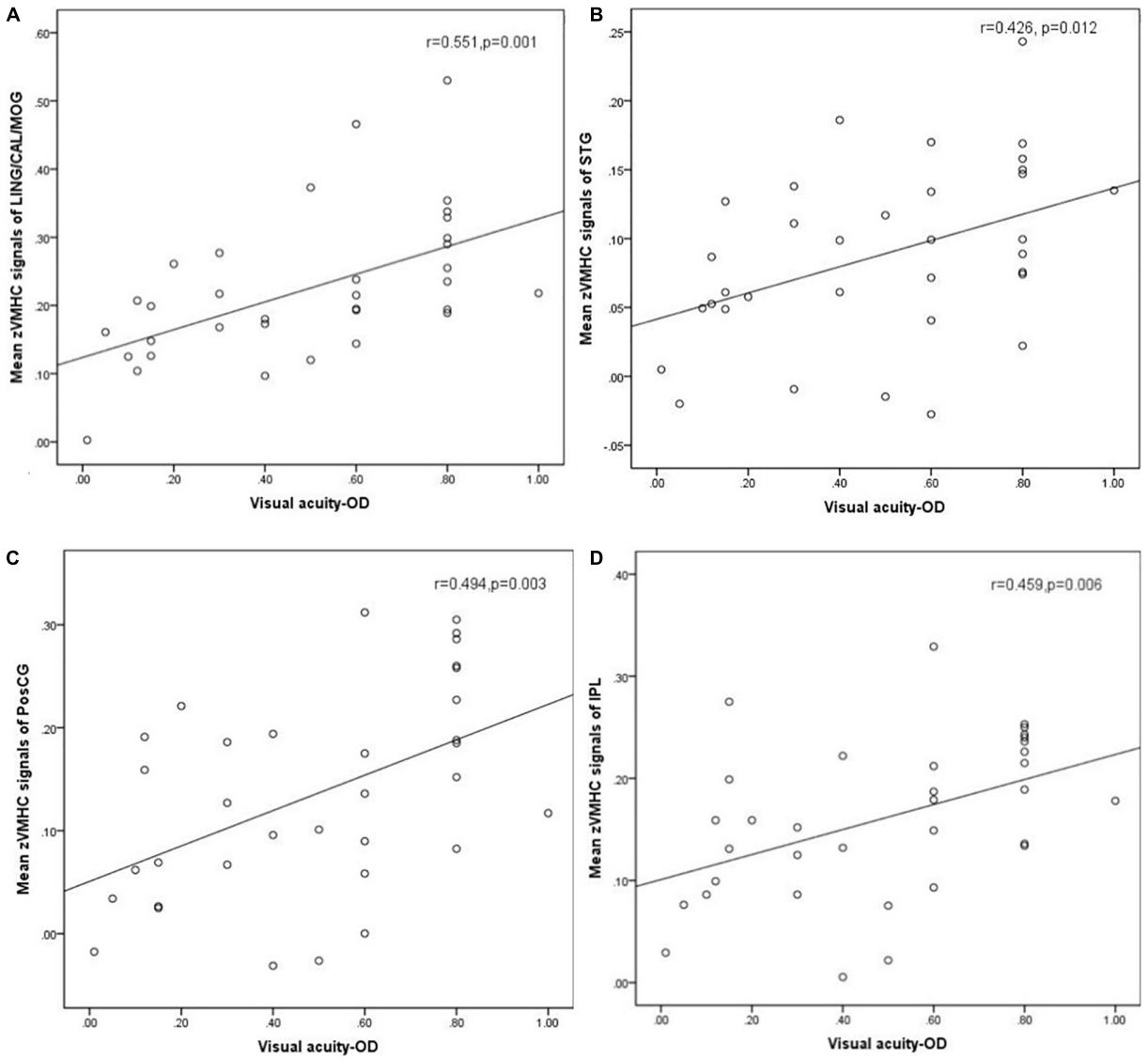

FIGURE 5 | Correlation was found between the visual acuity-OD and zVMHC values in the bilateral LING/CAL/MOG (r = 0.551, p = 0.001), **(A)** STG (r = 0.426, p = 0.012), **(B)** PosCG (r = 0.494, p = 0.003), **(C)** and IPL (r = 0.459, p = 0.006) **(D)** in DR patients. DR, diabetic retinopathy; VMHC, voxel-mirrored homotopic connectivity; OD, oculus dexter; LING/CAL/MOG, lingual/calcarine/middle occipital gyrus; STG, superior temporal gyrus; PosCG, postcentral gyrus. IPL, inferior parietal lobule.

The main pathological changes of DR include microaneurysms, hemorrhages, hard exudates and macular edema, and even vitreous hemorrhage and tractional retinal detachment in the late stage. These pathological changes of the retina can lead to vision loss. Meanwhile, DR not only causes retinal changes, but also leads to structural and functional abnormalities in visual pathways. Li Y. M. et al. (2018) demonstrated that DR patients were accompanied by abnormal white matter integrity in visual pathway. Qi et al. (2021) found that DR patients had a significant lower FC within the visual cortex, relative to HC group. Corduneanu et al. (2019) also reported that DR patients had latency of waves on the visual evoked potential pathway wave relative to the HC group. Moreover, Wang et al. (2017) found that the increased apparent diffusion coefficient values of the visual cortex were observed in patients with proliferative and non-proliferative DR. With the support of these findings, we also demonstrated that DR patients showed decreased interhemispheric FC within the visual network, which might reflect the impaired interhemispheric coordination in processing of visual information in DR patients. We speculated that visual loss might contribute to the reduced interhemispheric FC within the visual network.

Another important finding is that DR patients had reduced interhemispheric FC within the auditory network. Prior studies demonstrated that diabetes patients were accompanied by hearing impairment. Li J. et al. (2018) reported that diabetes

patients had bilateral sensorineural hearing loss, especially at high frequencies. AlJasser et al. (2020) also found that the T1DM group showed significantly reduced frequency-following response to both temporal envelope and temporal fine structure. Braite et al. (2019) reported that T1DM patients were associated with auditory efferent pathway dysfunction. Meanwhile, Willette et al. (2013) found that diabetes patients showed medial temporal lobe atrophy and decreased white matter in the left temporal lobe (Northam et al., 2009). Chen et al. (2012) demonstrated that T2DM patients were accompanied by gray matter atrophy in the temporal gyri. With these findings, our study revealed that DR patients had reduced interhemispheric FC within auditory network, which might reflect the impaired auditory function in DR patients. However, the exact neural mechanism of auditory function dysfunction in DR patients remain unclear.

In addition, we found that DR patients had reduced interhemispheric FC within the sensorimotor network. The sensorimotor network plays an important role in motor control and sensory function. Previous studies demonstrated that diabetic peripheral neuropathy patients were associated with sensorimotor dysfunction (Khan et al., 2020; Van Eetvelde et al., 2020). Zhang et al. (2020) demonstrated that diabetic peripheral neuropathy patients had abnormal gray matter in pre- and PosCG relative to health controls. Hansen et al. (2019) found that diabetes patients' diabetes had 9.3% lower ratio of *N*-acetyl aspartate/creatine (NAA/cre) in the parietal region including the sensorimotor fiber tracts. Meanwhile, van Duinkerken et al. (2017) also reported that one diabetes mellitus patient had decreased FC within the sensorimotor network. Thus, we also found that DR patients had reduced interhemispheric FC within the sensorimotor network, which might indicate the impaired sensorimotor function.

We found that DR patients had widespread decreased interhemispheric FC within the default mode network (DMN). Previous neuroimaging studies demonstrated that diabetes patients were associated with DMN dysfunction, which is closely related with cognitive decline (Cui et al., 2015; Chen et al., 2016; Yang et al., 2016; Tan et al., 2019). In our study, we found that DR patients had widespread decreased interhemispheric FC within the DMN, which reflect the interhemispheric FC dysfunction in DMN functional communication.

Some limitations should be acknowledged in this study. First, VMHC results based on blood oxygenation level-dependent (BOLD) signals would still be affected by physiological noise. Second, BOLD signals may be influenced by the subject's subjective thinking. We asked subjects not to think of anything in particular during MRI scanning in the study. Third, the exact neural mechanisms of interhemispheric FC dysfunction are still unclear, and multimodal neuroimaging and machine learning algorithms should be combined to evaluate the neural mechanisms changes in DR patients in future studies.

In conclusion, our results highlighted that DR patients are associated with substantial impairment of interhemispheric coordination in auditory network, visual network, DMN, and sensorimotor network. These findings shed a new light on the neural mechanism of DR patients.

DATA AVAILABILITY STATEMENT

The raw data supporting the conclusions of this article will be made available by the authors, without undue reservation.

ETHICS STATEMENT

The studies involving human participants were reviewed and approved by the Jiangxi Provincial People's Hospital Affiliated to Nanchang University. The patients/participants provided their written informed consent to participate in this study.

AUTHOR CONTRIBUTIONS

SW, WX, and YZ contributed to the data collection, statistical analyses, wrote the manuscript, design the protocol, and MRI analysis. SW and WX designed the study and oversaw all clinical aspects of study conduct and manuscript preparation. All authors contributed to the article and approved the submitted version.

REFERENCES

AlJasser, A., Uus, K., Prendergast, G., and Plack, C. J. (2020). Subclinical auditory neural deficits in patients with type 1 diabetes mellitus. *Ear Hear.* 41, 561–575. doi: 10.1097/AUD.0000000000000781

Bartha-Doering, L., Kollndorfer, K., Schwartz, E., Fischmeister, F. P. S., Alexopoulos, J., Langs, G., et al. (2021). The role of the corpus callosum in language network connectivity in children. *Dev. Sci.* 24:e13031. doi: 10.1111/desc.13031

Biswal, B., Yetkin, F. Z., Haughton, V. M., and Hyde, J. S. (1995). Functional connectivity in the motor cortex of resting human brain using echo-planar MRI. *Magn. Reson. Med.* 34, 537–541. doi: 10.1002/mrm.1910340409

Braite, N., da Cruz Fernandes, L., Rissatto Lago, M. R., and de Aragao Dantas Alves, C. (2019). Effects of type 1 diabetes mellitus on efferent auditory system in children and adolescents. *Int. J. Pediatr. Otorhinolaryngol.* 127:109660. doi: 10.1016/j.ijporl.2019.109660

Chen, Y., Liu, Z., Wang, A., Zhang, J., Zhang, S., Qi, D., et al. (2016). Dysfunctional organization of default mode network before memory impairments in type 2 diabetes. *Psychoneuroendocrinology* 74, 141–148. doi: 10.1016/j.psyneuen.2016.08.012

Chen, Z., Li, L., Sun, J., and Ma, L. (2012). Mapping the brain in type II diabetes: voxel-based morphometry using dartel. *Eur. J. Radiol.* 81, 1870–1876. doi: 10.1016/j.ejrad.2011.04.025

Corduneanu, A., Chisca, V., Ciobanu, N., and Groppa, S. (2019). Evaluation of visual pathways using visual evoked potential in patients with diabetic retinopathy. *Rom. J. Ophthalmol.* 63, 367–371. doi: 10.22336/rjo.2019.57

Cui, Y., Jiao, Y., Chen, H. J., Ding, J., Luo, B., Peng, C. Y., et al. (2015). Aberrant functional connectivity of default-mode network in type 2 diabetes patients. *Eur. Radiol.* 25, 3238–3246. doi: 10.1007/s00330-015-3746-8

Cui, Y., Tang, T. Y., Lu, C. Q., Lu, T., Wang, Y. C., Teng, G. J., et al. (2021). Disturbed interhemispheric functional and structural connectivity in type 2 diabetes. *J. Magn. Reson. Imaging* 1–11. doi: 10.1002/jmri.27813

Dai, H., Zhang, Y., Lai, L., Hu, S., Wang, X., Li, Y., et al. (2017). Brain functional networks: correlation analysis with clinical indexes in patients with diabetic retinopathy. *Neuroradiology* 59, 1121–1131. doi: 10.1007/s00234-017-1900-5

Friston, K. J., Williams, S., Howard, R., Frackowiak, R. S., and Turner, R. (1996). Movement-related effects in fMRI time-series. *Magn. Reson. Med.* 35, 346–355. doi: 10.1002/mrm.1910350312

Guo, L., Zhou, F., Zhang, N., Kuang, H., and Feng, Z. (2019). Frequency-specific abnormalities of functional homotopy in alcohol dependence: a resting-state functional magnetic resonance imaging study. *Neuropsychiatr. Dis. Treat.* 15, 3231–3245. doi: 10.2147/NDT.S221010

Hagg, S., Thorn, L. M., Putaala, J., Liebkind, R., Harjutsalo, V., Forsblom, C. M., et al. (2013). Incidence of stroke according to presence of diabetic nephropathy and severe diabetic retinopathy in patients with type 1 diabetes. *Diabetes Care* 36, 4140–4146. doi: 10.2337/dc13-0669

Hansen, T. M., Brock, B., Juhl, A., Drewes, A. M., Vorum, H., Andersen, C. U., et al. (2019). Brain spectroscopy reveals that N-acetylaspartate is associated to peripheral sensorimotor neuropathy in type 1 diabetes. *J. Diabetes Complications* 33, 323–328. doi: 10.1016/j.jdiacomp.2018.12.016

Huang, X., Tong, Y., Qi, C. X., Xu, Y. T., Dan, H. D., and Shen, Y. (2019). Disrupted topological organization of human brain connectome in diabetic retinopathy patients. *Neuropsychiatr. Dis. Treat.* 15, 2487–2502. doi: 10.2147/NDT.S214325

Khan, N., Ahmad, I., and Noohu, M. M. (2020). Association of disease duration and sensorimotor function in type 2 diabetes mellitus: beyond diabetic peripheral neuropathy. *Somatosens. Mot. Res.* 37, 326–333. doi: 10.1080/08990220.2020.1830757

Li, J., Zhang, Y., Fu, X., Bi, J., Li, Y., Liu, B., et al. (2018). Alteration of auditory function in type 2 diabetic and pre-diabetic patients. *Acta Otolaryngol.* 138, 542–547. doi: 10.1080/00016489.2017.1422084

Li, Y. M., Zhou, H. M., Xu, X. Y., and Shi, H. S. (2018). Research progress in MRI of the visual pathway in diabetic retinopathy. *Curr. Med. Sci.* 38, 968–975. doi: 10.1007/s11596-018-1971-5

Liang, M., Xie, B., Yang, H., Yin, X., Wang, H., Yu, L., et al. (2017). Altered interhemispheric functional connectivity in patients with anisometropic and strabismic amblyopia: a resting-state fMRI study. *Neuroradiology* 59, 517–524. doi: 10.1007/s00234-017-1824-0

Lynch, S. K., and Abramoff, M. D. (2017). Diabetic retinopathy is a neurodegenerative disorder. *Vis. Res.* 139, 101–107. doi: 10.1016/j.visres.2017.03.003

Northam, E. A., Rankins, D., Lin, A., Wellard, R. M., Pell, G. S., Finch, S. J., et al. (2009). Central nervous system function in youth with type 1 diabetes 12 years after disease onset. *Diabetes Care* 32, 445–450. doi: 10.2337/dc08-1657

Qi, C. X., Huang, X., and Shen, Y. (2020). Altered intrinsic brain activities in patients with diabetic retinopathy using amplitude of low-frequency fluctuation: a resting-state fMRI study. *Diabetes Metab. Syndr. Obes.* 13, 2833–2842. doi: 10.2147/DMSO.S259476

Qi, C. X., Huang, X., Tong, Y., and Shen, Y. (2021). Altered functional connectivity strength of primary visual cortex in subjects with diabetic retinopathy. *Diabetes Metab. Syndr. Obes.* 14, 3209–3219. doi: 10.2147/DMSO.S311009

Roland, J. L., Snyder, A. Z., Hacker, C. D., Mitra, A., Shimony, J. S., Limbrick, D. D., et al. (2017). On the role of the corpus callosum in interhemispheric functional connectivity in humans. *Proc. Natl. Acad. Sci. U.S.A.* 114, 13278–13283. doi: 10.1073/pnas.1707050114

Sundstrom, J. M., Hernandez, C., Weber, S. R., Zhao, Y., Dunklebarger, M., Tiberti, N., et al. (2018). Proteomic analysis of early diabetic retinopathy reveals mediators of neurodegenerative brain diseases. *Invest. Ophthalmol. Vis. Sci.* 59, 2264–2274. doi: 10.1167/iovs.17-23678

Tan, X., Liang, Y., Zeng, H., Qin, C., Li, Y., Yang, J., et al. (2019). Altered functional connectivity of the posterior cingulate cortex in type 2 diabetes with cognitive impairment. *Brain Imaging Behav.* 13, 1699–1707. doi: 10.1007/s11682-018-0017-8

van Duinkerken, E., Schoonheim, M. M., Rg, I. J., Moll, A. C., Landeira-Fernandez, J., Klein, M., et al. (2017). Altered eigenvector centrality is related to local resting-state network functional connectivity in patients with longstanding type 1 diabetes mellitus. *Hum. Brain Mapp.* 38, 3623–3636. doi: 10.1002/hbm.23617

Van Eetvelde, B. L. M., Lapauw, B., Proot, P., Vanden Wyngaert, K., Celie, B., Cambier, D., et al. (2020). The impact of sensory and/or sensorimotor neuropathy on lower limb muscle endurance, explosive and maximal muscle strength in patients with type 2 diabetes mellitus. *J. Diabetes Complications* 34:107562. doi: 10.1016/j.jdiacomp.2020.107562

Wang, Z., Lu, Z., Li, J., Pan, C., Jia, Z., Chen, H., et al. (2017). Evaluation of apparent diffusion coefficient measurements of brain injury in type 2 diabetics with retinopathy by diffusion-weighted MRI at 3.0 T. *Neuroreport* 28, 69–74. doi: 10.1097/WNR.0000000000000703

Wang, Z., Wang, J., Zhang, H., McHugh, R., Sun, X., Li, K., et al. (2015). Interhemispheric functional and structural disconnection in Alzheimer's disease: a combined resting-state fMRI and DTI study. *PLoS One* 10:e0126310. doi: 10.1371/journal.pone.0126310

Willette, A. A., Xu, G., Johnson, S. C., Birdsill, A. C., Jonaitis, E. M., Sager, M. A., et al. (2013). Insulin resistance, brain atrophy, and cognitive performance in late middle-aged adults. *Diabetes Care* 36, 443–449. doi: 10.2337/dc12-0922

Wong, K. H., Hu, K., Peterson, C., Sheibani, N., Tsivgoulis, G., Majersik, J. J., et al. (2020). Diabetic retinopathy and risk of stroke: a secondary analysis of the ACCORD eye study. *Stroke* 51, 3733–3736. doi: 10.1161/STROKEAHA.120.030350

Yan, C. G., Wang, X. D., Zuo, X. N., and Zang, Y. F. (2016). DPABI: data processing & analysis for (resting-state) brain imaging. *Neuroinformatics* 14, 339–351. doi: 10.1007/s12021-016-9299-4

Yang, S., Wu, M., Ajilore, O., Lamar, M., and Kumar, A. (2016). Metabolic aberrations impact biophysical integrity of macromolecular protein pools in the default mode network. *Diabetes* 65, 3464–3472. doi: 10.2337/db15-1714

Yau, J. W., Rogers, S. L., Kawasaki, R., Lamoureux, E. L., Kowalski, J. W., Bek, T., et al. (2012). Global prevalence and major risk factors of diabetic retinopathy. *Diabetes Care* 35, 556–564. doi: 10.2337/dc11-1909

Yu, Y., Lan, D. Y., Tang, L. Y., Su, T., Li, B., Jiang, N., et al. (2020). Intrinsic functional connectivity alterations of the primary visual cortex in patients with proliferative diabetic retinopathy: a seed-based resting-state fMRI study. *Ther. Adv. Endocrinol. Metab.* 11:2042018820960296. doi: 10.1177/2042018820960296

Zhang, X., Saaddine, J. B., Chou, C. F., Cotch, M. F., Cheng, Y. J., Geiss, L. S., et al. (2010). Prevalence of diabetic retinopathy in the United States, 2005-2008. *JAMA* 304, 649–656. doi: 10.1001/jama.2010.1111

Zhang, Y., Qu, M., Yi, X., Zhuo, P., Tang, J., Chen, X., et al. (2020). Sensorimotor and pain-related alterations of the gray matter and white matter in Type 2 diabetic patients with peripheral neuropathy. *Hum. Brain Mapp.* 41, 710–725. doi: 10.1002/hbm.24834

Zhang, Y., Wang, J., Wei, P., Zhang, J., Zhang, G., Pan, C., et al. (2021). Interhemispheric resting-state functional connectivity abnormalities in type 2 diabetes patients. *Ann. Palliat. Med.* 10, 8123–8133. doi: 10.21037/apm-21-1655

Zuo, X. N., Kelly, C., Di Martino, A., Mennes, M., Margulies, D. S., Bangaru, S., et al. (2010). Growing together and growing apart: regional and sex differences in the lifespan developmental trajectories of functional homotopy. *J. Neurosci.* 30, 15034–15043. doi: 10.1523/JNEUROSCI.2612-10.2010

Conflict of Interest: The authors declare that the research was conducted in the absence of any commercial or financial relationships that could be construed as a potential conflict of interest.

Publisher's Note: All claims expressed in this article are solely those of the authors and do not necessarily represent those of their affiliated organizations, or those of the publisher, the editors and the reviewers. Any product that may be evaluated in this article, or claim that may be made by its manufacturer, is not guaranteed or endorsed by the publisher.

frontiers in Human Neuroscience

ORIGINAL RESEARCH
published: 24 December 2021
doi: 10.3389/fnhum.2021.762970

Altered Processing of Visual Stimuli in Vestibular Migraine Patients Between Attacks: A Combined VEP and sLORETA Study

Jiahao Liu[1,2†], Qi Zhang[3†], Maojin Liang[1,2†], Yajing Wang[1,2], Yuebo Chen[1,2], Junbo Wang[1,2], Jiahong Li[1,2], Ling Chen[1,2], Leyin Yu[4], Yinglin Cai[4], Yiqing Zheng[1,2] and Yongkang Ou[1,2*]*

[1]Department of Otolaryngology, Sun Yat-sen Memorial Hospital, Sun Yat-sen University, Guangzhou, China, [2]Institute of Hearing and Speech-Language Sciences, Sun Yat-sen University, Guangzhou, China, [3]School of Foreign Languages, Shenzhen University, Shenzhen, China, [4]Department of Hearing and Speech Science, Guangzhou Xinhua College, Guangzhou, China

OPEN ACCESS

Edited by:
Michael Strupp,
Ludwig Maximilian University of Munich, Germany

Reviewed by:
Mark Obermann,
University of Duisburg-Essen, Germany
Figen Gokcay,
Ege University, Turkey

***Correspondence:**
Yiqing Zheng
zhengyiq@mail.sysu.edu.cn
Yongkang Ou
ouyk@mail.sysu.edu.cn

[†]These authors have contributed equally to this work

Specialty section:
This article was submitted to Sensory Neuroscience, a section of the journal Frontiers in Human Neuroscience

Received: 23 August 2021
Accepted: 02 December 2021
Published: 24 December 2021

Citation:
Liu J, Zhang Q, Liang M, Wang Y, Chen Y, Wang J, Li J, Chen L, Yu L, Cai Y, Zheng Y and Ou Y (2021) Altered Processing of Visual Stimuli in Vestibular Migraine Patients Between Attacks: A Combined VEP and sLORETA Study. Front. Hum. Neurosci. 15:762970. doi: 10.3389/fnhum.2021.762970

Objective: Vestibular migraine (VM) is one of the most common causes of recurrent vertigo, but the neural mechanisms that mediate such symptoms remain unknown. Since visual symptoms and photophobia are common clinical features of VM patients, we hypothesized that VM patients have abnormally sensitive low-level visual processing capabilities. This study aimed to investigate cortex abnormalities in VM patients using visual evoked potential (VEP) and standardized low-resolution brain electromagnetic tomography (sLORETA) analysis.

Methods: We employed visual stimuli consisting of reversing displays of circular checkerboard patterns to examine "low-level" visual processes. Thirty-three females with VM and 20 healthy control (HC) females underwent VEP testing. VEP components and sLORETA were analyzed.

Results: Patients with VM showed significantly lower amplitude and decreased latency of P1 activation compared with HC subjects. Further topographic mapping analysis revealed a group difference in the occipital area around P1 latency. sLORETA analysis was performed in the time frame of the P1 component and showed significantly less activity (deactivation) in VM patients in the frontal, parietal, temporal, limbic, and occipital lobes, as well as sub-lobar regions. The maximum current density difference was in the postcentral gyrus of the parietal lobe. P1 source density differences between HC subjects and VM patients overlapped with the vestibular cortical fields.

Conclusion: The significantly abnormal response to visual stimuli indicates altered processing in VM patients. These findings suggest that abnormalities in vestibular cortical fields might be a pathophysiological mechanism of VM.

Keywords: vestibular migraine, visual evoked potential, sLORETA, cortex abnormalities, neural mechanism

INTRODUCTION

Vestibular migraine (VM) is one of the most common conditions contributing to recurrent vertigo and afflicts up to 1% of the whole population with female predominance (Russo et al., 2014). Typical signs of VM include a heightened sensitivity to head motion or visual stimuli, spatial misperceptions, and/or sudden feelings of lopsidedness or tilt. These symptoms often severely limit daily functioning in VM patients. Different from typically brief migraine auras, VM symptoms can last from hours to several days (Beh, 2019). Despite well-defined diagnostic criteria, like those proposed by the Bárány Society and the Migraine Classification Subcommittee of the International Headache Society (Lempert et al., 2012), VM pathophysiology is still unclear and remains controversial. While it is agreed that genetic, epigenetic, and environmental factors are probably involved in VM progression, there is an ongoing dispute concerning whether its primary origin is central or peripheral (Espinosa-Sanchez and Lopez-Escamez, 2015).

Modern neuroimaging methods have been used to observe how neural pathways work in subjects with VM, with a particular focus on the multisensory integration network. Functional neuroimaging showed dysmodulation attributed to vestibulo-thalamo-cortical dysfunction—the pathogenic mechanism underlying VM—in the multimodal sensory integration and processing of vestibular and nociceptive information (Espinosa-Sanchez and Lopez-Escamez, 2015). In 2016, Teggi et al. (2016) reported enhanced responses of multimodal association brain areas [Brodmann area (BA) 40, BA 31/5] and reduced activation of occipital regions in VM patients. In 2017, Messina et al. (2017) indicated that unusual brain sensitization might result in dismodulation of multimodal sensory integration and processing cortical areas in VM patients. As visual symptoms and photophobia are common clinical features of VM, we hypothesized that patients with VM have abnormally sensitive low-level visual processing capabilities. A primary approach to analyzing visual processing integrity is the use of visual evoked potentials (VEPs; Sulejmanpasic and Drnda, 2017). Most of the above studies focused on brain activation using functional magnetic resonance imaging with high spatial resolution but relatively poor temporal resolution. We pay particular attention to the temporal dimensions of these abnormalities, which seem crucial to understanding functional brain changes in VM patients and their clinical correlations. The temporal precision, low cost, and noninvasiveness of VEP measurement make it particularly well suited to study functional brain changes associated with VM (de Tommaso et al., 2014). We specifically selected patients between VM attacks because altered brain metabolism has been found, and patients show activation of the bilateral cerebellum and frontal cortices and deactivation of the bilateral posterior parietal and occipitotemporal areas during VM attacks (Shin et al., 2014).

Vestibular symptoms are also extremely common during the interictal period (Beh et al., 2019), likely because vestibular-sensitive neurons respond to a range of modalities (Grusser et al., 1990a,b; Vuralli et al., 2018). No primary vestibular cortex has been identified, and vestibular signals are generally conveyed to the cerebral cortex (Guldin and Grusser, 1998; Vuralli et al., 2018). Vestibular information processing involves polymodal association areas in the parietal, temporal, and insular cortices and cortical areas associated with spatial orientation (e.g., primary somatosensory cortex, primary visual cortex; Vuralli et al., 2018).

The existing evidence suggests that the central nervous system is altered in VM patients. The aim of the present study was to compare VEP responses between patients with VM patients and healthy control (HC) subjects. We hypothesized that cortex responses activated by visual stimuli would be different between groups. To test this hypothesis, we used parametrically modulated reversing checkerboard images to examine how the physical property of luminance affects early VEPs (i.e., initial stages of visual processing that are strongly influenced by physical stimulus properties). A previous study demonstrated larger VEP responses for higher luminance levels in the visual stimuli (Johannes et al., 1995), leading to our prediction of parametric modulation of early VEP components as a function of overall luminance in the checkerboard images. Moreover, we expected a functional difference between VM patients and HC subjects already at early processing levels in the visual hierarchy. Thus, we applied electroencephalography (EEG)-standardized low-resolution brain electromagnetic tomography (sLORETA; Pascual-Marqui, 2002) to analyze cortex activity in response to visual stimulation. We employed the VEP and sLORETA differences between VM patients and HC subjects to identify disordered cortical activities associated with VM. We hypothesized that VM patients would show decreased P1 amplitudes and lower P1 neural activities in VM-related brain regions.

MATERIALS AND METHODS

Participants

Thirty-three female patients (30 without aura and three with aura), diagnosed as typical VM according to previously described criteria [Lempert et al., 2012; Headache Classification Committee of the International Headache Society (IHS), 2013] were prospectively recruited from the population seen at the Department of Otolaryngology, Sun Yat-Sen Memorial Hospital, Sun Yat-Sen University. All patients were clinically evaluated and diagnosed by the same otolaryngologist after excluding other etiologies which could cause recurrent vertigo attacks, and all patients underwent VEP recordings on days 2–10 after a VM attack, they were attack-free at least 12 h before and after the recordings. Peripheral vestibular dysfunction was found in 7 of 33 VM patients on videonystagmography (VNG) recordings. Furthermore, they did not have any way to prevent migraine, vertigo, or dizziness, and no topiramate, magnesium, or other vestibular inhibitor drugs were allowed during the preceding 1 month. Twenty female subjects with no family history of migraine and no history of chronic pain, substance abuse, or neurologic, psychiatric, or systemic disorders were recruited as HC subjects. There were no significant differences in age between groups. All participants were right-handed

TABLE 1 | Demographic and clinical characteristics of patients.

Characteristics	VM (n = 33) Mean ± SD	HC (n = 20) Mean ± SD
Sex	Female	Female
Age	44.55 ± 13.70	43.80 ± 11.85
VM disease duration (years)	6.20 ± 6.28	
Migraine disease duration (years)	10.67 ± 6.22	
Attack frequency per month	2.74 ± 5.25	

HC, healthy control; VM, vestibular migraine.

with normal or corrected-to-normal visual acuity. Patients with VM, and healthy controls did not report other neurological, psychiatric, audiovestibular, diabetes mellitus, hypertension, vascular/heart diseases, hyper-cholesterolaemia, or other major systemic disorders. Moreover, participants who abused alcohol, nicotine, or other substances were excluded. The clinical and demographic characteristics of the VM and HC groups are summarized in **Table 1**.

Visual Stimuli

We adopted visual stimuli consisting of reversing displays of circular checkerboard patterns reported by Sandmann and colleagues (Sandmann et al., 2012), which have been used to examine cross-modal reorganization in the auditory cortex of cochlear implant users. There were four different pairs of patterns that varied in terms of luminance ratio. The proportions of white pixels in the stimulus patterns were 12.5% (Level 1), 25% (Level 2), 37.5% (Level 3), and 50% (Level 4). The contrast between white and black pixels was identical in all stimuli.

Subjects were comfortably seated in front of a high-resolution 19-inch VGA computer monitor at a viewing distance of approximately 1 m in a soundproof and electromagnetically shielded room. All stimuli were presented via E-prime 2.0 stimulus software that is compatible with Net Station 4 (Electrical Geodesics, Inc.). The checkerboard stimulus remained on the monitor for 500 ms and was immediately followed by blank-screen inter-stimulus intervals that also lasted for 500 ms. Each presented blank stimulus image included a fixation point (a white cross) on the center of the screen. Participants performed four experimental blocks (i.e., conditions) in which they were presented with one of the four image pairs. The block order was counterbalanced across participants. In the course of the experimental session, each checkerboard image was repeated 60 times, resulting in a total of 480 stimuli (four conditions, two images, 60 repetitions). Participants were instructed to keep their eyes on the pictures before each condition and were allowed to have rest for 1 min between blocks.

EEG Recording and Analyses

EEG data were continuously recorded by a 128-Channel Dense Array EEG System with Hydrogel Geodesic Sensor Nets (EGI, USA). The sampling rate was 1 kHz, and electrode impedances were kept below 50 kΩ. For ERP analyses, individual participant data were band-pass filtered offline at 0.3–30 Hz and segmented with 100-ms pre-stimulus and 600-ms post-stimulus times. Artifact rejection set at 200 mV was applied to visual EEG signals, and epochs were rejected if they contained any eye blinking (eye channel > 140 mV) or eye movement (eye channel > 55 mV). Bad channels were removed from the recording. Data were then re-referenced using a common average reference. The data were baseline corrected to the pre-stimulus time of −100 to 0 ms.

Amplitudes and latencies of the P1-N1-P2 complex on the 75(Oz) electrode for individual participants were analyzed. The time frames for the P1, N1, and P2 were set between 50 and 120 ms, 100 and 170 ms, and 200 and 290 ms, respectively. The amplitudes of the P1, N1, and P2 peaks were measured from the baselines to the peak values. Individual subject latencies were defined at the highest peak amplitude for each VEP component. Individual waveform averages were averaged together for each group to compute a grand-average waveform. We compared the amplitudes and latencies of the VEP components between groups with respect to the four checkerboard images.

For statistical analysis, VEP components were subjected to separate repeated-measures analyses of variance (ANOVAs) with condition (Levels 1–4) as the within-subject factor and group (VM patients and HC subjects) as the between-subjects factor. Significant main effects and interactions ($p < 0.05$) were followed-up with *post hoc* t-tests, and Greenhouse–Geisser corrections were applied when the sphericity assumption was violated. Topographical displays are based on the whole scalp region.

sLORETA

ERP source analyses were performed using a standardized head model to estimate the intracerebral sources on the basis of an sLORETA algorithm (Pascual-Marqui, 2002), which is a functional imaging method based on electrophysiological and neuroanatomical constraints. This method offers precise localization (Wagner et al., 2004; Sekihara et al., 2005) but low spatial resolution. sLORETA software was provided online by the KEY Institute for Brain-Mind Research, Zurich, Switzerland[1]. Source analyses were only performed in the time frame of the P1 component since scalp-recorded potentials revealed systematic differences between groups specifically for P1 latency. The latency (mean ± SD) from the Oz electrode in each group was used to calculate the time frames of the source images and to consider different peak latency variations among the VM patients (66–102 ms) and HC subjects (86–104 ms). Afterward, non-parametric statistical analyses of sLORETA images (statistical non-parametric mapping; SnPM) were performed to identify differences in source activity generators between VM patients and HC subjects. This was done using sLORETA's built-in voxel-wise randomization tests with 5000 permutations and employing a log-F-ratio statistic for independent groups with a threshold of $p < 0.01$ (corrected for multiple comparisons).

RESULTS

VEPs

Individual waveform averages were averaged together for each group to produce a grand-average waveform and topographic

[1]https://www.uzh.ch/keyinst/NewLORETA/Software/Software.htm

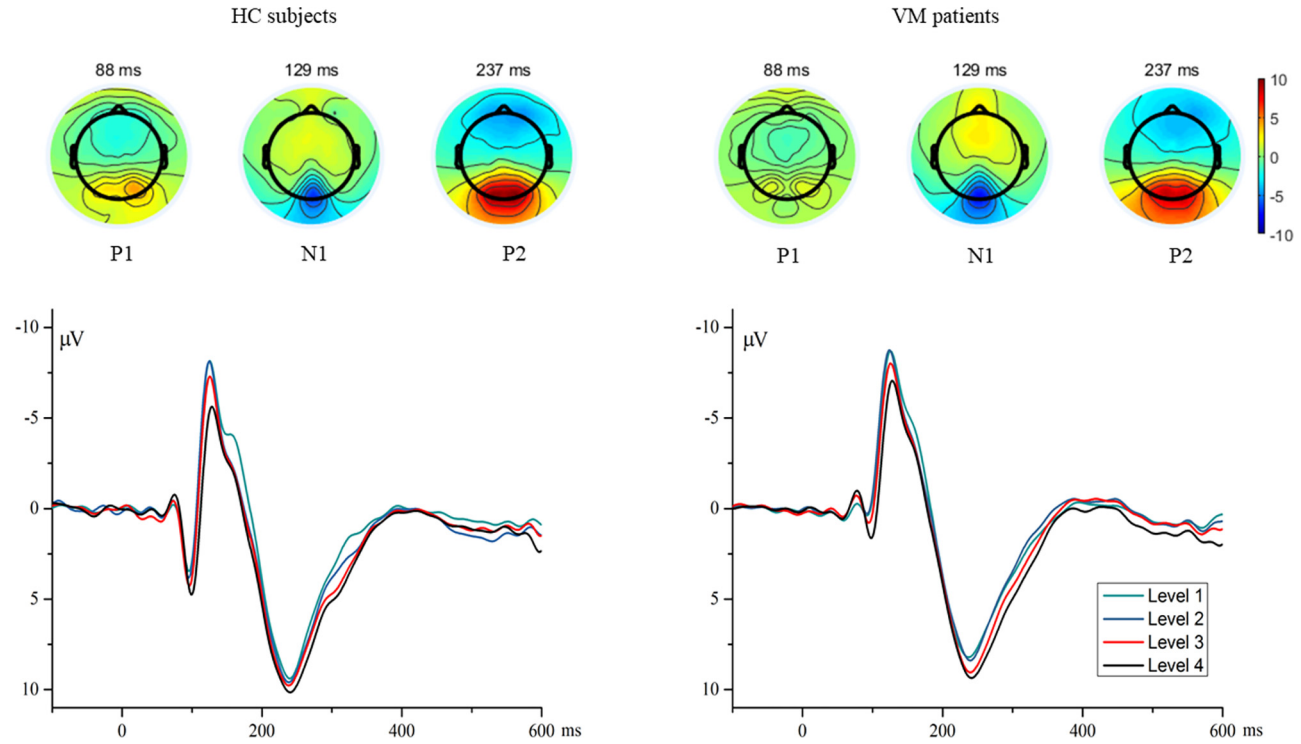

FIGURE 1 | The topographies show the P1 (88 ms), N1 (129 ms), and P2 (237 ms) VEP and are given separately for HC subjects and VM patients. Grand average VEP waveforms recorded at channel Oz are shown for different luminance ratios (Levels 1–4). Levels 1 and 4 refer to the smallest (12.5%) and largest (50%) proportions of white pixels in the stimulus pattern, respectively. VEP, visual evoked potential; HC, healthy control; VM, vestibular migraine.

maps of HC subjects and VM patients as shown in **Figure 1**. The results revealed smaller amplitudes and reduced latencies of the P1 component in VM patients. We compared the amplitudes and latencies of the VEP components of both groups with respect to the four checkerboard images.

Figure 2 shows the VEP amplitudes and latencies for different luminance ratios separately for VM patients and HC subjects. Repeated-measures ANOVAs on P1 amplitudes and latencies both revealed significant main effects for condition [$F = 7.072$, $p = 0.001$; $F = 9.871$, $p = 0.000$] and group [$F = 12.127$, $p = 0.001$; $F = 7.267$, $p = 0.009$]; there was no significant interaction between condition and group [$F = 0.637$, $p = 0.542$; $F = 0.289$, $p = 0.736$]. Multiple comparisons on VEP amplitudes and latencies in separate conditions showed that Level 1 evoked significantly smaller amplitudes and shorter latencies than Level 4 [$p = 0.015$; $p = 0.004$], and Level 2 evoked significantly smaller amplitudes and shorter latencies than Level 4 [$p = 0.014$; $p = 0.000$].

Repeated-measures ANOVAs on N1 amplitudes and latencies revealed significant main effects for condition [$F = 12.509$, $p = 0.000$; $F = 21.889$, $p = 0.000$]. There was no significant main effect for group [$F = 0.014$, $p = 0.906$; $F = 0.319$, $p = 0.575$] and no significant interaction between condition and group [$F = 0.672$, $p = 0.534$; $F = 1.167$, $p = 0.313$]. Multiple comparisons on VEP amplitudes and latencies in separate conditions showed that Level 1 evoked significantly smaller amplitudes and shorter latencies than Level 4 [$p = 0.001$; $p = 0.000$], Level 2 evoked significantly smaller amplitudes and shorter latencies than Level 4 [$p = 0.000$; $p = 0.000$], and Level 3 evoked significantly smaller amplitudes and shorter latencies than Level 4 [$p = 0.042$; $p = 0.000$].

Repeated-measures ANOVAs on P2 amplitudes and latencies revealed significant main effects for condition [$F = 4.076$, $p = 0.011$; $F = 3.449$, $p = 0.043$], but no significant main effects for group [$F = 1.067$, $p = 0.306$; $F = 0.314$, $p = 0.577$] and no significant interaction between condition and group [$F = 0.271$, $p = 0.822$; $F = 3.012$, $p = 0.062$]. Multiple comparisons on VEP amplitudes and latencies in separate conditions showed that Level 1 stimuli evoked significantly smaller amplitudes than Level 4 [$p = 0.028$].

sLORETA Group Comparisons

Group comparisons of the sLORETA source imaging are shown in **Figure 3**. Locations with significant differences between VM patients and HC subjects are shown in two different forms: MRI views of three sides of the brain (**Figure 3A**) and 3D brain maps (**Figure 3B**). These maps and figures were created by assigning the SnPM t-values (two-tailed threshold) to their corresponding BAs, and color-coded (**Figure 3C**) using a range of light blue over dark blue, black, and red to yellow. Light blue represents negative t-values, which shows that the current source density of this location has significantly decreased. Compared with the P1 source densities of HC subjects, significant current density decrements (threshold log-F-ratio = 0.836, $p < 0.01$) of VM patients were distributed over the frontal lobe, parietal

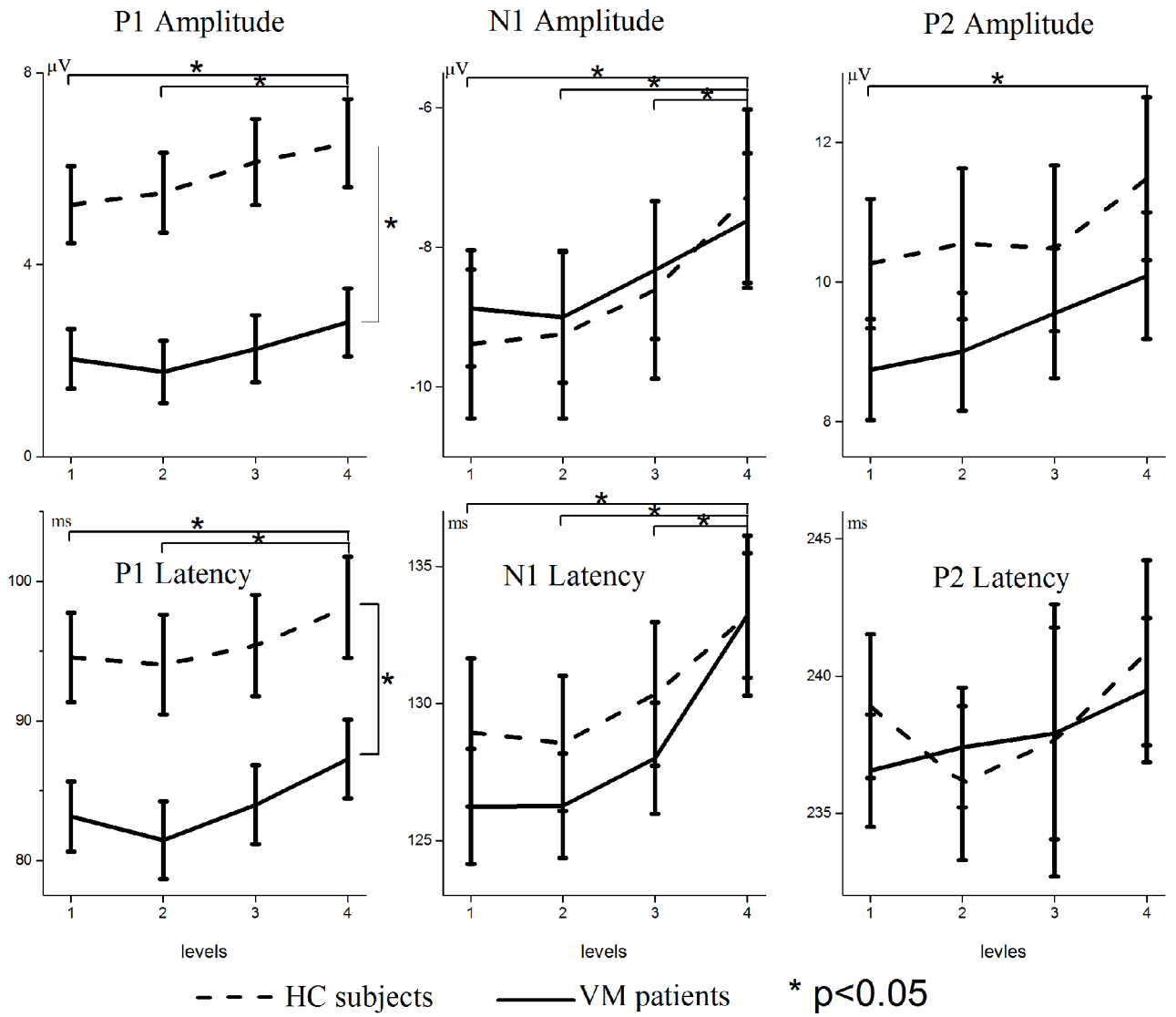

FIGURE 2 | Modulation of scalp-recorded VEPs across different luminance ratios. The amplitudes and latencies of the P1, N1, and P2 VEPs are shown separately for VM patients (solid line) and HC subjects (dashed line). Levels 1 and 4 refer to the smallest (12.5%) and largest (50%) proportions of white pixels in the stimulus pattern, respectively. Asterisks indicate significant differences between VM patients and HC subjects ($p < 0.05$). Note the different scaling for different VEP components.

lobe, temporal lobe, limbic lobe, occipital lobe, and sub-lobar regions. **Table 2** provides a complete overview of all retrieved statistically significant results including all anatomical regions and the number of activated voxels. The difference in the current density maximum was highest in the postcentral gyrus of the parietal lobe [Montreal Neurological Institute (MNI) coordinates (x, y, $z = -35, -40, 55$), BA 40] (logF = −1.93, $p < 0.001$).

DISCUSSION

The present study examined VEP responses in patients with VM and HC subjects. For the P1 VEP, our results revealed significantly lower amplitude and decreased latency, and reduced cortical activation in VM patients compared with HC subjects. The mechanisms underlying abnormal VEP responses to visual stimulation in patients with VM are currently unknown, but we know that the P1 source density differences between HC subjects and VM patients overlapped with the vestibular cortical fields (**Figures 3**, **4**).

We found reduced P1 amplitude and shorter P1 latency for VM patients compared with HC subjects, which indicates that VM is associated with functional changes in the central visual system. This observation may be explained by a lowered cortical preactivation level or reduced baseline activation of sensory cortices leading to abnormal information processing. sLORETA analysis was used to identify which brain regions contributed to these alterations. We identified reduced source activation of P1 in the frontal, parietal, temporal, limbic, and occipital lobes and

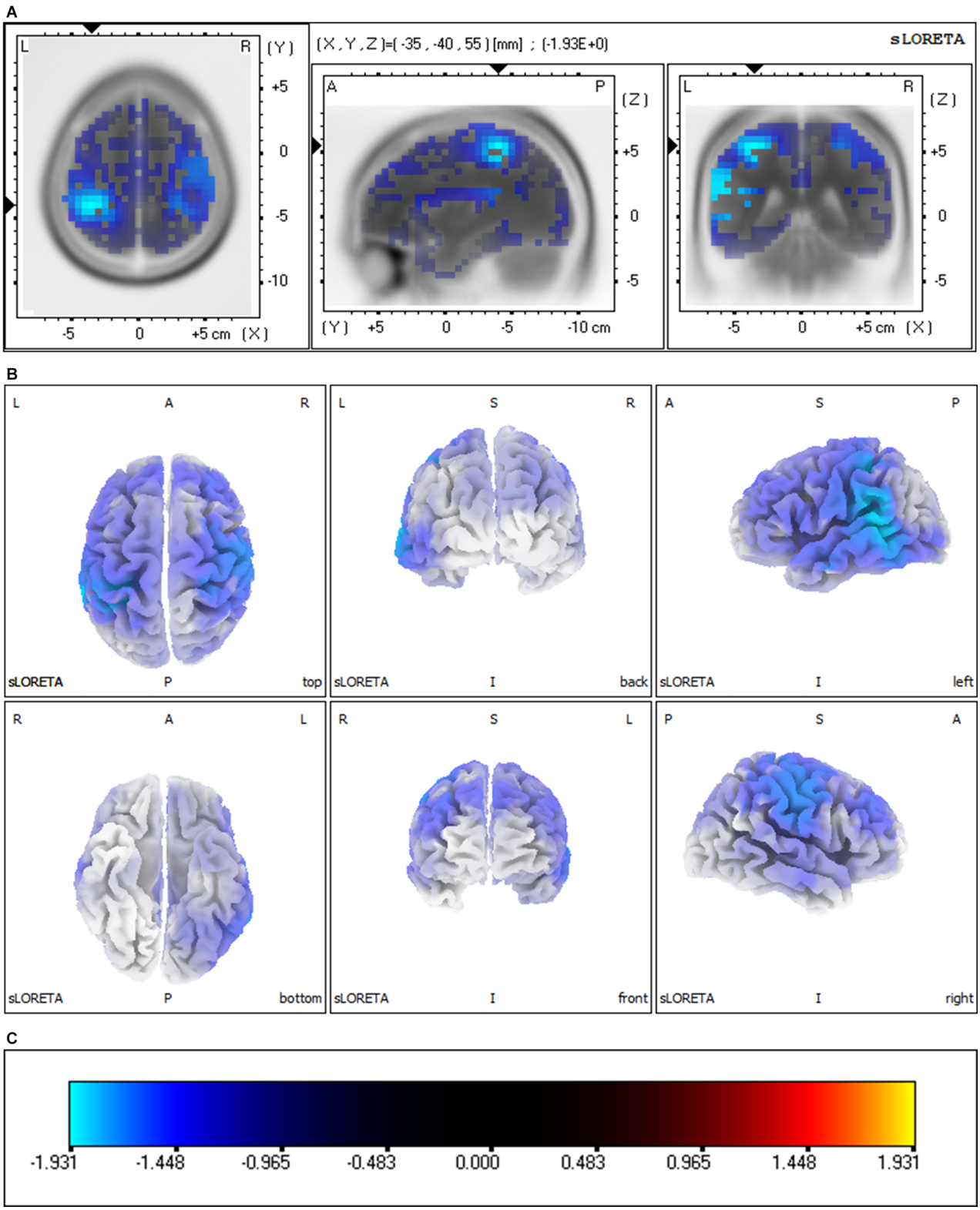

FIGURE 3 | Significant group comparisons of the sLORETA source imaging between the VM and HC groups. Regions with significant differences between groups are shown in three MRI views of the head **(A)** and 3D brain map views **(B)**. The color scale **(C)** represents log-F ratio values (threshold: log-F = 0.836, $p < 0.01$, two-tailed). The difference in current density maximum was highest in the postcentral gyrus of the parietal lobe [MNI coordinates (x, y, z = −35, −40, 55), BA 40; logF = −1.93, $p < 0.001$]. L, left; R, right; A, anterior; P, posterior; BA, Brodmann area.

TABLE 2 | Significant brain regions of P1 source activities and the numbers of voxels differing between VM patients and HC subjects.

Lobe	L	R	Total
Frontal lobe	**994**	**889**	**1,883**
Middle frontal gyrus	219	230	449
Precentral gyrus	177	180	357
Inferior frontal gyrus	176	150	326
Superior frontal gyrus	151	130	281
Medial frontal gyrus	151	123	274
Paracentral lobule	50	22	72
Rectal gyrus	21	22	43
Orbital gyrus	15	9	24
Subcallosal gyrus	14	9	23
Sub-gyral	9	7	16
Cingulate gyrus	6	4	10
Postcentral gyrus	4	2	6
Precuneus	1	1	2
Parietal lobe	**582**	**547**	**1,129**
Postcentral gyrus	175	178	353
Precuneus	160	132	292
Inferior parietal lobule	142	142	284
Superior parietal lobule	63	63	126
Supramarginal gyrus	20	15	35
Angular gyrus	11	7	18
Sub-gyral	9	8	17
Paracentral lobule	2	2	4
Temporal lobe	**568**	**403**	**971**
Superior temporal gyrus	199	173	372
Middle temporal gyrus	165	144	309
Inferior temporal gyrus	74	35	109
Fusiform gyrus	85	15	100
Transverse temporal gyrus	18	18	36
Sub-gyral	12	8	20
Supramarginal gyrus	8	4	12
Angular gyrus	5	4	9
Inferior frontal gyrus	1	1	2
Insula	1	1	2
Limbic lobe	**368**	**226**	**594**
Cingulate gyrus	143	119	262
Anterior cingulate	65	45	110
Parahippocampal gyrus	85	21	106
Posterior cingulate	38	21	59
Uncus	31	15	46
Precuneus	2	3	5
Sub-gyral	2	1	3
Paracentral lobule	1	1	2
Inferior temporal gyrus	1		1
Occipital lobe	**337**	**132**	**469**
Cuneus	124	86	210
Middle occipital gyrus	67	16	83
Lingual gyrus	65		65
Precuneus	21	18	39
Fusiform gyrus	29		29
Inferior occipital gyrus	16	2	18
Superior occipital gyrus	7	6	13
Middle temporal gyrus	6	2	8
Inferior temporal gyrus	2	2	4
Sub-lobar	**111**	**106**	**217**
Insula	104	101	205
Extra-nuclear	7	5	12

sub-lobar regions in VM patients compared with HC subjects, which is in line with previous functional magnetic resonance imaging (fMRI) studies that showed cortical gray matter changes in vestibular migraine (Zhe et al., 2021). Vestibular-sensitive neurons respond to a variety of modalities including proprioception or visual motion. Vestibular information and somatosensory and/or visual inputs are conveyed through ventral posterolateral, ventral posteromedial, and ventral posterior inferior thalamic nuclei and lateral geniculate nucleus. We found that the P1 source density differences between HC subjects and VM patients overlapped with the vestibular cortical fields. This led us to hypothesize deactivation of the vestibular cortex regions in VM patients, where excessive inhibition of the vestibular cortex regions leads to peripheral loss of control, resulting in peripheral dysfunction such as photophobia and vestibular dysfunction.

Vestibular information processing involves polymodal association areas in the parietal, temporal, and insular cortices and cortical areas associated with spatial orientation (e.g., primary somatosensory cortex, primary visual cortex; Vuralli et al., 2018). When visual, vestibular, and somatosensory stimuli incorporation and/or processing of one of these three components is damaged, VM victims may experience vestibular symptoms. We hypothesized a central disruption in multisensory component processing, though how this would affect visual or vestibular system processing remains unknown in VM.

Few studies have thoroughly examined VEPs at different luminance ratios in VM patients. Our results indicated parametric regulation of P1 amplitudes based on the luminance ratio in the checkerboard images. This result was found in both VM patients and HC subjects and is in accordance with previous findings of larger VEP reactions for higher luminance levels in visual stimuli (Johannes et al., 1995; Sandmann et al., 2012). Further topographic mapping analysis revealed that VM patients and HC subjects had a P1 latency difference in the occipital area, which corroborates the previous finding that reduced metabolism in the occipital cortex may signify mutual suppression between the visual and vestibular systems (Shin et al., 2014).

Compared with HC subjects, we found that VM patients showed considerably shorter P1 latencies. As VEP latencies can be used to approximate visual processing time (Thorpe et al., 1996) and might change with latency in the behavioral reaction in visual tasks (Fort et al., 2005), we predict that this finding may reveal quicker, more effective visual information processing that enables faster behavioral reactions in these subjects. However, while increased sensitivity to visual stimuli might be linked to the quicker low-level visual processing observed in migraineurs with aura (Wray et al., 1995), it is not clear whether patients with VM exhibit enhanced (behavioral) response speed in visual tasks compared with HC subjects. The fact that the VM group showed marked response time advantages in basic tasks provides psychophysical validation of their expected hypersensitivity to visual stimuli. These results suggest that since signals to the primary visual cortex are processed more promptly, VM patients are faster at low-level visual processing.

VM patient processing speed for low-level visual tasks should perhaps be seen as reflecting an interaction between more or less visual excitation and more or less regional inhibitory failure (Wray et al., 1995). To test this hypothesis, future research should combine electrophysiological recordings with neuroimaging studies so that the temporal patterns of sensory

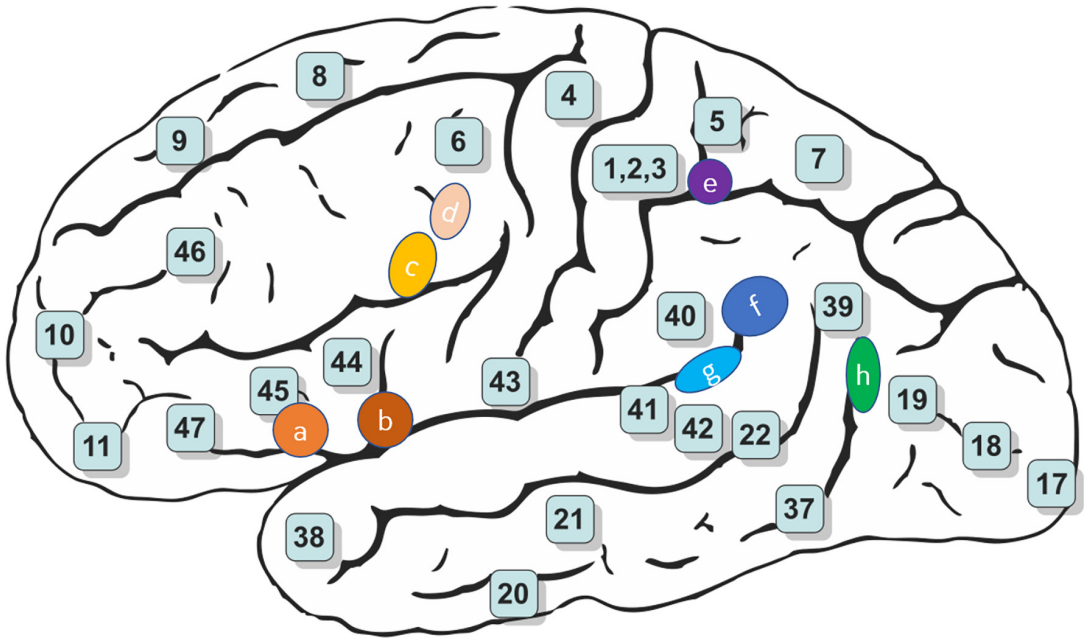

FIGURE 4 | Schematic brain representations illustrating the topography of the vestibular cortical fields experimentally identified in humans. The numbers indicate the architectonically defined BAs [based on Gray's (1918) Anatomy of the Human Body]. The letters represent the vestibular sites with their localization in the cortical regions in the right panel (Ventre-Dominey, 2014).

processing can be correlated with the accompanying anatomical and functional changes in patients with VM.

CONCLUSIONS

Using a combined VEP and sLORETA approach, we found smaller P1 amplitudes and decreased latency, and reduced visual cortex activation in VM patients compared with HC subjects. These findings suggest altered processing of visual stimuli in VM patients between attacks. Specifically, we found that the P1 source density differences between HC subjects and VM patients overlap with the vestibular cortical fields. These results suggest that abnormalities in vestibular cortical fields might be a pathophysiological mechanism of VM.

DATA AVAILABILITY STATEMENT

The original contributions presented in the study are included in the article, further inquiries can be directed to the corresponding author/s.

ETHICS STATEMENT

The studies involving human participants and the protocol were reviewed and approved by the Ethics Committee of Sun Yat-sen University. The patients/participants provided their written informed consent to participate in this study.

AUTHOR CONTRIBUTIONS

YO designed the experiment and revised the manuscript. JLiu and ML performed the experiment, interpreted the results, and wrote the manuscript. QZ and YW improved the experiment and the article. YCh, JW, and JLi helped to analyze the data. LC, LY, and YCa helped to collect patient. YZ supervised the work. All authors read and approved the final manuscript. All authors contributed to the article and approved the submitted version.

FUNDING

This project was supported by the National Natural Science Foundation of China (to JLiu, Grant No. 81900954 and to ML, No. 81800922).

ACKNOWLEDGMENTS

We thank the VM patients and participants in control group for their participation.

REFERENCES

Beh, S. C. (2019). Vestibular migraine: how to sort it out and what to do about it. *J. Neuroophthalmol.* 39, 208–219. doi: 10.1097/WNO.0000000000000791

Beh, S. C., Masrour, S., Smith, S. V., and Friedman, D. I. (2019). The spectrum of vestibular migraine: clinical features, triggers and examination findings. *Headache* 59, 727–740. doi: 10.1111/head.13484

de Tommaso, M., Ambrosini, A., Brighina, F., Coppola, G., Perrotta, A., Pierelli, F., et al. (2014). Altered processing of sensory stimuli in patients with migraine. *Nat. Rev. Neurol.* 10, 144–155. doi: 10.1038/nrneurol.2014.14

Espinosa-Sanchez, J. M., and Lopez-Escamez, J. A. (2015). New insights into pathophysiology of vestibular migraine. *Front. Neurol.* 6:12. doi: 10.3389/fneur.2015.00012

Fort, A., Besle, J., Giard, M. H., and Pernier, J. (2005). Task-dependent activation latency in human visual extrastriate cortex. *Neurosci. Lett.* 379, 144–148. doi: 10.1016/j.neulet.2004.12.076

Gray, H. (1918). *Henry Gray's Anatomy of the Human Body*. Philadelphia, PA: Lea & Febiger. doi: 10.5962/bhl.title.20311

Grusser, O. J., Pause, M., and Schreiter, U. (1990a). Localization and responses of neurones in the parieto-insular vestibular cortex of awake monkeys (Macaca fascicularis). *J. Physiol.* 430, 537–557. doi: 10.1113/jphysiol.1990.sp018306

Grusser, O. J., Pause, M., and Schreiter, U. (1990b). Vestibular neurones in the parieto-insular cortex of monkeys (Macaca fascicularis): visual and neck receptor responses. *J. Physiol.* 430, 559–583. doi: 10.1113/jphysiol.1990.sp018307

Guldin, W. O., and Grusser, O. J. (1998). Is there a vestibular cortex?. *Trends Neurosci.* 21, 254–259. doi: 10.1016/s0166-2236(97)01211-3

Headache Classification Committee of the International Headache Society (IHS). (2013). The international classification of headache disorders, 3rd edition (beta version). *Cephalalgia* 33, 629–808. doi: 10.1177/0333102413485658

Johannes, S., Munte, T. F., Heinze, H. J., and Mangun, G. R. (1995). Luminance and spatial attention effects on early visual processing. *Brain Res. Cogn. Brain Res.* 2, 189–205. doi: 10.1016/0926-6410(95)90008-x

Lempert, T., Olesen, J., Furman, J., Waterston, J., Seemungal, B., Carey, J., et al. (2012). Vestibular migraine: diagnostic criteria. *J. Vestib. Res.* 22, 167–172. doi: 10.3233/VES-2012-0453

Messina, R., Rocca, M. A., Colombo, B., Teggi, R., Falini, A., Comi, G., et al. (2017). Structural brain abnormalities in patients with vestibular migraine. *J. Neurol.* 264, 295–303. doi: 10.1007/s00415-016-8349-z

Pascual-Marqui, R. D. (2002). Standardized low-resolution brain electromagnetic tomography (sLORETA): technical details. *Methods Find Exp. Clin. Pharmacol.* 24, 5–12.

Russo, A., Marcelli, V., Esposito, F., Corvino, V., Marcuccio, L., Giannone, A., et al. (2014). Abnormal thalamic function in patients with vestibular migraine. *Neurology* 82, 2120–2126. doi: 10.1212/WNL.0000000000000496

Sandmann, P., Dillier, N., Eichele, T., Meyer, M., Kegel, A., Pascual-Marqui, R. D., et al. (2012). Visual activation of auditory cortex reflects maladaptive plasticity in cochlear implant users. *Brain* 135, 555–568. doi: 10.1093/brain/awr329

Sekihara, K., Sahani, M., and Nagarajan, S. S. (2005). Localization bias and spatial resolution of adaptive and non-adaptive spatial filters for MEG source reconstruction. *Neuroimage* 25, 1056–1067. doi: 10.1016/j.neuroimage.2004.11.051

Shin, J. H., Kim, Y. K., Kim, H. J., and Kim, J. S. (2014). Altered brain metabolism in vestibular migraine: comparison of interictal and ictal findings. *Cephalalgia* 34, 58–67. doi: 10.1177/0333102413498940

Sulejmanpasic, G., and Drnda, S. (2017). Magnetic resonance imaging (MRI) and visual evoked potentials (VEPs) of occipital region in patients with schizophrenia and migraine headache. *Acta Inform. Med.* 25, 103–107. doi: 10.5455/aim.2017.25.103-107

Teggi, R., Colombo, B., Rocca, M. A., Bondi, S., Messina, R., Comi, G., et al. (2016). A review of recent literature on functional MRI and personal experience in two cases of definite vestibular migraine. *Neurol. Sci.* 37, 1399–1402. doi: 10.1007/s10072-016-2618-6

Thorpe, S., Fize, D., and Marlot, C. (1996). Speed of processing in the human visual system. *Nature* 381, 520–522. doi: 10.1038/381520a0

Ventre-Dominey, J. (2014). Vestibular function in the temporal and parietal cortex: distinct velocity and inertial processing pathways. *Front. Integr. Neurosci.* 8:53. doi: 10.3389/fnint.2014.00053

Vuralli, D., Yildirim, F., Akcali, D. T., Ilhan, M. N., Goksu, N., and Bolay, H. (2018). Visual and postural motion-evoked dizziness symptoms are predominant in vestibular migraine patients. *Pain Med.* 19, 178–183. doi: 10.1093/pm/pnx182

Wagner, M., Fuchs, M., and Kastner, J. (2004). Evaluation of sLORETA in the presence of noise and multiple sources. *Brain Topogr.* 16, 277–280. doi: 10.1023/b:brat.0000032865.58382.62

Wray, S. H., Mijovic-Prelec, D., and Kosslyn, S. M. (1995). Visual processing in migraineurs. *Brain* 118, 25–35. doi: 10.1093/brain/118.1.25

Zhe, X., Zhang, X., Chen, L., Zhang, L., Tang, M., Zhang, D., et al. (2021). Altered gray matter volume and functional connectivity in patients with vestibular migraine. *Front. Neurosci.* 15:683802. doi: 10.3389/fnins.2021.683802

Conflict of Interest: The authors declare that the research was conducted in the absence of any commercial or financial relationships that could be construed as a potential conflict of interest.

frontiers in Neuroscience

ORIGINAL RESEARCH
published: 21 January 2022
doi: 10.3389/fnins.2021.791436

Altered Neurovascular Coupling in Unilateral Pulsatile Tinnitus

Xiaoshuai Li[1], Ning Xu[1], Chihang Dai[1], Xuxu Meng[1], Xiaoyu Qiu[1], Heyu Ding[1], Rong Zeng[2], Han Lv[1], Pengfei Zhao[1]*, Zhenghan Yang[1], Shusheng Gong[2] and Zhenchang Wang[1]**

[1] Department of Radiology, Beijing Friendship Hospital, Capital Medical University, Beijing, China, [2] Department of Otolaryngology Head and Neck Surgery, Beijing Friendship Hospital, Capital Medical University, Beijing, China

Objective: Altered cerebral blood flow (CBF) and regional homogeneity (ReHo) have been reported in pulsatile tinnitus (PT) patients. We aimed to explore regional neurovascular coupling changes in PT patients.

Materials and Methods: Twenty-four right PT patients and 25 sex- and age-matched normal controls were included in this study. All subjects received arterial spin labeling imaging to measure CBF and functional MRI to compute ReHo. CBF/ReHo ratio was used to assess regional neurovascular coupling between the two groups. We also analyzed the correlation between CBF/ReHo ratio and clinical data from the PT patients.

Results: PT patients exhibited increased CBF/ReHo ratio in left middle temporal gyrus and right angular gyrus than normal controls, and no decreased CBF/ReHo ratio was found. CBF/ReHo ratio in the left middle temporal gyrus of PT patients was positively correlated with Tinnitus Handicap Inventory score ($r = 0.433$, $p = 0.035$).

Conclusion: These findings indicated that patients with PT exhibit abnormal neurovascular coupling, which provides new information for understanding the neuropathological mechanisms underlying PT.

Keywords: cerebral blood flow, arterial spin labeling, regional homogeneity, functional magnetic resonance imaging, pulsatile tinnitus

OPEN ACCESS

Edited by:
Julian Keil,
University of Kiel, Germany

Reviewed by:
David Wack,
University at Buffalo, United States
Matthew ManHin Cheung,
CUHK Medical Centre, Hong Kong SAR, China

***Correspondence:**
Han Lv
chrislvhan@126.com
Pengfei Zhao
zhaopengf05@163.com
Zhenchang Wang
cjr.wzhch@vip.163.com

Specialty section:
This article was submitted to Perception Science, a section of the journal Frontiers in Neuroscience

Received: *08 October 2021*
Accepted: *09 December 2021*
Published: *21 January 2022*

Citation:
Li X, Xu N, Dai C, Meng X, Qiu X, Ding H, Zeng R, Lv H, Zhao P, Yang Z, Gong S and Wang Z (2022) Altered Neurovascular Coupling in Unilateral Pulsatile Tinnitus. Front. Neurosci. 15:791436. doi: 10.3389/fnins.2021.791436

INTRODUCTION

Pulsatile tinnitus (PT) manifests as vascular somatosound synchronized with the pulse (Haraldsson et al., 2019). Sigmoid sinus wall anomalies are considered the most common and curable cause of PT (Dong et al., 2015; Mundada et al., 2015). Sounds and vibrations produced by abnormal hemodynamics in the venous sinus are perceived by the inner ear through the incomplete sinus wall (Li et al., 2021a). Sigmoid sinus wall reconstruction can effectively eliminate PT (Zhang et al., 2019). This disease state seriously affects patients' daily lives, leading to irritability, anxiety, sleep disturbance, depression and even suicide (Li et al., 2020).

Recently, more attention has been given to the neuronal activity of patients with PT (Lv et al., 2015a,b, 2016b, 2017). Spontaneous neuronal activity can be reflected by blood oxygen

level-dependent (BOLD) signals in resting-state fMRI (Fox and Raichle, 2007). Lv et al. (2015a) used fMRI to measure altered amplitude of low-frequency fluctuation (ALFF) and regional homogeneity (ReHo) values in multiple brain regions of patients with unilateral PT, suggesting that abnormal brain activity existed in such patients. Subsequently, numerous studies also found abnormal functional connectivity between multiple brain regions and networks in these patients (Lv et al., 2015b, 2017, 2018). The above studies indicated that there are neuropathological changes in PT patients.

According to the neurovascular coupling hypothesis, an increase in neuronal activity is accompanied by an increase in cerebral metabolic demand, leading to an increase in cerebral perfusion (Raichle and Mintun, 2006; Lanting et al., 2009; Venkat et al., 2016). Previous studies have used PET and SPECT to explore cerebral blood flow (CBF) changes in tinnitus patients, and found that there are altered CBF in multiple brain regions (Geven et al., 2014; Laureano et al., 2016). Perfusion and metabolism are tightly coupled in the brain (Aubert and Costalat, 2002). Several studies have found that the brain perfusion measured by arterial spin labeling (ASL) (Dai et al., 2009; Yoshiura et al., 2009; Wolk and Detre, 2012; Binnewijzend et al., 2013) has a good correlation with the brain metabolism measured by PET (Herholz et al., 2002; Du et al., 2006; Pagani et al., 2010; Bozoki et al., 2012) in the field of mild cognitive impairment and Alzheimer's dementia. Due to its advantages of non-invasiveness, low cost and simplicity, ASL can be used to perform repeated studies on subjects. Thus, this technique has become a promising alternative technique and is widely used in various disease states (Haller et al., 2016). Recent studies have used ASL to identify CBF changes in multiple brain regions of PT patients (Li et al., 2020, 2021b).

However, the above studies were based on a single imaging technique to assess neuronal activity or cerebral perfusion in patients with PT, which cannot comprehensively reflect the neurovascular coupling disorder underlying this disease. Liang et al. combined BOLD and ASL techniques and found that neurovascular coupling reflects aspects of the underlying physiological function of the brain (Liang et al., 2013). Subsequently, some studies have found changed neurovascular coupling in the context of various diseases, confirming that it is related to the pathophysiological mechanism underlying the disease (Phillips et al., 2016; Tarantini et al., 2017; Zhu et al., 2017; Guo et al., 2018). To date, the neurovascular coupling status of PT patients remains unclear. In this study, vascular response was evaluated by CBF, and neuronal activity was calculated by ReHo. CBF/ReHo ratio was used to assess regional neurovascular coupling. We expect to understand the neuropathological changes underlying PT from a new perspective.

MATERIALS AND METHODS

Participants

In this study, 24 right PT patients and 25 age- and sex-matched normal controls (NCs) were included. All patients showed pulse-synchronous noise (Li et al., 2021a), and sigmoid sinus wall dehiscence was considered the key etiology of PT by DSA and CTA/V. The exclusion criteria for all patients and NCs included hearing loss, MRI contraindications, hyperacusis, neuropsychiatric diseases, and history of head trauma. Tinnitus Handicap Inventory (THI) scores were exploited to assess PT severity. All participants signed written informed consent approved by the ethical committee.

Data Acquisition

MRI data were acquired on a GE Discovery MR750 3.0 T scanner. The parameters for 3D pseudocontinuous ASL were as follows: repetition time (TR), 4854 ms; echo time (TE), 10.7 ms; slice thickness, 4 mm with no gap; in-plane resolution, 3.37 mm × 3.37 mm; number of excitations, 3; field of view (FOV), 240 mm × 240 mm; postlabel delay (PLD), 2025 ms; flip angle, 111°; and 36 slices. Resting-state BOLD imaging was obtained with the following parameters: TE, 35 mm; TR, 2000 ms; FOV, 240 × 240 mm; matrix, 64 × 64; flip angle, 90°; slice thickness, 4 mm with 1 mm gap; 200 time points; and 28 slices. During the scanning, all participants were asked to relax without thinking of anything, to remain motionless and awake, and to close their eyes.

Cerebral Blood Flow Calculation

CBF maps were preprocessed using previously described methods (Li et al., 2021a,b). First, the CBF maps of 25 NCs were coregister to MNI space to generate a standard template using SPM8 software. Then, we registered the CBF maps from all participants to this standard MNI template. CBF maps were normalized by dividing the participant's global mean CBF (Aslan and Lu, 2010). Finally, we smoothed the CBF maps using an 8 mm full-width at half-maximum (FWHM) Gaussian kernel.

fMRI Data Preprocessing

BOLD images were preprocessed using Data Processing Assistant for Resting-State fMRI (DPARSF) software. To allow the signal to stabilize, the first 10 time points were removed from analysis. The specific processing steps included slice timing, realignment (head translation $> 2.5°$ or motion > 2.5 mm were excluded), nuisance covariate regressions, filtering (0.01–0.08 Hz), and spatial normalization into MNI space with resampling to $3 \times 3 \times 3\text{mm}^3$.

ReHo was calculated using Kendall's coefficient concordance of a given voxel with its twenty-six nearest neighboring voxels (Zang et al., 2004). Individual ReHo maps were divided by the global average ReHo value and then smoothed.

Statistical Analysis

Statistical analysis was performed using SPSS v.22.0 software. We used two-sample *t*-test to investigate the difference in age and handedness between groups, and Fisher's exact test was used to detect the difference in sex between groups ($P < 0.05$).

In CBF/ReHo ratio analysis, we used two-sample *t*-test to explore significant CBF/ReHo ratio differences between the NCs

TABLE 1 | Demographic data for PT patients and NCs.

	PT (n = 24)	NC (n = 25)	P value
Age (years)	38.5 ± 9.9	34.0 ± 9.7	0.114[b]
Sex (male/female)	2/22	4/21	0.667[a]
Handedness	24 right-handed	25 right-handed	1.000[b]
PT duration (months)	34.5 ± 31.1	NA	NA
THI score	52.0 ± 23.6	NA	NA

Data are presented as the mean ± standard deviation. PT: pulsatile tinnitus; NC: normal control; THI: Tinnitus Handicap Inventory; NA: not applicable.
[a] Fisher's exact test; [b] Two-sample t-test.

and PT patients, with gender and sex serving as nuisance covariates. Cluster-level false discovery rate (FDR) correction was used for multiple comparisons with $P < 0.05$. The same method was performed to explore group differences of ReHo and CBF. A correlation analysis (Pearson's correlation) was performed to assess relationships between clinical data and altered CBF/ReHo ratio.

RESULTS

Demographic Data

Table 1 shows the demographic data for all participants. The PT patients and NCs were well matched for sex ($p = 0.667$), age ($p = 0.114$), and handedness ($p = 1.000$). Across all patients, the THI score was 52.0 ± 23.6, and the PT duration was 34.5 ± 31.1 months.

Altered Cerebral Blood Flow/Regional Homogeneity Ratio in Pulsatile Tinnitus Patients

Figure 1 and **Table 2** shows the CBF/ReHo ratio difference between the two groups. The PT patients exhibited increased CBF/ReHo ratio in the right angular gyrus and left middle temporal gyrus than the NCs, and no decreased CBF/ReHo ratio was found in the PT patients ($p < 0.05$, FDR corrected).

Altered Regional Homogeneity and Cerebral Blood Flow in Pulsatile Tinnitus Patients

Pulsatile tinnitus (PT) patients exhibited significantly increased CBF in the right angular gyrus and precuneus than the NCs ($p < 0.05$, FDR corrected) (**Figure 2** and **Table 3**). There were no significant ReHo differences between the two groups.

Correlation Analyses

In the PT patients, increased CBF/ReHo ratio in the left middle temporal gyrus was positively correlated with THI scores ($r = 0.433$, $p = 0.035$) (**Figure 3**). We found no significant correlation between CBF/ReHo ratio in the right angular gyrus and clinical data.

DISCUSSION

This study investigated altered neurovascular coupling in PT patients by combining ASL and BOLD MRI. We found that patients with PT had increased CBF/ReHo ratio in the left middle temporal gyrus and right angular gyrus. Furthermore, the altered CBF/ReHo ratio in the left middle temporal gyrus was positively correlated with THI scores. These findings may help us understand the neuropathological mechanism underlying PT from the perspective of neurovascular coupling.

Previous studies have confirmed that CBF/ReHo ratio can offer more information on local neurovascular coupling alterations in diseases (Guo et al., 2018; Liu et al., 2021; Zhang et al., 2021). In a normal brain, CBF/ReHo ratio remains balanced. In PT, the deviation in the balance (i.e., abnormal neurovascular coupling) may lead to increases or decreases in CBF/ReHo ratio. Decreased CBF/ReHo ratio represents a relatively insufficient blood supply per unit of neuronal activity, while increased CBF/ReHo ratio represents a relative excess blood supply per unit of neuronal activity (Guo et al., 2018). The clinical correlation analysis found that CBF/ReHo ratio was related to the severity of PT, thus confirming the disruptive effect of altered CBF/ReHo ratio. More importantly, this ratio

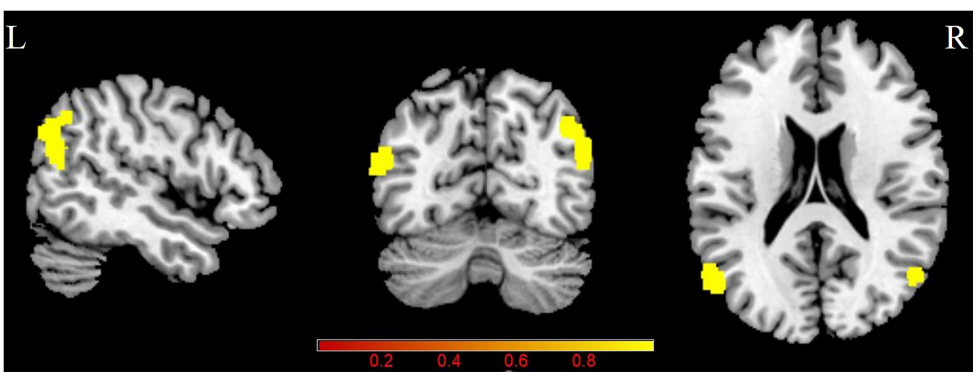

FIGURE 1 | Group differences in CBF/ReHo ratio between patients with PT and NCs ($P < 0.05$, FDR corrected). PT: pulsatile tinnitus; NC: normal control; CBF: cerebral blood flow; ReHo: regional homogeneity.

TABLE 2 | Brain regions with significant group differences in CBF/ReHo ratio.

Brain region	Peak MNI (mm)			Peak T value	Cluster size (mm^3)
	x	y	z		
PT > NC					
R angular gyrus	52	−66	26	4.73	226
L middle temporal gyrus	−54	−68	18	5.06	118

PT: pulsatile tinnitus; NC: normal control; CBF: cerebral blood flow; ReHo: regional homogeneity; MNI: Montreal Neurological Institute; L: left; R: right.

can identify abnormal brain areas with no obvious alterations in ReHo and CBF. Changes in CBF and ReHo in opposite directions may disrupt this balance. Therefore, slightly decreased ReHo and increased CBF may lead to significantly increased CBF/ReHo ratio in PT patients, while slightly increased ReHo and decreased CBF may lead to significant decrease in CBF/ReHo ratio (Guo et al., 2018). This mechanism can be used to explain why there were significant group differences in the CBF/ReHo ratio in these brain regions, but no significant differences were found in ReHo or CBF measurements. Thus, CBF/ReHo ratio can be used as a novel functional imaging index to evaluate neurovascular coupling alterations in disease.

Pulsatile tinnitus (PT) patients had increased CBF/ReHo ratio in the right angular gyrus than the NCs. Moreover, in the present study, increased CBF and normal ReHo were found in the right angular gyrus, suggesting that the increase in the CBF/ReHo ratio was mainly caused by increases in CBF. Prior studies showed that in patients with unilateral tinnitus, synchronized activity and connectivity within the gamma band were increased in the right angular gyrus as assessed using electroencephalography (Vanneste et al., 2011; Zhang et al., 2020). Chen et al. (2014) based on fMRI, found increased low-frequency fluctuations in chronic tinnitus patients, indicating increased neuronal activity in this region (Chen et al., 2014). A PET study also confirmed the increased angular gyrus activity in patients with chronic tinnitus (Song et al., 2012). This may be related to the function of the angular gyrus to participate in the integration of auditory stimuli, memory-related activities, self-awareness, and self-perception (Daselaar et al., 2006; De Ridder et al., 2014; Zhang et al., 2020). Moreover, the angular gyrus is involved in shifting the attention of chronic tinnitus patients from auditory phantom percept to visual cues in Heidelberg neuro-music therapy (Krick et al., 2017). Stimulating the hyperactive angular gyrus can eliminate tinnitus (Plewnia et al., 2007), indicating that there is a causal relationship between this area and tinnitus perception. In addition, this region is an important node in the dorsal auditory pathway, which converts auditory representations into premotor reactions (Karabanov et al., 2009). Schubotz et al. (2003) further found that coactivation of the superior premotor motor cortex and angular area is critical to the spatial positioning of auditory input (Schubotz et al., 2003). Note that the above studies included non-PT patients. Xu et al. used fMRI and found that the angular gyrus is participated in abnormal functional connectivity in PT patients (Xu et al., 2019), suggesting that this brain area plays a critical role in the pathophysiological mechanism underlying PT.

In addition, our preliminary results show that the CBF/ReHo ratio in the left middle temporal gyrus was higher in the PT patients than the NCs. The middle temporal gyrus is a part of the auditory association cortex (Verger et al., 2017), which is involved in auditory information processing. Animal studies have confirmed that tinnitus may be related to synaptic structure remodeling, enhanced synchronous and spontaneous neuronal activity in the auditory cortex (Adjamian et al., 2009; Henry et al., 2014). Voxel-based morphometry study has shown that tinnitus can cause significant cortical changes in the middle temporal gyrus [MNI coordinates (x, y, z):49, −70, 13; cluster size: 747] (Boyen et al., 2013). fMRI studies observed increased ALFF and ReHo in the middle temporal gyrus in tinnitus patients [MNI coordinates (x, y, z):60, −51, −9; cluster size:87] [MNI coordinates (x, y, z):60, −36, −3; cluster size:87] (Chen et al., 2014; Han et al., 2018), which also reflected abnormal regional functional changes in the auditory-related cortex in tinnitus patients. However, the above studies have focused on individuals without PT. Functional connectivity analysis conducted by Lv et al. (2016a) found that the middle temporal gyrus was involved in abnormal functional connectivity in PT [MNI coordinates (x, y, z):55, −52, 8; cluster size:79], thus confirming the vital role of this brain area. Wang et al. (2019) further found that functional connectivity in the middle temporal gyrus in PT patients changes over time, and its intensity can be used to

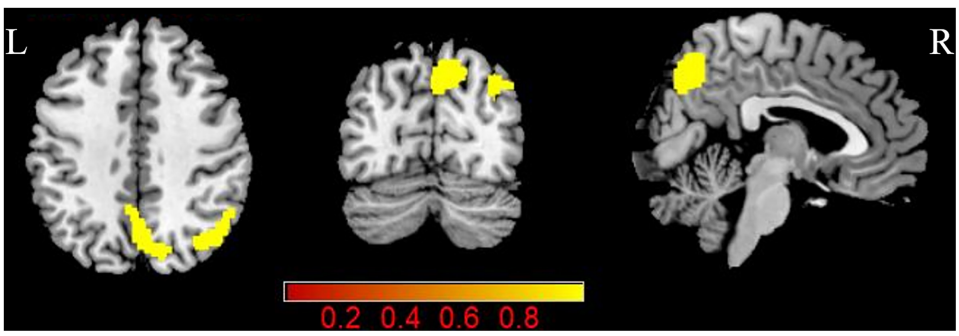

FIGURE 2 | Group differences in CBF between patients with PT and NCs ($P < 0.05$, FDR corrected). PT: pulsatile tinnitus; NC: normal control; CBF: cerebral blood flow; ReHo: regional homogeneity.

TABLE 3 | Brain regions with significant group differences in CBF.

Brain region	Peak MNI (mm)			Peak T value	Cluster size (mm^3)
	x	y	z		
PT > NC					
R angular gyrus	46	−66	42	4.75	330
R precuneus	8	−72	48	4.62	345

PT: pulsatile tinnitus; NC: normal control; CBF: cerebral blood flow; MNI: Montreal Neurological Institute; R: right.

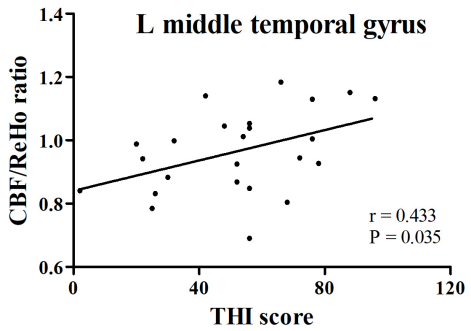

FIGURE 3 | The correlation between CBF/ReHo ratio in the left middle temporal gyrus in PT patients and THI score. PT: pulsatile tinnitus; NC: normal control; CBF: cerebral blood flow; ReHo: regional homogeneity; THI: Tinnitus Handicap Inventory.

quantitatively measure PT duration (Wang et al., 2019). These findings indicated that this brain area has important significance in the neuropathology underlying PT. In addition, the increased CBF/ReHo ratio in the left middle temporal gyrus were positively correlated with THI score in the PT patients, indicating the CBF/ReHo ratio in this region is more likely to reflect the severity of the disease.

This study has several limitations. First, we enrolled only right PT patients. In clinical work, right PT patients are more common than left PT patients (Eisenman et al., 2018) and may represent the general state of most patients. As the number of included patients increases, we will further explore the effect of PT side on neurovascular coupling changes. Second, the CBF/ReHo ratio is only an indirect reflection of neurovascular coupling. In the future, we expect that there will be direct neurovascular coupling indicators to describe the neuropathological mechanisms underlying PT. Third, this study found that the altered neurovascular coupling in the left middle temporal gyrus, which is a relatively large area. Thus, we have added MNI coordinates and cluster size of the middle temporal gyrus of other studies in the discussion section, and that found the location of this brain area is close to our result. Fourth, Changes in brain morphology may affect neuronal activity. Previous studies found that there was no significant difference in brain volume between PT patients and the NCs (Lv et al., 2015b, 2016a, 2017). Therefore, we did not carry out repeated morphological studies in this study. Fifth, this was a cross-sectional study. In the next step, we will explore changes in neurovascular coupling after PT is eliminated, and further explore the neuropathological changes associated with this condition.

CONCLUSION

In conclusion, this study combined CBF and ReHo to describe regional neurovascular coupling changes in PT patients. Specifically, these patients exhibited increased CBF/ReHo ratio in the right angular gyrus and left middle temporal gyrus, and the altered CBF/ReHo ratio in the left middle temporal gyrus was positively correlated with the severity of PT. Our results provide potential imaging markers for understanding the neuropathological mechanism underlying PT.

DATA AVAILABILITY STATEMENT

The original contributions presented in the study are included in the article/**Supplementary Material**, further inquiries can be directed to the corresponding authors.

ETHICS STATEMENT

The studies involving human participants were reviewed and approved by Ethics Committee of Beijing Friendship Hospital, Capital Medical University, Beijing, China. The patients/participants provided their written informed consent to participate in this study.

AUTHOR CONTRIBUTIONS

XL, NX, CD, XM, XQ, and RZ performed the experiment and collected, analyzed, or interpreted the data involved in the study. XL preprocessed image data, performed the statistical results, and drafted the manuscript. XL, PZ, HL, and ZW designed the study and ensured the questions related to all aspects of the work. PZ, HL, ZY, SG, and ZW gave critical comments on the manuscript. All authors contributed to the article and approved the submitted version.

FUNDING

This study was supported by Grant Nos. 61931013, 82171886, and 62171297 from the National Natural Science Foundation of China.

SUPPLEMENTARY MATERIAL

The Supplementary Material for this article can be found online at: https://www.frontiersin.org/articles/10.3389/fnins.2021.791436/full#supplementary-material

REFERENCES

Adjamian, P., Sereda, M., and Hall, D. A. (2009). The mechanisms of tinnitus: perspectives from human functional neuroimaging. *Hear. Res.* 253, 15–31. doi: 10.1016/j.heares.2009.04.001

Aslan, S., and Lu, H. (2010). On the sensitivity of ASL MRI in detecting regional differences in cerebral blood flow. *Magn. Reson. Imaging* 28, 928–935. doi: 10.1016/j.mri.2010.03.037

Aubert, A., and Costalat, R. (2002). A model of the coupling between brain electrical activity, metabolism, and hemodynamics: application to the interpretation of functional neuroimaging. *Neuroimage* 17, 1162–1181. doi: 10.1006/nimg.2002.1224

Binnewijzend, M. A., Kuijer, J. P., Benedictus, M. R., van der Flier, W. M., Wink, A. M., Wattjes, M. P., et al. (2013). Cerebral blood flow measured with 3D pseudocontinuous arterial spin-labeling MR imaging in Alzheimer disease and mild cognitive impairment: a marker for disease severity. *Radiology* 267, 221–230. doi: 10.1148/radiol.12120928

Boyen, K., Langers, D. R., de Kleine, E., and van Dijk, P. (2013). Gray matter in the brain: differences associated with tinnitus and hearing loss. *Hear. Res.* 295, 67–78. doi: 10.1016/j.heares.2012.02.010

Bozoki, A. C., Korolev, I. O., Davis, N. C., Hoisington, L. A., and Berger, K. L. (2012). Disruption of limbic white matter pathways in mild cognitive impairment and Alzheimer's disease: a DTI/FDG-PET study. *Hum. Brain Mapp.* 33, 1792–1802. doi: 10.1002/hbm.21320

Chen, Y. C., Zhang, J., Li, X. W., Xia, W., Feng, X., Gao, B., et al. (2014). Aberrant spontaneous brain activity in chronic tinnitus patients revealed by resting-state functional MRI. *Neuroimage Clin.* 6, 222–228. doi: 10.1016/j.nicl.2014.09.011

Dai, W., Lopez, O. L., Carmichael, O. T., Becker, J. T., Kuller, L. H., and Gach, H. M. (2009). Mild cognitive impairment and alzheimer disease: patterns of altered cerebral blood flow at MR imaging. *Radiology* 250, 856–866. doi: 10.1148/radiol.2503080751

Daselaar, S. M., Fleck, M. S., and Cabeza, R. (2006). Triple dissociation in the medial temporal lobes: recollection, familiarity, and novelty. *J. Neurophysiol.* 96, 1902–1911. doi: 10.1152/jn.01029.2005

De Ridder, D., Vanneste, S., Weisz, N., Londero, A., Schlee, W., Elgoyhen, A. B., et al. (2014). An integrative model of auditory phantom perception: tinnitus as a unified percept of interacting separable subnetworks. *Neurosci. Biobehav. Rev.* 44, 16–32. doi: 10.1016/j.neubiorev.2013.03.021

Dong, C., Zhao, P., Yang, J., Liu, Z., and Wang, Z. (2015). Incidence of vascular anomalies and variants associated with unilateral venous pulsatile tinnitus in 242 patients based on dual-phase contrast-enhanced computed tomography. *Chin. Med. J.* 128, 581–585. doi: 10.4103/0366-6999.151648

Du, A. T., Jahng, G. H., Hayasaka, S., Kramer, J. H., Rosen, H. J., Gorno-Tempini, M. L., et al. (2006). Hypoperfusion in frontotemporal dementia and Alzheimer disease by arterial spin labeling MRI. *Neurology* 67, 1215–1220. doi: 10.1212/01.wnl.0000238163.71349.78

Eisenman, D. J., Raghavan, P., Hertzano, R., and Morales, R. (2018). Evaluation and treatment of pulsatile tinnitus associated with sigmoid sinus wall anomalies. *Laryngoscope* 128(Suppl. 2), S1–S13.

Fox, M. D., and Raichle, M. E. (2007). Spontaneous fluctuations in brain activity observed with functional magnetic resonance imaging. *Nat. Rev. Neurosci.* 8, 700–711. doi: 10.1038/nrn2201

Geven, L. I., de Kleine, E., Willemsen, A. T., and van Dijk, P. (2014). Asymmetry in primary auditory cortex activity in tinnitus patients and controls. *Neuroscience* 256, 117–125. doi: 10.1016/j.neuroscience.2013.10.015

Guo, X., Zhu, J., Zhang, N., Zhang, L., Qi, Y., Cai, H., et al. (2018). Altered neurovascular coupling in neuromyelitis optica. *Hum. Brain Mapp.* 40, 976–986. doi: 10.1002/hbm.24426

Haller, S., Zaharchuk, G., Thomas, D. L., Lovblad, K. O., Barkhof, F., and Golay, X. (2016). Arterial spin labeling perfusion of the brain: emerging clinical applications. *Radiology* 281, 337–356. doi: 10.1148/radiol.2016150789

Han, Q., Zhang, Y., Liu, D., Wang, Y., Feng, Y., Yin, X., et al. (2018). Disrupted local neural activity and functional connectivity in subjective tinnitus patients: evidence from resting-state fMRI study. *Neuroradiology* 60, 1193–1201. doi: 10.1007/s00234-018-2087-0

Haraldsson, H., Leach, J. R., Kao, E. I., Wright, A. G., Ammanuel, S. G., Khangura, R. S., et al. (2019). Reduced jet velocity in venous flow after csf drainage: assessing hemodynamic causes of pulsatile tinnitus. *AJNR Am. J. Neuroradiol.* 40, 849–854. doi: 10.3174/ajnr.A6043

Henry, J. A., Roberts, L. E., Caspary, D. M., Theodoroff, S. M., and Salvi, R. J. (2014). Underlying mechanisms of tinnitus: review and clinical implications. *J. Am. Acad. Audiol.* 25, 5–22. doi: 10.3766/jaaa.25.1.2

Herholz, K., Salmon, E., Perani, D., Baron, J. C., Holthoff, V., Frölich, L., et al. (2002). Discrimination between Alzheimer dementia and controls by automated analysis of multicenter FDG PET. *Neuroimage* 17, 302–316. doi: 10.1006/nimg.2002.1208

Karabanov, A., Blom, O., Forsman, L., and Ullén, F. (2009). The dorsal auditory pathway is involved in performance of both visual and auditory rhythms. *Neuroimage* 44, 480–488. doi: 10.1016/j.neuroimage.2008.08.047

Krick, C. M., Argstatter, H., Grapp, M., Plinkert, P. K., and Reith, W. (2017). Heidelberg neuro-music therapy restores attention-related activity in the angular gyrus in chronic tinnitus patients. *Front. Neurosci.* 11:418. doi: 10.3389/fnins.2017.00418

Lanting, C. P., de Kleine, E., and van Dijk, P. (2009). Neural activity underlying tinnitus generation: results from PET and fMRI. *Hear. Res.* 255, 1–13. doi: 10.1016/j.heares.2009.06.009

Laureano, M. R., Onishi, E. T., Bressan, R. A., Neto, P. B., Castiglioni, M. L., Batista, I. R., et al. (2016). The effectiveness of acupuncture as a treatment for tinnitus: a randomized controlled trial using (99m)Tc-ECD SPECT. *Eur. Radiol.* 26, 3234–3242. doi: 10.1007/s00330-015-4164-7

Li, X., Qiu, X., Ding, H., Lv, H., Zhao, P., Yang, Z., et al. (2021a). Effects of different morphologic abnormalities on hemodynamics in patients with venous pulsatile tinnitus: a four-dimensional flow magnetic resonance imaging study. *J. Magn. Reson. Imaging* 53, 1744–1751. doi: 10.1002/jmri.27503

Li, X., Zhao, P., Qiu, X., Lv, H., Ding, H., Yang, Z., et al. (2021b). Altered cerebral blood flow in patients with unilateral venous pulsatile tinnitus: an arterial spin labeling study. *Br. J. Radiol.* 94:20200990. doi: 10.1259/bjr.20200990

Li, X., Zhao, P., Qiu, X., Ding, H., Lv, H., Yang, Z., et al. (2020). Lateralization effects on cerebral blood flow in patients with unilateral pulsatile tinnitus measured with arterial spin labeling. *Front. Hum. Neurosci.* 14:591260. doi: 10.3389/fnhum.2020.591260

Liang, X., Zou, Q., He, Y., and Yang, Y. (2013). Coupling of functional connectivity and regional cerebral blood flow reveals a physiological basis for network hubs of the human brain. *Proc. Natl. Acad. Sci. U.S.A.* 110, 1929–1934. doi: 10.1073/pnas.1214900110

Liu, X., Cheng, R., Chen, L., Gong, J., Luo, T., and Lv, F. (2021). Altered neurovascular coupling in subcortical ischemic vascular disease. *Front. Aging Neurosci.* 13:598365. doi: 10.3389/fnagi.2021.598365

Lv, H., Liu, Z., Yan, F., Zhao, P., Li, T., Dong, C., et al. (2015a). Disrupted neural activity in unilateral vascular pulsatile tinnitus patients in the early stage of disease: evidence from resting-state fMRI. *Prog. Neuropsychopharmacol. Biol. Psychiatry* 59, 91–99. doi: 10.1016/j.pnpbp.2015.01.013

Lv, H., Zhao, P., Liu, Z., Li, R., Zhang, L., Wang, P., et al. (2016a). Abnormal resting-state functional connectivity study in unilateral pulsatile tinnitus patients with single etiology: a seed-based functional connectivity study. *Eur. J. Radiol.* 85, 2023–2029. doi: 10.1016/j.ejrad.2016.09.011

Lv, H., Zhao, P., Liu, Z., Li, R., Zhang, L., Wang, P., et al. (2017). Abnormal regional activity and functional connectivity in resting-state brain networks associated with etiology confirmed unilateral pulsatile tinnitus in the early stage of disease. *Hear. Res.* 346, 55–61. doi: 10.1016/j.heares.2017.02.004

Lv, H., Zhao, P., Liu, Z., Liu, X., Ding, H., Liu, L., et al. (2018). Lateralization effects on functional connectivity of the auditory network in patients with unilateral pulsatile tinnitus as detected by functional MRI. *Prog. Neuropsychopharmacol. Biol. Psychiatry* 81, 228–235. doi: 10.1016/j.pnpbp.2017.09.020

Lv, H., Zhao, P., Liu, Z., Wang, G., Zeng, R., Yan, F., et al. (2016b). Frequency-dependent neural activity in patients with unilateral vascular pulsatile tinnitus. *Neural Plast.* 2016:4918186. doi: 10.1155/2016/4918186

Lv, H., Zhao, P., Liu, Z., Yan, F., Liu, T., Dong, C., et al. (2015b). Resting-state functional connectivity density mapping of etiology confirmed unilateral pulsatile tinnitus patients: altered functional hubs in the early stage of disease. *Neuroscience* 310, 27–37. doi: 10.1016/j.neuroscience.2015.09.032

Mundada, P., Singh, A., and Lingam, R. K. (2015). CT arteriography and venography in the evaluation of Pulsatile tinnitus with normal otoscopic examination. *Laryngoscope* 125, 979–984. doi: 10.1002/lary.25010

Pagani, M., Dessi, B., Morbelli, S., Brugnolo, A., Salmaso, D., Piccini, A., et al. (2010). MCI patients declining and not-declining at mid-term follow-up: FDG-PET findings. *Curr. Alzheimer Res.* 7, 287–294. doi: 10.2174/156720510791162368

Phillips, A. A., Chan, F. H., Zheng, M. M., Krassioukov, A. V., and Ainslie, P. N. (2016). Neurovascular coupling in humans: physiology, methodological advances and clinical implications. *J. Cereb. Blood Flow Metab.* 36, 647–664. doi: 10.1177/0271678X15617954

Plewnia, C., Reimold, M., Najib, A., Brehm, B., Reischl, G., Plontke, S. K., et al. (2007). Dose-dependent attenuation of auditory phantom perception (tinnitus) by PET-guided repetitive transcranial magnetic stimulation. *Hum. Brain Mapp.* 28, 238–246. doi: 10.1002/hbm.20270

Raichle, M. E., and Mintun, M. A. (2006). Brain work and brain imaging. *Annu. Rev. Neurosci.* 29, 449–476. doi: 10.1146/annurev.neuro.29.051605.112819

Schubotz, R. I., von Cramon, D. Y., and Lohmann, G. (2003). Auditory what, where, and when: a sensory somatotopy in lateral premotor cortex. *Neuroimage* 20, 173–185. doi: 10.1016/s1053-8119(03)00218-0

Song, J. J., De Ridder, D., Van de Heyning, P., and Vanneste, S. (2012). Mapping tinnitus-related brain activation: an activation-likelihood estimation metaanalysis of PET studies. *J. Nucl. Med.* 53, 1550–1557. doi: 10.2967/jnumed.112.102939

Tarantini, S., Tran, C. H. T., Gordon, G. R., Ungvari, Z., and Csiszar, A. (2017). Impaired neurovascular coupling in aging and Alzheimer's disease: contribution of astrocyte dysfunction and endothelial impairment to cognitive decline. *Exp. Gerontol.* 94, 52–58. doi: 10.1016/j.exger.2016.11.004

Vanneste, S., Plazier, M., van der Loo, E., Van de Heyning, P., and De Ridder, D. (2011). The difference between uni- and bilateral auditory phantom percept. *Clin. Neurophysiol.* 122, 578–587. doi: 10.1016/j.clinph.2010.07.022

Venkat, P., Chopp, M., and Chen, J. (2016). New insights into coupling and uncoupling of cerebral blood flow and metabolism in the brain. *Croat. Med. J.* 57, 223–228. doi: 10.3325/cmj.2016.57.223

Verger, A., Roman, S., Chaudat, R. M., Felician, O., Ceccaldi, M., Didic, M., et al. (2017). Changes of metabolism and functional connectivity in late-onset deafness: evidence from cerebral (18)F-FDG-PET. *Hear. Res.* 353, 8–16. doi: 10.1016/j.heares.2017.07.011

Wang, Z., Zhang, P., Zhao, P., Li, J., Ding, H., Yin, H., et al. (2019). Long-term reactions to pulsatile tinnitus are marked by weakened short-range functional connectivity within a brain network in the right temporal lobe. *J. Magn. Reson. Imaging* 49, 1629–1637. doi: 10.1002/jmri.26545

Wolk, D. A., and Detre, J. A. (2012). Arterial spin labeling MRI: an emerging biomarker for Alzheimer's disease and other neurodegenerative conditions. *Curr. Opin. Neurol.* 25, 421–428. doi: 10.1097/WCO.0b013e328354ff0a

Xu, Y., Shi, Y., Yao, J., Yang, H., Ding, Z., Chen, Q. Q., et al. (2019). Altered brain functional connectivity and correlation with psychological status in patients with unilateral pulsatile tinnitus. *Neurosci. Lett.* 705, 235–245. doi: 10.1016/j.neulet.2019.04.046

Yoshiura, T., Hiwatashi, A., Yamashita, K., Ohyagi, Y., Monji, A., Takayama, Y., et al. (2009). Simultaneous measurement of arterial transit time, arterial blood volume, and cerebral blood flow using arterial spin-labeling in patients with Alzheimer disease. *AJNR Am. J. Neuroradiol.* 30, 1388–1393. doi: 10.3174/ajnr.A1562

Zang, Y., Jiang, T., Lu, Y., He, Y., and Tian, L. (2004). Regional homogeneity approach to fMRI data analysis. *Neuroimage* 22, 394–400. doi: 10.1016/j.neuroimage.2003.12.030

Zhang, C., Li, Q., and Li, S. (2019). Physical and psychological outcomes of simple sigmoid sinus bony wall repair for pulsatile tinnitus due to sigmoid sinus wall anomalies. *Eur. Arch. Otorhinolaryngol.* 276, 1327–1334. doi: 10.1007/s00405-019-05380-1

Zhang, J., Zhang, Z., Huang, S., Zhou, H., Feng, Y., Shi, H., et al. (2020). Differences in clinical characteristics and brain activity between patients with low- and high-frequency tinnitus. *Neural Plast.* 2020:5285362. doi: 10.1155/2020/5285362

Zhang, Y., Zhang, X., Ma, G., Qin, W., Yang, J., Lin, J., et al. (2021). Neurovascular coupling alterations in type 2 diabetes: a 5-year longitudinal MRI study. *BMJ Open Diabetes Res. Care* 9:e001433. doi: 10.1136/bmjdrc-2020-001433

Zhu, J., Zhuo, C., Xu, L., Liu, F., Qin, W., and Yu, C. (2017). Altered coupling between resting-state cerebral blood flow and functional connectivity in schizophrenia. *Schizophr. Bull.* 43, 1363–1374. doi: 10.1093/schbul/sbx051

Conflict of Interest: The authors declare that the research was conducted in the absence of any commercial or financial relationships that could be construed as a potential conflict of interest.

Publisher's Note: All claims expressed in this article are solely those of the authors and do not necessarily represent those of their affiliated organizations, or those of the publisher, the editors and the reviewers. Any product that may be evaluated in this article, or claim that may be made by its manufacturer, is not guaranteed or endorsed by the publisher.

frontiers in Human Neuroscience

ORIGINAL RESEARCH
published: 04 February 2022
doi: 10.3389/fnhum.2021.805945

Diffusion Tensor Imaging Technology to Quantitatively Assess Abnormal Changes in Patients With Thyroid-Associated Ophthalmopathy

*Li Rui, Li Jing and Wang Zhenchang**

Department of Radiology, Beijing Friendship Hospital, Capital Medical University, Beijing, China

Objective: We aim to investigate the feasibility of using diffusion tensor imaging (DTI) to evaluate changes in extraocular muscles (EOMs) and lacrimal gland (LG) in patients with thyroid-associated ophthalmopathy (TAO) and to evaluate disease severity.

Materials and Methods: A total of 74 participants, including 17 healthy controls (HCs), 22 patients with mild TAO, and 35 patients with moderate-severe TAO, underwent 3-Tesla DTI to measure fractional anisotropy (FA) and mean diffusivity (MD) of the EOMs and LG. Ophthalmological examinations, including visual acuity, exophthalmos, intraocular pressure, and fundoscopy, were performed. FA and MD values were compared among patients with different disease severity. Multiple linear regression was adopted to predict the impact of clinical variables on DTI parameters of orbital soft tissue.

Results: TAO patients' EOMs and LG showed significantly lower FA values and higher MD compared to HCs' ($P < 0.05$). Moderate-severe TAO patients' EOMs and LG had dramatically lower FA and higher MD compared with HCs ($P < 0.05$). In addition, only the DTI parameters of the medial rectus were considerably different between mild and moderate-severe TAO patients ($P = 0.017$, $P = 0.021$). Multiple linear regression showed that disease severity had a significant impact on the DTI parameters of orbital soft tissue.

Conclusion: DTI is a useful tool for detecting microstructural changes in TAO patients' orbital soft tissue. DTI findings, especially medial rectus DTI parameters, can help to indicate the disease severity in TAO patients.

Keywords: thyroid-associated ophthalmopathy, extraocular muscle, lacrimal gland, diffusion tensor imaging (DTI), MRI

Edited by:
Yu-Chen Chen,
Nanjing First Hospital, Nanjing Medical University, China

Reviewed by:
Jyothilakshmi Vasavan,
Algonquin College, Canada
Koji Kamagata,
Juntendo University, Japan
Chao Zhang,
The Affiliated Hospital of Xuzhou Medical University, China

***Correspondence:**
Wang Zhenchang
cjr.wzhch@vip.163.com

Specialty section:
This article was submitted to Sensory Neuroscience, a section of the journal Frontiers in Human Neuroscience

Received: *31 October 2021*
Accepted: *28 December 2021*
Published: *04 February 2022*

Citation:
Rui L, Jing L and Zhenchang W (2022) Diffusion Tensor Imaging Technology to Quantitatively Assess Abnormal Changes in Patients With Thyroid-Associated Ophthalmopathy. Front. Hum. Neurosci. 15:805945. doi: 10.3389/fnhum.2021.805945

INTRODUCTION

Thyroid-associated ophthalmopathy (TAO) is an autoimmune inflammatory disease that causes inflammation and fibrosis of orbital fat, extraocular muscles (EOMs) and the lacrimal gland (LG) (Weiler, 2017). The medial rectus and inferior rectus are the most common lesion sites. The expansion of both EOMs and orbital fat is responsible for various clinical symptoms, such as diplopia, proptosis, and restricted eye movement (Drui et al., 2018). A previous study found that approximately 30–45% of TAO patients only showed significant dry eye symptoms, and about 65–75% of TAO patients had dry eye symptoms (Kashkouli et al., 2018). Besides the changes of

widened palpebral fissure and increased exophthalmos that accelerate the evaporation of tears, decreased secretion of tears due to LG involvement has been considered as another vital factor (Inoue et al., 2020). TAO is divided into two phases: The active phase of inflammation usually lasts for 6–18 months. It is characterized by monocyte infiltration, edema and fibroblast proliferation. The inactive phase is characterized by orbital soft tissue fibrosis, collagen and fat deposition (Dolman, 2018).

Currently, imaging examination is an important supplement to ophthalmic examination and laboratory examination (Chen L. et al., 2020; Ma et al., 2021). It plays an important role in the clinical diagnosis, evaluation, disease treatment and monitoring TAO patients. Computed tomography (CT) is usually utilized to provide data for an initial diagnosis or pre-surgery evaluation. Magnetic resonance imaging (MRI) has superior soft tissue resolution, T2-weighted imaging (T2WI) signal intensity of the EOMs and dynamic MRI enhancement can assist in diagnosing and staging TAO patients (Politi et al., 2014; Wu et al., 2017). Quantitative measurement of the signal intensity and volume of orbital soft tissue can indicate the response of moderate-severe TAO patients' to hormone therapy (Hu et al., 2020). Diffusion weighted imaging (DWI) has shown promise in the evaluation of EOMs and LG. Studies have demonstrated a higher ADC in TAO patients' EOMs and LG compared with HCs (Abdel Razek et al., 2017; Hiwatashi et al., 2018; Razek et al., 2019). In addition, the ADC of EOMs combined with CAS is helpful in guiding clinical decisions (Feeney et al., 2020).

Diffusion tensor imaging (DTI) is an extension of DWI, it can provide quantitative information about the microstructural integrity of highly oriented tissues (Assaf et al., 2019). Fractional anisotropy (FA) and mean diffusivity (MD), as common parameters of DTI, can, respectively, reflect the magnitude and directionality of water diffusion (Norris et al., 2020). DTI has also been widely applied in patients with optic neuritis, glaucoma, and other eye diseases (Kuchling et al., 2017; Colbert et al., 2021). At present, relatively few studies have performed DTI on TAO patients to assess orbital soft tissue microstructural changes (Han et al., 2016; Chen H.H. et al., 2020; Chen et al., 2021). To our knowledge, several studies included EOMs and lacrimal glands in the same research, but only focusing on each separately instead of studying the orbital soft tissues as a whole.

Therefore, the purpose of this study was to evaluate the utility of DTI in detecting microstructural changes in orbit soft tissue in TAO patients and to assess disease severity.

MATERIALS AND METHODS

This study was approved by our Institutional Review Board and informed consent was obtained from all subjects.

Patient Population

From September 2018 to January 2020, 74 subjects were collected, including 57 diagnosed TAO patients and 17 sex- and age-matched HCs. Their diagnosis was according to American Ophthalmological Association standards. Patients who had experienced or had one of the following treatments, including orbital decompression, eyelid surgery, radiotherapy, strabismus surgery, and inadequate image quality were excluded.

The clinical features included age, gender, clinical activity score (CAS) and European Group on Graves' Orbitopathy (EUGOGO) classification. The CAS is used to evaluate the patient's disease activity, so as to determine the patient's sensitivity to hormone therapy (Du et al., 2021). The CAS includes 7 points, one point for each item; a patient with a CAS $\geq$ 3 is considered in the active phase, and a patient with a

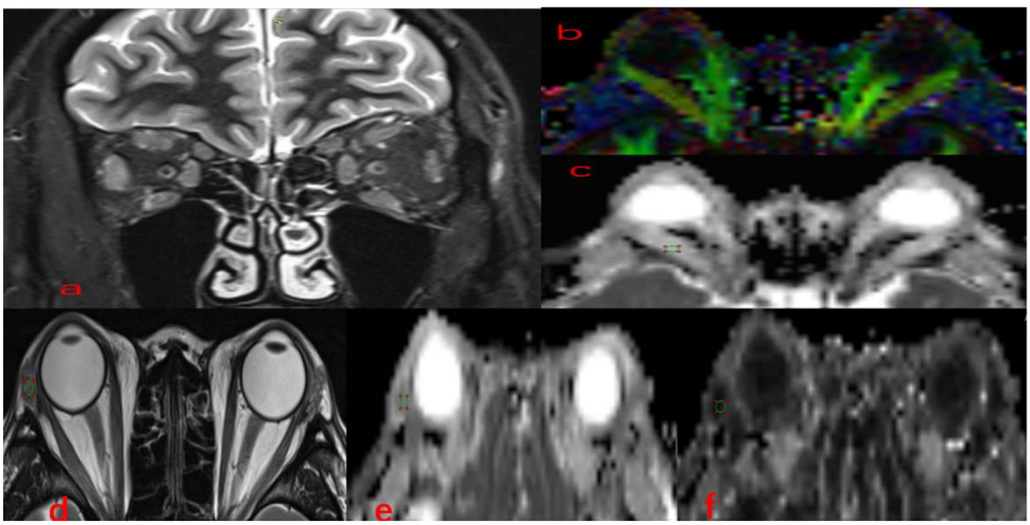

FIGURE 1 | Methods for DTI parameters measurements in EOMs and LG. Coronal **(a)** fat-suppressed T2-weighted images and color-coded FA **(b)**, MD **(c)**, in a 36-year-old man with TAO. A circular region of interest was manually set on each EOM locating the clearest cross-section. Axial **(d)** T2-weighted images, FA **(e)**, MD **(f)** maps of the same patient. A circular region of interest was manually set on each LG indicating the clearest cross-section. TAO, thyroid-associated ophthalmopathy; EOMs, extraocular muscle; DTI, diffusion tensor imaging; LG, lacrimal gland; FA, fractional anisotropy; MD, mean diffusivity.

TABLE 1 | Demographics of the control and TAO groups.

	Normal (n = 17)	Mild (n = 22)	Moderate to sever (n = 35)	F/X^2	P-value
Age	35.4 ± 12.3	39.1 ± 12.3	47.1 ± 14.5	–	0.143[a]
Gender (F/M)	10/7	13/9	20/15	0.026	0.989[b]
Antithyroid drug use, %(n)	–	54.5% (12)	57.1% (20)	0.037	0.847[b]
Smoking,%(n)	17.6% (3)	13.6% (3)	17.1% (6)	–	1.000[c]

Numeric data are reported as means ± standard deviations. Statistical significance was indicated by p-values < 0.05.
F, female; M, male; TAO, thyroid-associated orbitopathy.
[a]*One-way ANOVA.*
[b]*Chi-squared test.*
[c]*Fisher's Exact test.*

CAS < 3 is considered in the inactive phase. 114 eyes (57 TAO patients) were collected in this study, including 56 eyes in the active phase and 58 eyes in the static phase. Disease severity was assessed by adopting 2016 EUGOGO (Perros et al., 2017). The patients were divided into two categories: mild (22 subjects, with 13 females and 9 males), and moderate-severe (35 subjects, with 20 females and 15 males).

Magnetic Resonance Examination

MRI was performed on a 3.0 Tesla MR scanner (Prisma, Siemens Medical systems, Erlangen, Germany) with a 64-channel head coil. Every volunteer was instructed to look at a fixed point with both eyes closed to reduce motion-related errors. The sagittal 3D thin-layer T1-weighted imaging (T1WI) parameters were as follows: repetition time (TR) 2,530 ms, echo time (TE) 2.98 ms, matrix 250 × 250, 1 mm slice thickness, field of view (FOV), 256 mm × 256 mm. DTI was acquired on an axial plane using the RESOLVE sequence. The scan location line was set parallel to the optic nerve intraorbital segment, and scan parameters were as follows: b = 0 and l,000 s/mm^2; number of diffusion gradient directions (NDGDs), 64; readout segments, 5; TR/TE, 5,500 ms/63 ms; Field of view (FOV)224 mm × 224 mm; matrix 200 × 200;slice thickness 2 mm; the resolution of voxel spacing, 2 mm × 2 mm × 2 mm. The total imaging time was 10 min and 56 s.

Conventional imaging protocols using fast spin echo (FSE) included axial, coronal, and sagittal T2WI imaging with fat suppression, and axial T1WI.

Imaging Processing

DTI images were postprocessed using Siemens Prisma 3.0T with Syngo.Via post-processing software. Image analysis was performed in a double-blind manner by two neuroimaging diagnostic physicians who had over 5 years' working experience in the relevant field, each analysis was performed twice, and the mean values of the two analyses were recorded. The FA, apparent diffusion coefficient (ADC), and TRACEW images were opened in the MR Basic program, and TRACEW images were adjusted to display the clearest level of the EOMs; then, a circular region of interest (ROI) was drawn on EOMs, and the diameter of the ROI was set to 6 mm. After this process, the software could automatically calculate the FA values and the MD values. The study followed a similar method to measure LG. Circular ROIs on the LGs were carefully positioned (**Figure 1**).

Statistical Analysis

All numeric data in our research were reported as the mean ± standard deviation, Kolmogorov-Smirnov test was used for analyzing the normality. Since CAS does not conform to the normal distribution, they were reported as median with interquartile range (IQR). One-way analysis of variance (ANOVA) was used to compare age-related differences, the chi-squared test was applied to compare differences regarding medication categories and sex between groups. The Fisher's exact test was used to compare differences in smoking history between groups. It is worth mentioning that all subjects had the same severity of disease in the right and left eyes, and the average values for left/right eye parameters were calculated. The independent -samples t-test was used to compare DTI parameters of EOMs and LG between TAO patients and HCs. Comparisons about the EOMs and LG DTI parameters of participants in the HC, mild, and moderate-severe groups were performed using one-way ANOVA, and intergroup comparisons regarding DTI parameters of orbital soft tissue were conducted using least significant difference (LSD). A correlation matrix was applied to evaluate correlations between EOMs' and LGs' DTI parameters. Multi linear regression was performed to assess whether the influencing factors of clinical features (age, gender, disease severity) would affect orbital soft tissue DTI parameters. The odds ratios and their 95% confidence intervals (CIs) were calculated.

Interobserver agreements of quantitative parameters were assessed by the intraclass correlation coefficients (ICCs).

TABLE 2 | Comparison of left and right orbital soft tissue DTI parameters and clinical parameters.

Parameters		Left eye	Right eye	Mean	T-value	P-value
Lateral rectus	FA	0.463 ± 0.059	0.451 ± 0.053	0.457 ± 0.056	1.652	0.103
	MD(×10–2 mm^2/s)	0.162 ± 0.014	0.164 ± 0.013	0.163 ± 0.011	−1.234	0.221
Medial rectus	FA	0.461 ± 0.069	0.462 ± 0.065	0.462 ± 0.050	−0.040	0.968
	MD(×10–2 mm^2/s)	0.159 ± 0.013	0.159 ± 0.013	0.159 ± 0.013	−0.011	0.991
Lacrimal gland	FA	0.383 ± 0.046	0.380 ± 0.048	0.382 ± 0.037	0.400	0690
	MD(×10–2 mm^2/s)	0.138 ± 0.010	1	0.138 ± 0.008	0.281	0.779
Clinical parameters	Exophthalmometry (mm)	19.7 ± 3.0	19.2 ± 2.8	19.5 ± 2.9	0.416	0.680
	CAS(range)	3.8(1–6)	3.5(1–6)	3.7	1.756	0.088
	Intraocular pressure (mmHg)	18.2 ± 3.9	17.9 ± 3.4	18.1 ± 3.7	1.318	0.196

Numeric data are reported as means ± standard deviations; CAS are reported as median with interquartile range (IQR).
FA, fractional anisotropy; MD, mean diffusivity; CAS, clinical activity score.

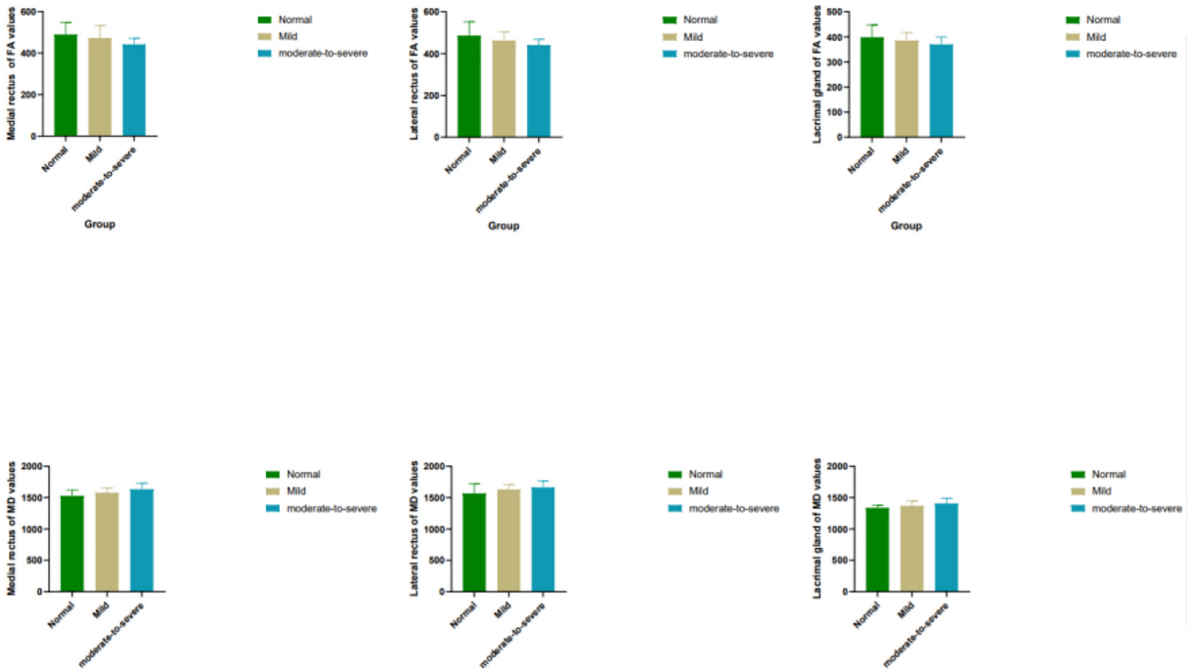

FIGURE 2 | Box plots show comparisons of all DTI parameters in EOMs and LG between groups. Units of MD are $\times 10^{-6}$ mm^2/s. FA, fractional anisotropy; MD, mean diffusivity.

Two-way ICCs with random rater assumptions were applied. The results were interpreted as follows: < 0.40, poor; 0.40–0.60, moderate; 0.61–0.80, good; and ≥ 0.81, excellent. A value of $p < 0.05$ was considered statistically significant. All statistical analyses were carried out using the SPSS 20.0 software package.

RESULTS

The clinical and demographic information are shown in **Table 1**. No significant differences in age, gender, or smoking among participants in the HCs, mild and moderate-severe groups ($P > 0.05$). In addition, 12 mild patients and 20 moderate - severe patients took antithyroid drugs. There was no statistically significant difference in the orbital soft tissue DTI parameters or clinical features of the left and right eyes of the participants (*p*-values are given in **Table 2**). Therefore, statistical analysis was performed after calculating the average value of each parameter.

TABLE 3 | DTI parameters of orbital soft tissue between TAO and HC.

Parameters		HC	TAO	*P*
Lateral rectus	FA	0.487 ± 0.066	0.450 ± 0.035	0.038
	MD(× 10–2 mm^2/s)	0.157 ± 0.015	0.165 ± 0.009	0.046
Medial rectus	FA	0.490 ± 0.058	0.454 ± 0.046	0.009
	MD(× 10–2 mm^2/s)	0.153 ± 0.009	0.161 ± 0.009	0.002
Lacrimal gland	FA	0.399 ± 0.049	0.376 ± 0.031	0.027
	MD(× 10–2 mm^2/s)	0.134 ± 0.004	0.139 ± 0.008	0.001

Numeric data are reported as means ± standard deviations.
HC, healthy control group; TAO, thyroid-associated ophthalmopathy; FA, fractional anisotropy; MD, mean diffusivity.

Excellent inter-observer reproducibility were obtained when measuring all DTI parameters (ICC ranged from 0.898 to 0.995). The FA of EOMs and LG in patients with TAO was significantly lower, the MD was dramatically higher than that of the HCs (FA: $P_{Lateralrectus} = 0.038$, $P_{Medialrectus} = 0.009$, $P_{Lacrimalgland} = 0.027$; MD: $P_{Lateralrectus} = 0.046$, $P_{Medialrectus} = 0.002$, $P_{Lacrimalgland} = 0.001$) (**Table 3**).

Moderate- severe TAO patients showed significantly lower FA and higher MD compared with HCs' and those from the mild group (all $P < 0.05$). In addition, comparing the moderate-severe patients with mild patients, the former's medial rectus' FA were considerably lower and its MD were significantly higher ($P = 0.017$, $P = 0.021$) (**Figure 2** and **Table 4**).

The correlation matrix showed that there was a positive correlation between the DTI parameters of the medial rectus and that of the lateral rectus ($P_{FA} = 0.002$, $P_{MD} = 0.042$). No correlation was discovered between EOMs and LG DTI parameters. Detailed p and r values are presented in **Table 5**. Multi linear regression demonstrated that disease severity was a significant influencing factor for orbital soft tissue DTI parameters ($P_{FA} < 0.01$, $P_{MD} = 0.050$), whereas gender was the influencing factor which affect orbital soft tissue MD only ($P = 0.017$) (**Table 6**).

DISCUSSION

In this study, comparing TAO patients with the HC ones, the FA of the EOMs and LG were significantly lower, while the MD were significantly higher. This result was in agreement

TABLE 4 | DTI parameters of orbital soft tissue and clinical parameters in the normal, mild and moderate-to-severe TAO groups.

Parameters		Normal	Mild	Moderate-to- severe	*F*-value	*P*-value	*P*-value		
							a	b	c
Lateral rectus	FA	0.487 ± 0.066	0.463 ± 0.042	0.441 ± 0.028	6.569	0.002	0.094	0.001	0.066
	MD (× 10–2 mm^2/s)	0.157 ± 0.015	0.163 ± 0.008	0.166 ± 0.010	4.293	0.017	0.075	0.005	0.301
Medial rectus	FA	0.490 ± 0.058	0.473 ± 0.060	0.442 ± 0.029	6.775	0.002	0.273	0.001	0.017
	MD (×10–2 mm^2/s)	0.154 ± 0.017	0.156 ± 0.008	0.163 ± 0.010	4.998	0.009	0.558	0.006	0.021
Lacrimal gland	FA	0.400 ± 0.049	0.386 ± 0.031	0.370 ± 0.030	3.911	0.024	0.264	0.008	0.112
	MD (×10–2 mm^2/s)	0.134 ± 0.004	0.137 ± 0.008	0.141 ± 0.008	5.523	0.006	0.159	0.002	0.071
Clinical parameters	CAS	0 (0, 0)	2.00 (1.00, 2.00)	4.00 (3.00, 5.00)	51.884	<0.001	0.001	<0.001	0.002
	Exophthalmometry(mm)	13.1 ± 0.8	18.2 ± 2.9	19.7 ± 3.0	35.927	<0.001	<0.001	<0.001	0.051
	Intraocular pressure (mmHg)	14.6 ± 2.7	17.9 ± 3.1	18.2 ± 4.0	6.687	0.002	0.005	0.001	0.701

Numeric data are reported as means ± standard deviations. Continuous data are reported as median (interquartile range). Statistical significance was indicated by p-values < 0.05.
HC, healthy control group; TAO, thyroid-associated ophthalmopathy; FA, fractional anisotropy; MD, mean diffusivity.
a, normal compared to mild; b, norma compared to moderate-to-severe; c, Mild compared to moderate to severe.
Bonferroni correction P< 0.05/3 = 0.017.

TABLE 5 | Correlations matrix of orbital soft tissue DTI parameters.

		DTI-FA			DTI-MD		
		Medial rectus	Lateral rectus	Lacrimal gland	Medial rectus	Lateral rectus	Lacrimal gland
DTI-FA	Medial rectus		r = 0.360 P = 0.002	r = 0.005 P = 0.967			
	Lateral rectus			r = −0.215 P = 0.066			
	Lacrimal gland						
DTI-MD	Medial rectus					r = 0.237 P = 0.042	r = 0.129 P = 0.274
	Lateral rectus						r = −0.188 P = 0.109
	Lacrimal gland						

FA, fractional anisotropy; MD, mean diffusivity.

TABLE 6 | Multivariate logistic regression analysis results for predicting impact to orbital soft tissue DTI parameters.

	Parameters	β coefficient	SE	Odds ratio(95% CI)	*p*-value
Orbital soft tissue FA values	Disease severity	−0.637	10.315	1.708(−86.812 to −45.667)	<0.001
	Gender	−0.122	15.924	1.022(−52.461 to 11.058)	0.198
	Age	0.123	0.614	2.134(−0.466 to 1.983)	0.221
Orbital soft tissue MD values	Disease severity	−0.236	29.629	2.023(−118.256 to −0.069)	0.050
	Gender	−0.275	45.742	2.200(−203.268 to −20.808)	0.017
	Age	0.032	1.763	1.606(−3.043 to 3.991)	0.789

SE, standard error; CI, confidence interval; FA, fractional anisotropy; MD, mean diffusivity.

with the findings of previous studies (Chen H.H. et al., 2020; Chen et al., 2021). Moreover, comparing mild TAO patients with moderate-severe patients, the medial rectus' FA were dramatically lower while its MD were higher. Previous studies (Abdel Razek et al., 2017) have found that the medial rectus was more affected than the lateral rectus muscle; therefore, our research suggests that DTI can well detect microstructural changes in the medial rectus of TAO patients.

DTI is a non-invasive MRI technology which is very sensitive to water molecules' micromovement. Thus, it can provide quantitative information of water molecule diffusion movement (Jeon et al., 2018). Common parameters of DTI include FA and MD values. The MD can reflect the magnitude of water diffusion dominated by interstitial space. Researchers found an inverse correlation between tumor cells and MD values (Razek et al., 2018; Abdel Razek et al., 2019). FA can represent the directionality of water molecules, hence it can reflect tissue's integrity of microstructural architectures (Gholizadeh et al., 2019). The FA value is a number between 0 and 1. It is equal to 0 under isotropic conditions, and it approaches 1 in case of extreme directional inequality.

TAO patients' orbital soft tissues were thought to experience two phase: the initial acute inflammation is characterized by hyaluronic acid accumulation and mononuclear inflammatory cell infiltration. Subsequently, chronic inactive phase was

featured with interstitial fibrosis, and fatty infiltration (Taylor et al., 2020). In our study, most TAO patients were in the active phase. During this phase, the mononuclear cell infiltration, fibroblast proliferation and edema in EOMs and LG causes an increase in the extracellular space, which also enhances the ability of water molecules to diffuse. Since MD reflects the magnitude of water diffusion, an escalating trend of MD values can be acquired. The acute inflammation stage is also associated with cell lysis and fibrous disruption (Men et al., 2021). FA can reflect integrity of microstructural architectures, as mentioned. In our research, EOMs and LG of TAO patients exhibited lower FA compared with those in HCs.

In our study, the correlations matrix of orbital soft tissue DTI parameters revealed that the DTI parameters of the EOMs had a positive correlation, however, there was no correlation between the LG and the EOMs. This result indicates that in the process of mononuclear cell infiltration, fibroblast proliferation, and edema in EOMs, the medial rectus and the lateral rectus affect each other. The interaction between the extraocular muscles and the lacrimal gland in the development of the disease is not obvious. Several previous researches (Lee et al., 2018; Razek et al., 2019; Chen H.H. et al., 2020; Chen et al., 2021) have examined extraocular muscles and lacrimal gland DTI separately, but these studies did not discuss the relevance of orbital soft tissue in the development of the disease. In addition, as previous studies state (Cao et al., 2021; Neag and Smith, 2021), TAO mainly involves orbital fat, extraocular muscles, and lacrimal gland. In this study, we placed the lacrimal gland and extraocular muscles in the same picture, that is the orbital soft tissues, and we calculated their DTI parameters. Multivariate analysis along with clinical factors revealed that disease severity significantly impacted orbital soft tissue DTI parameters. We believe it is a unique finding which has not yet been discovered.

Several previous studies have focused on the use of functional MRI technique, such as measuring EOMs or LG apparent diffusion coefficient (ADC) values, to diagnose TAO (Abdel Razek et al., 2017; Feeney et al., 2020; Chen et al., 2021). Other studies have mainly focused on assessing disease activity and predicting the response to glucocorticoid therapy using methods such as calculating the T1 mapping or T2 mapping values of EOMs (Das et al., 2019; Chen L. et al., 2020; Hu et al., 2021). Few reports have focused on functional MRI of orbital soft tissue in patients with different severities of TAO. To our knowledge, accurately staging for patients with TAO is crucial for clinical decision making, especially for moderate-severe TAO patients (Farag et al., 2021). In this research, DTI parameters of the medial rectus are sensitive imaging indicators, which could distinguish mild from moderate-severe TAO patients.

Our study had several limitations. First, the study cohort of this study was relatively small, so expanding the sample size in future studies is necessary. Second, No common standard has been settled for DTI acquisition technology and for post-processing. This may lead to poor compatibility among different research results. In addition, since the scan for DTI sequence is axial, the lack of information on inferior EOMs might be a major drawback of our study. We will continue to optimize the DTI sequence in future studies. Furthermore, the patients were not followed up after their treatment in this study, and these patients will also be included in the future, so we can have a more comprehensive understanding of TAO.

CONCLUSION

In conclusion, our results suggest that DTI technology can well detect the changes in orbital soft tissue microstructure. It can also provide more objective imaging biological indicators for clinical applications. DTI parameters of the medial rectus, especially the FA of medial EOMs, can serve as an effective indicator of disease severity.

DATA AVAILABILITY STATEMENT

The original contributions presented in the study are included in the article/supplementary material, further inquiries can be directed to the corresponding author/s.

ETHICS STATEMENT

The studies involving human participants were reviewed and approved by the Department of Ethics Committee, Beijing Friendship Hospital, Capital Medical University. The patients/participants provided their written informed consent to participate in this study.

AUTHOR CONTRIBUTIONS

LR, WZ, and LJ: conception and design. WZ and LJ: administrative support. LR: provision of study materials or patients, collection, and assembly of data. LR and LJ: data analysis and interpretation. All authors: manuscript writing, final approval of manuscript.

REFERENCES

Abdel Razek, A. A., El-Hadidy, M., Moawad, M. E., El-Metwaly, N., and El-Said, A. A. (2017). Performance of apparent diffusion coefficient of medial and lateral rectus muscles in Graves' orbitopathy. *Neuroradiol. J.* 30, 230–234. doi: 10.1177/1971400917691993

Abdel Razek, A. A. K., Talaat, M., El-Serougy, L., Abdelsalam, M., and Gaballa, G. (2019). Differentiating glioblastomas from solitary brain metastases using arterial spin labeling perfusion- and diffusion tensor imaging-derived metrics. *World Neurosurg.* 127, e593–e598. doi: 10.1016/j.wneu.2019.03.213

Assaf, Y., Johansen-Berg, H., and de Schotten, M. T. (2019). The role of diffusion MRI in neuroscience. *NMR Biomed.* 32:e3762. doi: 10.1002/nbm.3762

Cao, J., Wang, N., Hou, S., Qi, X., Chen, Y., and Xiong, W. (2021). Overview of graves ophthalmopathy literature from 1999 to 2019: bibliometric analysis. *Interact. J. Med. Res.* 10:e24831. doi: 10.2196/24831

Chen, H.H., Hu, H., Chen, W., Cui, D., Xu, X. Q., Wu, F. Y., et al. (2020). Thyroid-associated orbitopathy: evaluating microstructural changes of extraocular muscles and optic nerves using readout-segmented echo-planar imaging-based diffusion tensor imaging. *Korean J. Radiol.* 21, 332–340. doi: 10.3348/kjr.2019.0053

Chen, L., Chen, W., Chen, H. H., Wu, Q., Xu, X. Q., Hu, H., et al. (2020). Radiological staging of thyroid-associated ophthalmopathy: comparison of T1 mapping with conventional MRI. *Int. J. Endocrinol.* 2020:2575710. doi: 10.1155/2020/2575710

Chen, L., Hu, H., Chen, W., Wu, Q., Zhou, J., Chen, H. H., et al. (2021). Usefulness of readout-segmented EPI-based diffusion tensor imaging of lacrimal gland for detection and disease staging in thyroid-associated ophthalmopathy. *BMC Ophthalmol.* 21:281. doi: 10.1186/s12886-021-02044-9

Colbert, M. K., Ho, L. C., van der Merwe, Y., Yang, X., McLellan, G. J., Hurley, S. A., et al. (2021). Diffusion tensor imaging of visual pathway abnormalities in five glaucoma animal models. *Invest. Ophthalmol. Vis. Sci.* 62:21. doi: 10.1167/iovs.62.10.21

Das, T., Roos, J. C. P., Patterson, A. J., Graves, M. J., and Murthy, R. (2019). T2-relaxation mapping and fat fraction assessment to objectively quantify clinical activity in thyroid eye disease: an initial feasibility study. *Eye* 33, 235–243. doi: 10.1038/s41433-018-0304-z

Dolman, P. J. (2018). Grading severity and activity in thyroid eye disease. *Ophthalmic Plast. Reconstr. Surg.* 34(4S Suppl. 1), S34–S40. doi: 10.1097/IOP.0000000000001150

Drui, D., Du Pasquier Fediaevski, L., Vignal Clermont, C., and Daumerie, C. (2018). Graves' orbitopathy: diagnosis and treatment. *Ann. Endocrinol.* 79, 656–664. doi: 10.1016/j.ando.2018.08.005

Du, B., Wang, Y., Yang, M., and He, W. (2021). Clinical features and clinical course of thyroid-associated ophthalmopathy: a case series of 3620 Chinese cases. *Eye* 35, 2294–2301. doi: 10.1038/s41433-020-01246-7

Farag, S., Feeney, C., Lee, V., Nagendran, S., Jain, R., Aziz, A., et al. (2021). A 'real life' service evaluation model for multidisciplinary thyroid eye services. *Front. Endocrinol.* 12:669871. doi: 10.3389/fendo.2021.669871

Feeney, C., Lingam, R. K., Lee, V., Rahman, F., and Nagendran, S. (2020). Non-EPI-DWI for detection, disease monitoring, and clinical decision-making in thyroid eye disease. *AJNR Am. J. Neuroradiol.* 41, 1466–1472. doi: 10.3174/ajnr.A6664

Gholizadeh, N., Greer, P. B., Simpson, J., Denham, J., Lau, P., Dowling, J., et al. (2019). Characterization of prostate cancer using diffusion tensor imaging: a new perspective. *Eur. J. Radiol.* 110, 112–120. doi: 10.1016/j.ejrad.2018.11.026

Han, J. S., Seo, H. S., Lee, Y. H., Lee, H., Suh, S. I., Jeong, E. K., et al. (2016). Fractional anisotropy and diffusivity changes in thyroid-associated orbitopathy. *Neuroradiology* 58, 1189–1196. doi: 10.1007/s00234-016-1764-0

Hiwatashi, A., Togao, O., Yamashita, K., Kikuchi, K., Momosaka, D., and Honda, H. (2018). Diffusion-weighted magnetic resonance imaging of extraocular muscles in patients with Grave's ophthalmopathy using turbo field echo with diffusion-sensitized driven-equilibrium preparation. *Diagn. Interv. Imaging* 99, 457–463. doi: 10.1016/j.diii.2018.02.007

Hu, H., Chen, H. H., Chen, W., Wu, Q., Chen, L., Zhu, H., et al. (2021). T2 mapping histogram at extraocular muscles for predicting the response to glucocorticoid therapy in patients with thyroid-associated ophthalmopathy. *Clin. Radiol.* 76, 159.e1–159.e8. doi: 10.1016/j.crad.2020.09.005

Hu, H., Xu, X. Q., Chen, L., Chen, W., Wu, Q., Chen, H. H., et al. (2020). Predicting the response to glucocorticoid therapy in thyroid-associated ophthalmopathy: mobilizing structural MRI-based quantitative measurements of orbital tissues. *Endocrine* 70, 372–379. doi: 10.1007/s12020-020-02367-5

Inoue, S., Kawashima, M., Arita, R., Kozaki, A., and Tsubota, K. (2020). Investigation of meibomian gland function and dry eye disease in patients with graves' ophthalmopathy. *J. Clin. Med.* 9:2814. doi: 10.3390/jcm9092814j

Jeon, T., Fung, M. M., Koch, K. M., Tan, E. T., and Sneag, D. B. (2018). Peripheral nerve diffusion tensor imaging: overview, pitfalls, and future directions. *J. Magn. Reson. Imaging* 47, 1171–1189. doi: 10.1002/jmri.25876

Kashkouli, M. B., Alemzadeh, S. A., Aghaei, H., Pakdel, F., Abdolalizadeh, P., Ghazizadeh, M., et al. (2018). Subjective versus objective dry eye disease in patients with moderate-severe thyroid eye disease. *Ocul. Surf.* 16, 458–462. doi: 10.1016/j.jtos.2018.07.003

Kuchling, J., Brandt, A. U., Paul, F., and Scheel, M. (2017). Diffusion tensor imaging for multilevel assessment of the visual pathway: possibilities for personalized outcome prediction in autoimmune disorders of the central nervous system. *EPMA J.* 8, 279–294. doi: 10.1007/s13167-017-0102-x

Lee, H., Lee, Y. H., Suh, S. I., Jeong, E. K., Baek, S., and Seo, H. S. (2018). Characterizing intraorbital optic nerve changes on diffusion tensor imaging in thyroid eye disease before dysthyroid optic neuropathy. *J. Comput. Assist. Tomogr.* 42, 293–298. doi: 10.1097/RCT.0000000000000680

Ma, R. Q., Geng, Y., Gan, L., Peng, Z. Y., Cheng, J. W., Guo, J., et al. (2021). Quantitative T1 mapping MRI for the assessment of extraocular muscle fibrosis in thyroid-associated ophthalmopathy. *Endocrine* [Epub ahead of print]. doi: 10.1007/s12020-021-02873-0

Men, C. J., Kossler, A. L., and Wester, S. T. (2021). Updates on the understanding and management of thyroid eye disease. *Ther. Adv. Ophthalmol.* 13:25158414211027760. doi: 10.1177/25158414211027760

Neag, E. J., and Smith, T. J. (2021). 2021 Update on thyroid-associated ophthalmopathy. *J. Endocrinol. Invest.* [Epub ahead of print]. doi: 10.1007/s40618-021-01663-9

Norris, C. D., Quick, S. E., Parker, J. G., and Koontz, N. A. (2020). Diffusion MR imaging in the head and neck: principles and applications. *Neuroimaging Clin. N. Am.* 30, 261–282. doi: 10.1016/j.nic.2020.04.001

Perros, P., Hegedus, L., Bartalena, L., Marcocci, C., Kahaly, G. J., Baldeschi, L., et al. (2017). Graves' orbitopathy as a rare disease in Europe: a European Group on Graves' Orbitopathy (EUGOGO) position statement. *Orphanet J. Rare Dis.* 12:72. doi: 10.1186/s13023-017-0625-1

Politi, L. S., Godi, C., Cammarata, G., Ambrosi, A., Iadanza, A., Lanzi, R., et al. (2014). Magnetic resonance imaging with diffusion-weighted imaging in the evaluation of thyroid-associated orbitopathy: getting below the tip of the iceberg. *Eur. Radiol.* 24, 1118–1126. doi: 10.1007/s00330-014-3103-3

Razek, A., El-Serougy, L., Abdelsalam, M., Gaballa, G., and Talaat, M. (2018). Differentiation of residual/recurrent gliomas from postradiation necrosis with arterial spin labeling and diffusion tensor magnetic resonance imaging-derived metrics. *Neuroradiology* 60, 169–177. doi: 10.1007/s00234-017-1955-3

Razek, A. A., El-Hadidy, E. M., Moawad, M. E., El-Metwaly, N., and El-Said, A. A. E. (2019). Assessment of lacrimal glands in thyroid eye disease with diffusion-weighted magnetic resonance imaging. *Pol. J. Radiol.* 84, e142–e146. doi: 10.5114/pjr.2019.84096

Taylor, P. N., Zhang, L., Lee, R. W. J., Muller, I., Ezra, D. G., Dayan, C. M., et al. (2020). New insights into the pathogenesis and nonsurgical management of Graves orbitopathy. *Nat. Rev. Endocrinol.* 16, 104–116. doi: 10.1038/s41574-019-0305-4

Weiler, D. L. (2017). Thyroid eye disease: a review. *Clin. Exp. Optom.* 100, 20–25. doi: 10.1111/cxo.12472

Wu, T., Tang, D. R., Wang, F., Xia, S., and Sun, F. Y. (2017). [The value of DCE-MRI in assessing the course of thyroid associated ophthalmopathy]. *Zhonghua Yan Ke Za Zhi* 53, 430–435. doi: 10.3760/cma.j.issn.0412-4081.2017.06.007

Conflict of Interest: The authors declare that the research was conducted in the absence of any commercial or financial relationships that could be construed as a potential conflict of interest.

Publisher's Note: All claims expressed in this article are solely those of the authors and do not necessarily represent those of their affiliated organizations, or those of the publisher, the editors and the reviewers. Any product that may be evaluated in this article, or claim that may be made by its manufacturer, is not guaranteed or endorsed by the publisher.

frontiers in Human Neuroscience

ORIGINAL RESEARCH
published: 16 February 2022
doi: 10.3389/fnhum.2022.823455

Effects of Different Degrees of Extraluminal Compression on Hemodynamics in a Prominent Transverse-Sigmoid Sinus Junction

Xiaoyu Qiu[1], Pengfei Zhao[1], Zhenxia Mu[2], Chihang Dai[1], Xiaoshuai Li[1], Ning Xu[1], Heyu Ding[1]*, Shusheng Gong[3], Zhenghan Yang[1], Bin Gao[2]* and Zhenchang Wang[1]**

[1] Department of Radiology, Beijing Friendship Hospital, Capital Medical University, Beijing, China, [2] Faculty of Environment and Life, Beijing University of Technology, Beijing, China, [3] Department of Otolaryngology Head and Neck Surgery, Beijing Friendship Hospital, Capital Medical University, Beijing, China

OPEN ACCESS

Edited by:
Yuexin Cai,
Sun Yat-sen University, China

Reviewed by:
Wuqing Wang,
Fudan University, China
Shan Tian,
Beihang University, China
Lizhen Wang,
Beihang University, China

***Correspondence:**
Pengfei Zhao
zhaopengf05@163.com
Heyu Ding
dingheyu1987@163.com
Bin Gao
gaobin@bjut.edu.cn
Zhenchang Wang
cjr.wzhch@vip.163.com

Specialty section:
This article was submitted to Sensory Neuroscience, a section of the journal Frontiers in Human Neuroscience

Received: 27 November 2021
Accepted: 18 January 2022
Published: 16 February 2022

Citation:
Qiu X, Zhao P, Mu Z, Dai C, Li X, Xu N, Ding H, Gong S, Yang Z, Gao B and Wang Z (2022) Effects of Different Degrees of Extraluminal Compression on Hemodynamics in a Prominent Transverse-Sigmoid Sinus Junction. Front. Hum. Neurosci. 16:823455. doi: 10.3389/fnhum.2022.823455

Objectives: To simulate hemodynamic changes after extraluminal compression in pulsatile tinnitus (PT) patients with a prominent transverse-sigmoid sinus junction (PTSJ).

Methods: One patient-specific case was reconstructed based on computed tomography venography (CTV) images of a PT patient. The compression degree served as a new index in this study. Cases with 10, 20, 30, 40, 50, 60, 70, 80, and 90% of the compression degree of the control subject were constructed. Steady-state computational fluid dynamics (CFD) were assessed. The wall pressure distribution, wall maximum pressure (P_{max}) and flow pattern (velocity streamlines and velocity vector) of the PTSJ were calculated to evaluate hemodynamic differences among all cases.

Results: With increasing compression, the wall pressure at the compression point and downstream of the PTSJ decreased but increased upstream. When the compression degree exceeded 70%, the upstream pressure increased significantly. Above 50% compression, the blood flow pattern downstream of the sigmoid sinus tended to spiral, especially after 80% compression. Beyond 60% compression, the blood flow pattern under the compression axis became more medial.

Conclusion: Mechanical compression of PTSJ changes wall pressure and blood flow patterns. The degree of compression should be carefully observed to avoid possible complications or reoccurrence.

Keywords: pulsatile tinnitus, cranial venous sinuses, compression degree, computational fluid dynamics (CFD), hemodynamics

INTRODUCTION

Pulsatile tinnitus (PT) is a kind of rhythmic, conscious or even objective noise that is often transmitted to the ear through the temporal bone or vascular structures; the frequency is mostly consistent with the heartbeat. The noise often occurs in childbearing women and has varying degrees of negative impact on the work and life of patients, resulting in insomnia, irritability,

anxiety, depression and even suicide. PT can be classified as arterial or venous according to the vascular origin, and venous origin is much more common (Dong et al., 2015; Han et al., 2017). Venous PT can be reduced or eliminated by compression on the affected side of the neck. There are many known causes of venous PT, including ipsilateral venous outflow dominance, transverse sinus stenosis, sigmoid sinus abnormalities (diverticulum, wall dehiscence, and enlargement), emissary vein enlargement, and high jugular bulb localization (Krishnan et al., 2006; Han et al., 2017; Zhao et al., 2020). According to the above different causes, the commonly used surgical methods include stent placement in stenosis, diverticulum restoration, bone wall reconstruction, vein ligation, and so on.

Although previous studies (Guo and Wang, 2015; Hsieh and Wang, 2020) have suggested that a prominent transverse-sigmoid sinus junction (PTSJ) is one of the causes of PT, related reports are limited. In recent years, it has been reported that extraluminal sigmoid sinus angioplasty (ESSA) was used to resolve PT caused by a PTSJ (Wee et al., 2012; Guo and Wang, 2015; Kim et al., 2016), and computational fluid dynamics (CFD) was used to simulate the changes in hemodynamics before and after surgery (Hsieh and Wang, 2020). Although the prognosis is good after this surgical treatment, the compression degree on the enlargement area is determined by the subjective feeling of patients under local anesthesia, and no objective studies on the influence of different compression degrees on the hemodynamics of the PTSJ have been reported to date. Therefore, for PT caused by a PTSJ, relevant research on hemodynamic changes with different surgical compression degrees at this stage is lacking.

In this study, based on the images of one PT case caused by a PTSJ, we used the finite element method to construct models with different compression degrees to perform CFD simulation and analyze the hemodynamic changes in the PTSJ. The inlet velocity was set according to the real blood flow velocity measured by 4D Flow magnetic resonance (MR). To qualitatively and quantitatively evaluate the hemodynamic differences in the enlargement area with different compression degrees, the vessel wall pressure distribution, maximum wall pressure (P_{max}) and blood flow pattern (velocity streamlines and velocity vectors) were calculated. The aim was to provide a basis for the degree of ESSA.

MATERIALS AND METHODS

Patient Information and Study Design

The medical data used in this study were obtained from our institution and were provided with the patient's consent. This study was based on a 29-year-old female who presented with a 2-year history of left-sided PT. The noise could be eliminated by compressing the ipsilateral jugular vein. The otoscopic and audiometric evaluations were normal. Computed tomography venography (CTV) and magnetic resonance venography (MRV) revealed ipsilateral venous outflow dominance and a PTSJ. The definition of PTSJ (**Figure 1**) was based on a study by Hsieh and Wang (2020).

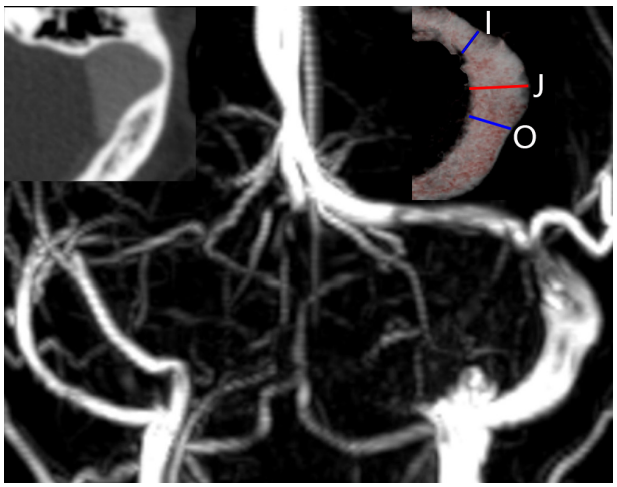

FIGURE 1 | Imaging features of a prominent transverse-sigmoid sinus junction (PTSJ). The PTSJ is located between the blue lines indicating inlet flow (I) and outlet flow (O). The red line (J) indicates the largest PTSJ area.

TABLE 1 | Cases with different compression degrees and the depth of blood vessels after compression.

Case number	Compression degree (%)	Depth of PTSJ (mm)
Control	0	15
1	10	13.5
2	20	12
3	30	10.5
4	40	9
5	50	7.5
6	60	6
7	70	4.5
8	80	3
9	90	1.5

PTSJ, prominent transverse-sigmoid sinus junction.

Imaging Features

Computed tomography venography images were obtained by a 256-slice spiral CT scanner (Philips Medical Systems, Netherlands), and the CTV data consisted of 231 slices (512 × 512 pixels; slice thickness, 0.625 mm) in Digital Imaging and Communications in Medicine format. Iodinated non-ionic contrast material was applied to display the lumen of the transverse sinus to the jugular vein on CTV images. The patient underwent MRV and 4D Flow scans using a 3.0 T MR scanner (Philips, Ingenia, Netherlands). All visualization, assessment and interpretation of 4D Flow data was performed using dedicated GT Flow 2.2.15 software (GyroTools, Switzerland).

Vascular Model Construction

A preliminary 3D geometric vessel model was reconstructed using Mimics 20.0 software (Materialise, Belgium), including the left transverse sinus, sigmoid sinus and jugular vein. The processed case was imported into Freeform and Geomagic Studio software (Geomagic, North Carolina, United States) for

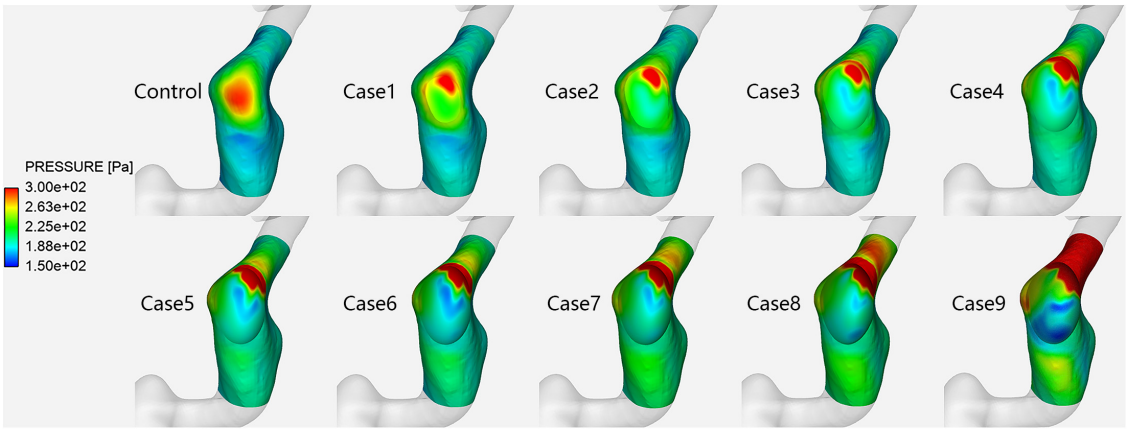

FIGURE 2 | Vessel wall pressure distribution in each case at the prominent transverse-sigmoid sinus junction (PTSJ).

smoothing, and the obtained model was taken as the control subject. The enlargement depth was measured using SolidWorks 2018 software (Dassault systems, Paris, France). The depth was defined as the distance from the highest point on the lateral section of the PTSJ to the lowest point on the inner section. All models with different compression degrees were assembled by SolidWorks. Based on the control subject, the simulated exposed surgical field was established referring to research by Hsieh and Wang (2020), when drawing an ellipse with a short axis and a long axis of 10 and 15 mm, respectively, perpendicular to the enlargement depth. The simulated degree of surgical compression was quantified by depth. With the enlargement depth as the reference line, nine groups of models with different compression degrees from 10 to 90% in increments of 10% were set along the line. The names of cases with different compression degrees and the depth of blood vessels after compression are shown in **Table 1**.

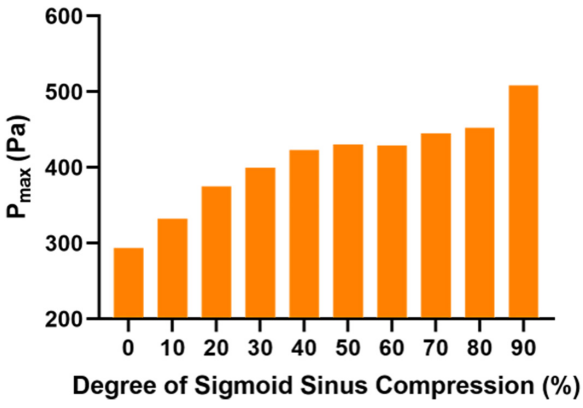

FIGURE 3 | Maximum wall pressure (P_{max}) in each case at the prominent transverse-sigmoid sinus junction (PTSJ).

Computational Models and Simulations

All steps in this section were completed by using the components of ANSYS 2020 R1 software (ANSYS, Inc., Cecil Township, PA, United States). The standard tessellation language format models from SolidWorks were imported into Workbench for Boolean subtraction modeling and then imported into Fluent for meshing, allowing adaptive polyhedral 3D meshing of high quality. Three boundary layers were generated to resolve the flow field at the fluid-wall interface. To confirm the applicable grid size, the average wall pressure of the PTSJ (colored area in **Figure 2**) was used as the criterion for the grid-independence test. An error of less than 5% was acceptable. A steady-state CFD calculation was performed, the boundary condition of the inlet was set at 0.30 m/s, which was based on the real blood flow velocity measured by 4D Flow MR, and the boundary condition of the outlet was set at 0 absolute pressure. A total of 877,448 elements were developed, and they were sufficient for this study. The maximum element size of each case was set to 0.3 mm. The vessel wall was assumed to be rigid, with no-slip conditions. The blood was assumed to be a laminar, isotropic, homogeneous and incompressible Newtonian fluid with a viscosity of 0.0035 Pa/s and density of 1,050 kg/m^3. The conservation of mass and momentum for the Navier-Stokes equation, solved with Fluent, was used as the governing equation for calculations. The convergence precision was set at 10^{-3}. Based on the CFD simulation results, several flow parameters were calculated and colored by Ensight according to distribution and magnitude to evaluate the effects of model hemodynamics quantitatively. These parameters included the wall pressure distribution, P_{max}, average wall pressure (P_{avg}), flow streamlines, velocity vector, maximum velocity (V_{max}) and average velocity (V_{avg}).

RESULTS

Vessel Wall Pressure

Figure 2 shows the vessel wall pressure distribution at the PTSJ. In the control subject, the wall pressure of the PTSJ was greater than that of the surrounding area. This finding is consistent

TABLE 2 | Quantitative values of wall pressure and velocity of the PTSJ with different compression degrees.

Case	P_{max} (Pa)	P_{avg} (Pa)	V_{max} (m/s)	V_{avg} (m/s)
Control	293.7	191.5	0.45	0.13
1	332.5	194.6	0.53	0.14
2	375.0	193.9	0.54	0.15
3	400.0	195.8	0.52	0.15
4	422.9	200.4	0.50	0.16
5	430.7	203.6	0.49	0.17
6	429.1	204.7	0.46	0.18
7	445.0	215.8	0.46	0.19
8	452.6	224.0	0.51	0.23
9	508.7	242.5	0.62	0.30

P_{max}, wall maximum pressure; P_{avg}, wall average pressure; V_{max}, maximum velocity; V_{avg}, average velocity.

with previous studies and suggested that increased vessel wall pressure at the PTSJ was a significant cause of PT (Huang et al., 2020; Mu et al., 2020). With increasing compression degree, the wall pressure at the compression point and downstream of the PTSJ decreased, but the wall pressure upstream of the PTSJ slightly increased. The quantitative results (**Figure 3** and **Table 2**) clearly show that the wall pressure changed non-linearly with increasing compression. In addition, **Figure 2** shows that when the compression degree reached 70%, the wall pressure increased prominently, especially at the upstream transverse sinus side.

Blood Flow Pattern

Figure 4 shows the velocity streamlines of the PTSJ. The streamlines in cases 1–4 were similar to those in the control subjects. When the compression degree exceeded 50%, the blood through the compression area showed eccentric flow, which led to the gradual transition of blood flow downstream of the compression area from laminar to spiral, especially when the compression degree reached 80%.

Figure 5 shows the velocity vectors of the PTSJ. After the compression degree increased to 60%, the high-speed blood flow in the lateral area downstream of the compression site gradually moved toward the medial region, the lateral blood flow pattern was more turbulent than before, and the overall blood flow velocity downstream was faster. The quantitative results are shown in **Table 2**. In addition, there was a sharply defined low-velocity blood flow area immediately below the compression site in cases 2–4, causing local blood flow stasis.

DISCUSSION

A PTSJ is known as the most vulnerable site for venous PT (Guo and Wang, 2015; Kim et al., 2016). Because of the sharp angle between the transverse sinus and sigmoid sinus (Xue et al., 2012; Kim et al., 2016; Zhao et al., 2016; Huang et al., 2020; Mu et al., 2020), local irregular blood flow and increased wall pressure easily occur. This blood flow impacts and erodes the adjacent temporal bone, resulting in sigmoid sinus wall dehiscence and subsequently producing noise. Therefore, it is important to observe the hemodynamic changes in blood flow in this position. The literature (Cho et al., 2012; Wee et al., 2012; Kim et al., 2016) indicates that high venous blood perfusion is one of the causes of PT. Considering that the blood flow is proportional to the fourth power of the radius (Poiseuille's law), when the asymmetry between the bilateral venous sinuses is significant, the dominant side may receive almost all the venous blood flow (Roos, 1962). This feature may lead to slow progressive erosion of the bony wall adjacent to the PTSJ (Cho et al., 2012), and the diameter of the PTSJ may gradually increase (Kim et al., 2016). Therefore, in this study, we selected a PT patient with a PTSJ on the affected side and the dominant side of venous sinus returns to construct relevant models for CFD simulation analysis.

The effect and hemodynamic changes of ESSA on PT induced by a PTSJ have been confirmed by relevant studies (Wee et al., 2012; Guo and Wang, 2015; Kim et al., 2016; Hsieh and Wang, 2020). However, this study is the first to objectively simulate the effect of different degrees of surgical compression on the hemodynamics of the PTSJ. In this study, 10 finite element models with different compression degrees were constructed for CFD simulation and analysis. We found that the hemodynamics of the PTSJ were significantly affected by different degrees of surgical compression. With increasing compression, the wall pressure upstream of the compression site increased non-linearly. When the compression degree was greater than 70%, the wall pressure at the PTSJ increased significantly. Moreover, with increasing compression, the blood flow velocity accelerated downstream of the compression site, and the blood flow pattern gradually changed into a spiral shape, significantly changing after the degree of compression reached 80%. These results show that the hemodynamic changes at the PTSJ are significant when the surgical compression degree is large, so the compression degree should be carefully planned.

The vessel wall pressure is the most representative hemodynamic parameter of PT. The PTSJ is known as the most vulnerable site for venous PT. Previous studies (Tian et al., 2017; Mu et al., 2020) have shown that increased wall pressure at the PTSJ may lead to the occurrence or recurrence of sigmoid sinus wall dehiscence and PT. The results of our study show that the pressure at the compression site decreased, which is consistent with the findings of Hsieh and Wang's (2020) study, which demonstrated that venous sinus compression at the site of wall dehiscence can reduce the pressure and eliminate PT. However, when the degree of compression reached 70%, the pressure upstream of the compression site increased significantly. It is hypothesized that this increase may be related to the different compression methods and other factors, such as irregular compression morphology, inaccurate compression depth and orientation in the actual operation. Therefore, from the perspective of intravascular hemodynamics, it can be inferred that excessive compression is not only not conducive to the elimination of PT but also leads to a wider range of wall dehiscence in the long term. In addition, the mechanism of excessive compression is similar to that of vein ligation and may increase the risk of other complications, such as increased intracranial pressure, contralateral PT and neurological symptoms (Jackler et al., 2001). The compression

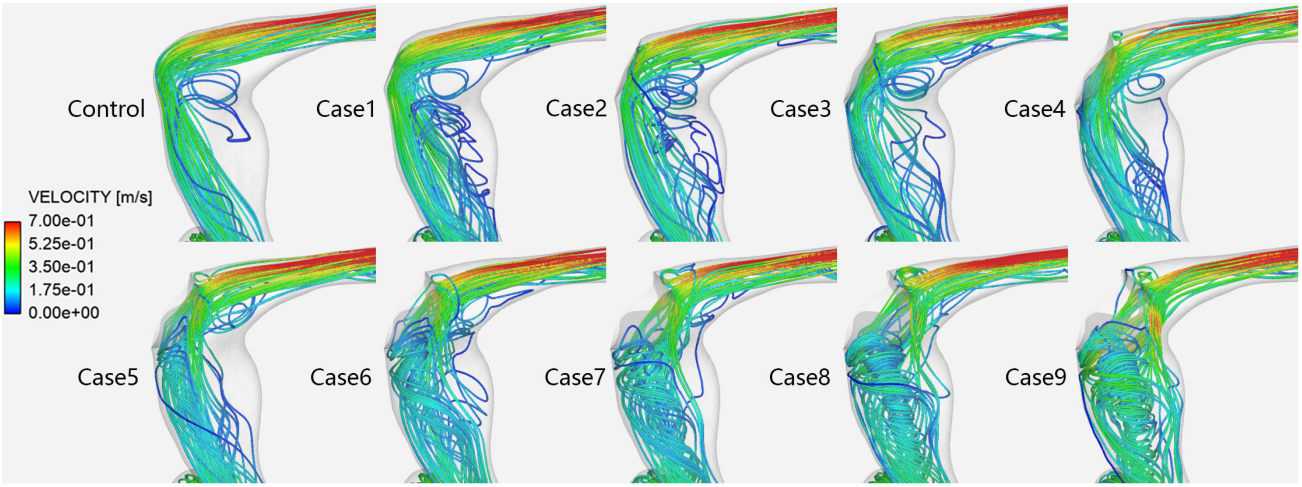

FIGURE 4 | Velocity streamlines in each case at the prominent transverse-sigmoid sinus junction (PTSJ).

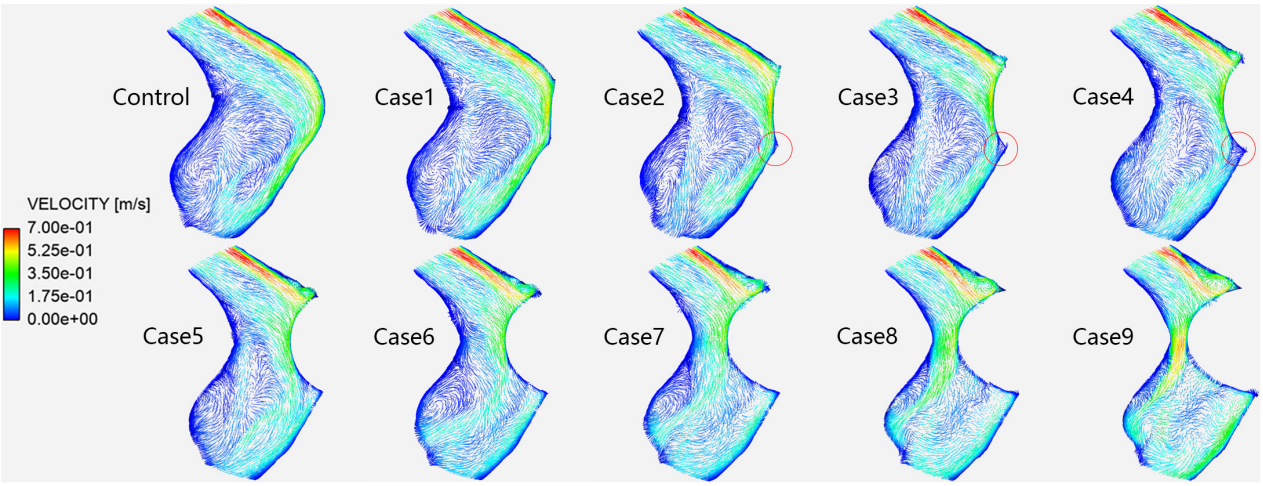

FIGURE 5 | Velocity vectors in each case at the prominent transverse-sigmoid sinus junction (PTSJ). The red circles represent the blood stasis area.

degree in a previous study (Guo and Wang, 2015) mostly ranged from 46–69% and did not exceed 70%, with a good curative effect, which is indirectly consistent with the results of this study. These findings suggest that when choosing ESSA, the degree of compression should not be excessive (70%) to avoid adverse effects on the veins themselves and related complications.

It has also been considered that turbulence in blood vessels is one of the important causes of PT (Tian et al., 2017; Hsieh and Wang, 2020). In this study, the lateral blood flow of the PTSJ in the control subject was stable laminar flow, which is not involved in the pathogenesis of PT. This finding is different from that reported by Hsieh and Wang (2020), which showed a local turbulence pattern. This difference may be related to the different shapes and expansion degrees of the PTSJ. When the compression degree was less than 50%, the blood flow pattern was almost unchanged. This may be indirectly consistent with the literature (Guo and Wang, 2015), which indicates that the therapeutic effect on PT is the best when the degree of compression is 46–69% and that a patient with a compression degree of only 30% experiences no relief. However, spiral blood flow gradually appeared downstream of the sigmoid sinus when the degree of compression continued to increase, especially when the degree of compression reached 80%. After the normal laminar flow transforms into a spiral blood flow, the blood flow pattern, direction and velocity change, which affects the vascular wall and stimulates vascular endothelial remodeling (Kruger-Genge et al., 2019). In the long run, this may cause PT recurrence or other vascular diseases. Therefore, we should avoid long-term injury caused by excessive compression. In addition, our results also revealed an interesting phenomenon; when the degree of compression was 20–40%, there was a sharp, low-speed, blood stasis area below the compression site, potentially leading to long-term thrombosis. Although real compression does not produce

an absolutely sharp edge in the area of compression, there are still similar slightly smooth areas. Thus, this condition plays a certain role in clinical practice.

There are some limitations to this study. First, all models are based on one special patient. Although this approach cannot fully represent the characteristic changes of related cases, the construction of the case morphology and the selection of the boundary conditions are consistent with the real situation. The sample size should be increased for further verification in future work. Second, this study evaluated the effect of simulated surgery, and there was a certain gap with the real surgical state. In follow-up work, the simulation process will be optimized to be as close as possible to the actual situation. Third, the setting of boundary conditions in CFD simulation affects the results, but it does not hinder the horizontal comparison in our research. Final, although venous wall pressure and spiral flow have an important impact on PT, they cannot be used as direct evidence for the elimination or aggravation of PT. We will conduct multi physical field coupling analysis in subsequent research.

CONCLUSION

Different degrees of surgical compression produce different pressure fields and flow fields closely related to PT. In this study, although there was no unified threshold to simulate the effects of different compression degrees on the characteristics of vascular wall pressure, blood flow pattern and velocity, it was found that when the compression degree increased, the hemodynamics of the PTSJ exhibited significant abnormal changes. Excessive upstream wall pressure, accelerated blood flow velocity and spiral blood flow instead of laminar flow cause immediate or long-term effects on blood vessels, potentially leading to surgical failure or PT recurrence. Therefore, for PT patients with a PTSJ, it is necessary to avoid excessive compression when deciding to perform ESSA.

DATA AVAILABILITY STATEMENT

The original contributions presented in the study are included in the article/supplementary material, further inquiries can be directed to the corresponding authors.

ETHICS STATEMENT

The studies involving human participants were reviewed and approved by the Beijing Friendship Hospital, Capital Medical University. The patients/participants provided their written informed consent to participate in this study.

AUTHOR CONTRIBUTIONS

XQ, CD, XL, and NX collected the clinical and imaging data. XQ, PZ, and ZM performed the experiment. XQ drafted the manuscript. ZW, PZ, HD, and BG designed the study and ensured the questions related to all aspects of the work. ZY and SG gave critical comments on the manuscript. All authors contributed to the article and approved the submitted version.

FUNDING

This study was supported by grant nos. 61931013 and 82171886 from the National Natural Science Foundation of China and no. (2015)160 from the Beijing Scholar Program.

REFERENCES

Cho, I. K., Jung, J. Y., Yoo, D. S., and Suh, M. W. (2012). 3-Dimensional reconstruction of the venous system in patients suffering from pulsatile tinnitus. *Acta Otolaryngol.* 132, 285–289. doi: 10.3109/00016489.2011.631190

Dong, C., Zhao, P. F., Yang, J. G., Liu, Z. H., and Wang, Z. C. (2015). Incidence of vascular anomalies and variants associated with unilateral venous pulsatile tinnitus in 242 patients based on dual-phase contrast-enhanced computed tomography. *Chin. Med. J.* 128, 581–585. doi: 10.4103/0366-6999.151648

Guo, P., and Wang, W. Q. (2015). Degree of sigmoid sinus compression and the symptom relief using magnetic resonance angiography in venous pulsating tinnitus. *Clin. Exp. Otorhinolaryngol.* 8, 111–116. doi: 10.3342/ceo.2015.8.2.111

Han, Y., Yang, Q., Yang, Z., Xia, J., Su, T., Yu, J., et al. (2017). Computational fluid dynamics simulation of hemodynamic alterations in sigmoid sinus Diverticulum and Ipsilateral upstream sinus stenosis after stent implantation in patients with pulsatile tinnitus. *World Neurosurg.* 106, 308–314. doi: 10.1016/j.wneu.2017.06.168

Hsieh, Y. L., and Wang, W. (2020). Extraluminal sigmoid sinus angioplasty: a pertinent reconstructive surgical method targeting Dural Sinus Hemodynamics to resolve pulsatile tinnitus. *Otol. Neurotol.* 41, e132–e145. doi: 10.1097/MAO.0000000000002464

Huang, S., Li, X., Xue, X., Qiu, X., Mu, Z., Fu, M., et al. (2020). Hemodynamic study of the therapeutic effects of the different degrees of sigmoid sinus diverticulum reconstruction on patients. *Med. Eng. Phys.* 86, 8–15. doi: 10.1016/j.medengphy.2020.10.008

Jackler, R. K., Brackmann, D. E., and Sismanis, A. (2001). A warning on venous ligation for pulsatile tinnitus. *Otol. Neurotol.* 22, 427–428. doi: 10.1097/00129492-200105000-00036

Kim, C. S., Kim, S. Y., Choi, H., Koo, J. W., Yoo, S. Y., An, G. S., et al. (2016). Transmastoid reshaping of the sigmoid sinus: preliminary study of a novel surgical method to quiet pulsatile tinnitus of an unrecognized vascular origin. *J. Neurosurg.* 125, 441–449. doi: 10.3171/2015.6.JNS15961

Krishnan, A., Mattox, D. E., Fountain, A. J., and Hudgins, P. A. (2006). CT arteriography and venography in pulsatile tinnitus: preliminary results. *Am. J. Neuroradiol.* 27, 1635–1638.

Kruger-Genge, A., Blocki, A., Franke, R. P., and Jung, F. (2019). Vascular endothelial cell biology: an update. *Int. J. Mol. Sci.* 20:4411. doi: 10.3390/ijms20184411

Mu, Z., Qiu, X., Zhao, D., Li, X., Fu, M., Liu, Y., et al. (2020). Hemodynamic study on the different therapeutic effects of SSWD resurfacing surgery on patients with pulsatile tinnitus. *Comput. Methods Prog. Biomed.* 190:105373. doi: 10.1016/j.cmpb.2020.105373

Roos, A. (1962). Poiseuille's law and its limitations in vascular systems. *Med. Thorac.* 19, 224–238. doi: 10.1159/000192223

Tian, S., Wang, L., Yang, J., Mao, R., Liu, Z., and Fan, Y. (2017). Sigmoid sinus cortical plate dehiscence induces pulsatile tinnitus through amplifying sigmoid sinus venous sound. *J. Biomech.* 52, 68–73. doi: 10.1016/j.jbiomech.2016.12.012

Wee, J. H., Song, J. J., Koo, J. W., and Kim, C. S. (2012). Increased intracranial pressure after surgical treatment of pulsatile tinnitus from a prominent sigmoid sinus. *Otol. Neurotol.* 33, e41–e42. doi: 10.1097/MAO.0b013e318245cb22

Xue, J., Li, T., Sun, X., and Liu, Y. (2012). Focal defect of mastoid bone shell in the region of the transverse-sigmoid junction: a new cause of pulsatile tinnitus. *J. Laryngol. Otol.* 126, 409–413. doi: 10.1017/S0022215111003458

Zhao, P., Ding, H., Lv, H., Li, X., Qiu, X., Zeng, R., et al. (2020). CT venography correlate of transverse sinus stenosis and venous transstenotic pressure gradient in unilateral pulsatile tinnitus patients with sigmoid sinus wall anomalies. *Eur. Radiol.* 31, 2896–2902. doi: 10.1007/s00330-020-07415-2

Zhao, P., Lv, H., Dong, C., Niu, Y., Xian, J., and Wang, Z. (2016). CT evaluation of sigmoid plate dehiscence causing pulsatile tinnitus. *Eur. Radiol.* 26, 9–14.

Conflict of Interest: The authors declare that the research was conducted in the absence of any commercial or financial relationships that could be construed as a potential conflict of interest.

Publisher's Note: All claims expressed in this article are solely those of the authors and do not necessarily represent those of their affiliated organizations, or those of the publisher, the editors and the reviewers. Any product that may be evaluated in this article, or claim that may be made by its manufacturer, is not guaranteed or endorsed by the publisher.

frontiers in Neuroscience

ORIGINAL RESEARCH
published: 08 March 2022
doi: 10.3389/fnins.2022.833937

Effect of Impaired Stereoscopic Vision on Large-Scale Resting-State Functional Network Connectivity in Comitant Exotropia Patients

Han Jin[1†], Ri-Bo Chen[2†], Yu-Lin Zhong[1†], Ping-Hong Lai[1†] and Xin Huang[1]*

[1] Department of Ophthalmology, Jiangxi Provincial People's Hospital, The First Affiliated Hospital of Nanchang Medical College, Nanchang, China, [2] Department of Radiology, Jiangxi Provincial People's Hospital, The First Affiliated Hospital of Nanchang Medical College, Nanchang, China

OPEN ACCESS

Edited by:
Yu-Chen Chen,
Nanjing Medical University, China

Reviewed by:
Xiuxiu Qin,
Southern Medical University, China
Wen-Qing Shi,
Fudan University, China
Jyothilakshmi Vasavan,
Algonquin College, Canada
Vijaya Prakash Krishnan Muthaiah,
University at Buffalo, United States

****Correspondence:***
Xin Huang
2017103020035@whu.edu.cn

[†] These authors have contributed equally to this work

Specialty section:
This article was submitted to Perception Science, a section of the journal Frontiers in Neuroscience

Received: *12 December 2021*
Accepted: *31 January 2022*
Published: *08 March 2022*

Citation:
Jin H, Chen R-B, Zhong Y-L, Lai P-H and Huang X (2022) Effect of Impaired Stereoscopic Vision on Large-Scale Resting-State Functional Network Connectivity in Comitant Exotropia Patients. Front. Neurosci. 16:833937. doi: 10.3389/fnins.2022.833937

Background: Comitant exotropia (CE) is a common eye movement disorder, characterized by impaired eye movements and stereoscopic vision. CE patients reportedly exhibit changes in the central nervous system. However, it remains unclear whether large-scale brain network changes occur in CE patients.

Purpose: This study investigated the effects of exotropia and stereoscopic vision dysfunction on large-scale brain networks in CE patients *via* independent component analysis (ICA).

Methods: Twenty-eight CE patients (mean age, 15.80 ± 2.46 years) and 27 healthy controls (HCs; mean age, 16.00 ± 2.68 years; closely matched for age, sex, and education) underwent resting-state magnetic resonance imaging. ICA was applied to extract resting-state networks (RSNs) in both groups. Two-sample's *t*-tests were conducted to investigate intranetwork functional connectivity (FC) within RSNs and interactions among RSNs between the two groups.

Results: Compared with the HC group, the CE group showed increased intranetwork FC in the bilateral postcentral gyrus of the sensorimotor network (SMN). The CE group also showed decreased intranetwork FC in the right cerebellum_8 of the cerebellum network (CER), the right superior temporal gyrus of the auditory network (AN), and the right middle occipital gyrus of the visual network (VN). Moreover, functional network connectivity (FNC) analysis showed that CER-AN, SMN-VN, SN-DMN, and DMN-VN connections were significantly altered between the two groups.

Conclusion: Comitant exotropia patients had abnormal brain networks related to the CER, SMN, AN, and VN. Our results offer important insights into the neural mechanisms of eye movements and stereoscopic vision dysfunction in CE patients.

Keywords: comitant exotropia, independent component analysis, resting-state networks, functional connectivity, functional network connectivity, fMRI

INTRODUCTION

Comitant exotropia (CE) is a common eye movement disorder, characterized by ocular deviation and impaired stereoscopic vision function; CE affects 1.0% of all children (Govindan et al., 2005). Impaired stereoscopic vision is an important clinical manifestation of CE (Feng et al., 2015). Binocular vision is an important physiological basis for stereoscopic vision. Symmetrical eye positioning allows considerable visual field overlapping between eyes, which is essential for both binocular and stereoscopic vision (Chopin et al., 2019). CE patients exhibit impaired stereoscopic vision because of anomalous retinal correspondence for the same object in both eyes. The fundamental nature of stereoscopic vision depends on good vision in both eyes, good oculomotor control, and intact cortical mechanisms (Li et al., 2017). Moreover, central nervous system function is important for stereoscopic vision.

Stereoscopic vision is a fundamental aspect of human visual function. The visual cortex has an important role in maintaining stereoscopic vision. Neuroimaging studies have shown that the medial temporal lobe plays important roles in stereoscopic depth processing (Backus et al., 2001; Chen et al., 2020). Moreover, the dorsal visual pathway is involved in stereoscopic depth processing (Goncalves et al., 2015). Ban et al. (2012) demonstrated that the dorsal stream is important for binocular vision fusion, while Zheng et al. (2020) found that the dorsal visual regions showed predominant advantages in decoding the disparities present in three-dimensional images. Furthermore, stereoscopic vision is closely related to gray and white matter structures in the brain. Numerous cortical areas are reportedly involved in binocular disparity processing (Ohzawa et al., 1990; Parker, 2007). Abed Rabbo et al. (2018) describe extensive white matter connections between the visual areas and the lateral geniculate nucleus within stereoscopic visual areas. Prins et al. (2017) found that volumetric decreases in the superior lateral occipital cortices are associated with depth perception in monocularly blind patients. Oishi et al. (2018) demonstrated that stereoscopic depth discrimination is involved in dorsoventral communication through the vertical occipital fasciculus. Gillebert et al. (2015) found that the right posterior inferior temporal cortex and right premotor cortex are responsible for three-dimensional shape processing. The aforementioned studies showed that stereoscopic vision is closely related to specific brain structures and functions. However, the effects of impaired stereoscopic vision on large-scale resting-state functional network connectivity (FNC) have not been explored in CE patients.

The human brain exhibits blood oxygenation level-dependent (BOLD) signals in the resting state. Low-frequency fluctuations (<0.01 Hz) in resting-state BOLD signals reflect spontaneous neural activity and imply spatiotemporal correlations in functional networks (Auer, 2008). Low-frequency fluctuations are closely related to several physiological functions including motor (Biswal et al., 1995), vision (Oke et al., 2010), and higher cognitive function (Kong et al., 2016). The low-frequency fluctuations (<0.01 Hz) in BOLD signals reportedly correspond to functionally relevant resting-state networks (RSNs) (e.g., visual, sensorimotor, auditory, default mode, executive, and salience) (Damoiseaux et al., 2006; Smith et al., 2009). The independent component analysis (ICA) method is a powerful data-driven approach for the identification of independent patterns in multivariate data (van de Ven et al., 2004). Importantly, the ICA method does not require a preset seed point, compared with resting-state functional connectivity-based seed points. Moreover, the ICA method has been successfully used to investigate changes in neurophysiological mechanisms that occur in neurological diseases (Du et al., 2015; Chen et al., 2019). To our knowledge, the effects of impaired stereoscopic vision on large-scale resting-state FNC have not been investigated in CE patients.

This study was performed to investigate how impaired stereoscopic vision influences large-scale resting-state FNC in CE patients. We hypothesized that CE patients might exhibit widespread RSN changes involving VNs and vision-related supporting networks. Our findings might provide new insights into the mechanisms of RSN changes that contribute to impaired stereoscopic vision in CE patients.

MATERIALS AND METHODS

Participants

Twenty-eight CE patients and twenty-seven healthy controls (HCs) were recruited from Jiangxi Provincial People's Hospital, The First Affiliated Hospital of Nanchang Medical College. The diagnostic criteria of CE patients were as follows: (1) comitant exotropia, exodeviation angles between 15 and 80Δ; (2) without a history of strabismus surgery; (3) participant should have undergone fusional control score, Worth 4-dot test, and Titmus stereopsis test.

The exclusion criteria of CE individuals in the study were as follows: (1) additional ocular-related complications (e.g., cataract, glaucoma, high myopia, or optic neuritis); (2) sensory exotropia, fixed exotropia; and (3) concomitant exotropia was associated with amblyopia.

Magnetic Resonance Imaging Acquisition

Magnetic resonance imaging (MRI) scanning was performed on a 3-T magnetic resonance scanner (Discovery MR 750W system; GE Healthcare, Milwaukee, WI, United States) with eight-channel head coil. Functional images were obtained by using a gradient-echo-planar imaging sequence. All the subjects were instructed to rest quietly with their eyes closed and relaxed without thinking about anything in particular or falling asleep. Whole-brain T1 weights were obtained with three-dimensional brain volume imaging (3D-BRAVO) MRI with the following parameters: repetition time [TR]/echo time [TE] = 8.5/3.3, thickness = 1.0 mm, no intersection gap, acquisition matrix = 256 × 256, field of view = 240 mm × 240 mm, and flip angle = 12°. Functional images were obtained by using a gradient-echo-planar imaging sequence with the following parameters: TR/TE = 2,000 ms/25 ms, thickness = 3.0 mm, gap = 1.2 mm, acquisition matrix = 64 × 64,

flip angle = 90°, field of view = 240 mm × 240 mm, voxel size = 3.6 mm × 3.6 mm × 3.6 mm, and 35 axial slices.

fMRI Data Analysis

All pre-processing was performed using the toolbox for Data Processing and Analysis of Brain Imaging (DPABI[1]) (Yan et al., 2016), which is based on Statistical Parametric Mapping (SPM12)[2] implemented in MATLAB 2013a (MathWorks, Natick, MA, United States) and briefly the following steps: (1) Remove the first 10 volumes. (2) Slice timing effects, motion corrected. For head motion parameters, more than 2 mm or for whom rotation exceeded 1.5° during scanning were excluded (Van Dijk et al., 2012). (3) Normalized data [in Montreal Neurological Institute (MNI) 152 space] were re-sliced at a resolution of 3 mm × 3 mm × 3 mm. (4) Spatial smoothing by convolution with an isotropic Gaussian kernel of 6 mm × 6 mm × 6 mm full width at half maximum.

Group Independent Component Analysis

Group ICA was performed to decompose the data into independent components (ICs) using the GIFT toolbox (version 3.0b).[3] First, 31 IC maps were estimated in this study using the minimum description length criterion to adjust for spatial correlation. Second, the ICs for each subject were derived from the group ICA back-reconstruction step and were converted into *z*-scores (Zuo et al., 2010). Components retained for further analysis among the 31 estimated ICs were selected based on the largest spatial correlation with specific RSN templates (Shirer et al., 2012; Wang et al., 2014). The IC time courses and spatial maps for each subject were transformed to *z*-scores. Fourteen RSNs were identified in this study.

Intranetwork Functional Connectivity Analysis

The intranetwork FC was represented by the *z*−score of each voxel, which reflects the degree to which the time series of a given voxel correlates with the mean time series of its corresponding component.

Functional Network Connectivity Analysis

The FNC analysis was performed using the MANCOVAN toolbox in GIFT software to explore changes in the predefined 14 spatial IC pairs of functional connections. First, at 0.01–0.15 Hz, de-trend, de-peak, and low-pass filtering were performed on the selected IC. Then, the pair correlations of these ICs were calculated and transformed using Fisher's *Z*-transform.

Statistical Analysis

Spatial Maps for Each of the Resting-State Networks

The ICs corresponding to fourteen RSNs were extracted from all subjects. Fourteen of these components coincided with RSNs, namely, IC1 (LECN, left executive control network); IC5 (DAN, dorsal attention network); IC6 (CER, cerebellum network); IC8 (RECN, right executive control network); IC12 (VN1, visual network1); IC13 (DMN1, default mode network1); IC18 (SN, salience network); IC22 (SMN, sensorimotor network); IC23 (AN, auditory network); IC24 (VN2, visual network2); IC26 (VN3, visual network3); IC27 (DMN2, default mode network2); IC29 (VN4, visual network4); and IC30 (DMN3, default mode network3).

Intranetwork Functional Connectivity Analysis

Two-sample's *t*-tests were used to compare differences between the two groups in the intranetwork FC within RSN maps; the Gaussian random field method was used to correct for multiple comparisons and regressed covariates of age and sex using SPM12 software. Group comparisons were masked to the voxels within corresponding RSNs (two-tailed, voxel-level $p < 0.01$, Gaussian random field correction, cluster-level $p < 0.05$).

Internetwork Functional Connectivity Analysis

Internetwork functional connectivity analysis was used to calculate temporal relationships between RSNs. Corresponding to the significant correlation combinations, the average time lags were calculated for each group; these represented the amount of delay between time courses of two correlated RSNs. Two-sample's *t*-tests were used to compare distinct temporal relationships between RSNs between the two groups ($p < 0.05$, uncorrected).

RESULTS

Demographics and Visual Measurements

There were no significant differences in the gender and age between the groups (**Table 1**).

Identifications of the Resting-State Networks

The group ICA approach automatically generated 31 ICs. The typical spatial patterns in each RSN of both CE and HC groups are illustrated in **Figure 1**. Fourteen of these components coincided with RSNs, namely, IC1 (LECN, left executive control network); IC5 (DAN, dorsal attention network); IC6 (CER, cerebellum network); IC8 (RECN, right executive control network); IC12

TABLE 1 | Demographics and visual measurements between two groups.

Condition	CE group	HC group	*T*-values	*P*-values
Gender (male/female)	(15/13)	(15/12)	N/A	N/A
Comitant category	Congenital exotropia	N/A	N/A	N/A
Age (years)	15.80 ± 2.46	16.00 ± 2.68	−0.240	0.812
Handedness	28 R	27 R	N/A	N/A

Independent t-test for the other normally distributed continuous data (means ± SD).
CE, comitant exotropia; HC, healthy control.

[1]http://www.rfmri.org/dpabi
[2]http://www.fil.ion.ucl.ac.uk
[3]http://icatb.sourceforge.net/

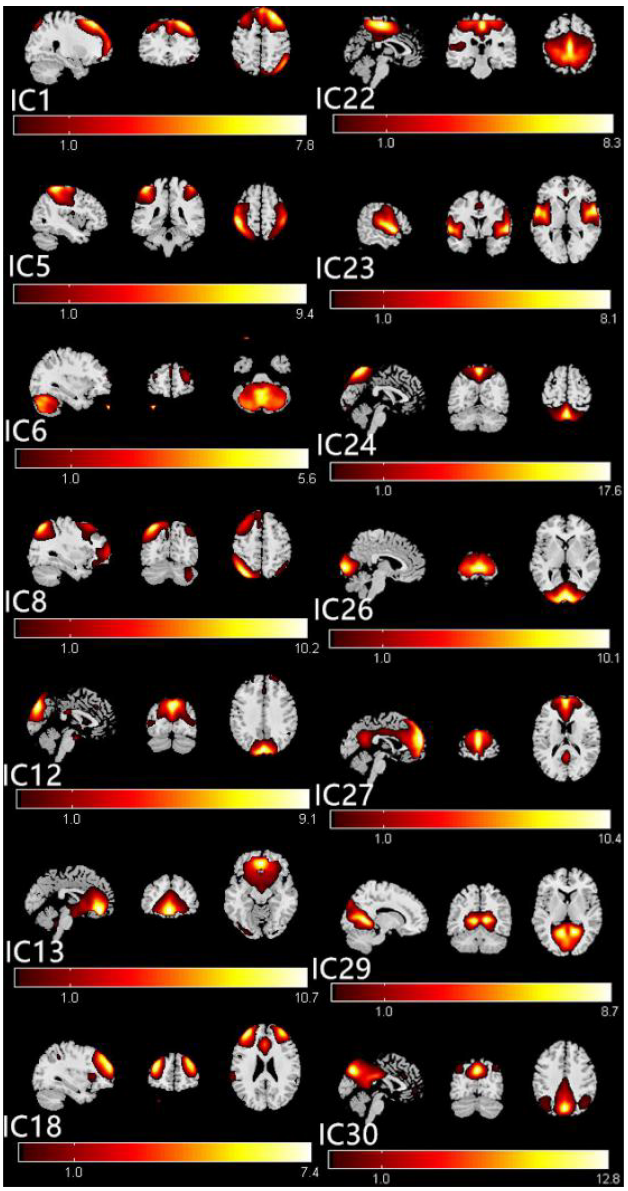

FIGURE 1 | The typical spatial patterns in each RSN of both CE and HC groups, including IC1(LECN), IC5(DAN), IC6(CER), IC8(RECN), IC12(VN1), C13(DMN1), IC18(SN), IC22(SMN), IC23(AN), IC24(VN2), IC26(VN3), IC27(DMN2), IC29(VN4), and IC30 (DMN3). Scale represents *T*-values with a range of 1–17.6 in each RSN. CE, comitant exotropia; HC, healthy control; lECN, left executive control network; DAN, dorsal attention network; CER, cerebellum network; RECN, right executive control network; VN, visual network; DMN, default mode network; SN, salience network; SMN, sensorimotor network; AN, auditory network.

(VN1, visual network1); C13 (DMN1, default mode network1); IC18 (SN, salience network); IC22 (SMN, sensorimotor network); IC23 (AN, auditory network); IC24 (VN2, visual network2); IC26 (VN3, visual network3); IC27 (DMN2, default mode network2); IC29 (VN4, visual network4); and IC30 (DMN3, default mode network3).

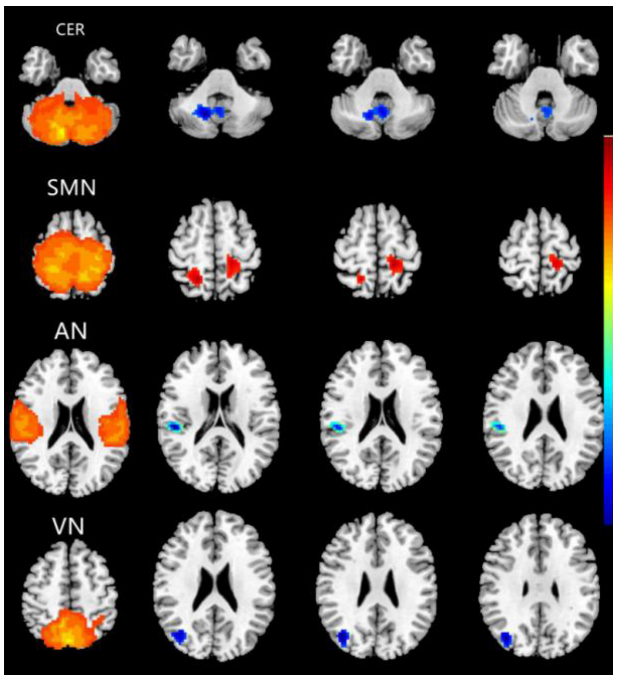

FIGURE 2 | Brain regions with significant differences for five RSNs in the CE group vs. the HC group (two-tailed, voxel-level $p < 0.01$, GRF correction, cluster-level $p < 0.05$). Compared with the HC group, cool colors indicated the decreased functional connectivity and hot colors indicated the increased functional connectivity in the CE group. The pictures correspond to different resting-state networks. CER, SMN, AN and VN. CE, comitant exotropia; HC, healthy control; CER, cerebellum network; SMN, sensorimotor network; AN, auditory network; VN, visual network.

Abnormal Intranetwork Functional Connectivity Changes Between Groups

Compared with the HC group, the CE group showed increased intranetwork FC in the bilateral postcentral gyrus of the SMN. Meanwhile, the PD group showed decreased intranetwork FC in the right cerebelum_8 of the CER, the right superior temporal gyrus of the AN, and the right middle occipital gyrus of the VN (**Figure 2** and **Table 2**) (two-tailed, voxel-level $p < 0.01$, GRF correction, cluster-level $p < 0.05$).

Functional Network Connectivity Analysis

The markers indicate significant functional connection between networks IC1 (LECN), IC5 (DAN), IC6 (CER), IC8 (RECN), IC12 (VN1), C13 (DMN1), IC18 (SN), IC22 (SMN), IC23 (AN), IC24 (VN2), IC26 (VN3), IC27 (DMN2), IC29 (VN4), and IC30 (DMN3) ($p < 0.05$, uncorrected). Matrix shows differences of internetwork functional connectivity between two groups (**Figures 3A,B**). Significance and direction following two-sample *t*-tests (CE-HC) on each pairwise correlation are depicted as the −sign(*t* val)log10(*p* val) (**Figure 3C**); the CER-AN, SMN-VN, SN-DMN, and DMN-VN connections were found to be significantly altered between two groups ($p < 0.05$) (**Figure 3D**).

TABLE 2 | Different intranetwork FC of RSNs between two groups.

Condition	RSN	Brain regions	BA	Peak *T*-scores	MNI coordinates (*x*, *y*, *z*)	Cluster size (voxels)
CE < HC	CER	Right Cerebelum_8	–	−4.6045	15, −63, −39	177
CE > HC	SMN	Bilateral postcentral gyrus	–	4.2861	24, −51, 54	152
CE < HC	AN	Right Superior Temporal Gyrus	40	−4.6977	51, −27, 18	96
CE < HC	VN	Right Middle Occipital Gyrus	19	−4.3329	39, −75, 27	88

The statistical threshold was set at the voxel level with $p < 0.01$ for multiple comparisons using Gaussian random-field theory (voxel-level $p < 0.01$, GRF correction, cluster-level $p < 0.05$). T-score represents the statistical value of peak voxel showing the differences in FC between the two groups.
CE, comitant exotropia; HC, healthy control; FC, functional connectivity; RSNs, resting-state networks; BA, Brodmann area; MNI, Montreal Neurologic Institute; CER, cerebellum network; SMN, sensorimotor network; AN, auditory network; VN, visual network.

DISCUSSION

To our knowledge, this is the first study to investigate the effects of impaired stereoscopic vision on large-scale resting-state FNC in CE patients using the ICA method. Compared with the HC group, the CE group showed increased intranetwork FC in the bilateral postcentral gyrus of the SMN; it also showed decreased intranetwork FC in the right cerebellum_8 of the CER, the right superior temporal gyrus of the AN, and the right middle occipital gyrus of the VN. Moreover, CER-AN, SMN-VN, SN-DMN, and DMN-VN connections were significantly altered between the two groups.

Altered Intranetwork Functional Connectivity in the Comitant Exotropia Group

The CE group showed decreased intranetwork FC in the right cerebellum_8 of the CER. The CER is closely related to movement and balance functions. Moreover, the cerebellum is important for controlling eye movements and binocular disparity (Gulyas and Roland, 1994; Versino et al., 1996; Beh et al., 2017). Ouyang et al. (2017) reported that comitant strabismus patients showed changes in gray matter volume in the left cerebellum. Musazadeh et al. (2004) reported that cerebellar tumors caused esotropia. Leguire et al. (2011) demonstrated that patients with idiopathic infantile nystagmus syndrome exhibited significant activation increases in the declive of the cerebellum. Consistent with these prior reports, we found that the CE group had decreased functional connectivity in the right cerebellum_8 of the CER, which might lead to impaired eye movement and binocular vision in CE patients.

Notably, the CE group exhibited increased intranetwork FC in the bilateral postcentral gyrus of the SMN. The postcentral gyrus (i.e., the sensorimotor gyrus) has an important role in proprioception, which implies involvement in providing sensory information that helps to control voluntary movement. Sweeney et al. (2007) demonstrated that sensorimotor brain systems have critical roles in eye movement control, while van Beers et al. (2001) reported that sensorimotor integration is involved in the localization of static objects during smooth pursuit eye movements. Sensorimotor function is also closely related to the formation of stereovision (Ringach et al., 1996). Here, we found that CE patients showed decreased functional connectivity within the SMN, which might lead to the impaired eye movements and stereoscopic vision observed in such patients.

The AN is located in the temporal lobe, which is involved in auditory information processing. The CE group showed decreased intranetwork FC in the right superior temporal gyrus of the AN. There are close relationships between the visual and auditory systems; cross-modal interactions between these systems have been observed in patients with vision loss (Collignon et al., 2007; Lunghi et al., 2014). Petrus et al. (2015) demonstrated that vision loss contributes to cross-modal interactions between the primary auditory and visual cortices. To our knowledge, no studies have shown that the loss of stereovision might contribute to auditory dysfunction. In the present study, the CE group showed decreased functional connectivity within the AN, which might lead to the loss of stereoscopic vision and thus contribute to auditory dysfunction. In the future, we plan to investigate the underlying neural mechanism of AN dysfunction in CE patients.

Furthermore, we found that the CE group showed decreased intranetwork FC in the right middle occipital gyrus of the VN. The VN is located in the occipital cortex, which is involved in visual information processing. Wong et al. (2005) revealed metabolic suppression in the visual cortices of strabismic macaques (Economides et al., 2021). Additionally, Yan et al. (2019) reported that CE patients had increased functional connectivity between the primary visual cortex and other brain areas. Yang et al. (2014) found that the infantile esotropia group showed lower BOLD signals in the left cingulate gyrus, bilateral precuneus, and left angular gyrus during a visual stimulus, compared with controls. Yan et al. (2010) reported that adult strabismus patients had decreased white matter volumes in the right middle occipital gyrus and right occipital lobe/cuneus. Consistent with these prior reports, we also found that the CE group showed decreased functional connectivity within the VN.

Finally, FNC analysis showed that CER-AN, SMN-VN, SN-DMN, and DMN-VN connections were significantly altered between the two groups. We speculate that altered interactions among these networks might lead to RSN compensation in CE patients with stereoscopic vision loss.

Some limitations should be acknowledged in this study. First, the sample size of CE patients in our study was small. Second, RSN values based on fMRI signals would still be affected by physiological noise, such as cardiac and respiratory activity.

CONCLUSION

Comitant exotropia patients had abnormal brain networks related to the CER, SMN, AN, and VN. Our results offer

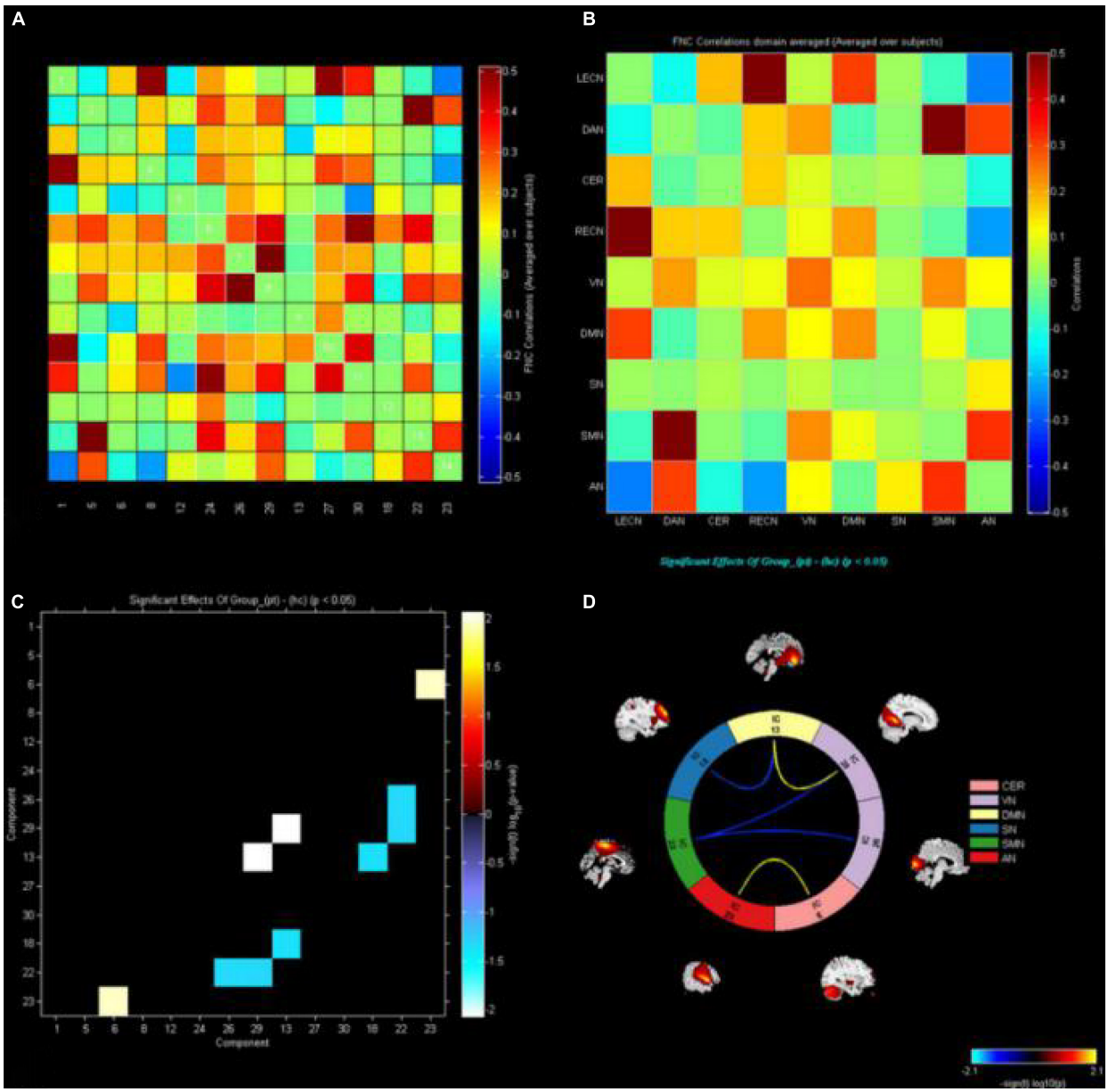

FIGURE 3 | The functional connectivity correlation matrix between all RSNs. The color scale represents the value of the correlations. Warm color represents positive correlations, and cold color represents anti–correlations. The markers indicate significant functional connection between networks IC1(LECN), IC5(DAN), IC6(CER), IC8(RECN), IC12(VN1), C13(DMN1), IC18(SN), IC22(SMN), IC23(AN), IC24(VN2), IC26(VN3), IC27(DMN2), IC29(VN4), and IC30 (DMN3) ($p < 0.05$ uncorrected). **(A,B)** Matrix shows differences of internetwork functional connectivity between two groups. **(C)** Significance and direction following two–sample's *t*–tests (CE–HC) on each pairwise correlation are depicted as the –sign (*t* value) log10 (*p* value); the CER-AN, SMN-VN, SN-DMN, and DMN-VN connections were found to be significantly altered between two groups ($p < 0.05$). **(D)**. CE, comitant exotropia; HC, healthy control; lECN, left executive control network; DAN, dorsal attention network; CER, cerebellum network; RECN, right executive control network; VN, visual network; DMN, default mode network; SN, salience network; SMN, sensorimotor network; AN, auditory network.

important insights into the neural mechanisms of eye movements and stereoscopic vision dysfunction in CE patients.

DATA AVAILABILITY STATEMENT

The raw data supporting the conclusions of this article will be made available by the authors, without undue reservation.

ETHICS STATEMENT

The studies involving human participants were reviewed and approved by the Medical Ethics Committee of the Jiangxi Provincial People's Hospital Affiliated to Nanchang University. Written informed consent to participate in this study was provided by the participants' legal guardian/next of kin.

AUTHOR CONTRIBUTIONS

HJ, R-BC, Y-LZ, P-HL, and XH contributed to data collection and statistical analyses and wrote the manuscript and designed the protocol, and contributed to the MRI analysis. HJ, R-BC, and Y-LZ designed the study and oversaw all clinical aspects of study conduct and manuscript preparation. All authors contributed to the article and approved the submitted version.

ACKNOWLEDGMENTS

We acknowledge the assistance provided by the Natural Science Foundation of Jiangxi Province (20192BAB205048 and 20212BAB216058), the National Nature Science Foundation of China (grant no. 81060080), and the Jiangxi Provincial Health Technology Project (202210012).

REFERENCES

Abed Rabbo, F., Koch, G., Lefevre, C., and Seizeur, R. (2018). Stereoscopic visual area connectivity: a diffusion tensor imaging study. *Surg. Radiol. Anat.* 40, 1197–1208. doi: 10.1007/s00276-018-2076-3

Auer, D. P. (2008). Spontaneous low-frequency blood oxygenation level-dependent fluctuations and functional connectivity analysis of the 'resting' brain. *Magn. Reson. Imaging* 26, 1055–1064. doi: 10.1016/j.mri.2008.05.008

Backus, B. T., Fleet, D. J., Parker, A. J., and Heeger, D. J. (2001). Human cortical activity correlates with stereoscopic depth perception. *J. Neurophysiol.* 86, 2054–2068. doi: 10.1152/jn.2001.86.4.2054

Ban, H., Preston, T. J., Meeson, A., and Welchman, A. E. (2012). The integration of motion and disparity cues to depth in dorsal visual cortex. *Nat. Neurosci.* 15, 636–643. doi: 10.1038/nn.3046

Beh, S. C., Frohman, T. C., and Frohman, E. M. (2017). Cerebellar Control of Eye Movements. *J. Neuroophthalmol.* 37, 87–98. doi: 10.1097/WNO.0000000000000456

Biswal, B., Yetkin, F. Z., Haughton, V. M., and Hyde, J. S. (1995). Functional connectivity in the motor cortex of resting human brain using echo-planar MRI. *Magn. Reson. Med.* 34, 537–541. doi: 10.1002/mrm.1910340409

Chen, H., Shi, M., Zhang, H., Zhang, Y. D., Geng, W., Jiang, L., et al. (2019). Different patterns of functional connectivity alterations within the default-mode network and sensorimotor network in basal ganglia and pontine stroke. *Med. Sci. Monit.* 25, 9585–9593. doi: 10.12659/MSM.918185

Chen, N., Chen, Z., and Fang, F. (2020). Functional specialization in human dorsal pathway for stereoscopic depth processing. *Exp. Brain Res.* 238, 2581–2588. doi: 10.1007/s00221-020-05918-4

Chopin, A., Chan, S. W., Guellai, B., Bavelier, D., and Levi, D. M. (2019). Binocular non-stereoscopic cues can deceive clinical tests of stereopsis. *Sci. Rep.* 9:5789. doi: 10.1038/s41598-019-42149-2

Collignon, O., Lassonde, M., Lepore, F., Bastien, D., and Veraart, C. (2007). Functional cerebral reorganization for auditory spatial processing and auditory substitution of vision in early blind subjects. *Cereb. Cortex* 17, 457–465. doi: 10.1093/cercor/bhj162

Damoiseaux, J. S., Rombouts, S. A., Barkhof, F., Scheltens, P., Stam, C. J., Smith, S. M., et al. (2006). Consistent resting-state networks across healthy subjects. *Proc. Natl. Acad. Sci. U. S. A.* 103, 13848–13853. doi: 10.1073/pnas.0601417103

Du, Y., Pearlson, G. D., Liu, J., Sui, J., Yu, Q., He, H., et al. (2015). A group ICA based framework for evaluating resting fMRI markers when disease categories are unclear: application to schizophrenia, bipolar, and schizoaffective disorders. *Neuroimage* 122, 272–280. doi: 10.1016/j.neuroimage.2015.07.054

Economides, J. R., Adams, D. L., and Horton, J. C. (2021). Interocular suppression in primary visual cortex in strabismus. *J. Neurosci.* 41, 5522–5533. doi: 10.1523/JNEUROSCI.0044-21.2021

Feng, X., Zhang, X., and Jia, Y. (2015). Improvement in fusion and stereopsis following surgery for intermittent exotropia. *J. Pediatr. Ophthalmol. Strabismus* 52, 52–57. doi: 10.3928/01913913-20141230-08

Gillebert, C. R., Schaeverbeke, J., Bastin, C., Neyens, V., Bruffaerts, R., De Weer, A. S., et al. (2015). 3D shape perception in posterior cortical atrophy: a visual neuroscience perspective. *J. Neurosci.* 35, 12673–12692. doi: 10.1523/JNEUROSCI.3651-14.2015

Goncalves, N. R., Ban, H., Sanchez-Panchuelo, R. M., Francis, S. T., Schluppeck, D., and Welchman, A. E. (2015). 7 tesla FMRI reveals systematic functional organization for binocular disparity in dorsal visual cortex. *J. Neurosci.* 35, 3056–3072. doi: 10.1523/JNEUROSCI.3047-14.2015

Govindan, M., Mohney, B. G., Diehl, N. N., and Burke, J. P. (2005). Incidence and types of childhood exotropia: a population-based study. *Ophthalmology* 112, 104–108. doi: 10.1016/j.ophtha.2004.07.033

Gulyas, B., and Roland, P. E. (1994). Processing and analysis of form, colour and binocular disparity in the human brain: functional anatomy by positron emission tomography. *Eur. J. Neurosci.* 6, 1811–1828. doi: 10.1111/j.1460-9568.1994.tb00574.x

Kong, F., Xue, S., and Wang, X. (2016). Amplitude of low frequency fluctuations during resting state predicts social well-being. *Biol. Psychol.* 118, 161–168. doi: 10.1016/j.biopsycho.2016.05.012

Leguire, L. E., Kashou, N. H., Fogt, N., Smith, M. A., Lewis, J. R., Kulwin, R., et al. (2011). Neural circuit involved in idiopathic infantile nystagmus syndrome based on FMRI. *J. Pediatr. Ophthalmol. Strabismus* 48, 347–356. doi: 10.3928/01913913-20110118-03

Li, Y., Zhang, C., Hou, C., Yao, L., Zhang, J., and Long, Z. (2017). Stereoscopic processing of crossed and uncrossed disparities in the human visual cortex. *BMC Neurosci.* 18:80. doi: 10.1186/s12868-017-0395-7

Lunghi, C., Morrone, M. C., and Alais, D. (2014). Auditory and tactile signals combine to influence vision during binocular rivalry. *J. Neurosci.* 34, 784–792. doi: 10.1523/JNEUROSCI.2732-13.2014

Musazadeh, M., Hartmann, K., and Simon, F. (2004). Late onset esotropia as first symptom of a cerebellar tumor. *Strabismus* 12, 119–123. doi: 10.1080/09273970490517557

Ohzawa, I., DeAngelis, G. C., and Freeman, R. D. (1990). Stereoscopic depth discrimination in the visual cortex: neurons ideally suited as disparity detectors. *Science* 249, 1037–1041. doi: 10.1126/science.2396096

Oishi, H., Takemura, H., Aoki, S. C., Fujita, I., and Amano, K. (2018). Microstructural properties of the vertical occipital fasciculus explain the variability in human stereoacuity. *Proc. Natl. Acad. Sci. U. S. A.* 115, 12289–12294. doi: 10.1073/pnas.1804741115

Oke, O. O., Magony, A., Anver, H., Ward, P. D., Jiruska, P., Jefferys, J. G., et al. (2010). High-frequency gamma oscillations coexist with low-frequency gamma oscillations in the rat visual cortex in vitro. *Eur. J. Neurosci.* 31, 1435–1445. doi: 10.1111/j.1460-9568.2010.07171.x

Ouyang, J., Yang, L., Huang, X., Zhong, Y. L., Hu, P. H., Zhang, Y., et al. (2017). The atrophy of white and gray matter volume in patients with comitant strabismus: evidence from a voxel-based morphometry study. *Mol. Med. Rep.* 16, 3276–3282. doi: 10.3892/mmr.2017.7006

Parker, A. J. (2007). Binocular depth perception and the cerebral cortex. *Nat. Rev. Neurosci.* 8, 379–391. doi: 10.1038/nrn2131

Petrus, E., Rodriguez, G., Patterson, R., Connor, B., Kanold, P. O., and Lee, H. K. (2015). Vision loss shifts the balance of feedforward and intracortical circuits in opposite directions in mouse primary auditory and visual cortices. *J. Neurosci.* 35, 8790–8801. doi: 10.1523/JNEUROSCI.4975-14.2015

Prins, D., Jansonius, N. M., and Cornelissen, F. W. (2017). Loss of binocular vision in monocularly blind patients causes selective degeneration of the superior lateral occipital cortices. *Invest. Ophthalmol. Vis. Sci.* 58, 1304–1313. doi: 10.1167/iovs.16-20404

Ringach, D. L., Hawken, M. J., and Shapley, R. (1996). Binocular eye movements caused by the perception of three-dimensional structure from motion. *Vision Res.* 36, 1479–1492. doi: 10.1016/0042-6989(95)00285-5

Shirer, W. R., Ryali, S., Rykhlevskaia, E., Menon, V., and Greicius, M. D. (2012). Decoding subject-driven cognitive states with whole-brain connectivity patterns. *Cereb. Cortex* 22, 158–165. doi: 10.1093/cercor/bhr099

Smith, S. M., Fox, P. T., Miller, K. L., Glahn, D. C., Fox, P. M., Mackay, C. E., et al. (2009). Correspondence of the brain's functional architecture during activation

and rest. *Proc. Natl. Acad. Sci. U. S. A.* 106, 13040–13045. doi: 10.1073/pnas.0905267106

Sweeney, J. A., Luna, B., Keedy, S. K., McDowell, J. E., and Clementz, B. A. (2007). fMRI studies of eye movement control: investigating the interaction of cognitive and sensorimotor brain systems. *Neuroimage* 36, T54–T60. doi: 10.1016/j.neuroimage.2007.03.018

van Beers, R. J., Wolpert, D. M., and Haggard, P. (2001). Sensorimotor integration compensates for visual localization errors during smooth pursuit eye movements. *J. Neurophysiol.* 85, 1914–1922. doi: 10.1152/jn.2001.85.5.1914

van de Ven, V. G., Formisano, E., Prvulovic, D., Roeder, C. H., and Linden, D. E. (2004). Functional connectivity as revealed by spatial independent component analysis of fMRI measurements during rest. *Hum. Brain Mapp.* 22, 165–178. doi: 10.1002/hbm.20022

Van Dijk, K. R., Sabuncu, M. R., and Buckner, R. L. (2012). The influence of head motion on intrinsic functional connectivity MRI. *Neuroimage* 59, 431–438. doi: 10.1016/j.neuroimage.2011.07.044

Versino, M., Hurko, O., and Zee, D. S. (1996). Disorders of binocular control of eye movements in patients with cerebellar dysfunction. *Brain* 119, 1933–1950. doi: 10.1093/brain/119.6.1933

Wang, D., Qin, W., Liu, Y., Zhang, Y., Jiang, T., and Yu, C. (2014). Altered resting-state network connectivity in congenital blind. *Hum. Brain Mapp.* 35, 2573–2581. doi: 10.1002/hbm.22350

Wong, A. M., Burkhalter, A., and Tychsen, L. (2005). Suppression of metabolic activity caused by infantile strabismus and strabismic amblyopia in striate visual cortex of macaque monkeys. *J. AAPOS* 9, 37–47. doi: 10.1016/j.jaapos.2004.09.004

Yan, C. G., Wang, X. D., Zuo, X. N., and Zang, Y. F. (2016). DPABI: data processing & analysis for (resting-state) brain imaging. *Neuroinformatics* 14, 339–351. doi: 10.1007/s12021-016-9299-4

Yan, X., Lin, X., Wang, Q., Zhang, Y., Chen, Y., Song, S., et al. (2010). Dorsal visual pathway changes in patients with comitant extropia. *PLoS One* 5:e10931. doi: 10.1371/journal.pone.0010931

Yan, X., Wang, Y., Xu, L., Liu, Y., Song, S., Ding, K., et al. (2019). Altered functional connectivity of the primary visual cortex in adult comitant strabismus: a resting-state functional MRI study. *Curr. Eye Res.* 44, 316–323. doi: 10.1080/02713683.2018.1540642

Yang, X., Zhang, J., Lang, L., Gong, Q., and Liu, L. (2014). Assessment of cortical dysfunction in infantile esotropia using fMRI. *Eur. J. Ophthalmol.* 24, 409–416. doi: 10.5301/ejo.5000368

Zheng, H., Yao, L., Chen, M., and Long, Z. (2020). 3D contrast image reconstruction from human brain activity. *IEEE Trans. Neural Syst. Rehabil. Eng.* 28, 2699–2710. doi: 10.1109/TNSRE.2020.3035818

Zuo, X. N., Kelly, C., Adelstein, J. S., Klein, D. F., Castellanos, F. X., and Milham, M. P. (2010). Reliable intrinsic connectivity networks: test-retest evaluation using ICA and dual regression approach. *Neuroimage* 49, 2163–2177. doi: 10.1016/j.neuroimage.2009.10.080

Conflict of Interest: The authors declare that the research was conducted in the absence of any commercial or financial relationships that could be construed as a potential conflict of interest.

Publisher's Note: All claims expressed in this article are solely those of the authors and do not necessarily represent those of their affiliated organizations, or those of the publisher, the editors and the reviewers. Any product that may be evaluated in this article, or claim that may be made by its manufacturer, is not guaranteed or endorsed by the publisher.

frontiers | Frontiers in Human Neuroscience

ORIGINAL RESEARCH
published: 15 June 2022
doi: 10.3389/fnhum.2022.862420

Retroauricular/Transcranial Color-Coded Doppler Ultrasound Approach in Junction With Ipsilateral Neck Compression on Real-Time Hydroacoustic Variation of Venous Pulsatile Tinnitus

Xiuli Gao[1†], Yue-Lin Hsieh[2,3†], Xing Wang[4] and Wuqing Wang[2,3]*

[1] Department of Radiology, Eye Ear Nose & Throat Hospital, Fudan University, Shanghai, China, [2] Department of Otology and Skull Base Surgery, Eye Ear Nose & Throat Hospital, Fudan University, Shanghai, China, [3] NHC Key Laboratory of Hearing Medicine, Shanghai, China, [4] School of Mechanical and Automotive Engineering, Xiamen University of Technology, Xiamen, China

OPEN ACCESS

Edited by:
Jae-Jin Song,
Seoul National University Bundang Hospital, South Korea

Reviewed by:
Aike Qiao,
Beijing University of Technology, China
Chin-Kuo Chen,
Linkou Chang Gung Memorial Hospital, Taiwan

***Correspondence:**
Wuqing Wang
wwuqing@eent.shmu.edu.cn

[†]These authors share first authorship

Specialty section:
This article was submitted to Sensory Neuroscience, a section of the journal Frontiers in Human Neuroscience

Received: 25 January 2022
Accepted: 12 May 2022
Published: 15 June 2022

Citation:
Gao X, Hsieh Y-L, Wang X and Wang W (2022) Retroauricular/Transcranial Color-Coded Doppler Ultrasound Approach in Junction With Ipsilateral Neck Compression on Real-Time Hydroacoustic Variation of Venous Pulsatile Tinnitus. Front. Hum. Neurosci. 16:862420. doi: 10.3389/fnhum.2022.862420

Alterations in dural venous sinus hemodynamics have recently been suggested as the major contributing factors in venous pulsatile tinnitus (PT). Nevertheless, little is known about the association between real-time alterations in hemodynamics and the subjective perception of venous PT. This study aimed to investigate the hydroacoustic correlations among diverticular vortices, mainstream sinus flow, and PT using various Doppler ultrasound techniques. Nineteen venous PT patients with protrusive diverticulum were recruited. The mainstream sinus and diverticular hemodynamics before and after ipsilateral internal jugular vein (IJV) compression were investigated using an innovative retroauricular color-coded Doppler (RCCD) method to examine the correlation between the disappearance of PT and hemodynamic alterations. To reveal the hydroacoustic characteristics of disparate segments of venous return, a computational fluid dynamics (CFD) technique combined with the transcranial color-coded Doppler method was performed. When the ipsilateral IJV was compressed, PT disappeared, as the mean velocity of mainstream sinus flow and diverticular vortex decreased by 51.2 and 50.6%, respectively. The vortex inside the diverticulum persisted in 18 of 19 subjects. The CFD simulation showed that the flow amplitude generated inside the transverse–sigmoid sinus was segmental, and the largest flow amplitude difference was 20.5 dB. The difference in flow amplitude between the mainstream sinus flow and the diverticular flow was less than 1 dB. In conclusion, the sensation of PT is closely associated with the flow of kinetic energy rather than the formation of a vortex, whereby the amplitude of PT is correlated to the magnitude of the flow velocity and pressure gradient. Additionally, the range of velocity reduction revealed by the RCCD method may serve as a presurgical individual baseline curative marker that may potentially optimize the surgical outcomes.

Keywords: pulsatile tinnitus, Doppler ultrasound, transcranial Doppler (TCD) ultrasonography, sigmoid sinus wall anomalies, diverticulum, computational fluid dynamics

INTRODUCTION

Vascular pulsatile tinnitus (PT) is an abnormal perception of pulse-synchronous vascular somatosounds (Kim et al., 2016; Lee et al., 2020). Venous PT represents the largest demographic among the vascular origins of PT (Dong et al., 2015). Venous PT is characterized by the reduction or elimination of a vascular sound when the ipsilateral internal jugular vein (IJV) is compressed (Mattox and Hudgins, 2008; Grewal et al., 2014). In addition, anatomical abnormalities related to the structural integrity of the sigmoid plate and the vascular shape are often revealed using imaging modalities (Dong et al., 2015; Cummins et al., 2021; Ding et al., 2021).

Sigmoid sinus wall anomalies (SSWAs) are the most identified findings in patients with venous PT (Dong et al., 2015). SSWAs refer to sigmoid sinus wall dehiscence and sigmoid sinus diverticulum. Without the bolster of the overlying sigmoid plate, a diverticulum forms when the sigmoid sinus vascular wall protrudes into the mastoid air cells and/or the mastoid cortex (Eisenman et al., 2018; Mu et al., 2022). Given the increase in flow velocity, sinus flow carries higher kinetic energy in the transverse–sigmoid junction region after releasing from transverse sinus stenosis (TSS; Hewes et al., 2020; Zhao et al., 2021a). A high degree of TSS can further exacerbate the *trans*-stenotic pressure gradient of the transverse sinus, which impairs intracranial pressure that may be less relevant to the production of PT (Zhao et al., 2021a,b). Additionally, studies have suggested that high wall pressure and wall shear stress induced by TSS may underpin the development of SSWAs (Hsieh and Wang, 2020; Mu et al., 2022), and the recent discovery of bone remodeling of the dehiscent sigmoid plate after excluding hemodynamic pathologies *via* endoluminal stenting surgery supports this postulation (Qiu et al., 2021a).

Despite the diverse anatomical anomalies, ipsilateral IJV compression has served as a diagnostic criterion and surgical indication for venous PT (Grewal et al., 2014; Guo and Wang, 2015; Li et al., 2021). This maneuver pinpoints a cause-and-effect relationship between the restriction of venous outflow and the diminution of PT (Wang et al., 2019; Hsieh and Wang, 2020), even though the correlation between PT symptomology and sinus hemodynamics has not been quantified hitherto. In addition to the volumetric asymmetry and high sinus flow velocity that are commonly discovered in PT subjects with SSWAs, some authors also speculated that a regional complex vortical flow structure might engender PT (Hsieh and Wang, 2020; Mu et al., 2020; Li et al., 2021). Considering that (a) the velocity profile varies among individuals with venous PT and (b) vortical flow structure emanates from the transverse–sigmoid junction with or without diverticulum (Mu et al., 2020; Ding et al., 2021; Hsieh et al., 2021a; Li et al., 2021; Qiu et al., 2021b), it is, however, unclear how the velocity and diverticular vortex affect the hydroacoustic production of PT and how fluctuations in the cross-sectional area of the transverse–sigmoid sinus lumen affect the flow acoustics.

Previous studies have implemented a Doppler ultrasound to capture *in vivo* hydroacoustic characteristics of PT by sensing the bilateral IJV outflow, in which the motion of IJV outflow displayed a high degree of resemblance to the patient's PT (Hsieh et al., 2021b). As the Doppler sampling depth and volume are adjustable, the vascular Doppler ultrasound has the advantage over unfolding the hemodynamics and flow acoustics at different regions of interest in simultaneity. Henceforth, the transcranial Doppler examination of the transverse–sigmoid sinus system may shed light on the hydroacoustic characteristics of mainstream sinus flow and diverticular vortex, which has not been attempted on subjects with venous PT in previous literature.

This study aimed to crystallize the quantitative correlation between PT and hemodynamics by combining the application of various Doppler techniques. Furthermore, we proposed the retroauricular color-coded Doppler (RCCD) ultrasound technique that allows a short-range insonation of the mainstream sinus and diverticular flows *via* the eroded mastoid cortical bone window. This technique has not been documented in previous literature and can be implemented in junction with ipsilateral IJV compression to unravel the hydroacoustic characteristics of mainstream sinus flow and diverticular vortex. Additionally, quantification of the simultaneous reduction of PT and outflow velocity may serve as a prospective indicator for surgical intervention, which can help clinicians establish the correct scope of surgery and optimize therapeutic outcomes.

MATERIALS AND METHODS

Patient Clinical Data and Study Design

This retrospective study recruited 19 venous PT patients with a protrusive diverticulum who underwent RCCD ultrasound examination. All participants were treated at the Otology and Skull Base Surgery Center of the Eye, Ear, Nose, and Throat Hospital at Fudan University from October 2020 to April 2022. The clinical diagnosis of venous PT included prudent cervical Doppler ultrasound and IJV compression, a water occlusion test, and radiological imaging [computed tomography (CT)/contrast-enhanced CT venogram and magnetic resonance (MR) venogram/contrast-enhanced MR venogram]. The inclusion criteria were strict radiological evidence of SSWAs and a positive response to IJV compression guided by color-coded Doppler visualization. The exclusion criteria included a non-venous origin of PT (arterial and arteriovenous causes of PT), PT secondary to intracranial/cervical neoplasms, and systemic diseases such as anemia and hyperthyroidism.

Schematic diagrams of the RCCD and transcranial color-coded Doppler (TCCD) techniques and their relative anatomical structures are shown in **Figure 1**. The diagnosis of venous PT was ascertained by the reduction or disappearance of the PT during IJV compression. SSWAs were defined based on the criteria described by Eisenman et al. (2018): (1) dehiscence: consecutive three 0.6 mm axial CT cuts in the absence of a sigmoid plate with an osseous structure overlying the sigmoid sinus vessel wall; and (2) diverticulum: outward protrusion of an irregularly shaped sigmoid sinus vascular wall into the mastoid air cells or the mastoid cortex. In the TSS measurement, the largest and smallest cross-sectional areas of the transverse sinus lumen on each side were measured between the proximal end (the intersecting point of the confluens sinuum and the superior

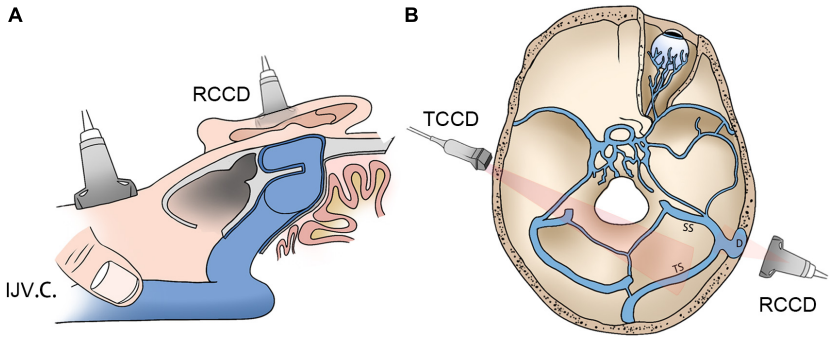

FIGURE 1 | Schematic diagrams of RCCD and TCCD application. **(A)** Assessment of hydroacoustics and PT using RCCD and IJV compression. **(B)** The TCCD technique for hemodynamic assessment of contralateral transverse sinus. RCCD, retroauricular color-coded Doppler; TCCD, transcranial color-coded Doppler; and PT, pulsatile tinnitus; IJV.C., internal jugular vein compression.

sagittal sinus) and the distal end (0.5 mm prior to the transverse–sigmoid junction) using MR venogram images *via* the software Mimics 19.0 (Materialise, Belgium). The normalized degree of TSS was scaled based on [Eq. (1)]:

$$TSS_{normalized} = \frac{cross.area_{max} - cross.area_{min}}{cross.area_{max}}, \quad (1)$$

where cross.area$_{max}$ and cross.area$_{min}$ indicate the largest and smallest cross-sectional areas of the ipsilateral transverse sinus lumen, respectively.

The index of TSS (ITSS) was used based on the Carvalho criteria (Da Silveira Carvalho et al., 2017) [Eq. (2)]:

$$ITSS = \text{degree of left } TSS \times \text{degree of right} TSS. \quad (2)$$

The degree of TSS was categorized into five distinctive scorings, where a score of 0 indicated normal, 1 indicated stenosis up to one-third (<33%), 2 indicated stenosis between one-third and two-thirds (33–66%), 3 indicated stenosis over two-thirds (>66%), and 4 indicated transverse sinus hypoplasia. Transverse sinus hypoplasia was defined as stenosis of 40% of the entire length of the transverse sinus (Durst et al., 2016).

Retroauricular Color-Coded Doppler Technique and Modulation of Pulsatile Tinnitus/Hemodynamics

An innovative RCCD technique was proposed to examine the mainstream sinus and diverticular flow characteristics at the transverse–sigmoid junction. RCCD was performed using the LISENDO 880 ultrasound system and Arietta 60 ultrasound system (Hitachi Aloka Medical Ltd., Japan) with S121 (5–1 MHz) and L441 (12–2 MHz) transducers in a silent room. Participants were asked to lie in a supine position. The transducer was placed in the retroauricular skin tissue above the diverticulum for insonation. Prior to Doppler insonation, sonologists carefully measured the 3D shape, size, and depth of the diverticulum and its relative anatomical landmarks using CT and MR venography to localize the diverticulum.

To reveal mainstream sinus and diverticular hydroacoustics, the coronal and sagittal footage of the diverticulum can be visualized using the B-mode (flow and anatomical features are shown in **Figure 2**). Due to the heterogeneity of participants, a thin layer of the remnant bony structure of the mastoid may present as the second layer of high-signal intensity interpolated between the lateral diverticulum and the medial mainstream. This can be a helpful reference landmark for differentiating the diverticulum from mainstream sinus lumen. After insonating using the color mapping mode, the mainstream sinus flow and diverticular flows can be appreciated, and the range and border of the sinus flow can be cross-referenced using CT/MR venogram images. Notably, the relative position of the mainstream sinus flow and the diverticular flow depends on the anterosuperior, anteroinferior, or lateral direction of the diverticular protrusion. Once the mainstream sinus and diverticular flows were both detected in simultaneity, the location of insonation was unchanged throughout all procedures of measurement. Following the initial RCCD examination, modulation of IJV outflow was performed by the first co-author (Y-LH) to assess changes in the intrasinus hemodynamics and PT. To obtain hemodynamics when PT subsides, the Doppler velocity spectra and hemodynamic parameters were acquired after the reduction of velocity stabilized at least five cardiac cycles during the ipsilateral IJV compression. The compression time was controlled within 15 s to prevent any potential adverse effects. The sampling volume was set within the detected vessel and adjusted from 1 to 3 mm. The depth was adjusted between 3 and 4.5 cm based on the intrasubject variability. The velocity range was modified based upon the individual sinus flow velocity. The transducer frequency was 4.0∼5.22 MHz. The color-Doppler gain was then adjusted to range from 20–120 until the pulsatile flow could be fully observed, while the surrounding subcutaneous tissue remained virtually free of color. The mean flow velocity (V_{mn}), peak velocity (V_{max}), flow volume, resistive index, and pulsatility index at the transverse–sigmoid junction were obtained.

Bilateral Jugular Vein Hemodynamics

The procedures used to obtain bilateral cervical hemodynamics were identical to our previously described methods

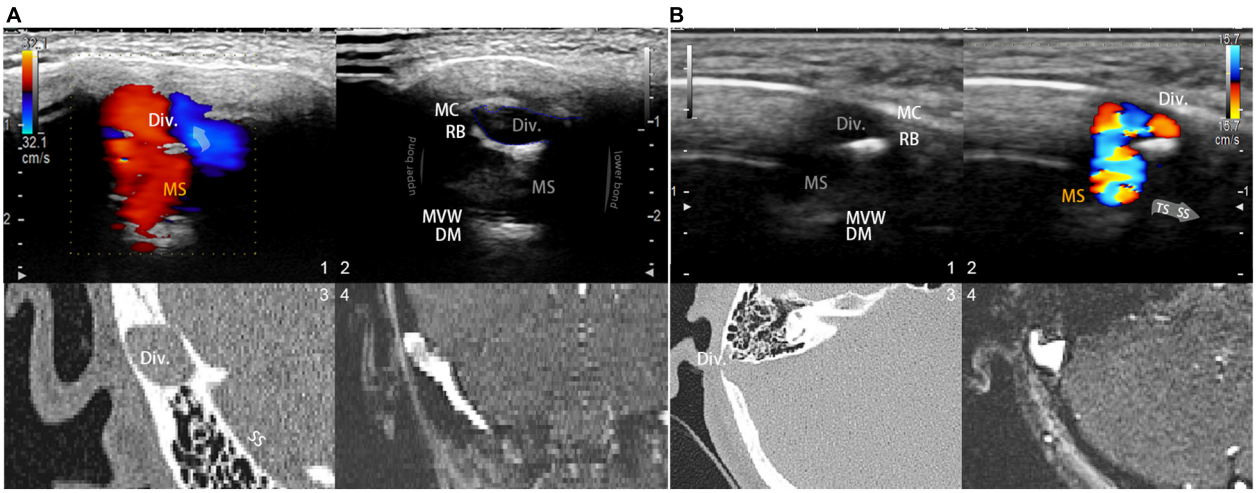

FIGURE 2 | Visualization and insights of the RCCD ultrasound method. (**A**; 1) Coronal RCCD continuous wave mode view of the mainstream sinus and diverticular flows. The transparent arrow indicates mainstream sinus flow diversion into the diverticulum. Div. indicates diverticulum; MS indicates mainstream sinus flow. (2) A 2D-planar cross-sectional view of the diverticulum and the mainstream sinus anatomical structures. MC indicates mastoid cortex; RB indicates the remnant mastoid bone; MVW indicates the medial vascular wall; and DM indicates the layers of dura mater. (3) Coronal CT view of the diverticulum and sigmoid sinus corresponding to the representative 2D ultrasonographic view. (4) Coronal 2D time-of-flight magnetic resonance imaging of the diverticulum and sigmoid sinus corresponding to the representative 2D ultrasonographic view. **(B)** A 2D-planar axial view of the diverticulum and mainstream sinus anatomical structures. MC indicates the mastoid cortex; RB indicates the remnant mastoid bone; MVW indicates the medial vascular wall; and DM indicates the layers of the dura mater. (1) A 2D-planar cross-sectional view of the diverticulum and mainstream sinus anatomical structures. MC indicates the mastoid cortex; RB indicates the remnant mastoid bone; MVW indicates the medial vascular wall; and DM indicates the layers of the dura mater. (2) Axial RCCD continuous wave mode view of the mainstream sinus and diverticular flows. The gray arrow indicates the flow direction from the transverse sinus to the sigmoid sinus. Div. indicates diverticulum; MS indicates mainstream sinus flow. (3) An axial CT view of the diverticulum and sigmoid sinus corresponding to the representative 2D ultrasonographic view. (4) Axial 2D time-of-flight magnetic resonance imaging of the diverticulum and sigmoid sinus corresponding to the representative 2D ultrasonographic view.

(Hsieh et al., 2021b). In brief, the hemodynamics of the upper bilateral IJV were gaged at the mandibular region at the level of the skull base using a sonographic transducer L441 with a center frequency of 2–12 MHz. Bilateral hemodynamic parameters were obtained, including the V_{mn}, V_{max}, flow volume, resistive index, and pulsatility index.

Transcranial Color-Coded Doppler Technique

A LISENDO 880 ultrasound system (Hitachi Aloka Medical Ltd., Japan) with transducer S121 was used to measure the hemodynamics of the ipsilateral transverse sinus. A contralateral bone window was used to examine the ipsilateral transverse sinus. The contralateral skeletal contour became visible after increasing the depth of the B-mode. A low-flow-sensitive color program with a low-wall-filter setting was used. The depth was adjusted approximately between 10 and 15 cm based on the individual differences. The velocity range of detection was adjusted approximately from 0 to 66.84 cm/s based on individual sinus flow velocity. The sample volume was set from 1 to 3 mm based on the width of the detected vessel, as appropriate. The transducer frequency ranged approximately from 1.5 to 1.88 MHz, and the color gain was modified between 20–120 until the contour of transverse sinus flow can be fully appreciated. To locate the transverse sinus using the contralateral temporal bone window, the great cerebral vein is instantly discovered behind the pineal gland, where the rostral part of the superior sagittal sinus can be successively exposed. The straight sinus is exposed by tilting the transducer upward to align the insonation plane with the apex of the cerebellar tentorium. The torcular herophili can be found by tracing the course of the straight sinus that drains posteriorly into the occipital region. Consequently, the transverse sinus is located. Doppler examination of the ipsilateral transverse–sigmoid sinus is demonstrated in **Figure 3**.

Hydroacoustic Computational Fluid Dynamics Simulation

To demonstrate and compare the ipsilateral transverse–sigmoid sinus flow and acoustic fields to the Doppler results, the computational fluid dynamics (CFD) technique was implemented in a participant with a complete proximal TCCD/RCCD sinus flow profile (case 3). Reconstruction of the participant's 3D vascular models was based on patient-specific MR venogram images using Mimics 19.0 and 3-Matic 11.0 (Materialise, Belgium), analogous to our previously described methods (Hsieh and Wang, 2020). The contralateral transverse–sigmoid sinus and branches of the sinus were removed.

For the simulation of the flow field, a total of 456,231 elements were established using ANSA version 22.0.1 (BETA CAE Systems), in which 10 layers with a boundary layer thickness of 0.4 mm were created for the flow field. There were 63,506 elements where three layers with a boundary layer thickness of 0.1 mm were established for the acoustic simulation. The outlet

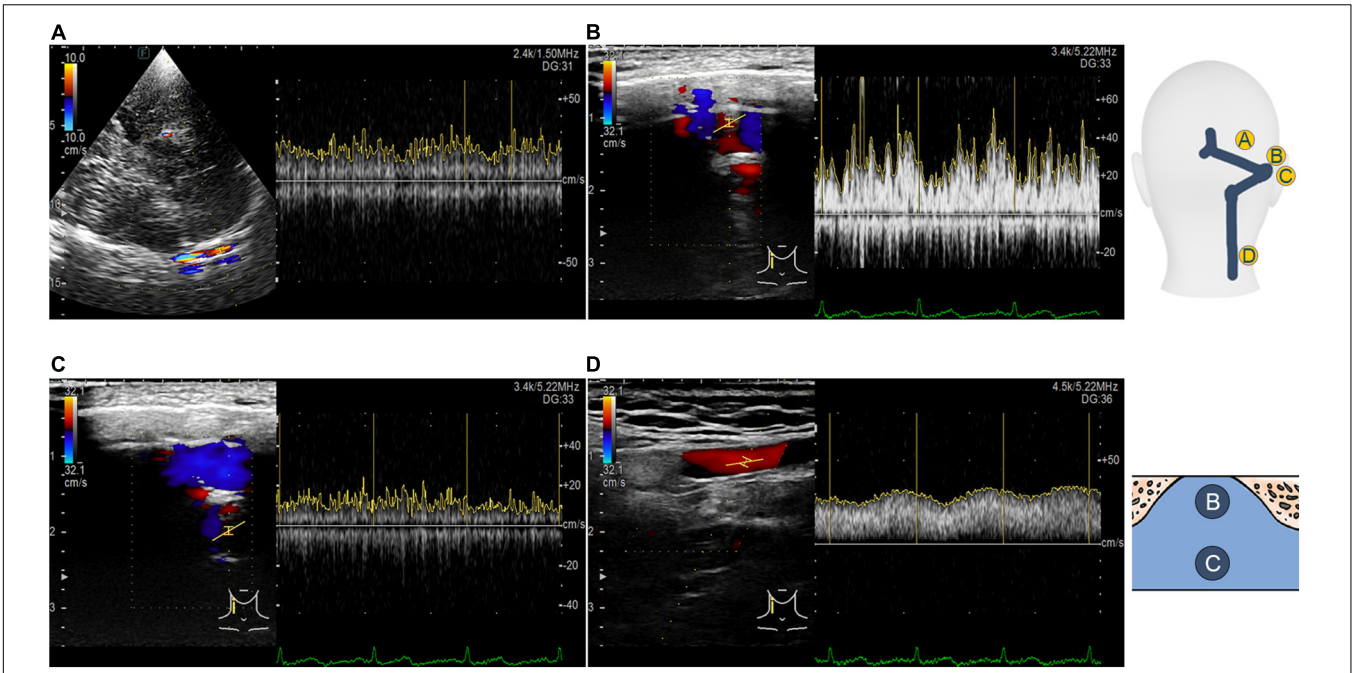

FIGURE 3 | Transcranial, retroauricular, and cervical color-coded Doppler methods to assess hydroacoustics of the transverse–sigmoid sinus system. **(A)** Visualization and velocity spectrum of the proximal transverse sinus flow using the TCCD. **(B)** Visualization and velocity spectrum of the diverticular flow using the RCCD. **(C)** Visualization and velocity spectrum of the mainstream intrasinus flow using the RCCD. **(D)** Visualization and velocity spectrum of the upper internal jugular flow using the RCCD.

pressure was set to zero. The flow velocity inlet was set based on the TCCD flow spectrum. The continuity equation and Navier–Stokes equations [Eqs (3, 4)] were solved using the transient laminar method with the software Star-CCM+ 2020 (Siemens, Germany):

$$\nabla \cdot \mathbf{u} = 0 \tag{3}$$

$$\rho \frac{\partial \mathbf{u}}{\partial t} + \rho \mathbf{u} \cdot \nabla \mathbf{u} = -\nabla p + \mu \nabla^2 \mathbf{u}, \tag{4}$$

where $\mathbf{u}$ is the velocity vector of the incompressible Newtonian blood flow, the blood density ρ is 1,050 kg/m^3, and the dynamic viscosity μ is 0.00345 Pa s. The results of the grid independence tests are shown in **Table 1**. The average velocity of the IJV outflow was selected as the criterion for generating a sufficient grid size and number. The relative error of average outflow velocity was less than 5%, which was considered acceptable for this study.

Computation of the hydroacoustic source using unsteady CFD data was achieved using the software Actran 2020 (MSC, Free Field Technology, Belgium). The workflow of the CFD method, which consists of five major steps, is illustrated in **Figure 4**. A quadrupole sound source was set up for the transformation of the pressure fluctuation and flow velocity. For incompressible CFD computations, only the velocity field is required (Free Field Technologies, 2020). The observed frequency range was 0–1,000 Hz. The reference pressure was set at 20 μPa. Three pulsatory cycles were calculated, and the second pulsatory cycle was chosen for data presentation.

Based on the manual instruction of Actran, the implementation of variational formulations of Lighthill's analogy derived by Oberai et al. (2000), starting with Lighthill's equation based on Actran user's guide (Free Field Technologies, 2020), is given as follows [Eq. (5)]:

$$\frac{\partial^2}{\partial t^2}(\rho - \rho_0) - c_0^2 \frac{\partial^2}{\partial x_i \partial x_j}(\rho - \rho_0) = \frac{\partial^2 T_{ij}}{\partial x_i \partial x_j}, \tag{5}$$

where T_{ij} is the Lighthill tensor [Eq. (6)]:

$$T_{ij} = \rho u_i u_j + \delta_{ij}\left((p - p_0) - c_c^2(\rho - \rho_0)\right) - \tau_{ij}, \tag{6}$$

where p and ρ are pressure and density, respectively. The reference value in the medium at rest was ρ_0, δ_{ij} is a Kronecker delta, τ_{ij} is the viscous stress tensor, and c_0 is the reference sound velocity. T_{ij} is the Lighthill tensor, and u_i and u_j are fluid velocity components. After a strong variational formulation of Eq. (5) and integration by parts along with spatial derivatives following Green's theorem, the variational formulation of Lighthill's

TABLE 1 | Mesh independence analysis.

Number of volume mesh element	Element size (mm)	Average IJV outlet velocity (m/s)	Relative error (%)
325,943	0.4	2.668164e-01	0.33%
456,231	0.3	2.675777e-01	0.04%
815,281	0.2	2.676987e-01	

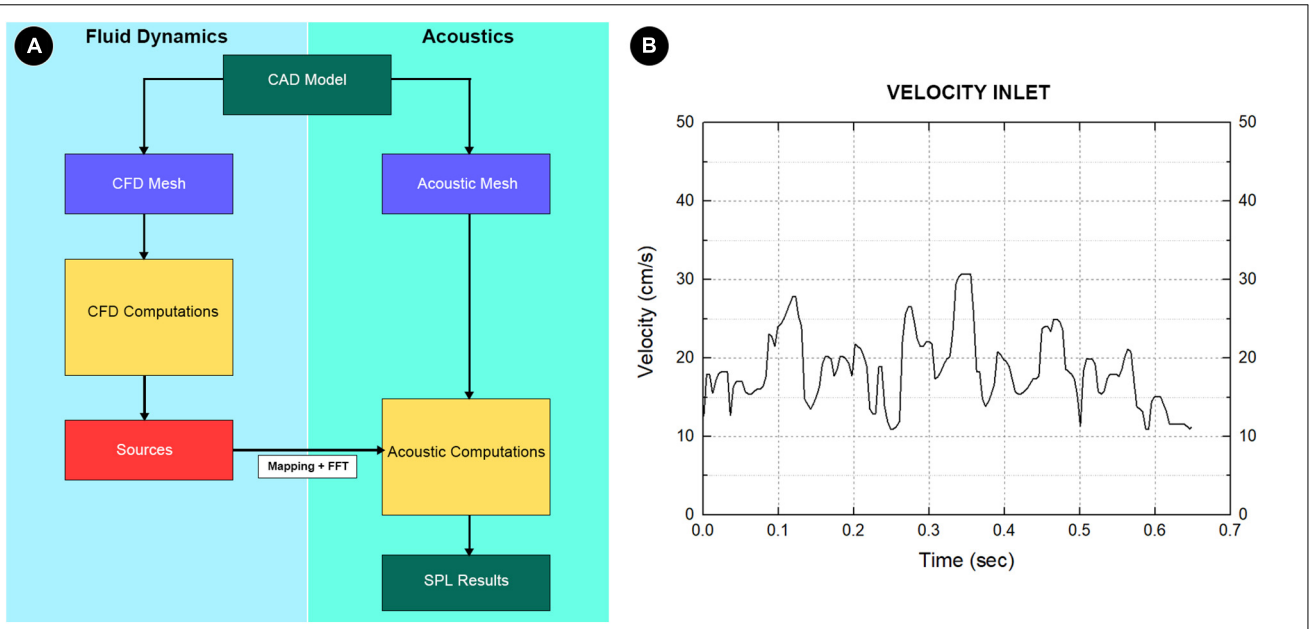

FIGURE 4 | (A) The complete workflow of computational fluid dynamics (CFD) simulation. First, the pressure, density, and velocity fields output by the CFD solver was read. Second, the contributions according to the finite element method formulation were implemented in Actran software. Third, the contributions were projected on the acoustic mesh. Fourth, the corresponding data were stored and displayed in the Actran software. Fifth, the quantities from the time to the frequency domain were transformed using the Fourier transform algorithm. **(B)** Boundary condition at the inlet section.

analogy based on the fluctuation of acoustic density $\rho_a = \rho - \rho_0$ was rewritten as [Eq. (7)]:

$$\int_{\Omega} \left(\frac{\partial^2 \rho_a}{\partial t^2} \delta\rho + c_c^2 \frac{\partial \rho_a}{\partial x_i} \frac{\partial \delta\rho}{\partial x_i} \right) dx = -\int_{\Omega} \frac{\partial T_{ij}}{\partial x_j} \frac{\partial \delta\rho}{\partial x_i} dx + \int_{\partial\Omega=\Gamma} \frac{\partial \Sigma_{ij}}{\partial x_j} n_i \delta\rho d\Gamma(x), \quad (7)$$

where $\delta\rho$ is a test function, Ω represents the computational domain. The Σ_{ij} [Eq. (8)] is:

$$\sum_{ij} = \rho u_i u_j + (p - p_0)\,\delta_{ij} - \tau_{ij}. \quad (8)$$

The Actran software computes two source terms, volume and surface contributions, using unsteady fluid velocity and density fields saved in the CFD files that relate to the acoustic mesh (Free Field Technologies, 2020). Because the vascular wall was set to be rigid, the normal acceleration was zero, so the boundary integral vanished. Thus, only the volume source term was considered in this study.

Doppler Auscultation and Sonification of Flow Sound

Doppler auscultation of the flow sound and CFD acoustics were measured and sampled at the transverse–sigmoid mainstream sinus flow/node 11,131 and the center of the diverticula/node 13,995 of case 3. An acoustic file containing three cycles of duplicated representative CFD outcomes was manually created using Adobe Audition cc 2020 (Adobe Inc.) for likeness rating purposes. The participants were asked to rate the likeness of the acoustic files using a visual analog score from 0 to 10. Sonification of the PT was performed in accordance with our previous reports using MATLAB R2017a (MathWorks). To visualize the frequency component of the recorded venous sound, a short-time Fourier transform [Eq. (9)] was implemented:

$$\mathrm{STFT}\{x[n]\}(m,\omega)\, X(\tau,\omega) = \sum_{n=-\infty}^{\infty} x[n]\, w[n-m]\, e^{-j\omega n}, \quad (9)$$

where $x[n]$ represents the sequence of discretized time-domain signals to be transformed, m is the time index, ω is the frequency, and $w[n]$ denotes the sequence of discretized window functions. The amplitude of the acoustic data was normalized for data comparison.

Statistical Analysis

Statistical analysis was performed using RStudio software (RStudio, Boston, MA, United States) and Origin 9.1.0 Pro (OriginLab Corporation, Northampton, United States). The normality of continuous data was checked using the Shapiro–Wilk test. A two-sample *t*-test or the Mann–Whitney *U* test was performed based on the outcome of data normality, as appropriate. The Pearson or Spearman correlation coefficients were computed to examine the correlations among the objective measurements. Based on Cohen's criteria (Cohen, 1988), the correlation strength was defined as very strong (0.5–1.0), moderate (0.3–0.5), or weak (<0.3). Statistical significance was set at $P < 0.05$.

RESULTS

Clinical and Radiological Characteristics

Nineteen participants (3 men and 16 women) were enrolled in this study. Most of these participants had right-sided PT ($n = 14$, 73.6%). The mean age of the participants was 36.9 ± 8.2 years. The mean PT duration was 53.0 ± 58.5 months, and the shortest and longest duration of PT were 2 and 204 months, respectively.

Of the 19 cases, 18 of them (94.7%) had PT on the dominant side of the transverse–sigmoid sinus system. The remaining patient had a co-dominant bilateral transverse–sigmoid sinus system. The average normalized degrees of TSS on the PT and contralateral sides were 71.6 ± 14.2% (one case < 33%, three cases = 33–66%, and 13 cases > 66%) and 72.4 ± 11.0% (three cases = 33–66% and five cases > 66%), respectively. Contralateral hypoplastic transverse sinuses were found in 11 (57.8%) cases. The average ITSS was 9.4 ± 2.9. An empty sella was found in eight (42.1%) participants.

Results of Retroauricular Color-Coded Doppler

When the ipsilateral IJV was compressed, the PT completely disappeared in all participants, and the vortex inside the diverticulum persisted in 18 out of 19 patients. The remaining patients' mainstream sinus flow and diverticular flow velocity were undetectable, that is, reduced to zero. The figures and data of RCCD hemodynamics are shown in **Figure 5** and **Table 2**. The median V_{mn} of the mainstream sinus flow and the diverticular flow was 40.2 (28.7/48.1) cm/s and 46.0 (34.4/63.0) cm/s, respectively, whereas after ipsilateral IJV compression, the median V_{mn} of the mainstream sinus flow and the diverticular flow dropped to 20.6 (13.4/25.5) cm/s (38.1%) and 23.3 (20.1/36.8) cm/s (39.8%). The median V_{max} of the mainstream sinus flow and the diverticular flow was 58.8 (45.2/64.5) cm/s and 70.6 (53.7/106.8) cm/s, respectively, whereas the median V_{max} of the mainstream sinus flow and the diverticular flow was 37.6 (25.0/43.5) cm/s and 49.8 (29.4/58.9) cm/s, respectively, when the ipsilateral IJV was compressed. There were significant differences in the reduction of V_{mn} (two-sample t-test, $p < 0.01$) and V_{max} (Mann–Whitney U test, $p < 0.01$) of the mainstream sinus flow. Additionally, a significant reduction in the V_{mn} (Mann–Whitney U test, $p < 0.01$) and V_{max} (Mann–Whitney U test, $p = 0.01$) of the diverticular flow was found. The median resistive index of the mainstream sinus flow and the diverticular flow was 0.60 (0.57/0.75) and 0.50 (0.41/0.69), respectively. The mean pulsatility index of the mainstream sinus flow and the diverticular flow was 1.01 (0.66/1.32) and 0.72 (0.60/1.27), respectively. No statistical significance was found in the resistive and pulsatility indices when the ipsilateral IJV was compressed.

The results of the correlation between hemodynamics, normalized TSS degree, and ITSS are shown in **Table 3**. There was no significant correlation among V_{mn}, V_{max}, and the degree of ipsilateral TSS, indicating high heterogeneity in the ipsilateral mainstream sinus and diverticular hemodynamics among subjects with venous PT.

Bilateral Internal Jugular Vein Outflow

The complete hemodynamic data of the bilateral IJV are shown in **Table 4**. The ipsilateral IJV outflow volume was 10.0 (6.9/11.8) g/s, and the contralateral IJV outflow volume was 3.6 (2.4/7.7) g/s. There was a statistically significant difference between the ipsilateral and contralateral IJV outflow volumes (Mann–Whitney U test, $p = 0.012$). The median V_{mn} of the ipsilateral and contralateral IJV flow was 20.5 (15.5/24.7) cm/s and 22.7 (13.9/32.3) cm/s, respectively, (Mann–Whitney U test, $p = 0.89$). The median V_{max} of the ipsilateral and contralateral IJV was 27.9 (23.9/41.6) cm/s and 30.2 (21.4/46.3) cm/s, respectively, (Mann–Whitney U test, $p = 0.782$). The resistive index of ipsilateral and contralateral IJV flow was 0.45 (0.27/0.69) and 0.46 (0.33/0.64), respectively, (Mann–Whitney U test, $p = 0.629$). The pulsatility index of the ipsilateral and contralateral IJV flow was 0.64 (0.33/1.12) and 0.78 (0.41/1.12), respectively, (Mann–Whitney U test, $p = 0.565$).

Hydroacoustic Outcome

The flow visualization and hemodynamics of the CFD results are shown in **Figure 6**. The peak velocity of the flow field was 0.74 m/s at the TSS. The TSS, the anteroinferior portion of the diverticulum, and the jugular bulb were regions with larger pressure gradients. The peak pressure gradient of the ipsilateral transverse–sigmoid sinus was 441,407.7 Pa/m. In contrast to the pressure gradient, the wall pressure of the transverse–sigmoid sinus gradually decreased from the inlet to the outlet, where the peak wall pressure was 1,097.9 Pa. Regarding the diverticulum, the greatest wall pressure appeared at the anteroinferior surface, which coincided with the location of dehiscence.

The results of CFD acoustics are shown in **Figure 7** and **Table 5**. The largest peak amplitude was 86.2 dBA, found in the TSS region. The TSS also presented the largest RMS amplitude of 67.7 dBA. In contrast, the peak and RMS amplitude of the upper curve sigmoid sinus were 65.7 and 48.0 dBA, respectively, which were the lowest among the observed anatomical locations. The largest difference in the flow amplitude was 20.5 dB. The peak amplitude at the middle diverticulum was 0.9 dBA larger than the mainstream transverse–sigmoid sinus flow, whereas the RMS amplitude of the mainstream transverse–sigmoid sinus flow was 1.8 dBA. The frequency of the largest peak amplitude ranged from 49.4 to 92.5 Hz.

The short-time Fourier transforms of the Doppler and CFD acoustic data are shown in **Figure 8**. The patient-based likeness scoring of the *in vivo* Doppler transverse–sigmoid mainstream sinus (**Supplementary Material 1**) and diverticular flows (**Supplementary Material 2**) were 7 and 5, whereas the ratings of CFD acoustics of the corresponding locations were 6 (**Supplementary Material 3**) and 6 (**Supplementary Material 4**), respectively.

DISCUSSION

The RCCD technique is a newly proposed Doppler ultrasound method for detecting mainstream sinus and diverticular hydroacoustic characteristics at the transverse–sigmoid

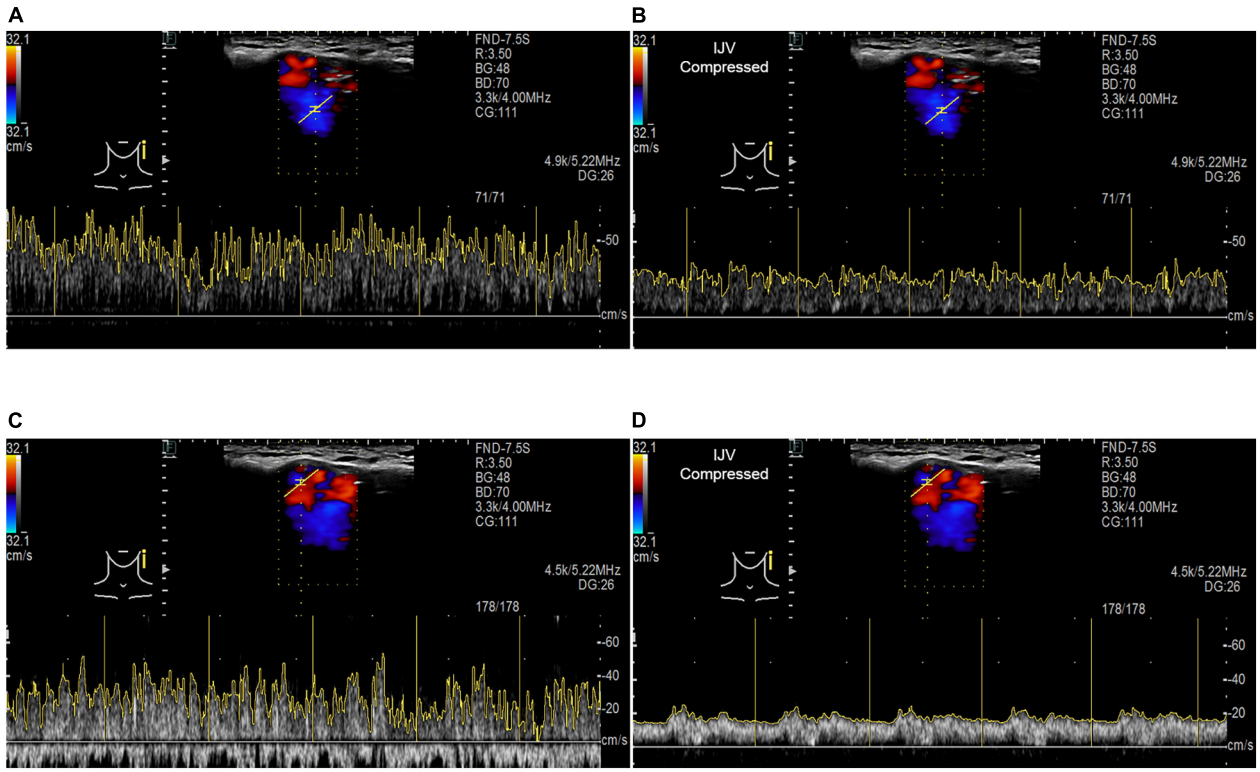

FIGURE 5 | RCCD and IJV compression examination of the association between PT and transverse–sigmoid junction hemodynamics. IJV indicates the internal jugular vein. The yellow vertical lines indicate the RR intervals of the electrocardiogram. **(A)** Real-time mainstream sinus flow velocity spectrum before IJV compression. **(B)** Real-time mainstream sinus flow velocity spectrum during IJV compression. **(C)** Real-time diverticular flow velocity spectrum before IJV compression. **(D)** Real-time diverticular flow velocity spectrum during IJV compression.

junction. By conflating the RCCD technique with ipsilateral IJV compression, the changes between PT and *in vivo* hemodynamics can be investigated non-invasively. It was discovered that PT subsided when the V_{mn} of sinus flow reduced by approximately 50%. From the presence to the disappearance of PT, it is postulatsed that this quantitative range of flow velocity reduction offers a bottom-line curative marker for both extraluminal compression and endoluminal surgeries. However, the former surgical technique conceivably requires less flow velocity reduction due to the thickening of the soundproof sigmoid

TABLE 2 | Results of RCCD transverse–sigmoid junction hemodynamics of 19 participants.

	Mainstream sinus flow			
	Mean velocity	**Peak velocity**	**Resistive index**	**Pulsatility index**
	cm/s	**cm/s**	**Dimensionless**	**Dimensionless**
RCCD	40.2 (28.7/48.1)	58.8 (45.2/64.5)	0.60 (0.57/0.75)	1.01 (0.66/1.32)
RCCD while IJV compression	20.6 (13.4/25.5)	37.6 (25.0/43.5)	0.60 (0.51/0.78)	0.98 (0.58/1.30)
p value	<0.01[a]	<0.01[b]	0.953[b]	0.860[a]
Diverticular flow				
	Mean velocity	Peak velocity	Resistive index	Pulsatility index
	cm/s	cm/s	Dimensionless	Dimensionless
RCCD	46.0 (34.4/63.0)	70.6 (53.7/106.8)	0.50 (0.41/0.69)	0.72 (0.60/1.27)
RCCD while IJV compression	23.3 (20.1/36.8)	49.8 (29.4/58.9)	0.55 (0.39/0.65)	0.73 (0.54/1.16)
p value	<0.01[b]	0.01[b]	0.831[a]	0.881[b]

Variables are expressed as median and interquartile range.
RCCD, retroauricular color-coded Doppler method.
[a]*Two-sample t-test;* [b]*Mann–Whitney U-test.*

TABLE 3 | Results of correlation analysis between hemodynamics and transverse sinus stenosis.

Ipsilateral normalized TSS	Mainstream sinus flow		Diverticular flow	
	Mean velocity	Peak velocity	Mean velocity	Peak velocity
Spearman *r* value	0.145	0.203	– 0.115	– 0.02
Spearman *p* value	0.551	0.403	0.636	0.914
ITSS score				
Spearman *r* value	0.225	0.249	0.167	0.290
Spearman *p* value	0.353	0.302	0.494	0.226

TSS, transverse sinus stenosis; ITSS, index of transverse sinus stenosis.
All correlation statistics were done using the Spearman correlation.

TABLE 4 | Results of bilateral internal jugular vein hemodynamics of 19 participants.

	Outflow volume	Mean velocity	Peak velocity	Resistive index	Pulsatility index
	g/s	cm/s	cm/s	Non-dimensional	Non-dimensional
Ipsilateral IJV	10.5 (9.3/17.9)	22.1 (16.9/31.9)	31.5 (25.2/44.2)	0.44 (0.27/0.62)	0.63 (0.33/0.99)
Contralateral IJV	4.7 (2.6/7.4)	24.4 (14.9/34.5)	33.8 (22.6/47.3)	0.46 (0.29/0.68)	0.70 (0.35/1.14)
p value	<0.01	0.792	0.609	0.682	0.619

Variables are expressed as median and interquartile range.
IJV, internal jugular vein.
All statistics were done using the Mann–Whitney U-test.

wall, although the compression depth of the transverse–sigmoid junction ought to be performed with circumspection to prevent the iatrogenic cause of intracranial pressure (Hsieh et al., 2022; Qiu et al., 2022). A recent clinical study revealed that sinus flow velocity is reduced after a lumbar puncture without a concomitant reduction in the bulk flow rate, resulting in a 3.8 ± 3.4 improvement of PT intensity on a 0–10 Likert scale in 10 subjects (Haraldsson et al., 2019). They hypothesized that velocity, not flow rate, was related to PT. However, in this study, planar velocity and flow volume were reduced at the transverse–sigmoid junction when the PT was completely suppressed by ipsilateral IJV compression. Furthermore, the ipsilateral sinus outflow volume was significantly larger than that of the contralateral side. Although the contralateral V_{mn} of the IJV was found to be slightly higher than that of the ipsilateral side, given the constant negative pressure produced by the heart during the diastolic phase, the flow velocity of the returning venous flow was conceivably determined by the cross-sectional area tangential to the flow direction. Regarding previous clinical discoveries, it is not uncommon for PT to intensify when the contralateral IJV is compressed, and in subjects with bilateral SSWAs, unilateral PT may alter to the contralateral side during compression of the ipsilateral IJV (Kline et al., 2020; Hsieh et al., 2021b). This signifies that the asymmetric distribution of the flow volume may underpin the development of PT. Thus, we extrapolate that a high flow velocity and flow volume, that is, a high flow kinetic energy, are prerequisite conditions for PT.

Due to the fluctuating shape of the transverse–sigmoid sinus, differences in the sinus flow velocity and pressure gradient distribution led to a segmental distribution of flow amplitude. A larger amplitude of the flow sound was detected at segments with a higher flow velocity and pressure gradient. This finding substantiates the therapeutic effect of endoluminal TSS stenting, which targets the reduction of regional flow velocity and relief of the *trans*-stenotic pressure gradient (Mu et al., 2021a). Previous computational studies found that the flow-induced displacement of the vascular wall could generate vibro-acoustic noise from 48.76 to 116.57 dB (Tian et al., 2017; Mu et al., 2021a,b). The amplitude of the vibro-acoustic sound surpassed that of the hydroacoustic source when the volume and surface contributions were juxtaposed (Hsieh et al., 2022). Nevertheless, based on intraoperative measurements, the frequency of vascular displacement was below the hearing threshold (Hsieh et al., 2022). It remains unclear whether the vibro-acoustic sound is generated solely from the vibration of the sigmoid sinus wall. To that end, PT likely results from hydroacoustic noise in the junction with the vibration of the vascular wall.

The vortex has been suggested to cause PT in subjects with SSWAs (Amans et al., 2018; Eisenman et al., 2018). A large 4D flow MR case series found that 68% of subjects with diverticulum presented a vortex (Li et al., 2021). In contrast to the mainstream sinus flow, RCCD unveiled that the vortex inside the diverticulum is characterized by low or no pulse synchronicity, and the hydroacoustic sound generated by the vortex is less similar to the participants' PT. The PT disappears despite the vortex remaining inside the diverticulum. This strongly indicates that the flow kinetic energy outweighs the formation of vortices in the acoustic production of the PT. In addition, a difference of less than 1 dB was detected by virtual microphones placed at the center of the mainstream and diverticular flows simulated using the CFD method. These results imply that the flow velocity outweighs the vortex in the acoustic production of PT. In fact, individuals with a diverticulum can be accidentally identified even in the absence of PT (Hsieh et al., 2021b). Furthermore, the therapeutic

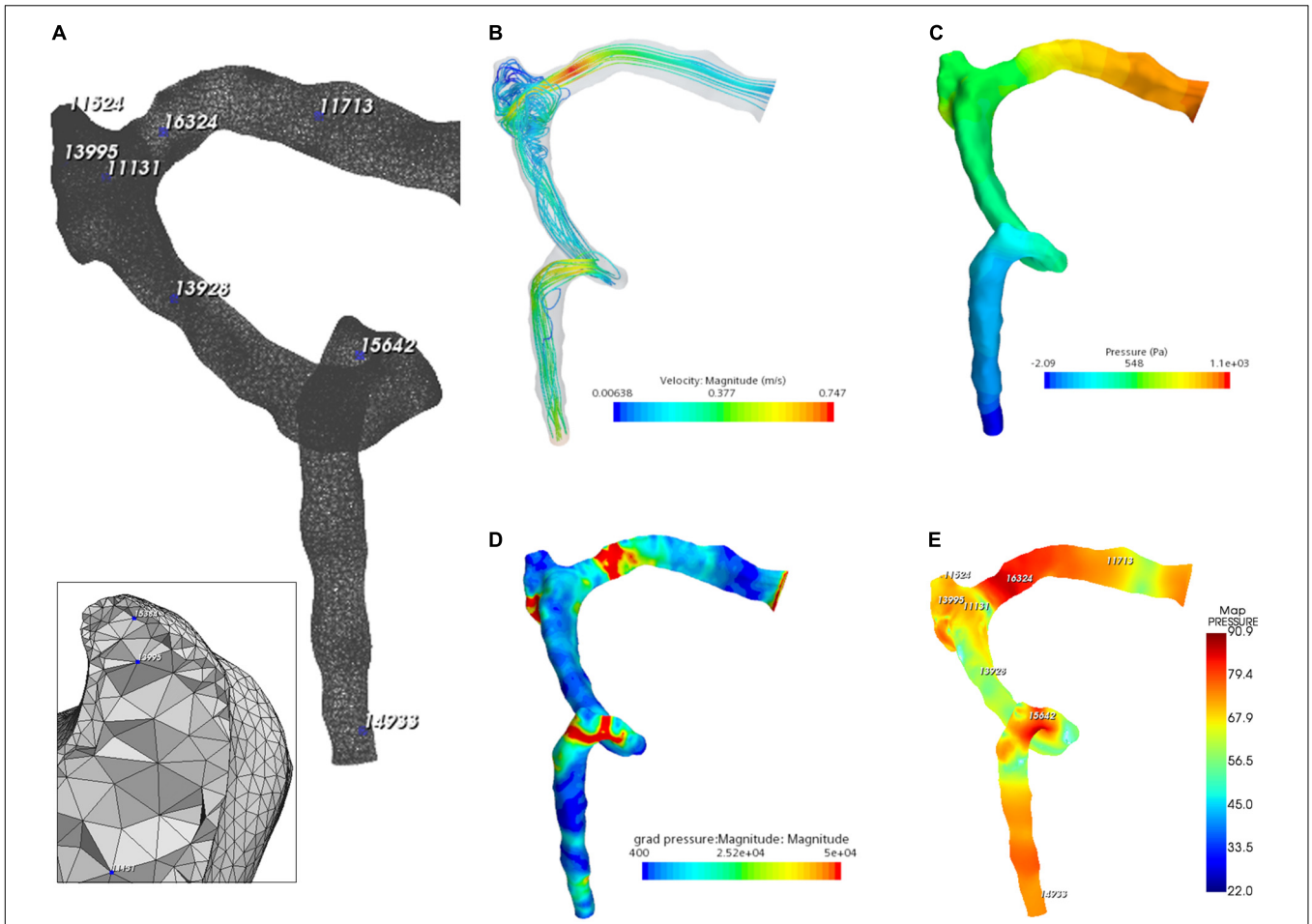

FIGURE 6 | Hydroacoustic characteristics of the ipsilateral transverse–sigmoid sinus. **(A)** A 3D finite element model of ipsilateral transverse–sigmoid sinus of case 3. Eight nodes were chosen for hydroacoustic evaluation. **(B)** Velocity streamline of the ipsilateral transverse–sigmoid sinus. **(C)** Wall pressure distribution of the ipsilateral transverse–sigmoid sinus. **(D)** Pressure gradient distribution of the ipsilateral transverse–sigmoid sinus (unit: Pa/m). **(E)** Acoustic distribution of the ipsilateral transverse–sigmoid sinus (unit: dBA).

effect of complete reduction of a diverticulum can be unreliable intraoperatively, and PT can be resolved by reducing the flow velocity even without the exclusion of the diverticulum from venous return (Han et al., 2017; Zhang et al., 2019; Hsieh and Wang, 2020). Based on the current RCCD results and previous incidences, a diverticulum is not an essential prerequisite for PT.

Transcranial Doppler ultrasound reveals intracranial real-time flow hydroacoustics using the Doppler wave effect, which yields higher spatial and temporal resolutions than MR techniques (Meckel et al., 2013). Studies have suggested that MR methods tend to underestimate the peak systolic velocity of intracranial and cervical arteries compared to ultrasound (Harloff et al., 2013). Compared to the only previous imaging study that investigated subjects with diverticulum independently, the V_{mn} detected by the current RCCD technique closely conforms to the results measured by 4D MR (Li et al., 2021), with 7.3% difference in V_{mn} (**Table 6**); nonetheless, a stark difference in V_{max} is found between their and our results. Additionally, ITSS in this study was also found uncorrelated with the hemodynamic parameters, which is antithetical to the study of Ding et al. (2021), since the Doppler insonation plane was more distant from the center of TSS, from which the sinus flow velocity can decelerate after issuing from a TSS. We reckon that these study discrepancies predominantly result from the fundamental difference in the selection of region/point of interest. Hence, the planar hemodynamic parameters gaged by the RCCD method can yield crucial hemodynamic insights and allow surgeons to cope with PT objectively.

The benefits of emerging 4D MR techniques for detecting the hemodynamics of dural venous sinus flows, however, are promising and conspicuous in comparison to ultrasound techniques. As the 4D MR technique allows 3D coverage of the transverse–sigmoid sinus, the possibility of measuring flow velocities at any time/spatial point of interest after scanning can be achieved. Amans and Wang/Gong's research teams have combined 4D flow MR techniques with CFD methods (Amans et al., 2018; Haraldsson et al., 2019; Ding et al., 2021; Li et al., 2021). It has been suggested that highly convoluted flow patterns

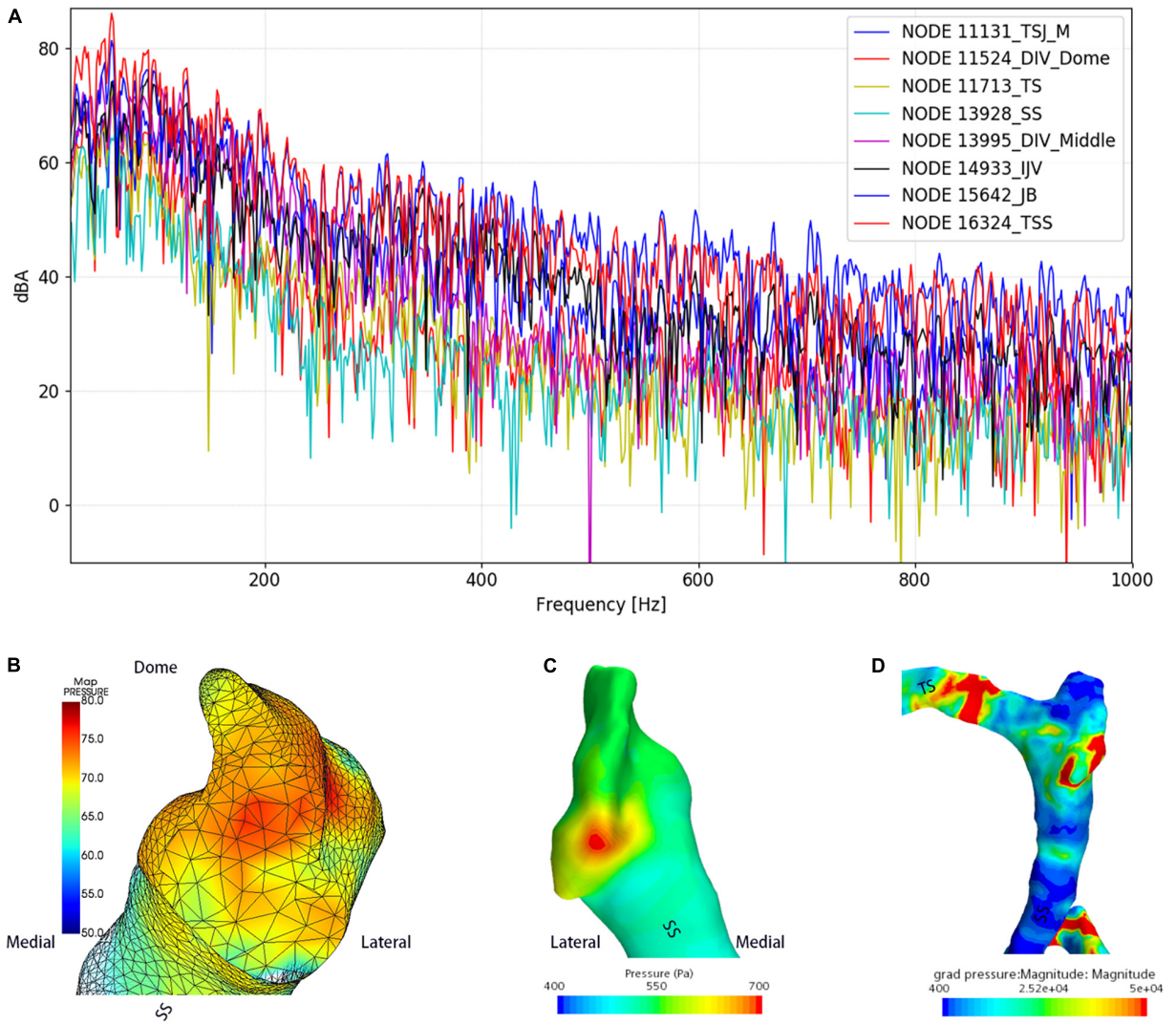

FIGURE 7 | Regional hydroacoustic characteristics of the ipsilateral transverse–sigmoid sinus. SS indicates the sigmoid sinus. **(A)** The amplitude–frequency spectrum of the ipsilateral transverse–sigmoid sinus. **(B)** The amplitude of the diverticular flow (unit: dBA). **(C)** Wall pressure distribution at the transverse–sigmoid junction and the diverticulum. **(D)** Pressure gradient distribution of the ipsilateral transverse–sigmoid sinus.

are observed in those with a diverticulum (Amans et al., 2018; Li et al., 2021). Furthermore, post-stenotic high jet flow velocity and *trans*-stenotic pressure gradient near the transverse–sigmoid junction, both of which are subjected to variations in intracranial pressure (Haraldsson et al., 2019), may be considered as the salient contributing factors of PT (Ding et al., 2021). The *in vivo* RCCD indicates that immediate reduction of flow velocity at the transverse–sigmoid junction is directly correlated to the

TABLE 5 | Results of CFD hydroacoustic outcomes.

Locations	TS	TSS	TSJ. M.	Div. Mid.	Div. dome	SS	JB	IJV
Node number	11,713	16,324	11,131	13,995	11,524	13,928	15,642	14,933
Peak amplitude (dBA)	72.5	86.2	74.3	75.2	71.4	65.7	81.4	74.9
Frequency at peak amplitude (Hz)	58.6	58.6	60.1	49.4	58.6	63.2	58.6	92.5
RMS amplitude* (dBA)	52.3	67.7	57.1	59.9	53.2	48.0	63.7	59.3

TS, transverse sinus; TSS, transverse sinus stenosis; TSJ. M., transverse–sigmoid junction mainstream; Div.Mid., middle portion of the diverticulum; Div. Dome, the dome of the diverticulum; SS, sigmoid sinus; JB, jugular bulb; and IJV, internal jugular vein.

**RMS amplitude measured from 0 to 1 kHz.*

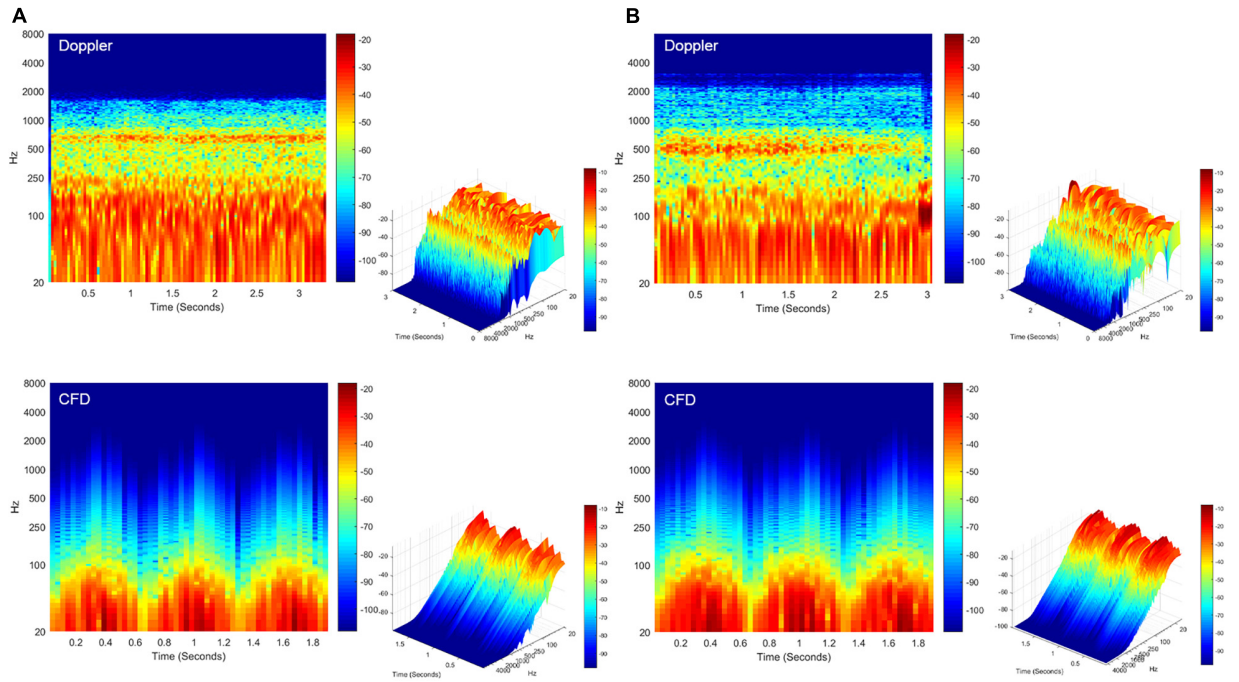

FIGURE 8 | Spectrotemporal results of *in vivo* Doppler and CFD. **(A)** Short-time Fourier transformation of the Doppler mainstream sinus flow (upper panel) and CFD mainstream sinus flow (lower panel, node 11131). **(B)** Short-time Fourier transformation of the Doppler diverticular flow (upper panel) and CFD diverticular flow (lower panel, node 13995). CFD, computational fluid dynamics.

TABLE 6 | Comparison of results in subjects with diverticulum.

	Number of subjects with diverticulum	V_{mn} (cm/s)	V_{max} (cm/s)	Measurement plane
Previous 4D-MR Study [1]	22	55.92 ± 20.08 [1]	147.58 ± 42.16 [1]	V_{max} at TS-SS [1]
Present study	19	52.08 ± 28.61[a]	85.14 ± 48.55[a]	TSJ

[a]*Largest value acquired from the TSJ region expressed in mean ± standard deviation.*
TS-SS, transverse–sigmoid sinus; TSJ, transverse–sigmoid junction; and V_{max}, peak velocity.
Comparison of our results with previously reported results: [1] Data from Li et al. (2021).

elimination of PT. However, it remains unknown whether PT arises owing to the formation of dehiscence or the fact that intracranial hemodynamics are altered in the first place.

This study is limited by the sample size for the RCCD examination. However, the current sample size is on par with the previous 4D-MR flow or CT venogram studies. As this study focuses on intracohort comparisons rather than group comparisons, the current Doppler results appear to demonstrate a convincing reduction in flow velocity modulated by ipsilateral IJV compression. Furthermore, RCCD is reserved for those with a protrusive diverticulum or laterally placed sigmoid sinus, which hampers the understanding of PT in patients with a complete mastoid cortex and in healthy controls. The TCCD technique can provide a high temporal and spatial resolution of the transverse sinus flow spectrum for CFD simulation, which benefits hydroacoustic investigations of the entire transverse–sigmoid sinus system. However, the poor temporal window can greatly reduce insonation of the contralateral skull base and sampling of the blood flow. Thus, we are currently working on increasing the TCCD data to reveal differences between subjects with and without PT. Although the current computational acoustic data reaches a high resemblance of PT sound, nuanced acoustic differences between Doppler and current CFD techniques require a thorough and comprehensive investigation in the future. Continuous refinement of the establishment of boundary conditions is warranted.

CONCLUSION

The currently proposed RCCD method unfolded transient hydroacoustic characteristics of sinus flow at the transverse–sigmoid junction with high spatial and temporal resolutions.

By implementing the RCCD method in junction with ipsilateral IJV compression, PT subsides as the V_{mn} of the mainstream sinus flow and the diverticular vortex decreases averagely by 51.2 and 50.6%, respectively. However, the diverticular vortex persisted during ipsilateral IJV compression, notwithstanding a holistic reduction in sinus flow kinetic energy. In addition, the amplitude difference between the mainstream sinus and diverticular flows was less than 1 dB based on our CFD analysis. Therefore, PT is associated with the flow kinetic energy instead of the sheer formation of vortex *per se*; regions with larger flow velocity and pressure gradient engender greater flow amplitude. As the combined implementation of the RCCD technique and ipsilateral IJV compression uncloaks individual quantitative range of velocity reduction to eliminate PT non-invasively, this marker can be applied as a presurgical curative index for surgeons to resolve PT efficiently.

DATA AVAILABILITY STATEMENT

The original contributions presented in this study are included in the article/**Supplementary Material**, further inquiries can be directed to the corresponding author.

ETHICS STATEMENT

The studies involving human participants were reviewed and approved by Ethical Committees of the Eye, Ear, Nose, and Throat Hospital in Shanghai, China. The patients/participants provided their written informed consent to participate in this study.

AUTHOR CONTRIBUTIONS

XG performed all Doppler examinations and drafted the article. Y-LH designed the study, assisted in drafting the manuscript, and performed all statistical, radiologic, and acoustic analyses in this study. XW performed computational fluid dynamics and post-analysis. WW is the lead surgeon who supervised this study. All authors contributed to the article and approved the submitted version.

FUNDING

This study was supported by the National Science Foundation of China (NSFC no. 81670933).

ACKNOWLEDGMENTS

XG would like to thank Y-LH from the WW research team for contriving the RCCD method to assess the correlation between PT and transient flow variations, providing major content/graphical designs for this study and assisting in the writing of this manuscript. We also would like to thank F. Wu, who assisted with the adjustment of Doppler parameters.

SUPPLEMENTARY MATERIAL

The Supplementary Material for this article can be found online at: https://www.frontiersin.org/articles/10.3389/fnhum.2022.862420/full#supplementary-material

REFERENCES

Amans, M. R., Haraldsson, H., Kao, E., Kefayati, S., Meisel, K., Khangura, R., et al. (2018). MR venous flow in sigmoid sinus diverticulum. *AJNR Am. J. Neuroradiol.* 39, 2108–2113. doi: 10.3174/ajnr.A5833

Cohen, J. (1988). *Statistical Power Analysis for the Behavioral Sciences*, 2nd Edn. Hillsdale, NJ: Lawrence Erlbaum Associates.

Cummins, D. D., Caton, M. T., Shah, V., Meisel, K., Glastonbury, C., and Amans, M. R. (2021). MRI and MR angiography evaluation of pulsatile tinnitus: a focused, physiology—based protocol. *J. Neuroimaging* 32, 253–263. doi: 10.1111/jon.12955

Da Silveira Carvalho, G. B., De Andrade Matas, S. L., Idagawa, M. H., Tibana, L. A. T., De Carvalho, R. S., Silva, M. L. S., et al. (2017). A new index for the assessment of transverse sinus stenosis for diagnosing idiopathic intracranial hypertension. *J. NeuroInterv. Surg.* 9, 173–177. doi: 10.1136/neurintsurg-2016-012605

Ding, H., Zhao, P., Lv, H., Li, X., Qiu, X., Zeng, R., et al. (2021). Correlation between trans-stenotic blood flow velocity differences and the cerebral venous pressure gradient in transverse sinus stenosis: a prospective 4-dimensional flow magnetic resonance imaging study. *Neurosurgery* 89, 549–556. doi: 10.1093/neuros/nyab222

Dong, C., Zhao, P. F., Yang, J. G., Liu, Z. H., and Wang, Z. C. (2015). Incidence of vascular anomalies and variants associated with unilateral venous pulsatile tinnitus in 242 patients based on dual-phase contrast-enhanced computed tomography. *Chin. Med. J.* 128, 581–585. doi: 10.4103/0366-6999.151648

Durst, C. R., Ornan, D. A., Reardon, M. A., Mehndiratta, P., Mukherjee, S., Starke, R. M., et al. (2016). Prevalence of dural venous sinus stenosis and hypoplasia in a generalized population. *J. Neurointerv. Surg.* 8, 1173–1177. doi: 10.1136/neurintsurg-2015-012147

Eisenman, D. J., Raghavan, P., Hertzano, R., and Morales, R. (2018). Evaluation and treatment of pulsatile tinnitus associated with sigmoid sinus wall anomalies. *Laryngoscope.* 128(Suppl. 2), S1–S13. doi: 10.1002/lary.27218

Free Field Technologies (2020). *Actran 2020 User's Guide, vol. 1. Installation, Operations, Theory and Utilities*. Mont-Saint-Guibert: Free Field Technologies.

Grewal, A. K., Kim, H. Y., Comstock, R. H., Berkowitz, F., Kim, H. J., and Jay, A. K. (2014). Clinical presentation and imaging findings in patients with pulsatile tinnitus and sigmoid sinus diverticulum/dehiscence. *Otol. Neurotol.* 35, 16–21. doi: 10.1097/MAO.0b013e31829ab6d7

Guo, P., and Wang, W. Q. (2015). Degree of sigmoid sinus compression and the symptom relief using magnetic resonance angiography in venous pulsating tinnitus. *Clin. Exp. Otorhinolaryngol.* 8, 111–116. doi: 10.3342/ceo.2015.8.2.111

Han, Y., Yang, Q., Yang, Z., Xia, J., Su, T., Yu, J., et al. (2017). Computational fluid dynamic simulation of hemodynamic alterations in sigmoid sinus diverticulum and ipsilateral upstream sinus stenosis after stent implantation in patients with pulsatile tinnitus. *World Neurosurg.* 106, 308–314. doi: 10.1016/j.wneu.2017.06.168

Haraldsson, H., Leach, J. R., Kao, E. I., Wright, A. G., Ammanuel, S. G., Khangura, R. S., et al. (2019). Reduced jet velocity in venous flow after CSF drainage: assessing hemodynamic causes of pulsatile tinnitus. *AJNR Am. J. Neuroradiol.* 40, 849–854. doi: 10.3174/ajnr.A6043

Harloff, A., Zech, T., Wegent, F., Strecker, C., Weiller, C., and Markl, M. (2013). Comparison of blood flow velocity quantification by 4D flow MR imaging with ultrasound at the carotid bifurcation. *AJNR Am. J. Neuroradiol.* 34, 1407–1413. doi: 10.3174/ajnr.A3419

Hewes, D., Morales, R., Raghavan, P., and Eisenman, D. J. (2020). Pattern and severity of transverse sinus stenosis in patients with pulsatile tinnitus associated with sigmoid sinus wall anomalies. *Laryngoscope* 130, 1028–1033. doi: 10.1002/lary.28168

Hsieh, Y. L., Gao, X., Wang, X., Hsiang, F. C., Sun, X., and Wang, W. (2022). Therapeutic validation of venous pulsatile tinnitus and biomaterial applications for temporal bone reconstruction surgery using multi-sensing platforms and coupled computational techniques. *Front. Bioeng. Biotechnol.* 9:777648. doi: 10.3389/fbioe.2021.777648

Hsieh, Y. L., and Wang, W. (2020). Extraluminal sigmoid sinus angioplasty: a pertinent reconstructive surgical method targeting dural sinus hemodynamics to resolve pulsatile tinnitus. *Otol. Neurotol.* 41, e132–e145. doi: 10.1097/MAO.0000000000002464

Hsieh, Y. L., Wang, X., Xu, X. B., Wu, Y., Wang, S., Yu, D., et al. (2021a). Hydroacoustic sonification and flow pattern investigation of venous pulsatile tinnitus using MEMS hydrophone sensing and dye flow visualization techniques: pilot 3D printing, computational fluid dynamics, and psychoacoustic study. *Sens. Mater.* 33, 3439–3457. doi: 10.18494/SAM.2021.3519

Hsieh, Y. L., Wu, Y., Wang, H., Xu, X., Guo, P., Wang, X., et al. (2021b). Associations among audiometric, doppler hydroacoustic, and subjective outcomes of venous pulsatile tinnitus. *ORL J. Otorhinolaryngol. Relat. Spec.* [Epub ahead of print]. doi: 10.1159/000517610

Kim, C. S., Kim, S. Y., Choi, H., Koo, J. W., Yoo, S. Y., An, G. S., et al. (2016). Transmastoid reshaping of the sigmoid sinus: preliminary study of a novel surgical method to quiet pulsatile tinnitus of an unrecognized vascular origin. *J. Neurosurg.* 125, 441–449. doi: 10.3171/2015.6.JNS15961

Kline, N. L., Angster, K., Archer, E., Raghavan, P., Morales, R. E., Mathews, M. K., et al. (2020). Association of pulse synchronous tinnitus and sigmoid sinus wall abnormalities in patients with idiopathic intracranial hypertension. *Am. J. Otolaryngol.* 41:102675. doi: 10.1016/j.amjoto.2020.102675

Lee, S. Y., Kim, M. K., Bae, Y. J., An, G. S., Lee, K., Choi, B. Y., et al. (2020). Longitudinal analysis of surgical outcome in subjects with pulsatile tinnitus originating from the sigmoid sinus. *Sci. Rep.* 10:18194. doi: 10.1038/s41598-020-75348-3

Li, X., Qiu, X., Ding, H., Lv, H., Zhao, P., Yang, Z., et al. (2021). Effects of different morphologic abnormalities on hemodynamics in patients with venous pulsatile tinnitus: a four−dimensional flow magnetic resonance imaging study. *J. Magn. Reson. Imaging* 53, 1744–1751. doi: 10.1002/jmri.27503

Mattox, D. E., and Hudgins, P. (2008). Algorithm for evaluation of pulsatile tinnitus. *Acta Otolaryngol.* 128, 427–431. doi: 10.1080/00016480701840106

Meckel, S., Leitner, L., Bonati, L. H., Santini, F., Schubert, T., Stalder, A. F., et al. (2013). Intracranial artery velocity measurement using 4D PC MRI at 3 T: comparison with transcranial ultrasound techniques and 2D PC MRI. *Neuroradiology* 55, 389–398. doi: 10.1007/s00234-012-1103-z

Mu, Z., Li, X., Zhao, D., Qiu, X., Dai, C., Meng, X., et al. (2022). Hemodynamics study on the relationship between the sigmoid sinus wall dehiscence and the blood flow pattern of the transverse sinus and sigmoid sinus junction. *J. Biomech.* 135:111022. doi: 10.1016/j.jbiomech.2022.111022

Mu, Z., Liu, L., Sun, Y., Gao, B., Lv, H., Zhao, P., et al. (2021a). Multiphysics coupling numerical simulation of flow−diverting stents in the treatment of patients with pulsatile tinnitus. *Int. J. Numer. Method. Biomed. Eng.* 37:e3526. doi: 10.1002/cnm.3526

Mu, Z., Sun, Y., Li, X., Qiu, X., Gao, B., Liu, Y., et al. (2021b). Multiphysics coupling study on the effect of blood flow pulsation in patients with pulsatile tinnitus. *Biocybern. Biomed. Eng.* 41, 1197–1207. doi: 10.1016/j.bbe.2021.08.008

Mu, Z., Qiu, X., Zhao, D., Li, X., Fu, M., Liu, Y., et al. (2020). Hemodynamic study on the different therapeutic effects of SSWD resurfacing surgery on patients with pulsatile tinnitus. *Comput. Methods Programs Biomed.* 190:105373. doi: 10.1016/j.cmpb.2020.105373

Oberai, A. A., Roknaldin, F., and Hughes, T. J. (2000). Computational procedures for determining structural-acoustic response due to hydrodynamic sources. *Comput. Methods Appl. Mech. Eng.* 190, 345–361. doi: 10.1016/S0045-7825(00)00206-1

Qiu, X., Zhao, P., Ding, H., Li, X., Lv, H., Yang, Z., et al. (2021a). Bone remodeling in sigmoid sinus diverticulum after stenting for transverse sinus stenosis in pulsatile tinnitus: a case report. *World J. Clin. Cases* 9, 2320–2325. doi: 10.12998/wjcc.v9.i10.2320

Qiu, X., Zhao, P., Li, X., Ding, H., Lv, H., Zeng, R., et al. (2021b). The relationships among transverse sinus stenosis measured by CT venography, venous transstenotic pressure gradient and intracranial pressure in patients with unilateral venous pulsatile tinnitus. *Front. Neurosci.* 15:694731. doi: 10.3389/fnins.2021.694731

Qiu, X., Zhao, P., Mu, Z., Dai, C., Li, X., Xu, N., et al. (2022). Effects of different degrees of extraluminal compression on hemodynamics in a prominent transverse–sigmoid sinus junction. *Front. Hum. Neurosci.* 16:823455. doi: 10.3389/fnhum.2022.823455

Tian, S., Wang, L., Yang, J., Mao, R., Liu, Z., and Fan, Y. (2017). Sigmoid sinus cortical plate dehiscence induces pulsatile tinnitus through amplifying sigmoid sinus venous sound. *J. Biomech.* 52, 68–73. doi: 10.1016/j.jbiomech.2016.12.012

Wang, J., Wang, Y., Zhang, J., Tian, S., Wei, J., Pu, F., et al. (2019). In vivo measurements of collapse behavior of human internal jugular vein during head-up tilt tests. *Physiol. Meas.* 40:075006. doi: 10.1088/1361-6579/ab1e10

Zhang, C., Li, Q., and Li, S. (2019). Physical and psychological outcomes of simple sigmoid sinus bony wall repair for pulsatile tinnitus due to sigmoid sinus wall anomalies. *Eur. Arch. Otorhinolaryngol.* 276, 1327–1334. doi: 10.1007/s00405-019-05380-1

Zhao, P., Ding, H., Lv, H., Li, X., Qiu, X., Zeng, R., et al. (2021a). CT venography correlate of transverse sinus stenosis and venous transstenotic pressure gradient in unilateral pulsatile tinnitus patients with sigmoid sinus wall anomalies. *Eur. Radiol.* 31, 2896–2902. doi: 10.1007/s00330-020-07415-2

Zhao, P., Jiang, C., Lv, H., Zhao, T., Gong, S., and Wang, Z. (2021b). Why does unilateral pulsatile tinnitus occur in patients with idiopathic intracranial hypertension? *Neuroradiology* 63, 209–216. doi: 10.1007/s00234-020-02541-6

Conflict of Interest: The authors declare that the research was conducted in the absence of any commercial or financial relationships that could be construed as a potential conflict of interest.

Publisher's Note: All claims expressed in this article are solely those of the authors and do not necessarily represent those of their affiliated organizations, or those of the publisher, the editors and the reviewers. Any product that may be evaluated in this article, or claim that may be made by its manufacturer, is not guaranteed or endorsed by the publisher.

Advantages of publishing in Frontiers

OPEN ACCESS
Articles are free to read for greatest visibility and readership

FAST PUBLICATION
Around 90 days from submission to decision

HIGH QUALITY PEER-REVIEW
Rigorous, collaborative, and constructive peer-review

TRANSPARENT PEER-REVIEW
Editors and reviewers acknowledged by name on published articles

Frontiers
Avenue du Tribunal-Fédéral 34
1005 Lausanne | Switzerland

Visit us: www.frontiersin.org
Contact us: frontiersin.org/about/contact

REPRODUCIBILITY OF RESEARCH
Support open data and methods to enhance research reproducibility

DIGITAL PUBLISHING
Articles designed for optimal readership across devices

FOLLOW US
@frontiersin

IMPACT METRICS
Advanced article metrics track visibility across digital media

EXTENSIVE PROMOTION
Marketing and promotion of impactful research

LOOP RESEARCH NETWORK
Our network increases your article's readership